AN ANALYSIS OF THE INFLUENCE OF SOME

EXTERNAL DISTURBANCES ON THE AERODYNAMIC

STABILITY OF TURBINE ENGINE AXIAL FLOW

FANS AND COMPRESSORS

ENGINE TEST FACILITY
ARNOLD ENGINEERING DEVELOPMENT CENTER
AIR FORCE SYSTEMS COMMAND
ARNOLD AIR FORCE STATION, TENNESSEE 37389

August 1977

Final Report for Period June 1973 — June 1977

Approved for public release; distribution unlimited.

. Air Force

Prepared for

DIRECTORATE OF TEST ENGINEERING
DEPUTY FOR OPERATIONS
ARNOLD ENGINEERING DEVELOPMENT CENTER
AIR FORCE SYSTEMS COMMAND
ARNOLD AIR FORCE STATION, TENNESSEE 37389

APPROVAL STATEMENT

This technical report has been reviewed and is approved for publication.

FOR THE COMMANDER

MARION L. LASTER
Director of Test Engineering
Deputy for Operations

ALAN L. DEVEREAUX
Colonel, USAF
Deputy for Operations

UNCLASSIFIED

REPORT DOCUMENTATION PAGE		READ INSTRUCTIONS BEFORE COMPLETING FORM
1 REPORT NUMBER AEDC-TR-77-80	2 GOVT ACCESSION NO.	3 RECIPIENT'S CATALOG NUMBER
4 TITLE (and Subtitle) AN ANALYSIS OF THE INFLUENCE OF SOME EXTERNAL DISTURBANCES ON THE AERODYNAMIC STABILITY OF TURBINE ENGINE AXIAL FLOW FANS AND COMPRESSORS		5 TYPE OF REPORT & PERIOD COVERED Final Report - June 1973 - June 1977
		6 PERFORMING ORG REPORT NUMBER
7 AUTHOR(s) William F. Kimzey, ARO, Inc.		8 CONTRACT OR GRANT NUMBER(s)
9 PERFORMING ORGANIZATION NAME AND ADDRESS Arnold Engineering Development Center Air Force Systems Command Arnold Air Force Station, Tennessee 37389		10 PROGRAM ELEMENT PROJECT, TASK AREA & WORK UNIT NUMBERS Program Element 65807F
11 CONTROLLING OFFICE NAME AND ADDRESS Arnold Engineering Development Center (XRFIS) Arnold Air Force Station, Tennessee 37389		12 REPORT DATE August 1977
		13 NUMBER OF PAGES 271
14 MONITORING AGENCY NAME & ADDRESS(if different from Controlling Office)		15 SECURITY CLASS. (of this report) UNCLASSIFIED
		15a DECLASSIFICATION DOWNGRADING SCHEDULE N/A

16 DISTRIBUTION STATEMENT (of this Report)

Approved for public release; distribution unlimited.

17 DISTRIBUTION STATEMENT (of the abstract entered in Block 20, if different from Report)

1. Compressors -- stability
2. Fans

18 SUPPLEMENTARY NOTES

Available in DDC

19 KEY WORDS (Continue on reverse side if necessary and identify by block number)

mathematical analysis	engines	compressors
external	turbine	
disturbances	axial flow	
aerodynamic stability	fans	

20 ABSTRACT (Continue on reverse side if necessary and identify by block number)

The overall objective of the work described herein was to develop an improved method for the computation of the influence of external disturbances on turbine engine compressor stability, and, in so doing, to gain added physical insight into the destabilizing processes. The objectives were accomplished through the development of a one-dimensional, time-dependent mathematical compressor model for analysis of planar disturbances and an

DD FORM 1473 EDITION OF 1 NOV 65 IS OBSOLETE
1 JAN 73

UNCLASSIFIED

20. ABSTRACT (Continued)

extension of the model to a three-dimensional form for analysis of distorted inflows. The models satisfy mass, momentum and energy equations on a time-dependent basis. Compressor stage force and shaft work were determined from empirical stage characteristics with corrections made for unsteady cascade airfoil aerodynamics. The system of equations comprising the model is solved using a digital computer. Example problems with comparisons to experiments are presented for three different compressors. Example problems solved using the one-dimensional analysis include: determination of the steady-state stability limit (surge line) with undisturbed flow, instability caused by oscillating planar inflow, dynamic response of a compressor to oscillating entry pressure, dynamic response to oscillating discharge pressure, and compressor instability caused by rapid upward ramps of entry temperature. Example problems solved using the distortion model include: stability limit (surge) line reduction caused by a combined radial and circumferential pressure distortion, time-variant distortion effects, pure radial pressure distortion effects, and pure pressure and temperature circumferential distortion effects. Comparisons are made with experimental results, and the models developed are shown to compute the compressor stability limits with reasonable accuracy.

AFSC
Arnold AFS Tenn

PREFACE

CONTENTS

ILLUSTRATIONS

APPENDIXES

CHAPTER I

INTRODUCTION

Stable aerodynamic operation of the compression system of an aircraft gas turbine engine is essential for the engine to operate safely and to satisfactorily deliver the performance which it is designed to provide. The compression system of an aircraft gas turbine engine consists of one or more compressors arranged in configurations such as those illustrated in Fig. 1 (Appendix A).[1] Aerodynamically stable operation refers to the condition in which the compressor delivers a desired quantity of airflow on a continuous basis, compressed to a desired pressure level, free of excessively large amplitude fluctuations in the flow properties throughout the compressor. The aerodynamic stability limit is most commonly represented as a locus of corrected rotor speed points denoting the minimum corrected flow rate value for stable operation on a plot of the total pressure ratio across the compressor versus corrected airflow rate as shown in Fig. 2. Operation to the right of the curve is stable and to the left of the curve is unstable.

The stability limit curve is often referred to as the surge line or stall line of the compressor stemming from

---

[1]All figures in Chapters I through VI appear in Appendix A.

1

the fact that surge is one possible specific form of
instability experienced in compressors, and all compressor
instabilities are initiated by aerodynamic stall of some
blades or vanes of the compressor.

The stability margin of the compressor is commonly
taken to be the percentage difference between the compressor
total pressure ratio at the stability limit and that at the
operating line holding corrected airflow constant (Fig. 2).
The position of the operating line is primarily determined
by the load imposed on the compressor by downstream engine
components. However, under actual flight conditions in an
aircraft, the positions of both the stability limit line and
the operating line are influenced by external disturbances
in the flow at either the entry or exit of the compressor.

The overall objective of this study is to develop
an improved analytical method which will allow prediction of
the loss of stability margin of the compressor caused by
external disturbances imposed upon it by flight conditions
in an aircraft. Also, the development of the method is
intended to provide some degree of physical understanding of
the processes which lead to compressor instability.

Prior to beginning the analysis it is helpful to
review the ramifications of stability on engine operation
and to review some of the experimentally observed influences
of the operating conditions and external disturbances on
compressor stability. Also, a review of some of the

previously accomplished works directed at stability predictions both with and without external disturbances will be made.

I. RAMIFICATIONS OF STABILITY TO ENGINE OPERATION

Operation of the compressor to the left of the stability limit (Fig. 2) will result in loss of thrust, possible loss of engine control, or possible engine structural damage caused by overheating and high cyclic stress induced in the engine by unstable flow conditions. Reference [1][2] presents evidence of thermal and cyclic stress effects imposed by compressor instability for one particular engine. Montgomery [2] has compiled a history of difficulties in the operation of several aircraft gas turbine engines which have been experienced because of compressor stability problems. Montgomery's work well illustrates the need for a method of determining the stability limit of the gas turbine engine compressor, especially as they are affected by the conditions of flight.

II. MAJOR OPERATING CONDITIONS AND EXTERNAL
DISTURBANCES INFLUENCING STABILITY

The position of the stability limit line and the operating line of the compressor of a given design are

---

[2]Numbers in brackets refer to similarly numbered references in the Bibliography.

affected in flight by the condition of the flow entering the compressor and by the throttling or back pressure provided by the compressor or engine component downstream of the compressor under consideration. The entry total temperature, the Reynolds number at which the compressor must operate, and the nonuniformity and unsteadiness of the flow at the compressor inlet have major influences on the stability of the compressor.

Because of the variation of total temperature at the compressor entry which occurs with flight Mach number and altitude, the compressor's operating region moves far from the design point of the compressor; thus, a relatively large region of the compressor map must be considered in any analysis of stability. Figure 3a depicts the variation of operating region with compressor inlet total temperature for a simple single spool turbojet compressor. Figure 3b shows the influence of flight Mach number and altitude on engine entry total temperature. The changes in flight conditions cause the Reynolds number to change. Figure 3c gives an example of the Reynolds number influence on the stability limit. The Reynolds Number Index (REI) used in Figure 3c is the ratio of the Reynolds number in flight to that which would exist at sea-level-static conditions at the same compressor inlet axial Mach number. Figure 3d shows the variation of REI with flight condition.

Figure 4 shows experimentally determined losses in stability margin caused by nonuniform (distorted) flow

conditions and unsteady flow conditions at the compressor
entry plane. In Fig. 4 the loss is illustrated by downward
shifts of the stability limit toward the operating line. In
some cases, the disturbances also cause stability margin
loss by moving the operating line upward. For purposes of
illustration, the entire loss is shown in Fig. 4 as a down-
ward movement of the stability limit. Figure 4a from [4] is
for the case of steady but distorted flow into the com-
pressor created by a wire screen of nonuniform porosity
placed in front of the compressor. Figure 4b from [5]
illustrates the loss in stability margin caused by uniform
but sinusoidally time-varying flow into the compressor
produced by a rotating flow interrupter upstream of the
compressor. The case of combined unsteady and distorted
flow, sometimes called time-variant distortion, is shown in
Figs. 4c and 4d for a turbojet engine compressor [6] and a
turbofan engine fan [7]. The engine entry flow fields were
produced by a venturi-centerbody arrangement which produced
an unstable shock wave boundary layer interaction which
causes the adverse flow field at the engine entry plane [6].
Figure 43, based on data from [8], indicates the influence
on the downstream compressor stability limit line of the
nonuniform and unsteady flow field exiting from a forward
compressor of a turbofan engine.

In addition to disturbances in the pressure enter-
ing the compressor, total temperature disturbances may occur.
Information from [9] shown in Fig. 4f, indicates the

experimentally determined influence of time-steady spatial
variation of total temperature entering the compressor.
Rapid uniform total temperature increases at the engine
inlet which could be caused by ingestion of hot gases pro-
duced by gun or rocket fire can also cause a loss of
stability [10].

Disturbances to the compressor may originate at
the exit of the compressor as well as at the inlet. An
experiment conducted on a turbofan engine described in [11]
demonstrated the influence of an oscillating back pressure
on fan stability.

The distortion examples of Fig. 4 all use total
pressure or total temperature variation to describe the
distortion pattern characteristics and to correlate with
loss in stability margin. The use of total pressure and
total temperature has been shown through experience and is
accepted in practice to be the most practical distortion
pattern description method (see Bibliography). The
Society of Automotive Engineers Aerospace Recommended
Practice on Gas Turbine Engine Inlet Flow Distortion
Methodology [12] specifies total pressure as the parameter
for distortion pattern description. Total pressure and
total temperature are used because they are much more
readily measured than velocity distribution, static pressure
and flow direction. Also, when a distorted flow field
approaches an engine, the interaction of the engine with the
distortion pattern produces a specific static pressure,

velocity and flow angularity pattern at the engine entry
(discussed in Chapter IV). Thus, the combination of a total
pressure or total temperature distortion pattern with an
engine at a given operating condition implicitly specifies
a velocity, static pressure and flow direction distribution
at the compressor entry and throughout the compressor.
Measurement of velocity and flow direction at the compressor
entry is sometimes suggested as a more physically meaningful
set of measurements for distortion pattern definition
because rotor blade angle of attack is related to the
velocity vectors at the rotor blade leading edge. However,
compressor instability caused by distortion can (and often
does) occur because of stall in any stage of the compressor.
Therefore, unless detailed velocity and flow direction
measurements are made at each and every compressor stage
entry, no real additional information is provided by the
more difficult velocity and flow direction measurements.
Further, the total pressure and total temperature distri-
butions produced by an aircraft inlet, if measured approxi-
mately an engine diameter ahead of the compressor entry
plane, will be the same with or without an engine installed
behind the inlet. Therefore, distortion pattern information
from scale model and full-scale inlet tests may be obtained
without the engine installed. This could not be done if
velocity static pressure and flow direction were chosen as
the distortion pattern definition parameters. For these
reasons, total pressure and total temperature variations

will also be used for disturbance description for the analytical work in this study.

Most of the influences shown in Fig. 4 were determined from simulations of actual flight in altitude test cells or wind tunnels using artificial methods of disturbance generation. These disturbances are, however, representative of actual disturbances experienced in flight. The influence on stability in actual flight is, however, more difficult to measure; thus, the ground test sources are used. More detailed information on the generation of these disturbances in flight is given in [13 through 16].

III. PREVIOUS ANALYSES OF COMPRESSOR STABILITY WITH UNDISTURBED FLOW

Early analysis of compressor instability dealt with "surging" described as "a violent fluctuation in delivery" by Whittle in an early work (1931) on the turbo-compressor as a supercharger [17]. In an even earlier work by Kearton [18] and in later works by Den Hartog [19] and Horlock [20], analysis of surge was performed using the shapes of the pressure-ratio-mass flow curves of the compressor and the throttle (back pressuring device) to locate stable and unstable combinations of the compressor and throttle and to qualitatively describe surging. (Figure 5 is a simple illustration of this analysis.) With the throttle set to an open condition, the match point, A, is a stable operating condition. This may be deduced by

imagining that the flow is momentarily perturbed upward. If
this should happen, the upward perturbation will cause a
reduction in the pressure exiting from the fan, and an
increase in the resistance to flow from the throttle. Both
of these effects tend to cause flow to decrease, thus
countering the original perturbation and restoring equi-
librium. A similar argument applies for a downward
perturbation of flow rate. If, however, the match point is
point C, instability will occur. Once more, imagine an
upward perturbation of flow. This will result in an
increase in compressor discharge pressure which is greater
than the increase in resistance to flow; thus, the upward
perturbation in flow will be reinforced causing the flow to
continue to increase. Thus, point C is unstable. This
analysis may be generalized to state that the compressor-
throttle combination will be unstable in regions where the
slope of the compressor characteristic curve is greater than
the slope of the throttle loss characteristic curve.
Applying this rule, if operation is attempted near point C,
and the flow is perturbed upward, it will continue to
increase until it reaches point B where the flow increase is
countered (that is, the compressor characteristic slope
becomes less than the throttle curve slope) and, ignoring
dynamic effects, is caused to begin to decrease. Once the
flow starts down, however, it will continue to decrease
until it reaches a region near point D where the slope of
the compressor characteristic is once more less than that of

9

the loss characteristic. Thus, a limit cycle, qualitatively describing surge based on characteristic curve nonlinearity, but ignoring dynamic effects, is constructed.

This simple explanation provided a reasonable qualitative explanation of the surge instability, but in actual use tended to predict a value of flow rate at which surge would be encountered which was often lower than that actually experienced [21]. It later became common practice to assume that instability would occur at the peak compressor ratio; that is, at the first point where the compressor characteristic slope became positive. This assumption was reasonably well borne out for high corrected rotor speeds by experiments [21, 22].

While the theories described to this point were based principally on observations made on centrifugal compressors, they are in principle applicable to axial flow units. (For example, the compressor characteristic curve of Fig. 5 in no way specifies the type of compressor which produced it.) Pearson and Bowmer (1949) [21] specifically addressed the problem of stability in axial flow compressors. Pearson and Bowmer observed the discrepancy which existed between compressor experiments and the simple nonlinear characteristic curve theory and noted that the nonlinear theory ignored the dynamic effects caused by volumetric capacitance, fluid column inertia, and flow resistance in the compressor and ducting. Pearson and Bowmer approached the problem by deriving an approximate set of dynamic

10

(time-dependent) equations for a twelve-stage axial flow compressor and related the compressor to an analogous electrical circuit. The compressor was stacked from assumed stage characteristics to form a representative multi-stage unit. It was then assumed that instability would occur at any condition where the impedance of any given part of the circuit representing a stage was zero. For positive impedance, disturbances in the circuit would be damped; for negative impedance the disturbances would be amplified, thus causing instability.

Howell (1964) [23] extended the work of Pearson and Bowmer by applying the same technique of drawing an electrical analogy to the compressor, but used a more detailed stability analysis on the resulting electrical net-work. Howell also applied the analysis to an actual compressor and compared those results to the experimentally determined stability limit. Howell's analysis produced a reasonably good prediction of the stability limit, but it was somewhat below the experimentally observed limit at design rotor speed.

Kimzey and Couch (1969) developed a stability criterion for predicting the position of the stability limit directly from an analysis of a simple set of dynamic equations representing the volumetric capacitance and inertial characteristics of the compressor on a stage-by-stage manner [24]. This stability criterion was based on the assumption that the compressor stages work in pairs,

11

and if any "pair" becomes an unstable combination, then instability of the entire compressor will result. (Any given stage in the compressor is a member of two pairs; one is formed in conjunction with the preceding stage and one with the following stage; for the last stage, the ducting and throttle form one pair; for the first stage, the up-stream ducting forms a pair with the first stage.) The criterion was applied to an actual compressor and compared to experimental data. Reasonably good agreement was shown.

Daniele, Blaha, and Seldner (1974) [25] applied more sophisticated stability criteria to an approximate set of linearized dynamic equations representing volumetric capacitance, inertial, and energy effects. These criteria were applied to a compressor for which detailed experimental data were available to predict the steady-state stability limit line. Very good agreement with the experimental data was achieved.

IV. PREVIOUS ANALYSES OF COMPRESSOR STABILITY WITH DISTURBED FLOW

The work described above was principally directed at the prediction of the compressor stability limit with steady and uniform flow entering the compressor. Work has also been performed in an effort to predict the influence of external disturbances on the stability limit. An excellent and comprehensive review of the work accomplished to date in this area is given in [16].

Steady Nonuniform (Distorted) Flow

Notable early work dealing with the influence of distortion at the compressor entry was accomplished by Alford (1957) [26]. Alford treated the problem of circumferential total pressure distortion with a penetration theory which postulated that the influence of circumferential distortion on stability margin was proportional to the depth of penetration of the distorted pattern into the compressor. The distortion pattern attenuation characteristics were computed in an approximate manner, thereby deriving the form of an index which correlated distortion pattern characteristics to loss in stability margin. Alford concluded that the loss in margin depended on the magnitude of the total pressure deficit in the low pressure region, on the area of the compressor entry annulus which had total pressure below the average value, and on the angular extent of the low pressure region.

Pearson (1963) [27] described the parallel compressor theory of circumferential distortion. The theory divides the compressor annulus into arc sectors, each sector being viewed as an independent compressor running in parallel with the other sectors. All sectors are assumed to discharge to a common static pressure. The pressure ratio-flow rate characteristic curve of each sector was assumed to be unchanged by the distortion. Crossflows between the adjacent parallel compressor sectors were ignored. Each sector will have a different inlet total pressure because of

13

the circumferential distortion existing at the compressor
entry plane. In its simplest form of application, the
entire compressor is assumed to reach its stability limit
when the stability limit of any sector is encountered. In
practice, correlating indexes, such as described in [28] are
developed which relate the actual loss in stability margin
to the size of the arc sector chosen and the size of the
deficiency of total pressure in the lowest pressure sector.
Total temperature distortion has also been treated using
parallel compressor theory [28].

Goethert and Kimzey [29] presented an analog
computer model for calculating the effect of circumferential
distortion which was principally based on the parallel com-
pressor theory, but did make provisions for approximating
crossflow effects between sectors. Fett (1969) [24]
combined parallel compressor theory with the Hurwitz
stability criteria to provide a method of directly pre-
dicting the loss of stability margin caused by circumfer-
ential distortion for simple two- and three-stage
compressors.

Comparisons between the degree of distortion
predicted to cause instability by the parallel compressor
theory in its simplest form and that observed experimentally
indicated that as the angular extent of the low pressure
region was reduced from 180 degrees, the compressor would
actually become more tolerant to the distortion than pre-
dicted.

Reid (1969) [30], and Calogeras, Mehalic, and
Burstadt (1971) [31] showed experimentally that as the
angular extent of the low pressure region was increased from
0 to 60 degrees, the loss in stability margin increased
drastically, but the loss was nearly constant between 90 and
180 degrees. The experiment also showed that somewhere
between 60 and 90 degrees, the prediction of loss of
stability margin from parallel compressor theory was more
reasonable. From these observations, a critical angle was
defined as the minimum distortion angle which would allow
prediction of stability margin loss by simple parallel com-
pressor theory.

Goethert and Reddy (1971) [32] arrived at a
critical angle of approximately 60 degrees based on a
theoretical treatment of a cascade of blades in a phase-
shifted oscillatory flow field such as would be produced by
a compressor rotor moving through a circumferentially dis-
torted flow field. In the unsteady cascade flow treatment,
it was shown that an airfoil (or cascade of airfoils) takes
a certain amount of time to change its lift in response to
rapid changes of angle of attack. It was also shown that
the change in the lift from the steady-state value during a
rapid oscillation of the approach flow direction diminishes
as the frequency of oscillation is increased. Thus, cir-
cumferential distortions with low pressure regions which
cover only small angular extents will be recognized by a
rotor blade passing through the region as a very rapid

15

change, and the change in lift will be small. As the angular extent of the distortion is increased, however, the rotor blade will have an increasingly longer time to adjust to the higher angles of attack existing in the low pressure region.

The portion of the compressor in the low pressure region will therefore operate at angles of attack nearer the stall value, thus reducing the stability margin of the compressor.

The analysis of Goethert and Reddy was particularly useful in that the difference in the response of a cascade compared to that of an isolated airfoil was clearly made. Also, the difference between oscillatory flow approaching a stationary cascade and stationary flow approaching an oscillating cascade was made. The influence of unsteady airfoil aerodynamics on compressor behavior in a distorted flow field was recognized and used by other investigators also [33, 34]. Extensions have also been made into unsteady airflow aerodynamics of stalled flow around an airfoil by Carta (1973) [35] and Melick (1973) [36].

Uniform Time-Varying Entry Flow

The effect of uniform time-dependent disturbances on the stability of compressors has also been investigated. Gabriel, Wallner, and Lubick (1957) [37] studied the effects of uniform fluctuations of compressor inlet total pressure on compressor stability. The influence of rapid ramps in

compressor inlet total temperature was also studied.
Analysis of the influence was performed by solving a set of
lumped volume unsteady mass conservation equations along
with equations representing the pressure-ratio-mass flow
characteristic curves of several compressor stage groups.
The characteristic curves of the stage groups were obtained
from steady-state tests of the compressor and were assumed
to be valid dynamically in this analysis. This is the
so-called quasi-steady-state stage characteristic assumption.
The behavior of a fifteen-stage turbojet engine compressor
was analyzed by dividing the stages into four stage groups.
The resulting equations were solved using an analog computer.
It was assumed in the analysis that if any stage group
characteristic curve reached its peak value, that is, the
characteristic curve slope changes from negative to posi-
tive, that compressor instability would occur. The work
indicated that for uniform, sinusoidal oscillations of
compressor inlet total pressure, the amplitude required to
cause instability decreased as the oscillation frequency
increased. Also, it was found that upward ramps in com-
pressor entry total temperature would cause compressor
instability, and that the effects become increasingly
severe as the ramp rate is increased. The calculated
results were compared to experimental data and showed
reasonably good agreement with the experimentally determined
stability limit. This particular analysis was limited to
compressor rotor speeds near the design value.

Later investigators extended Gabriel, Wallner, and Lubick's approach for calculating the effects on stability of uniform, time-dependent compressor inlet disturbances. Kimzey (1966) [38] improved the analysis by using each compressor stage separately (instead of combining into stage groups), and improved upon the form of the analog computer solution. Further refinements, including the approximation of unsteady momentum effects, unsteady energy effects, improvement of the criteria for instability, and implementation of the solution on the digital computer, have also been accomplished [24, 39, 40].

Time-Varying Distortion

Although a great deal of excellent experimental work has recently been accomplished on time-varying distortion [13 through 16], relatively little has been accomplished to provide a method of directly calculating its effects on stability. A quasi-steady approach, developed by Plourde and Brimlow (1968) [7], is most commonly used at the present time. This particular approach assumes that the compressor reacts to time-variant distortion in the same manner as it reacts to steady-state distortion if the time-variant distortion pattern "dwells" at the compressor entry for a time period approximately equal to the time required for the compressor rotor to make one revolution. A distortion index, which correlates the loss in stability margin to the spatial distortion pattern characteristics in the

same manner as is used with steady-state distortion, is then calculated as a function of time. Time-dependent fluctuations in the compressor entry flow field, which are at a frequency higher than that commensurate with the pattern "dwell time," are filtered out prior to making the distortion index computations. The loss in stability margin is then correlated with the maximum distortion index value observed over a given time period. Although Plourde and Brimlow's treatment does not directly account for some dynamic processes known to be present in the compressor with time-varying distortion, reasonably good correlation is achieved with the method, making it a most valuable engineering tool for practical applications.

Melick (1973) [36] applied unsteady airfoil theory to the analysis of the time-variant distortion problem. Additional detail on time-varying distortion analysis is provided in [41, 42].

V. OBJECTIVES AND APPROACH OF CURRENT WORK

As previously stated, the overall objective of this study is to develop an improved analytical method with general applicability for predicting compressor stability margin loss caused by the aforementioned external disturbances. The development of the method is intended to provide insight into some of the physical processes which lead to compressor aerodynamic instability.

The work described herein specifically extends the present state of knowledge through the following developments.

Improved One-Dimensional, Time-Dependent Model

An improved model, suitable for steady-state stability limit computation and for analysis of planar, transient and dynamic disturbances is developed. The model includes mass, momentum, and energy effects. The full non-linear form of the equations, not used in earlier works, is solved. Unsteady cascade influences, also not included in earlier works, based on the Goethert-Reddy analysis [32], are included in the analysis and their influences evaluated. The Goethert-Reddy unsteady cascade analysis is compared to experimental unsteady compressor blade aerodynamic data. Detailed comparisons of model computed steady-state stability limits are presented for three different compressors providing an indication of the generality of the analysis method. Four unsteady cases: compressor instability caused by planar oscillatory inflow, dynamic unstalled response of a compressor to oscillating inflow, dynamic unstalled response to oscillating back pressure, and response of a compressor to rapid inlet temperature ramps, are computed. Where possible, the computed results are compared to experimental results.

Extension to Multi-Dimensional Flow Case

The concepts of the one-dimensional, time-dependent model are extended to three dimensions to allow treatment of distorted flows into the compressor. The compressor is divided both radially and circumferentially into control volumes, and crossflows among the volumes caused by distortion and their effects on stability are computed. The influence of the radial work variation is approximated and included for the radial distortion evaluations. Unsteady cascade effects are included. Thus, a model capable of computing the influences of combined radial and circumferential distortion is produced. The model is used to compute the loss in stability margin for a compressor with steady-state, combined radial and circumferential distortion, and comparisons to experimental results are made. A time-dependent distortion case is computed. Parametric influence of pure radial and pure circumferential pressure distortion are analyzed. Pure circumferential temperature distortion is also analyzed.

Comparisons to Experimental Results

Emphasis was placed on comparisons of model computations to experimental results to maximize understanding of the physical processes and to test the validity of the computations. Experimental results on no single compressor were sufficient for the comparisons desired; thus, three different compressors were modeled. They are:

a four-stage Allison XC-1 compressor [43], an eight-stage NACA research compressor, the NACA-8 [44, 45, 46], and the General Electric eight-stage J85-13 engine compressor [47]. Information on these compressors used in this study are given in Appendix B. The NACA-8 and General Electric J85-13 compressors were modeled one-dimensionally and the models included a portion of inlet ducting and combustor ducting for more realistic time-dependent boundary conditions for the compressor. The Allison XC-1 compressor was used for one-dimensional, steady-state stall analysis and for the distortion studies. No ducting was included in the XC-1 models.

VI. ORGANIZATION

The development of the one-dimensional, time-dependent model is presented in Chapter II. Chapter III presents application of the one-dimensional analysis to example problems. The extension of the model to three dimensions is given in Chapter IV. Chapter V describes application to distortion cases. The work is summarized and recommendations for further work is given in Chapter VI.

CHAPTER II

DEVELOPMENT OF ONE-DIMENSIONAL,

TIME-DEPENDENT MODEL

The axial-flow compressor is made up of successive rows of airfoils, a moving row, the rotor, followed by a stationary row, the stator, as shown in Fig. 6. A rotor followed by a stator is defined as a stage for this study. A representative absolute velocity and static pressure distribution through the compressor is also shown in Fig. 6. The compressor increases the static pressure and density of the fluid passing through it by the dynamic action of the rotor which imparts kinetic energy to the fluid. Depending on the specific design, the static pressure through the rotor changes by varying amounts. The function of the stator row is to diffuse and redirect the flow to convert a portion of the imparted kinetic energy to internal energy. The flow is further diffused as it passes from the compressor through the compressor diffuser to the combustor. After leaving the combustor it passes through a turbine nozzle (if on an engine) or a throttling valve (if on a compressor test rig) which is usually choked.

In the formulation of the one-dimensional model, a control volume, enclosing the fluid in the compressor is drawn, as shown by the dashed lines in Fig. 7. For the one-dimensional analysis, all flow properties are "bulked"

in the radial and circumferential directions and variations
with the axial coordinate and with time only are considered.

The development of the one-dimensional model pro-
ceeds as follows. The governing equations are written. The
method of specifying the force and shaft work acting on the
fluid is developed. The finite difference forms of the
equations used for numerical solution on a digital computer
are then developed and the method of solution given.

I. GOVERNING EQUATIONS

Figure 7a illustrates the ducting-compressor-
burner-turbine vane system which was modeled. Figure 7b
shows the overall control volume representing the system.
The forces of the blading and walls of the system acting on
the fluid are represented by an effective axial time-
dependent force distribution, $F(z,t)$. Similarly, shaft
work done on the fluid and heat added to the fluid are
represented by the time-dependent distributions, $WS(z,t)$ and
$Q(z,t)$. Mass removal or addition (interstage bleed, for
example) are represented by another time-dependent bleed
flow distribution function, $WB(z,t)$. All bleed flows are
assumed to cross the control volume boundary normal to the
axial direction. Time-dependent boundary conditions are
provided by specification of the total pressure and total
temperature, $P(t)$ and $T(t)$, respectively, at the system
forward boundary and by specification of discharge static
pressure, $P_{exit}(t)$, at the aft boundary. For choked turbine

vanes, a sufficiently low discharge static pressure was specified to assure choking. In that case, the aft boundary condition is unity Mach number. If unchoked, specification of static pressure is the aft boundary condition.

The governing equations are derived by application of time-dependent mass, momentum, and energy conservation principles to the elemental volume of Fig. 7c.

Mass

Application of the mass conservation principle (mass is neither created nor destroyed) to the elemental control volume yields

$$
\underbrace{W + \frac{\partial W}{\partial z}\, dz + WB\, dz}_{\substack{\text{mass leaving} \\ \text{control volume} \\ \text{per unit time}}} + \underbrace{\frac{\partial (\rho A\, dz)}{\partial t}}_{\substack{\text{time rate of} \\ \text{increase of mass} \\ \text{"stored" in the} \\ \text{control volume}}} = \underbrace{W}_{\substack{\text{mass entering} \\ \text{control volume} \\ \text{per unit time}}} . \quad (1)
$$

Equation (1) may be reduced to

$$
\frac{\partial (\rho A)}{\partial t} = - \frac{\partial W}{\partial z} - WB . \quad (2)
$$

Momentum

The momentum principle, the summation of all forces in a given direction, is equal to the time rate of change of momentum in that direction, gives

$$F \, dz + PS \, A - \left[PS \, A + \frac{\partial(PS \, A)}{\partial z} \, dz \right] + PS \left[\left[A + \frac{\partial A}{\partial z} \, dz \right] - A \right]$$

$$\underbrace{\qquad\qquad\qquad\qquad\qquad\qquad\qquad\qquad\qquad\qquad\qquad\qquad}_{\text{axial forces acting on control volume}}$$

$$= \underbrace{\left[WU + \frac{\partial(WU)}{\partial z} \, dz \right]}_{\substack{\text{momentum} \\ \text{leaving} \\ \text{control volume} \\ \text{per unit time}}} - \underbrace{WU}_{\substack{\text{momentum} \\ \text{entering} \\ \text{control volume} \\ \text{per unit time}}} + \underbrace{\frac{\partial}{\partial t} \left[\rho UA \, dz \right]}_{\substack{\text{time rate} \\ \text{of increase} \\ \text{of momentum} \\ \text{"stored" in the} \\ \text{control volume}}} \qquad . \quad (3)$$

$$\underbrace{\qquad\qquad\qquad\qquad\qquad\qquad\qquad\qquad\qquad\qquad\qquad\qquad}_{\text{total time rate of change of momentum}}$$

Equation (3) may be reduced to give

$$\frac{\partial W}{\partial t} = -\frac{\partial(IMP)}{\partial z} + F + PS \, \frac{\partial A}{\partial z} \, , \qquad\qquad (4)$$

where, the impulse, IMP, is defined as

$$IMP = WU + PS \, A \, . \qquad\qquad (5)$$

Energy

Energy conservation gives,

$$\underbrace{H + \frac{\partial H}{\partial z} \, dz}_{\substack{\text{enthalpy leaving} \\ \text{control volume} \\ \text{per unit time}}} + \underbrace{\frac{\partial}{\partial t} \left[\rho \left[e + \frac{U^2}{2} \right] A \right] dz}_{\substack{\text{time rate of increase} \\ \text{of energy "stored" in} \\ \text{control volume}}}$$

$$= \underbrace{H}_{\substack{\text{enthalpy} \\ \text{entering} \\ \text{control volume} \\ \text{per unit time}}} + \underbrace{WS \, dz}_{\substack{\text{shaft work} \\ \text{done on} \\ \text{fluid in} \\ \text{control volume}}} + \underbrace{Q \, dz}_{\substack{\text{heat added} \\ \text{to fluid in} \\ \text{control volume}}} \qquad . \quad (6)$$

26

Equation (6) may be reduced to

$$\frac{\partial (XA)}{\partial t} = -\frac{\partial H}{\partial z} + WS + Q , \tag{7}$$

where

$$X = \rho \left[e + \frac{U^2}{2} \right] \tag{8}$$

and

$$H = c_p WT . \tag{9}$$

State and Additional Equations

Additional equations required include the perfect gas equation of state,

$$PS = \rho R TS , \tag{10}$$

calorically perfect internal energy and enthalpy relationships,

$$e = c_v TS + constant , \tag{11}$$

$$h = c_p TS + constant , \tag{12}$$

stagnation (total) state temperature,

$$T = c_p TS + \frac{U^2}{2} , \tag{13}$$

and stagnation (total) state pressure,

$$P = PS \left[\frac{T}{TS} \right]^{\frac{\gamma}{\gamma-1}} , \tag{14}$$

27

where

$$\gamma = \frac{c_p}{c_v} \ . \tag{15}$$

Also required is the Mach number,

$$M = \frac{U}{a} \ , \tag{16}$$

where the acoustic velocity, a, is

$$a = \sqrt{\gamma \ R \ TS} = \sqrt{\gamma \ \frac{PS}{\rho}} \ , \tag{17}$$

and the Mach number-static pressure form of the energy in the control volume,

$$X = \frac{PS}{\gamma - 1} \left[1 + \frac{\gamma(\gamma-1)}{2} M^2 \right] \ , \tag{18}$$

which results from combination of Eqs. (8), (10), (11), (15), (16), and (17).

The Mach number-static pressure form of the impulse, IMP, is also used,

$$IMP = PS \ A \left[1 + \gamma M^2 \right] \ . \tag{19}$$

This equation results from combination of

$$W = \rho AU \ , \tag{20}$$

with Eqs. (5) and (17).

28

II. STAGE FORCES AND SHAFT WORK

Steady-State Stage Characteristics

Consider the element of fluid contained between two blades in a rotor as shown in Fig. 8a. Entering the rotor, the tangential velocity is V_{θ_1}, and at the exit it is V_{θ_2}. Applying the conservation of angular momentum principle to the fluid element in steady flow gives the torque on the element,

$$t = W \left[r_2 V_{\theta_2} - r_1 V_{\theta_1} \right] . \qquad (21)$$

Multiplying Eq. (21) by rotor speed, ω, yields the time rate of doing work on the fluid, which is equal to the total enthalpy change across the rotor. Thus,

$$c_p W \left[T_2 - T_1 \right] = \omega W \left[r_2 V_{\theta_2} - r_1 V_{\theta_2} \right] . \qquad (22)$$

Replacing the difference between radius-velocity products using an effective radius yields,

$$c_p W \left[T_2 - T_1 \right] = \omega W \bar{r} \left[V_{\theta_2} - V_{\theta_1} \right] , \qquad (23)$$

where

$$\bar{r} = \frac{r_2 V_{\theta_2} - r_1 V_{\theta_1}}{V_{\theta_2} - V_{\theta_1}} . \qquad (24)$$

29

Writing wheel speed as

$$U_{wh} = \omega \bar{r} \tag{25}$$

and

$$V_{\theta_2} - V_{\theta_1} = \Delta V_\theta \tag{26}$$

gives

$$\frac{T_2 - T_1}{T_1} = \frac{U_{wh}}{c_p T_1} \Delta V_\theta \; . \tag{27}$$

Applying the linear momentum equation for steady flow to the element of Fig. 8a gives

$$F_\theta = W \; \Delta V_\theta = \rho_1 \; A_1 \; U \; \Delta V_\theta \; , \tag{28}$$

where F_θ is the force being applied to the fluid by the blading in the compressor.

The force, F_θ, can also be expressed in terms of blade lift and drag, as indicated in Fig. 8b,

$$F_\theta = L \; \cos(\alpha+\lambda) + D \; \sin(\alpha+\lambda) \; , \tag{29}$$

where α is the blade angle of attack, determined by the velocity triangle of Fig. 8b, and λ is the blade chord-to-axial direction angle, or, the cascade stagger angle.

The lift and drag may be expressed as coefficients,

$$C_\ell = \frac{L}{\frac{1}{2} \rho_1 V_{rel}^2 A_{ref}} \quad , \tag{30}$$

and

$$C_d = \frac{D}{\frac{1}{2} \rho_1 V_{rel}^2 A_{ref}} \quad . \tag{31}$$

Combining Eqs. (27) through (31) produces

$$\frac{T_2 - T_1}{T_1} = \left[\frac{1}{2c_p} \frac{A_{ref}}{A_1} \right] \frac{U_{wh} V_{rel}^2}{U T_1} \left[C_\ell \cos(\alpha+\lambda) + C_d \sin(\alpha+\lambda) \right] . \tag{32}$$

Returning once more to Fig. 8b, define the stage flow coefficient as

$$\phi \equiv \frac{U}{V_\theta} . \tag{33}$$

From Fig. 8b, the flow coefficient, ϕ, is related to the blade angle of attack, α, by the stagger angle, λ, which is a constant for any given blade row,

$$\phi = \cot(\lambda+\alpha) . \tag{34}$$

Thus, ϕ serves the same purpose in the compressor as α does for aircraft wing aerodynamics. It decreases with increasing α; therefore, small ϕ means large α, and vice versa. Also from Fig. 8b,

$$\frac{U}{V_{rel}} = \cos(\lambda + \alpha) \quad . \tag{35}$$

Combining Eqs. (32) through (35) yields

$$\frac{c_p \left[\frac{T_2}{T_1} - 1 \right]}{\frac{U_{wh}^2}{T_1}} = \frac{1}{2} \frac{A_{ref}}{A_1} \left\{ \frac{U^2}{U_{wh}^2} + \left[1 + \frac{V_{sw}}{U_{wh}} \right]^2 \right\}^{1/2} \left[C_\ell + \frac{C_d}{\phi} \right] \quad . \tag{36}$$

The left-hand side of Eq. (36) is defined as the stage loading parameter, ψ^T (following Horlock [20]), or simply as the stage temperature coefficient (more common in American works [40]). Thus,

$$\psi^T = \frac{c_p (TR-1)}{\frac{U_{wh}^2}{T_1}} \quad , \tag{37}$$

where TR is the stage total temperature ratio.

If the swirl component of tangential velocity is small,

$$\phi \approx \frac{U}{U_{wh}} \tag{38}$$

and

$$\psi^T \approx \frac{1}{2} \frac{A_{ref}}{A_1} \left[\phi^2 + 1 \right]^{1/2} \left[C_\ell + \frac{C_d}{\phi} \right] \quad . \tag{39}$$

At given Mach and Reynolds numbers, C_ℓ and C_d are functions of α; thus, ϕ, only. Therefore,

$$\psi^T \bigg|_{Re,M} = \psi^T(\phi) \ . \tag{40}$$

In principle, theoretical or experimental lift and drag coefficients could be used, along with stage geometry, $(\lambda,\ A_1,\ A_{ref})$ to compute the stage temperature coefficients following Eqs. (36) or (39). Corrections for blade row interference causing losses and secondary flows would be required. Another method is to measure the stage total temperature, flow rate, total pressure, and flow angularity at the stage entry and exit and directly compute ψ^T and ϕ from Eqs. (37) and (38). The stage characteristics used in this study were obtained in that manner and are summarized in Appendix B.

The temperature ratio of Eq. (37) for an ideal compressor stage is the isentropic temperature ratio defined from stage entry and exit stagnation pressure. Using this ratio, another stage parameter, the stage pressure coefficient, ψ^P, is produced,

$$\psi^P = \frac{c_p \left[PR^{\frac{\gamma-1}{\gamma}} - 1 \right]}{\dfrac{U_{wh}^2}{T_1}} \ . \tag{41}$$

33

The pressure coefficient is also a function of the flow coefficient, ϕ, in a manner similar to the temperature coefficient. The stage adiabatic efficiency is

$$\eta_{ad} = \frac{\Delta h_{isentropic}}{\Delta h_{actual}} = \frac{PR^{\frac{\gamma+1}{\gamma}} - 1}{TR - 1} . \qquad (42)$$

Thus,

$$\eta_{ad} = \frac{\psi^P}{\psi^T} . \qquad (43)$$

A set of curves,

$$\left.\begin{array}{l} \psi^T = \psi^T (\phi) \\[2ex] \psi^P = \psi^P (\phi) \\[2ex] \eta_{ad} = \eta_{ad} (\phi) \end{array}\right\} , \qquad (44)$$

is referred to as stage characteristics, and along with flow direction,

$$\beta = \tan^{-1} \left[\frac{V_{sw}}{U}\right] , \qquad (45)$$

or an equivalent set of flow direction information, fully defines a stage's performance from a one-dimensional standpoint. Note that the set of Eq. (44) is redundant; any two of the three variables are sufficient to compute the third.

Various forms of the stage characteristics are used. An alternate form used in NACA compressor research,

and used for the stage characteristics of the NACA-8 compressor treated in this study, is the equivalent temperature and pressure ratio form. They are defined as

$$ETR = \left[\psi^T \left[\frac{U_{wh}^2}{c_p T} \right]_{design} + 1 \right] ,$$ (46)

$$EPR = \left[\psi^P \left[\frac{U_{wh}^2}{c_p T} \right]_{design} + 1 \right]^{\frac{\gamma}{\gamma-1}} ,$$ (47)

and η_{ad} is defined as in Eq. (43).

Because

$$\left[\frac{U_{wh}^2}{c_p T} \right]_{design}$$

is a constant for a given compressor, the set remains a function of ϕ, as in Eq. (44), and contains the same information.

Figure 9 is an example set of stage characteristics for the first stage of the NACA-8 compressor [46]. To the right of the equivalent pressure ratio peak, the stage is unstalled (i.e., high ϕ and low α). To the left, the stage is stalled. Rapid decrease of stage efficiency at low ϕ (high α) where the blades are stalled, is evident. The data of Fig. 9 is seen to generalize well with the flow coefficient, ϕ, computed as in Eq. (38) with the swirl component of velocity ignored. This implies that for this set of data, the swirl velocity component was either small

35

relative to wheel speed, or, changed little as a fraction of
wheel speed over the range of compressor operation con-
sidered. Steady-state stage characteristics for the three
compressors treated in this study were obtained from [43,
46, 47], and are shown in Appendix B.

The foregoing discussion pertains primarily to the
compressor rotor which imparts the shaft work to the fluid.
No stagnation temperature change occurs across the stators
(with adiabatic boundaries) and the stagnation pressure
losses of the stator may be combined with the change across
the rotor to give a net change. Therefore, the character-
istics of Eq. (44) may be attributed to the overall stage.

Unsteady Cascade Effects

When the angle of attack of the flow into the
compressor stage varies slowly, the lift coefficient follows
the steady-state C_ℓ-α curve very closely, as illustrated in
Fig. 10. Similarly, the steady-state ψ-ϕ characteristics
are followed. When α rapidly changes, however, the lift
cannot instantaneously follow because a certain amount of
time is required for the flow around the blade to adjust to
the new condition. Lag loops or hysteresis in the C_ℓ-α and
ψ-ϕ curves appear (Fig. 10).

Goethert and Reddy analyzed the unsteady cascade
effects [32]. They analyzed unsteady incompressible
potential flow through a stationary cascade of thin, flat
plate foils with small oscillations in the axial velocity

producing angle-of-attack oscillations. The time-averaged angle of attack was zero. Their results are summarized in Fig. 11. The cascade stagger angle is λ; the blade chord length, C; and spacing is a. Rotor speed, ω, was constant and V_{sw} was zero. The axial velocity, U, was oscillated at frequency f, causing an inverse oscillation of α. This produced an oscillation in the lift coefficient. The results were presented in terms of maximum amplitude ratio at a given frequency, divided by the lift coefficient amplitude at f = 0 (quasi-steady-state). The resulting lift ratio is presented as a function of reduced frequency, k, for four values of cascade spacing, a/C. The case of a/C = ∞, a single, isolated airfoil, is shown for reference. Also treated for reference was the case of oscillating foils in a steady stream. The Goethert-Reddy work showed significant differences to exist between the oscillating foils, stationary stream, and the converse case. Their work also showed the unsteady effects for a cascade of finite spacing to be much less severe than that of an isolated airfoil. The unsteady influence was shown to increase with increasing spacing (a/C) and stagger angle, λ.

The lift coefficient ratio variation with reduced frequency is intuitively correct at k = 0 and as k $\rightarrow \infty$. Following Goethert and Reddy [32] the reduced frequency, k, may be viewed as an indication of the ratio of flow passage time to the disturbance stay time of the forced oscillation.

The passage time is defined as the time required for an air particle to pass through the blade row channel. Or,

$$\Delta t_{passage} = \frac{C}{V_{rel}} . \qquad (48)$$

The disturbance stay time is defined as the time that any one blade is exposed to the positive disturbance velocity of one velocity oscillation, that is,

$$\Delta t_{disturbance} = \frac{1}{2f} . \qquad (49)$$

Therefore,

$$\frac{\Delta t_{passage}}{\Delta t_{disturbance}} = \frac{2fC}{V_{rel}} = \frac{k}{\pi} . \qquad (50)$$

Alternately, k may be viewed as being proportional to the ratio of the blade chord length to the disturbance wave length,

$$\frac{chord \ length}{wave \ length} = \frac{C}{\frac{V_{rel}}{f}} = \frac{Cf}{V_{rel}} = \frac{k}{2\pi} . \qquad (51)$$

If k is near zero (i.e., the disturbance time period is large compared to the passage time), the blade lift will easily follow the disturbance. Similarly, the chord length is small relative to the disturbance wave length; thus, the lift can easily respond. If k → ∞, the disturbance time is small compared to the passage time and many disturbance wave

38

lengths reside within one chord length at any instant in time. The disturbance is then "averaged-out" by the blade yielding an instantaneous lift value of zero due to the disturbance.

Bruce and Henderson [48] conducted an experimental investigation of the unsteady force coefficients produced by a compressor rotor in unsteady flow. A single stage, low-speed compressor was fitted with a rotor blade having a segment of the blade on a small strain-gaged force balance. This installation allowed a direct measurement of the unsteady forces acting on that blade segment as the rotor passed through a distorted flow field produced by a distortion screen. A portion of their measurements was taken with stagger angle and cascade spacing near the values used by Goethert and Reddy. Figure 12 shows a comparison of the Goethert-Reddy analysis with the Bruce-Henderson experimental results. The trends with reduced frequency are in good agreement. The experimental results generally were from 10 to 20% higher than the analytical results. Considering the difficulties and assumptions involved in both the analytical and experimental evaluations, this level of agreement is considered reasonable at this time. Agreement among other theoretical treatments and experimental results surveyed was usually of this order or worse. (See comparisons made in [48] for example.)

The analysis of Goethert and Reddy was performed for an unloaded cascade, that is, the mean angle of attack

was zero. Figure 13 shows the variation of lift coefficient
ratio with mean angle of attack from the unsteady cascade
work of Ostdiek [49], and Bruce and Henderson's single-stage
compressor [48]. The dynamic lift coefficient ratio magni-
tudes were normalized by the value of a mean angle of attack
of eight degrees. The measurements were made over a range
of reduced frequency of 0.002 to 2.9, and from 0 to 12
degrees mean angle of attack. The results are all within
±10% and no generalized trend could be identified.

Unsteady Stage Characteristic Correction

The Goethert-Reddy analysis may be used to con-
struct a correction to the steady-state stage character-
istics. To facilitate application of the correction, the
dynamic lift coefficient ratio was represented by a simple,
first-order differential equation, as indicated in Fig. 14.
The equation,

$$\frac{dC_\ell}{dt} + \frac{C_\ell}{\tau} = \frac{C_{\ell ss}}{\tau} , \qquad (52)$$

represents the time-dependent lift coefficient, C_ℓ, in
response to the quasi-steady-state lift coefficient, $C_{\ell ss}$,
which would be produced if the lift exactly followed the
steady-state C_ℓ-α relationship.

The blade time constant, τ, depends on the chord
length and reduced frequency,

$$\tau = \frac{\varepsilon \, C}{V_{rel}} \, .$$ (53)

The constant, ε, depends on cascade geometry (i.e., a/C and λ). For a/C = 1.0, and λ = 50 degrees, ε = 0.3106. The value of ε is found by fitting the approximating differential equation, Eq. (52), to the response indicated by the Goethert-Reddy analysis.

For sinusoidal variation of angle of attack, the amplitude response of Eq. (52) is

$$\frac{\left| C_\ell \right|_{max}}{\left| C_\ell \right|_{ss}} = \sqrt{\frac{1}{1 + (\varepsilon \, k)^2}} \, .$$ (54)

The approximation of Eq. (52) is compared to the Goethert-Reddy solution in Fig. 14, and fidelity is excellent up to k = 8.

The cascade airfoil lift coefficient is related to the stage characteristics through Eq. (39). Consider oscillations of the flow into a stage around a given stage characteristic operating point (ψ_o, ϕ_o). Let ψ represent either ψ^T or ψ^P. Expanding Eq. (39) in a Taylor series, neglecting the drag coefficient term and retaining only the first-order terms of the series gives

$$\frac{\psi - \psi_o}{\frac{1}{2} \frac{A_{ref}}{A_1}} \approx \left[\frac{\phi_o^2}{\phi_o^2 + 1} \right]^{1/2} \left[\phi - \phi_o \right] + \left[\phi_o^2 + 1 \right]^{1/2} \left[C_\ell - C_{\ell_o} \right] \, .$$ (55)

41

Near the point, (ψ_o, ϕ_o),

$$\frac{\psi - \psi_o}{\phi - \phi_o} = \left.\frac{\partial \psi}{\partial \phi}\right|_o . \tag{56}$$

Then, from Eqs. (55) and (56),

$$C_\ell - C_{\ell_o} = \left\{ \phi_o \left[\left.\frac{\partial \psi}{\partial \phi}\right|_o \right]^{-1} - \frac{1}{2 \frac{A_{ref}}{A_1} \left[\phi_o^2 + 1 \right]^{1/2}} \right\} \left[\psi - \psi_o \right] . \tag{57}$$

Substituting Eq. (57) into Eq. (52) produces,

$$\frac{d\psi}{dt} + \frac{\psi}{\tau} = \frac{\psi_{ss}}{\tau} . \tag{58}$$

Thus, the stage characteristics may be corrected for unsteady cascade airfoil influences using the same first-order differential equation algorithm as that constructed for the unsteady lift coefficient.

The linearization of the unsteady correction implicit in Eqs. (55) and (56) is justified by: 1) the Goethert-Reddy analysis is itself a linearized analysis; 2) the correction magnitude is small in the range of reduced frequency normally encountered, as will be demonstrated later. The correction is actually proper only up to the stall point (i.e., up to the point where unsteady viscous effects become predominant).

Force and Shaft Work Distributions

The momentum equation, Eq. (4), requires an axial force distribution representing the force of the compressor blading and casings on the fluid. The function is constructed from the experimentally determined steady-state stage characteristics corrected for unsteady effects. (Or, alternately, the force may be computed in a quasi-steady-state manner from the steady-state stage characteristics and then directly corrected for unsteady effects using the dynamic lift coefficient ratio of Fig. 14.) The shaft work distribution required by the energy equation, Eq. (7), is similarly constructed.

The exact method of extracting the force and shaft work distributions depends partly on the finite difference method used to solve the governing equations, and is described in the next section.

III. METHOD OF SOLUTION

The basic governing equations are:

$$\frac{\partial (\rho A)}{\partial t} = - \frac{\partial W}{\partial z} - WB \;, \tag{2}$$

$$\frac{\partial W}{\partial t} = - \frac{\partial (IMP)}{\partial z} + F + PS \frac{\partial A}{\partial z} \;, \tag{4}$$

and

$$\frac{\partial (XA)}{\partial t} = - \frac{\partial H}{\partial z} + WS + Q \;. \tag{7}$$

43

The dependent variables to be integrated for are ρA, W, and XA. The area, A, was preserved in the derivative to allow for cases where exit area is rapidly changed.

Finite Difference Approximation, One-Sided Difference Form

The spatial derivatives were approximated in two different finite difference forms. When only the compressor was considered (no ducting), a simple, one-sided difference approximation was used. The control volume was divided into unequal lengths. Each length included a stage of the compressor as shown in Fig. 15. Figure 15 also shows the computation plane designations. The spatial derivatives at location i were approximated by

$$\frac{\partial W_i}{\partial z} \approx \frac{W_i - W_{im}}{z_i - z_{im}} , \tag{59}$$

$$\frac{\partial (IMP)_i}{\partial z} \approx \frac{IMP_{ip} - IMP_i}{z_{ip} - z_i} , \tag{60}$$

$$\frac{\partial A_i}{\partial z} = \text{constant} , \tag{61}$$

(the product of static pressure with the area-derivative was combined with the force term, F),
and

$$\frac{\partial H_i}{\partial z} = \frac{H_i - H_{im}}{z_i - z_{im}} . \tag{62}$$

44

Substitution into Eqs. (2), (4), and (7) produces the approximate equations,

$$\frac{\partial (\rho A)_{ip}}{\partial t} = \frac{W_i - W_{ip}}{z_{ip} - z_i} \, , \qquad (63)$$

$$\frac{\partial W_i}{\partial t} = \frac{IMP_i - IMP_{ip}}{z_{ip} - z_i} + F_i \, , \qquad (64)$$

and

$$\frac{\partial (XA)_{ip}}{\partial t} = \frac{H_i - H_{ip}}{z_{ip} - z_i} + WS_i + Q_i \, . \qquad (65)$$

Writing Eqs. (63), (64), and (65) from $i = 1$ to $i = in-1$; that is, from the forward to the aft control volume boundaries, results in $3 \times (in-1)$ first-order differential equations to be solved simultaneously.

Force and Shaft Work Computation

The division of the control volume into stage lengths was made because the forces and shaft work applied between stage entry and exit are obtainable from the stage characteristics. To determine the force and shaft work applied to each element, the flow coefficient into the element is calculated,

$$\varphi_i = \frac{U_i}{V_{\theta_i}} \, . \qquad (66)$$

45

The stage characteristic, represented as a polynomial curve fit, is then entered and ψ_i^P and ψ_i^T (or η_i) are found. Corrections for unsteady effects are made. The stage stagnation pressure ratio and temperature ratios which go into the force and shaft work computations are calculated from

$$PR_i = \frac{P_{ip}}{P_i} = \left[1 + \frac{U_{wh}^2}{c_p T_i} \psi_i^P \right]^{\frac{\gamma}{\gamma-1}} \qquad (67)$$

and

$$TR_i = \frac{T_{ip}}{T_i} = \left[1 + \frac{U_{wh}^2}{c_p T_i} \psi_i^T \right] . \qquad (68)$$

Shaft work is computed as

$$WS_i = W_i T_i \left[TR_i - 1 \right] . \qquad (69)$$

Similarly, the axial force is given by

$$F_i = IMP_i \left[IMPR_i - 1 \right] . \qquad (70)$$

$IMPR_i$ is the impulse function ratio across the stage, determined from the stagnation temperature and pressure ratios, area ratio, and flow directions,

$$IMPR_i = PR_i \frac{A_{ip}\left[1 + \gamma M_i^2 \cos^2 \beta_i \right]\left[1 + \frac{\gamma-1}{2} ME_i^2 \right]^{\frac{\gamma}{\gamma-1}}}{A_i \left[1 + \gamma ME_i^2 \cos^2 \beta_{ip}\right]\left[1 + \frac{\gamma-1}{2} M_i^2 \right]^{\frac{\gamma}{\gamma-1}}} . \qquad (71)$$

46

The variable, ME, is the equivalent Mach number downstream of the stage which would be present if steady flow existed. (Recall that the stage characteristics from which the forces and shaft work are determined, are based on experimental steady-state measurements). The value of ME is computed from a polynomial expression approximating the inverse of Eq. (72), for constant R and γ,

$$MFFE_i = \sqrt{\frac{\gamma}{R}} ME_i \left[1 + \frac{\gamma-1}{2} ME_i^2 \right]^{-\frac{1}{2}\left[\frac{\gamma+1}{\gamma-1}\right]} . \qquad (72)$$

MFFE is the downstream equivalent mass flow function,

$$MFFE_i = \frac{W_i \sqrt{T_i \ TR_i}}{P_i \ PR_i \ A_{ip} \ \cos \beta_{ip}} , \qquad (73)$$

defined in the same spirit as was ME.

The flow direction angles, β_i and β_{ip}, taken with respect to the axial direction, are input as functions of compressor corrected rotor speed, as constants, or, are assumed to be zero if no flow direction information is available.

Solution Procedure

Figure 16 outlines the overall digital computer solution procedure followed. The problem is solved as an initial condition problem. Following the flow path of Fig. 16, at time equal zero, initial values of the dependent

variables are specified. Entry plane, interior plane and exit plane conditions along with forces and shaft work are computed for time equal zero and are used to compute the time derivatives of the dependent variables. The time derivatives are then integrated using a fourth-order Runge-Kutta numerical integration method [50] for the dependent variable values at the next step in time. The new values are then used to compute conditions for that time step and the solution advances in time until the desired solution is obtained.

Some additional details of the computation procedure are as follows.

Entry plane conditions. At the forward boundary, $i = 1$, flow, W_1, will be available from integration of Eq. (64). Density, ρ_1, and the energy variable, X_1, are not available and must be supplied by the boundary condition. Stagnation pressure, P_1, and stagnation temperature, T_1, are supplied as boundary conditions. The mass flow function,

$$MFF_i = \frac{W_i \sqrt{T_1}}{P_1 A_1} , \qquad (74)$$

is computed. Mach number is related to the mass flow function by

$$MFF_1 = \sqrt{\frac{\gamma}{R}} M_1 \left[1 + \frac{\gamma-1}{2} M_1^2 \right]^{-\frac{1}{2}\left[\frac{\gamma+1}{\gamma-1}\right]} . \qquad (75)$$

The inverse form of Eq. (75) is approximated by a polynomial curve-fit of M_1 as a function of MFF_1 for constant R and γ. Static temperature, static pressure, density, and the energy variable may be computed knowing Mach number:

$$TS_1 = T_1 \left[1 + \frac{\gamma-1}{2} M_1^2 \right]^{-1} , \qquad (76)$$

$$PS_1 = P_1 \left[\frac{TS_1}{T_1} \right]^{\frac{\gamma}{\gamma-1}} , \qquad (77)$$

$$\rho_1 = \frac{PS_1}{R \ TS_1} , \qquad (78)$$

and

$$X_1 = \frac{PS_1}{\gamma-1} \left[1 + \frac{\gamma(\gamma-1)}{2} M_1^2 \right] . \qquad (79)$$

Interior plane values. On the interior planes, values of the three dependent variables are known from integration. To provide the other variables necessary for the solution, the following calculations are made at each plane:

$$U_i = \frac{W_i}{\rho_i \ A_i} , \qquad (80)$$

$$TS_i = \frac{1}{c_v} \left[\frac{X_i}{\rho_i} - \frac{U_i^2}{2} \right] , \qquad (81)$$

$$PS_i = \rho_i \ R \ TS_i , \qquad (82)$$

$$T_i = c_p \, TS_i + \frac{U_i^2}{2} \, , \tag{83}$$

$$P_i = PS_i \left[\frac{T_i}{TS_i} \right]^{\frac{\gamma}{\gamma-1}} , \tag{84}$$

$$a_i = \sqrt{\gamma \, R \, TS_i} \, , \tag{85}$$

$$M_i = \frac{U_i}{a_i} \, , \tag{86}$$

$$IMP_i = PS_i \, A_i \left[1 + \gamma \, M_i^2 \right] \, , \tag{87}$$

and

$$H_i = c_p \, W_i \, T_i \, . \tag{88}$$

Exit plane values. Density, ρ, and the energy variable, X, are available from integration. Flow, W, is not available from integration and must be found using the aft boundary condition. At the exit plane of the aft control volume, static pressure is specified. Exit stagnation-to-static pressure ratio is tested against critical pressure ratio to determine if the exit is choked or not, as follows:

$$\left[\frac{P}{PS} \right]_{crit} = \left[\frac{\gamma+1}{2} \right]^{\frac{\gamma}{\gamma-1}} \, . \tag{89}$$

If

$$\frac{P_{in}}{P_{exit}} \geq \left[\frac{P}{PS}\right]_{crit} \quad ,$$

the exit is choked and

$$M_{in} = 1.0 \ .$$

Then,

$$PS_{in} = \frac{(\gamma-1) \ X_{in}}{1 + \frac{\gamma(\gamma-1)}{2}} \ . \qquad (90)$$

If

$$\frac{P_{in}}{P_{exit}} < \left[\frac{P}{PS}\right]_{crit} \quad ,$$

the exit is unchoked, and

$$PS_{in} = P_{exit} \ .$$

Therefore,

$$M_{in} = \sqrt{\frac{2}{\gamma} \left[\frac{X_{in}}{PS_{in}} - \frac{1}{\gamma-1} \right]} \ . \qquad (91)$$

Mach number and static pressure are now known for either condition. Therefore, the remaining calculations are common for either case.

$$TS_{in} = \frac{PS_{in}}{R \, \rho_{in}} \, , \qquad (92)$$

$$U_{in} = M_{in} \sqrt{\gamma \, R \, TS_{in}} \, , \qquad (93)$$

and

$$W_{in} = \rho_{in} \, U_{in} \, A_{exit} \, . \qquad (94)$$

Impulse and enthalpy values at the exit and entry planes are computed using Eqs. (87) and (88).

Finite Difference Approximation, Central Difference Form

When ducting ahead of and behind the compressor was included in the system modeled, a noncentered, two-sided difference form of finite difference approximation was used to allow more accurate representation of the duct flow processes and to avoid some numerical stability difficulties experienced in attempts to apply the one-sided difference form to duct-flow cases.

The central difference algorithm used is derived as follows. Let $y(z)$ be any variable with continuous third derivative with respect to z, for which an approximation to $\frac{\partial y}{\partial z}$ is desired. Referring to Fig. 15, let

$$\Delta z_{ip} = z_{ip} - z_i \, , \qquad (95)$$

and

$$\Delta z_{im} = z_{im} - z_i \, . \qquad (96)$$

Expanding around the ith location,

$$Y_{ip} = Y_i + \frac{\partial y}{\partial z}\Big|_i \ \Delta z_{ip} + \frac{1}{2} \frac{\partial^2 y}{\partial z^2}\Big|_i \ \Delta z_{ip}^2 + 0\left[\Delta z_{ip}^3\right] \quad , \quad (97)$$

and

$$Y_{im} = Y_i + \frac{\partial y}{\partial z}\Big|_i \ \Delta z_{im} + \frac{1}{2} \frac{\partial^2 y}{\partial z^2}\Big|_i \ \Delta z_{im}^2 + 0\left[\Delta z_{im}^3\right] \quad . \quad (98)$$

Multiplying Eq. (97) by Δz_{im}^2, Eq. (98) by Δz_{ip}^2, differencing the results and solving for $\frac{\partial y}{\partial z}\Big|_i$ gives

$$\frac{\partial y}{\partial z}\Big|_i = a_{im} \ Y_{im} + a_i \ Y_i + a_{ip} \ Y_{ip} + 0\left[\Delta z^2\right] \quad , \quad (99)$$

where

$$\Delta_z = \max \left[\Delta z_{ip} \ , \ \Delta z_{im}\right] \quad , \quad (100)$$

and the weighting terms are

$$\left.\begin{array}{l} a_{im} = \dfrac{\Delta z_{ip}}{\Delta z_{im}} \ \dfrac{1}{\left[\Delta z_{ip} - \Delta z_{im}\right]} \\[3ex] a_i \ = \ - \dfrac{\Delta z_{im} + \Delta z_{ip}}{\Delta z_{ip} \ \Delta z_{im}} \\[3ex] a_{ip} = \dfrac{\Delta z_{im}}{\Delta z_{ip}} \ \dfrac{1}{\left[\Delta z_{im} - \Delta z_{ip}\right]} \end{array}\right\} . \qquad (101)$$

and

The sum of the coefficients,

$$a_{im} + a_i + a_{ip} = 0 \; . \tag{102}$$

Multiplying Eq. (102) by y_i and subtracting from Eq. (99) gives

$$\left. \frac{\partial y}{\partial z} \right|_i = a_{im} \left[y_{im} - y_i \right] + a_{ip} \left[y_{ip} - y_i \right] \; . \tag{103}$$

Replacing the spatial derivatives in the governing equations, Eqs. (2), (4), and (7), produces the alternate finite difference form,

$$\frac{\partial \left[\rho A \right]_i}{\partial t} = a_{im} \left[W_i - W_{im} \right] + a_{ip} \left[W_i - W_{ip} \right] - WB \; , \tag{104}$$

$$\frac{\partial W_i}{\partial t} = a_{im} \left[IMP_i - IMP_{im} \right] + a_{ip} \left[IMP_i - IMP_{ip} \right]$$

$$+ F + PS_i \left. \frac{\partial A}{\partial z} \right|_i \; , \tag{105}$$

and

$$\frac{\partial \left[XA \right]_i}{\partial t} = a_{im} \left[H_i - H_{im} \right] + a_{ip} \left[H_i - H_{im} \right] + WS + Q \; . \tag{106}$$

As was done with the one-sided case, the pressure-area partial derivative in Eq. (105) was combined with the axial force term.

The solution procedure followed (Fig. 16) was the same as used in the one-sided case except Eqs. (104), (105), and (106) were used instead of Eqs. (63), (64), and (65).

The bleed flow, forces, shaft work and heat added must also be made compatible with the two-sided difference form. Thus,

$$WB = a_{im} \, WB_{im} - a_{ip} \, WB_i \, , \tag{107}$$

$$F = -a_{im} \, F_{im} + a_{ip} \, F_i \, , \tag{108}$$

$$WS = -a_{im} \, WS_{im} + a_{ip} \, WS_i \, , \tag{109}$$

and

$$Q = -a_{im} \, A_{im} + a_{ip} \, Q_i \, . \tag{110}$$

Also, on the forward and aft boundary planes, an appropriate one-sided form of the differential equation was used. The force term for ducting was taken as a simple friction loss expressed as

$$F_i = -C_{d_i} \, \gamma \, PS_i \, A_i \, M_i^2 \, . \tag{111}$$

The value of C_{d_i} was adjusted to give a reasonable stagnation pressure loss in the ducting and to permit numerically stable operation of the model.

Interpretation and Limitations of
Differencing Methods

Differencing algorithm truncation error. The one-sided algorithm is a first-order approximation (i.e., it ignores terms of order (Δz) and above). The central difference algorithm is a second-order approximation (terms of order $(\Delta z)^2$ and above are ignored).

Let y again be any variable in the problem requiring spatial differentiation. The one-sided algorithm is found from expansion around a point,

$$y = y_i + \left.\frac{\partial y}{\partial z}\right|_i \left[z - z_i \right] + \frac{1}{2} \left.\frac{\partial^2 y}{\partial z^2}\right|_i \left[z - z_i \right]^2 + 0\left[\left[z - z_i\right]^3\right] . \quad (112)$$

Solving for the first partial derivative,

$$\left.\frac{\partial y}{\partial z}\right|_i = \frac{y - y_i}{z - z_i} - \frac{1}{2} \left.\frac{\partial^2 y}{\partial z^2}\right|_i \left[z - z_i \right] + 0\left[\left[z - z_i\right]^2\right] . \quad (113)$$

The truncation error in the governing equations is the error resulting from the substitution of the algorithm for the exact form of the spatial partial derivative. Therefore, an upper estimate for the truncation error for the one-sided case is

$$\varepsilon \approx \frac{1}{2} \left.\frac{\partial^2 y}{\partial z^2}\right|_i (\Delta z) . \quad (114)$$

The second partial derivative is finite, so, as $\Delta z \to 0$, the error vanishes and, referring to Eq. (112), the approximation is consistent of order one.

A similar analysis of truncation error for the central difference algorithm produces an error estimate of

$$\varepsilon \approx \frac{1}{3!} \left.\frac{\partial^3 y}{\partial z^3}\right|_i (\Delta z)^2 .\tag{115}$$

The central difference algorithm is therefore consistent of order two.

For the problems solved using the nonlinear system of equations produced by the approximation, numerical stability was investigated by running various time step sizes and observing the behavior of the solution at large times.

The system of equations constituting the model is for time-dependent, one-dimensional subsonic flow and is hyperbolic in nature, with specified boundary conditions and initial conditions. Thus, each integration step to compute the dependent variables at the new time, $(t + \Delta t)$, must be made within the region of influence of the known values at time, t. The Courant-Friedrichs-Lewy maximum time step criteria [51],

$$\Delta t_{max} = \frac{\Delta z_{min}}{a + U_{max}} ,\tag{116}$$

must be observed. For Δz_{min} = 0.25 ft, a = 1553 ft/sec (value at TS = 1000°R), U_{max} = a,

$$\Delta t_{max} = 8 \times 10^{-5} \text{ sec .}$$

Values used were typically one-half of Δt_{max}. Various values, depending on the nature of the specific analysis, were used.

With consistency and numerical stability, convergence is implied [51]. The best proof of convergence of the numerical solution is provided by the comparisons to experimental results given in Chapter III.

Disturbance frequency limitations. The differencing length is Δz; therefore, no disturbances having disturbance wave lengths of order Δz or less can be explicitly treated by the model. As a working limit, minimum wave lengths were restricted to 10 Δz_{max}. Therefore, the highest frequency phenomena with downstream propagation of pressure disturbances which could be explicitly treated by the model would be

$$f_{max} = \frac{(U + a)_{min}}{10 \, \Delta z_{max}} \, , \tag{117}$$

where U is a representative minimum axial velocity, and a is the acoustic velocity. For U = 300 ft/sec, a = 1116 ft/sec, and Δz_{max} = 0.25 ft,

$$f_{max} = 566 \text{ Hz} \; .$$

Similar limits can be computed for temperature rather than pressure oriented disturbances.

Steady-state solution. Inspection of the approximating equations, Eqs. (63), (64), and (65), or Eqs. (104), (105), and (106), shows that when the time derivatives are zero, the remaining equations are the exact mass, momentum and energy equations for steady, one-dimensional flow through a control volume of any specified size. The governing equations in the approximate form could also have been derived from an integral analysis of time-unsteady flow through a finite control volume.

CHAPTER III

EXAMPLE PROBLEMS WITH COMPARISON TO EXPERIMENTS,

ONE-DIMENSIONAL MODEL

Three steady-state examples and three dynamic examples are given. Three different compressors, the Allison XC-1, the NACA-8, and the General Electric J85-13, were driven to their stability limit for steady flow to demonstrate the physical processes and to test the models' ability to compute the steady-state stability limit. The NACA-8 compressor was stalled dynamically by imposed oscillating inflow. Dynamic response of the J85-13 for first oscillating inflow and then for oscillating back pressure was computed. Finally, the response of the NACA-8 compressor to a rapid inlet temperature ramp representing rocket exhaust gas ingestion is presented.

Three different compressors were modeled because experimental data necessary for comparison to the analytical model did not exist in a sufficiently complete set for any single compressor. A side benefit of modeling three compressors is the demonstration of the generality of the analysis method.

I. STEADY-STATE STABILITY LIMITS

The Allison XC-1 compressor is a four-stage compressor with design airflow and stall pressure ratio of 38.7 lbm/sec and 4.9:1. Details of the compressor, the overall compressor map, and the stage characteristics used in the model are presented in Appendix B. The information on this compressor was taken from [43]. The computational stations for the model are shown in Fig. 17a. No ducting was included in this model, thus, the one-sided difference formulation was used.

The compressor was loaded to the stability limit by increasing the exit pressure until flow breakdown was indicated. Inlet stagnation pressure and temperature were constant. Corrected rotor speed was 90% of design. Figure 18 illustrates the loading and the resulting stall process. Exit static pressure was ramped at a rapid rate to minimize computer time necessary for the computations. The rate was sufficiently slow, however, that transient effects were very small. Airflow at any stage never differed from compressor inlet airflow by more than 0.5% during loading. As the load on the compressor increased, compressor pressure ratio increased and airflow decreased until flow breakdown was indicated. Figure 19 shows some key compressor variables on an expanded time scale covering the flow breakdown as computed by the model. Stage 3 flow coefficient reaches its stall value at t = 55.7 msec. The flow, W_3,

into stage 3 is seen to begin to decrease at the same time. Shortly afterward the flows at each location begin to diverge one from the other and to oscillate. The static pressure behind stage 3 rapidly falls because the stage's pumping capacity is quite limited when stalled. The pressure forward of stage 3 rapidly increases in response to the sudden blockage to the flow which the stalled stage 3 produced. This static pressure signature is observed experimentally, and is a common means employed to determine which stage in a compressor stalled first, causing the instability to occur. (See Fig. X-27 in [14] for example.)

Figure 20 shows the 90% corrected rotor speed characteristic computed from the model compared to experimental measurements. The flow breakdown point indicated by the model agreed well with the experimental stability limit.

The model solution thus indicates the following sequence leading to compressor instability. The compressor is loaded and flow reduces until a stage somewhere in the compressor reaches its stall point (its maximum pressure coefficient point). The ability of that stage to continue to pump flow (i.e., to help support the pressure gradient over the length of the compressor imposed by the back pressure load) begins to diminish. As the flow reduction because of the increasing load continues, the ability of the stage to pump diminishes even further because of the increased load. Eventually, a point is reached where the flow into the stage becomes fully stalled, thus, little

force on the fluid is provided to pump the flow, and the
flow path through the compressor becomes blocked because of
the highly separated condition of the stalled flow in the
channels. In terms of the solution of the model equations,
as the loading is increased, a point is reached where no
stable solution to the governing equations exists which will
satisfy the imposed load (boundary conditions); thus, the
solution, like the flow through the compressor, becomes
unstable. However, the behavior of the model quickly
becomes nonrepresentative of the compressor shortly after
flow breakdown because the stage characteristics are not
valid for deeply stalled, dynamic situations.

NACA-8 Compressor

The NACA-8 compressor is an eight-stage com-
pressor with design airflow and stall pressure ratio of
65 lbm/sec and 10:1. Compressor details and stage charac-
teristics are given in Appendix B and are taken from [44,
45, 46]. The model included inlet ducting and combustor
ducting, thus, the central difference form was used.
Computation planes are shown in Fig. 17b. Figure 21
illustrates the loading of the NACA-8 model to the stability
limit by reducing the turbine nozzle area. The nozzle was
choked. Corrected rotor speed was 90% of design, inlet
stagnation pressure and temperature were constant. Pressure
ratio increased and corrected airflow decreased until
instability was encountered. The process was repeated at

70 and 80% corrected speed. The results are presented in
Fig. 22 and are compared to experimental data. Reasonable
agreement was obtained.

Extensive internal steady-state experimental
measurements were made on the NACA-8 compressor allowing
detailed model-to-experiment comparisons. Figure 23 shows
the variation of stage flow coefficients near the stability
limit as a function of corrected rotor speed. Both experi-
ment and model computed values are shown. Good agreement
was obtained.

It is also evident from Fig. 23 that this com-
pressor operates with forward stages below the stall value
of stage flow coefficient at corrected rotor speeds below
approximately 78%. Both experimental and computed flow
coefficient values for stage 1 are below stall at 70% speed.
This behavior is in agreement with previous theories and
experiment observations (see Chapter I and [21, 24]). An
explanation is as follows. At low corrected rotor speeds,
the forward stages are unable to deliver the design pressure
ratio. The flow density provided to the aft stages is
therefore much lower than that for which the compressor
axial area distribution was designed. Thus, to maintain
steady mass flow continuity, the flow coefficients (axial
velocity) in the aft stages are high. Indeed, at suffi-
ciently low corrected rotor speeds, the aft stages are even
choked. This limits the flow through the compressor to a
low value. It also means that the aft stage characteristics

will be steep relative to the forward stages (see Appendix
B). Therefore, at low corrected rotor speeds, as the load
on the compressor (the demanded pressure ratio) is increased,
flow reduces, and the following sequence occurs. The
ability of the aft stages to increase their pressure ratio
in response to the flow reduction is initially greater than
the decrease in pressure ratio occurring in the forward
stages in response to the same reduction in flow rate. Thus,
the increased load may be satisfied. As the loading con-
tinues, however, the forward stages become more and more
stalled, and a point is eventually reached where the aft
stages can no longer compensate. At that point, the load
can no longer be satisfied, and overall compressor insta-
bility occurs.

This example makes clear the need to distinguish
between stage stalling and overall compressor stalling or
instability. Overall compressor instability is always
preceded by stage stall, but is not always simultaneous with
stage stall.

General Electric J85-13 Compressor

The General Electric J85-13 compressor is an
eight-stage compressor with design airflow and stall
pressure ratio of 43 lbm/sec and 7.7:1. The compressor
employs a set of variable inlet guide vanes ahead of the
first-stage and compressor bleed from the second-, third-,
and fourth-stage stator cases. The guide vanes and bleed

65

valve are scheduled by the engine control as functions of corrected rotor speed. (Additional bias for inlet tempera- ture is also sometimes provided.) The schedules used in the model of this study are given in Appendix B. Stage charac- teristics and additional compressor details are also given in Appendix B and are taken from [47].

The steady-state stability limit and corrected speed characteristics were computed for 80 and 87% corrected rotor speed and are compared to experimental results (Fig. 24). Agreement was good. The compressor model was loaded by reducing turbine nozzle area. The nozzle was choked. The model included ducting, thus the central difference formulation was used.

II. DYNAMIC STABILITY LIMITS

Oscillating Inflow Loading, NACA-8 Compressor

Figure 25a shows the oscillation of the inlet total pressure imposed on the NACA-8 compressor model. Inlet total temperature and turbine nozzle area were constant. Corrected rotor speed was 70%. The pressure was oscillated at 20 Hz and the amplitude was slowly increased until compressor instability occurred. Overall compressor pressure ratio responded as shown in Fig. 25b. For con- venience, the model was started at 90% speed (initial conditions were previously calculated for 90% speed), rapidly decelerated to 70% speed, stabilized, and then the oscillation was imposed at t = 0.15 second.

The pressure ratio oscillations grew with the imposed pressure oscillations until instability was encountered. The response of the airflow into the compressor is shown in Fig. 25c. Initially, the flow variation is near sinusoidal, but, as the stages are driven into and out of their stalled regions, indications of flow breakdown begin to appear. Finally, the flow completely diverges to zero. The phase shifts and amplitude variations of the flow properties through the compressor due to the forced oscillations cause the stage flow coefficients to oscillate. Figures 25d through 25g show the flow coefficient dynamic variations. Also indicated are the individual stage stall values and the value of each flow coefficient at which the compressor steady-state stability limit was reached at 70% rotor speed. Excursions well below both values occur dynamically before total flow breakdown is experienced. This behavior is in qualitative agreement with experimental observations reported in [5, 37]. Examinations of the flow coefficient variations indicate that stage 7 was the stage which eventually became totally unstable and caused compressor instability (Fig. 25g).

Interpretation of the model results suggests the following physical process for instability with oscillating inflow. The stage flow coefficients are alternately driven into and out of their stalled regions. The stages must be held in the adversely loaded condition for a sufficiently long period of time for the flow breakdown to occur. Thus,

at a given frequency, the amount of time a stage (or group
of stages) will be in the highly loaded condition depends on
the amplitude of the imposed oscillation. Once a stage (or
group of stages) is transiently held in the adversely loaded
condition for a sufficient time period, the breakdown
process is locally like that which occurs in steady-state
loading.

The extent to which the flow coefficients oscil-
late depends on the dynamic response (phase angle and
amplitude ratio), which depends on oscillation frequency.
The loading process of Fig. 25 was repeated for frequencies
up to 320 Hz. The amplitude of imposed oscillation required
to drive the compressor to the stability limit is shown in
Fig. 26. As frequency increases, the amplitude required for
instability decreases. This occurs because, as frequency
increases, the phase lags and amplitude attenuations across
the stages increase; thus, the flow coefficient oscillations
are larger for a given imposed oscillation amplitude at
higher frequencies. (A fundamental discussion of the phase
shift and amplitude ratio effect is given in [24].)

A local minimum occurs in Fig. 26 near 80 Hz.
This occurs because, below 80 Hz, aft stages in the com-
pressor are critical, but, at frequencies higher than 80 Hz,
the amplitude attenuation across the forward stages
increases to the extent that it protects the aft stages, and
a new stage, farther forward in the compressor, becomes
critical.

The computations of Fig. 26 were made both with and without the unsteady cascade correction to the stage characteristics. First-stage reduced frequency is indicated at each value of oscillation frequency. Only small influences were experienced for this compressor in oscillatory inflow because of the relatively low reduced frequencies. Compressors and fans with larger blades would experience the influence of the correction at somewhat lower frequencies.

No experimental data were available for this compressor for direct comparison of stability limits. The general trend with frequency and the amplitude magnitudes are in agreement with the experiment of [37], however.

Oscillating Inflow Dynamic Response, J85-13 Compressor

As indicated in the previous section, the ability of the model to properly compute stability limits in oscillatory flow depends on its ability to compute the dynamic response of the various stages in the compressor to the imposed oscillations. Two experiments were carried out by NASA using the J85-13 turbojet engine to measure the unstalled dynamic response of the compressor to imposed inflow oscillations [52, 53]. Figure 27 is a sketch of the test arrangements. One test was conducted in a supersonic wind tunnel with an axisymmetric mixed compression inlet installed (Fig. 27a). Engine entry total pressure

oscillations were produced by oscillating the inlet bypass doors, causing the terminal normal shock in the inlet to oscillate, thus producing the downstream total pressure oscillations. The other test arrangement (Fig. 27b) used an airjet system in a section of ducting ahead of the engine. The airjet system operates by blowing high velocity air counter to the primary airstream. Planar oscillations in engine entry pressure were produced by oscillating the air-jet counterflow. In both cases, the oscillation amplitude was approximately 10%, peak-to-peak.

The J85-13 compressor model was subjected to imposed total pressure oscillations at the forward control volume plane, thus simulating the inlet experiment of Fig. 27a. The test setup of Fig. 27b differs from the model and the inlet experiment, in that the forward isolation plane provided by the supersonic flow in the throat of the inlet is not in the airjet test setup. The inlet and model dynamic systems consisted of the ducting downstream of the normal shock wave to the choked turbine nozzle in the engine. The airjet dynamic system includes all of the test cell ducting forward of the engine (until a choked valve, venturi, or other forward isolation point is reached) down to the choked turbine nozzle in the engine.

Figure 28 shows the variation of pressure amplitude ratio and phase angle for a 40-Hz oscillation through the compressor. Model computations are compared to the NASA data. The calculated trends are in good agreement with

experiment. Normalized magnitude differs by approximately 10% and phase angle by five degrees. The agreement, although reasonable for dynamic response data, could be improved by closer matching of engine operating condition between model and experiment. Also, the J85-13 engine run in the wind tunnel was likely not the same engine from which the stage characteristics were taken; thus, engine-to-engine variations are present. Further, the measurement uncertainties present in the experimental data (quoted as ±3% on pressure measurement and ±8 degrees on phase angle in [52]) may affect the comparison.

More detailed dynamic response results are shown in Fig. 29. Figures 29a and 29b represent the frequency response across one stage; Figs. 29c and 39d across approximately half of the compressor; and Figs. 29e and 29f across the entire compressor. Trend and level agreement between the model computations and the inlet results were reasonable, but, once again, could be improved by closer matching of the actual experimental hardware. In particular, the compressor discharge agreement suffered because the combustor volume of the actual engine was larger than that modeled. The combustor in the model was shortened during steady-state stability studies to keep the number of computation planes to a minimum, and was not increased for the dynamic response study.

Comparisons of the model and engine-with-inlet results with the airjet results show considerable

differences, especially near 40 Hz. The most likely cause
for the difference is the fact that the two dynamic systems
are not equivalent.

The model configuration used in the computations
was not tailored in detail to the experimental configuration
tested. The comparison shows that to obtain close agreement
dynamically, close attention to matching configuration must
be observed. The comparisons also show that considerable
care must be exercised in dynamic experimental work to
assure dynamic equivalency of systems (e.g., same isolation
points, volumes and geometry).

The results also suggest a potentially powerful
coupling of experimental work and analytical modeling. For
example, if it were not possible (or desired) to physically
dynamically isolate the airjet setup in the test cell to
simulate a given inlet-engine combination, the test setup,
including the airjet system and the compressor, could be
modeled and the model refined using experimental results to
closely match the test setup measurements. Then, the
analytical model inlet configuration could be modified to
match any desired configuration, and the desired information
derived from the model.

Oscillating Compressor Discharge Pressure,

J85-13 Compressor

Fuel flow to the J85-13 engine run with the super-
sonic inlet (Fig. 27a) was oscillated to determine the

propulsion system's dynamic response to oscillations induced within the engine. The oscillations produced compressor discharge oscillations of approximately 10%. The inlet was assumed to remain started, thus, the model dynamic system boundaries were the same as for the oscillating inlet bypass door case. Computations were made using the J85-13 model by adding heat to the combustor control volumes in an oscillatory manner to produce peak-to-peak oscillations in compressor back pressure of approximately 10%.

Figure 30 provides a comparison between computed and experimental amplitude ratio and phase angle variation through the compressor at a frequency of 40 Hz. Trend and level agreement were reasonable. Because of the high compressor rotor inertia, at 40 Hz, rotor speed cannot respond to the imposed fuel flow oscillations; thus, the effects of the oscillation are from aerodynamic upstream propagation only. The aft-stage characteristics (stages 4 through 8) (Appendix B) are quite steep, and at this condition, the stages are operating on the steep, negative slope part of the curves. Therefore, perturbations in the aft-stage airflow (or flow coefficient) will cause large oscillations in stage pressure ratio. Figure 30 indicates the magnification of the induced oscillation at the stage 4 entry. However, stages 1, 2, and 3 are operating in the flow coefficient range of 0.5 to 0.55 (i.e., on the shallow, positive slope part of the curves for stages 2 and 3, and the shallow, negative slope range for stage 1). As a result,

73

the forward stages oscillate pressure ratio very little in
response to a given airflow oscillation. Therefore, the
forward stages attenuate the upstream propagating dis-
turbance to the point that it is barely measurable at the
compressor inlet (Fig. 30a). Thus, it becomes clear that
the stage characteristic shapes and match points play a very
important role, not only in the steady-state stability of
the compressor, but also in the way disturbances are propa-
gated, thus, in the transient and dynamic stability
characteristics of the compressor.

Figures 31a and 31b present the dynamic response
to oscillating fuel flow across the compressor. Experi-
mental results are presented along with three different sets
of model computations. The first set is for constant rotor
speed and constant P_1 and T_1. The second set is for
variable rotor speed and constant P_1 and T_1. The third set
is for variable rotor speed, variable P_1 and constant T_1.
The three sets were computed to account for the three
dynamic effects caused by oscillating fuel flow. At fre-
quencies above approximately 20 Hz, the rotor speed cannot
respond to the oscillating fuel flow; thus, as already
discussed, upstream aerodynamic propagation is the chief
mechanism present. At frequencies below 20 Hz, rotor speed
can respond to the oscillations in fuel flow. thus, the
stage flow coefficients must now vary mechanically also
(i.e., wheel speed oscillates). Further, because wheel
speed varies, compressor airflow demand also must vary.

Inlet airflow varies as a result and causes the normal shock wave to oscillate. This causes the inlet total pressure, P_1, to oscillate.

Engine rotor speed response was represented in the model by a simple first-order differential equation simulating the engine control and rotor dynamic response. An oscillation in P_1, at the control volume forward boundary, was imposed to simulate the shock wave motion. As seen in Fig. 31, reasonable agreement with experiments was obtained only when all three of these effects were included. Because of the complicated nature of the three disturbance paths, agreement between model computations and experimental results at internal compressor locations was poor. Agreement could be improved by more exact modeling of the specific engine under consideration.

This example makes clear the importance of auxiliary perturbation propagation paths which must be considered, and which can have a strong influence on dynamic response, thus on stability.

Rapid Inlet Temperature Ramp to Stall,
NACA-8 Compressor

The NACA-8 compressor model was subjected to a rapid rise in inlet temperature simulating ingestion of hot gases from gun or rocket fire. Mechanical rotor speed, N, and P_1 were held constant. The initial corrected rotor speed was 70%. Figure 32a shows the imposed temperature

ramp. The engine entry temperature responded as shown in
the figure. Approximately 0.01 second was required for the
temperature pulse to be convected to the engine face.
Figure 32b shows the rapid reduction in corrected rotor
speed caused by the temperature ramp. Figure 32c shows the
stage flow coefficient variation caused by the temperature
ramp. The forward stages are rapidly driven downward by the
reduction in airflow accompanying the rapid temperature rise.
The resulting increase in forward stage loading immediately
prior to stall initially holds the mid-stage reduction to a
minimum, and actually unloads the aft stages. A point is
reached, however, where the forward stages stall and can no
longer support the load imposed on them. Flow breakdown
then occurs and is propagated back through the compressor.

In the example shown, the compressor may have
recovered from the instability with the removal of the
temperature pulse. On an actual engine, combustor flameout
would probably have occurred as a result of the compressor
instability which was initiated.

A series of ramps of differing ramp height was
computed at a ramp rate of 3600°R/second. The results are
compared in Fig. 33 to a scatter band for three different
engines from [16]. Although Fig. 33 is far from an exact
comparison, the results do indicate proper trend and
magnitude.

Gas composition was considered constant for these calculations. In the real experimental case, additional effects may be present because of the gas composition changes associated with ingestion of combustion products.

CHAPTER IV

DEVELOPMENT OF THREE-DIMENSIONAL MODEL

FOR DISTORTED FLOWS

The concepts used to develop the one-dimensional model can be extended to allow computation of spatial distortion effects on stability. Figure 34 depicts the control volume arrangement used for the distortion model. As was noted in Chapter II, the one-sided finite difference form of the governing equations could have been derived from a finite control volume integral analysis rather than a differential analysis. For greater simplicity in developing the distortion model, the finite control volume, integral approach is used.

The development of the distortion model is described as follows. The governing equations are written. Simplifications to allow distortion effects to be computed with a minimum amount of internal radial and circumferential flow detail are described. Special physical considerations for radial distortion effects and for circumferential distortion effects are presented. The method of solution, closely paralleling that used for the one-dimensional model is then described.

I. GOVERNING EQUATIONS

Figure 34 shows a finite control volume covering an arc sector of a concentric ring of the compressor annulus extending axially into the compressor one stage length. The compressor is divided into control volumes as indicated in Fig. 34. The subscript notation used to identify the location of a control volume is also shown. Subscript "i" indicates an axial position, "j" a radial position, and "k" a circumferential position. Control volume i,j,k is therefore the control volume whose axial-facing entry plane is on plane i, and whose axial-facing exit plane is on plane ip = i + 1. Its lower boundary surface approximately facing the radial direction is on surface j, its upper face is on surface jp = j + 1. Similarly, the control volume surface normal to the circumferential direction is on surface k and, advancing counterclockwise, its other surface normal to the circumferential direction is on plane kp = k + 1. The compressor inlet is at i = 1, the exit at i = in. The annulus inner surface is at j = 1, the outer surface is at j = jn. Circumferentially, k = 1 is the same plane as k = kn + 1. The compressor is therefore divided into inm · jnm · kn control volumes where inm = (in-1) and jnm = (jn-1). For the example of Fig. 34, the compressor is divided into 72 control volumes.

The compressor is divided radially on an equal axially-facing area basis. That is,

$$AZ_{ijk} = \frac{AZ_{total_i}}{\overline{jnm} \cdot \overline{kn}} , \qquad (118)$$

where AZ_{total_i} is the total axial facing area at any plane, i. Thus, all control volumes having the same index, i, are of equal volume because their lengths are equal.

Figure 35 illustrates a single control volume. For the purpose of this analysis, the control volume is assumed approximately rectangular on each face and therefore is a parallelepiped with the coordinate system; z, the axial direction, r, the radial direction, and s, a coordinate along the arc length of the control volume. The governing equations for each control volume may be written as follows.

Mass

$$
\left.
\begin{array}{c}
\underbrace{WZ_{ijk} + WR_{ijk} + WC_{ijk}}_{\substack{\text{mass flow entering the control} \\ \text{volume per unit time}}} = \\[2em]
\underbrace{WZ_{ipjk} + WR_{ijpk} + WC_{ijkp}}_{\substack{\text{mass flow leaving the control} \\ \text{volume per unit time}}} \\[2em]
+ \underbrace{\frac{\partial}{\partial t} \int_{vol_{ijk}} \rho \, d(vol)}_{\substack{\text{time rate of increase of mass} \\ \text{"stored" in the volume}}}
\end{array}
\right\} , \qquad (119)
$$

where,

$$WZ_{ijk} \;,\; WR_{ijk} \;,\; WC_{ijk}$$

are the mass flows into the axially-facing, radially-facing, and circumferentially-facing surfaces, respectively.

Axial Momentum

$$
\left.
\begin{array}{l}
\underbrace{\left[FZ_{ijk} + \overline{PS_{ijk}\;ARZ_{ijk}} + \overline{PS_{ijpk}\;ARZ_{ijpk}} + PS_{ijk}\;AZ_{ijk} - PS_{ipjk}\;AZ_{ipjk} \right]}_{\text{axial forces acting on control volume}} \\[3em]
= \;\; \underbrace{WZ_{ipjk}\;U_{ipjk} + \overline{WR_{ijpk}\;U_{ijpk}} + \overline{WC_{ijkp}\;U_{ijkp}}}_{\substack{\text{axial momentum leaving control volume} \\ \text{per unit time}}} \\[3em]
- \;\; \underbrace{WZ_{ijk}\;U_{ijk} - \overline{WR_{ijk}\;U_{ijk}} - \overline{WC_{ijk}\;U_{ijk}}}_{\substack{\text{axial momentum entering control volume} \\ \text{per unit time}}} \\[3em]
+ \;\; \underbrace{\frac{\partial}{\partial t} \int_{vol_{ijk}} (\rho U)\,d(vol)}_{\substack{\text{time rate of increase of axial momentum} \\ \text{"stored" in the control volume}}}
\end{array}
\right\} . \quad (120)
$$

The term, FZ, is the force of the blading and cases acting on the fluid in the axial direction. In Eq. (120), a projected area convention is used. The term, ARZ, means the projected area in the axial (Z) direction of the radially-facing (R) surface. Similarly, the projected area in the axial direction of the circumferentially-facing area is ACZ, and is zero because of the way the control volume was defined.

The bar above certain quantities of Eq. (120) indicates that these terms actually represent surface integrals. For example,

$$\overline{PS_{ijk}\ ARZ_{ijk}} = \int_{ARZ_{ijk}} PS\ d(ARZ)\ . \tag{121}$$

That is, the barred quantity indicates an integration of pressure over the projected area of interest. Similarly,

$$\overline{WR_{ijpk}\ U_{ijpk}} = \int_{ARR_{ijpk}} \rho v U\ d(ARR)\ . \tag{122}$$

Here, the barred quantity indicates integration over the radial-facing surface area of the axial momentum being carried across the surface by the radial flow. Implicit in Eq. (120) is the assumption that the flow properties are all uniform over the axially-facing surfaces of any given control volume because no surface integration is indicated over those surfaces.

Radial Momentum

$$
\left[FR_{ijk} + \overline{PS_{ijk}\ ACR_{ijk}} + \overline{PS_{ijkp}\ ACR_{ijkp}} \right.
$$

$$
\left. + \overline{PS_{ijk}\ ARR_{ijk}} - \overline{PS_{ijpk}\ ARR_{ijpk}} \right]
$$

$$
\underbrace{\qquad\qquad\qquad\qquad\qquad\qquad}_{\text{radial forces acting on control volume}}
$$

$$
= \underbrace{WZ_{ipjk}\ v_{ipjk} + \overline{WR_{ijpk}\ v_{ijpk}} + \overline{WC_{ijkp}\ w_{ijkp}}}_{\text{radial momentum leaving control volume}}
$$

$$
- \underbrace{WZ_{ijk}\ v_{ijk} + \overline{WR_{ijk}\ v_{ijk}} + \overline{WC_{ijk}\ w_{ijk}}}_{\text{radial momentum entering control volume}}
$$

$$
+ \underbrace{\frac{\partial}{\partial t}\int_{vol_{ijk}} (\rho v)\,d(vol)}_{\substack{\text{time rate of increase of radial momentum} \\ \text{"stored" in the control volume}}}
$$

$$
. \quad (123)
$$

The force, FR, includes centrifugal forces and viscous forces acting radially on the fluid in the control volume.

Circumferential Momentum

$$
\left.
\begin{aligned}
& \underbrace{FC_{ijk} + \overline{PS_{ijk}\ ACC_{ijk}} - \overline{PS_{ijkp}\ ACC_{ijkp}}}_{\substack{\text{circumferential forces acting on} \\ \text{control volume}}} \\[2em]
=\ & \underbrace{WZ_{ipjk}\ w_{ipjk} + \overline{WR_{ijpk}\ w_{ijpk}} + \overline{WC_{ijkp}\ w_{ijkp}}}_{\substack{\text{circumferential momentum leaving control} \\ \text{volume per unit time}}} \\[2em]
-\ & \underbrace{WZ_{ijk}\ w_{ijk} - \overline{WR_{ijk}\ w_{ijk}} - \overline{WC_{ijk}\ w_{ijk}}}_{\substack{\text{circumferential momentum entering control} \\ \text{volume per unit time}}} \\[2em]
+\ & \underbrace{\frac{\partial}{\partial t} \int_{vol_{ijk}} (\rho w)\,d(vol)}_{\substack{\text{time rate of increase of circumferential} \\ \text{momentum "stored" in the control volume}}}
\end{aligned}
\right\} . \quad (124)
$$

The force, FC, includes Coriolis and viscous forces acting on the fluid in the control volume.

Energy

$$
\left.
\begin{array}{c}
\underbrace{HZ_{ijk} + \overline{HR_{ijk}} + \overline{HC_{ijk}}} \\
\text{enthalpy entering the control} \\
\text{volume per unit time} \\[2em]
+ \quad \underbrace{WS + Q} \\
\text{shaft work done and heat added} \\
\text{to fluid in control volume per} \\
\text{unit time} \\[2em]
= \quad \underbrace{HZ_{ipjk} + \overline{HR_{ijpk}} + \overline{HC_{ijkp}}} \\
\text{enthalpy leaving the control} \\
\text{volume per unit time} \\[2em]
+ \quad \underbrace{\frac{\partial}{\partial t} \int_{vol_{ijk}} \rho \left[e + \frac{U^2 + v^2 + w^2}{2} \right] d(vol)} \\
\text{time rate of increase of energy} \\
\text{"stored" in the control volume}
\end{array}
\right\} \qquad (125)
$$

In Eq. (125), the barred quantities represent integrations over surfaces similar to those of the momentum equations. For example,

$$
\overline{HR_{ijk}} = \int_{AR} \left[c_p\, TS + \frac{U^2 + v^2 + w^2}{2} \right] \rho v\; d(AR) \quad . \quad (126)
$$

II. SIMPLIFICATIONS

In principle, the governing equations, Eqs. (119), (120), (123), (124), and (125), could be solved directly if all terms entering the equations could be evaluated. There are five differential equations for each control volume; therefore, for the example of Fig. 34, simultaneous solution of 360 differential equations would be required. This, in itself is not prohibitive, but, as finer divisions of the compressor, or, as larger compressors are considered, the computer storage and time requirements make the analysis inconvenient to use. Also, direct solution of the radial and circumferential momentum equations requires knowledge of equivalent radial and circumferential body forces not readily determinable. Further, numerical stability becomes more and more of a problem as the level of complexity and number of equations are increased.

The aim of this analysis is to compute the influence of distorted flows on compressor stability. This goal can be achieved with simplifications to the governing equations which circumvent, at least to an extent, the problems listed above and produce a practical model for distortion analysis. The simplifications are as follows.

Radial and Circumferential Flows

Each control volume of the compressor is assumed to be representable as a compressor element which is in radial and circumferential equilibrium with adjacent control

volumes when the compressor is running with uniform flow at its entry plane and uniform throttling at the exit. This means radial and circumferential crossflows are zero with no distortion present. Further, it is assumed that with distortion present, the radial and circumferential flow velocities are no greater than an order of magnitude less than the axial velocity.

The circumferential and radial crossflows into the control volume were computed using empirical relationships in place of the circumferential and radial momentum equations. Algebraic expressions, relating the crossflows to the static pressure differences between volumes, were used. This substitution reduced the number of differential equations requiring solution from five times to three times the number of control volumes.

Circumferential flows. Figure 36 illustrates a pair of control volumes circumferentially adjacent but with different static pressures. Looking down the blades in a spanwise direction, the flow path for the circumferential flow is through the blade row gaps. The blade row gaps, in effect, form a series of orifice-like restrictions to the circumferential flow. The circumferential flow is therefore computed by assuming that the static pressure in the high pressure region, PS_{high}, is a "reservoir" pressure driving flow to a lower pressure, PS_{low}, across a series of

orifices. The sequence of equations comprising the approxi-
mating algorithm is as follows.

$$M_{gap} = \sqrt{\left[\frac{2}{\gamma-1}\right]\left[\left[\frac{PS_{high}}{PS_{low}}\right]^{\frac{\gamma-1}{\gamma}}-1\right]} \quad , \qquad (127)$$

$$V_{gap} = M_{gap}\, a_{low\ pressure\atop region} \quad , \qquad (128)$$

$$WC_{gap} = \rho_{low\ pressure\atop region}\, V_{gap}\, A_{gap\atop effective} \quad . \qquad (129)$$

The approximations of using low pressure region acoustic
velocity and density are justified because the actual
differences between adjacent control volumes are not large.
The effective gap area is given by

$$A_{gap\atop effective} = CXFC\ A_{gap\atop physical} \quad , \qquad (130)$$

where CXFC is the circumferential crossflow coefficient.
For most cases, a nominal value of CXFC = 0.6 was used. The
best way to determine the coefficient value would be to
empirically calibrate it using compressor test data to pro-
vide observed crossflow values with circumferential
distortion applied to the compressor. The physical gap area
used included the space between the rotor and the stator
internal to each control volume plus the gap between the
trailing edge of the stator upstream of the control volume
and the rotor of the control volume. For the first stage,

the gap area was doubled to provide an accounting for the
additional circumferential flow adjustment which occurs
upstream of the compressor first rotor. Experimental data
is given in [54] which indicates the extent of the cir-
cumferential flow redistribution occurring at the compressor
entry. The process is described in detail in [38]. The
impact of crossflow magnitude on the solution is indicated
in Chapter V.

The circumferential velocity component across the
face of a control volume was computed as

$$W_{ijk} = \frac{V_{gap_{ijk}} + V_{gap_{ijkp}}}{2} .$$
(131)

The averaging is performed because the "gap" values apply
at the circumferential boundaries of the control volume.

Radial flows. Figure 37 shows a pair of radially
adjacent control volumes with different static pressure.
Viewed looking axially into the compressor, the blades form
channels in which radial flow may occur. In the actual
compressor, strong secondary flow fields caused by rotation
and viscous effects exist [55]. A considerable amount of
mass is carried back and forth across the control volume
radial boundary on a scale usually smaller than, or on the
order of, the control volume size. For the purposes of this
analysis, it is the net flow exchange, caused by distortion,

which is desired. An approximate, empirical form of the radial momentum equation is used.

$$WR_{net} = CXFR \sqrt{\rho_{low} \left[PS_{high} - PS_{low} \right]} + FR \quad . \quad (132)$$

The form of the equation is a simplification of the full radial momentum equation produced by neglecting the time-dependent term and flux terms across all but the radial-facing control volume boundaries. The force term, FR, is representative of the sum of viscous and centrifugal forces,

$$FR = F_{viscous} + \rho \ vol \ \omega^2 r \quad . \quad (133)$$

Because WR_{net} is the radial crossflow caused by distortion, the force, FR, is adjusted so as to cause WR_{net} to be zero with the compressor running with no distortion. This is, in a sense, equivalent to imposing the radial equilibrium condition,

$$\frac{\partial p}{\partial r} = \rho \ \omega^2 r \quad , \quad (134)$$

often used in three-dimensional analysis of compressor flows [20]. (In this application, however, FR conceptually includes viscous forces as well as centrifugal forces.) If the stage characteristics of each radially adjacent control volume were the same, with no distortion present, FR would be zero. If radial variation of stage characteristics is

considered (treated later in this chapter), FR is set to cause WR_{net} to be zero with no distortion present.

The term, CXFR, is the radial crossflow coefficient, and was determined by subjecting the model to radial inlet distortion and adjusting the coefficient to permit the stage exit radial static pressure gradient to vary as much as 2% from the undistorted value. This procedure was adopted because experimental data on radial distortion indicate that although the induced static pressure gradients relax as the flow progresses through the compressor, a slight gradient does remain [56]. The upper limit of CXFR was set by model numerical stability considerations. A value of CXFR = 0.01 was used for most cases computed in this study. For modeling a specific compressor, the value of CXFR would best be determined through tests of a compressor with radial distortion imposed and, adjustment of the coefficient made to match the observed change in stage exit flow distributions caused by the radial distortion.

The radial velocity across the boundary is computed from,

$$VR = \frac{WR_{net}}{\rho_{low} A_{channel}} .$$

(135)

The radial velocity component across the face of the control volume was computed as

$$v_{ijk} = \frac{VR_{ijk} + VR_{ijpk}}{2} \ . \tag{136}$$

III. SPECIAL CONSIDERATIONS FOR DISTORTION EFFECTS

Radial Distortion

Figure 38 illustrates the key physical processes occurring when a radially distorted flow approaches a rotor blade. On the left of Fig. 38, with uniform flow, considering the "design A" case, the tip and hub angles of attack and stage characteristic operating points are stable, near design conditions. On the right side of Fig. 38, a hub radial distortion (low velocity or total pressure in the hub region) case is shown. For case "A," the tip section operates at a lower angle of attack and higher flow coefficient while the hub becomes highly loaded, and, in case "A," is even stalled.

In the "design "B" case, the tip section in uniform flow is highly loaded while the hub section is only lightly loaded. Introduction of the radial distortion pattern for the "B" case causes the stage to operate at a better condition than was experienced with uniform flow. This illustrates that the way a compressor responds to radial distortion must depend on the spanwise work

distribution. Therefore, the one-dimensional stage characteristic used up to this point will not permit computation of radial distortion effects. As noted in Fig. 38, the distortion induced shift in radial work distribution, as well as the distorted flow pattern itself, induces radial crossflows.

The three effects which must be considered for radial distortion analysis are then as follows.

Radial variation of compressor entry flow properties. These are automatically treated by the model because of the division of the compressor into control volumes radially as well as circumferentially.

Radial variation of work and force distribution. Stage characteristics may be specified for each radial location in the same manner as a single, average stage characteristic was specified for the one-dimensional analysis. For the example of Fig. 34, each stage would have a hub, a midspan, and a tip set of stage characteristics.

For the XC-1 compressor used in example calculations in Chapter V, the compressor was divided radially into five annuli (jn = 6). Stage characteristics for each annulus were not available, but radial distributions of total pressure and total temperature at each stage discharge were given in [43] for one operating point at the corrected speed setting analyzed. These profile data were used to compute a correction to stage pressure ratio and stage

temperature ratio as a function of radius for each stage; thus, in effect, producing radially variant stage characteristics. A total temperature ratio correction factor,

$$CF^T(r) = \frac{TR(r)}{TR_{avg}} , \qquad (137)$$

and a total pressure ratio correction factor,

$$CF^P(r) = \frac{PR(r)}{PR_{avg}} , \qquad (138)$$

were determined for each stage from the profile data of [43]. The stage characteristics as functions of radius then become

$$\psi^T(r) = \psi^T_{avg} \left\{ CF^T + \left[\frac{U^2_{wh}}{c_p T} \right]^{-1} \left[CF^T - 1 \right] \right\} \qquad (139)$$

and

$$\psi^P(r) = \psi^P_{avg} \left\{ \left[CF^P \right]^{\frac{\gamma-1}{\gamma}} + \left[\frac{U^2_{wh}}{c_p T} \right]^{-1} \left[CF^{P^{\frac{\gamma-1}{\gamma}}} - 1 \right] \right\} . \qquad (140)$$

Inherent in this correction is the assumption that the pressure ratio and temperature ratio profiles, normalized by their averages, do not vary greatly over the range of flow coefficient of interest. Examination of data from other compressors where profile data were available over a wider range of operating conditions than used in this study showed the profiles' shapes to be consistent (within ±5%, and usually better) up to the point of stall.

Radial crossflows. Radial crossflows are computed
as described previously. A stage coefficient correction for
the distortion-induced radial flow velocity across the
control volume face is made by computing ϕ as

$$\phi = \sqrt{\frac{U^2 - v^2}{U_{wh}^2}} .$$ (141)

Circumferential distortion steady flow effects.
Figure 39a shows a compressor subjected to a simple circum-
ferential distortion pattern. Half of the face of the
compressor is in a lower than average total pressure region
and half is above. The example distortion waveform is a
simple sine wave. Upstream of the compressor face a length
of one compressor diameter or more, the static pressure
variation across the entry duct caused by the presence of
the compressor in the distorted flow field will be nearly
zero. The total pressure distortion at that location is
then principally an axial velocity distortion. Depending on
design characteristics and operating conditions of the
compressor, a portion of the high velocity region will be
diffused, creating a circumferential static pressure
gradient at the compressor face. This results in the
generation of a swirl velocity (Fig. 39a) carrying mass from
the high to the low pressure regions of the compressor face.
(This phenomenon is described in more detail in [27, 38,
54].) Figure 39a shows the influence of the variation in

95

axial and swirl velocities at four circumferential locations.
At θ = 0, there is no swirl velocity and axial velocity is
high; therefore, α is low and the stage is operating at a
lightly loaded condition. At θ = 90°, the axial velocity is
still fairly high, and the swirl component exists, and is in
the direction of rotor rotation. The swirl component
combines with wheel speed to reduce the angle of attack at
this point. At θ = 180°, the axial velocity is at a
minimum, thus causing a high angle of attack and high, even
stalled, stage loading. At θ = 270°, the axial velocity is
increased once more, but the swirl velocity component is
counter to rotor speed, thereby causing a higher angle of
attack and stage loading.

To a lesser extent, the same flow situation exists
at each stage entry. The effects on the stage character-
istic operating points are accounted for by computation of
the flow coefficient as

$$\phi = \frac{U}{U_{wh} + V_{sw}} \cdot$$
(142)

The swirl velocity, V_{sw}, is simply the circumferential
velocity component, w, at that particular location.

Unsteady effects. Figure 39b illustrates unsteady
airfoil effects for the same circumferential distortion
pattern. As indicated in Fig. 39b, the axial and swirl
velocities caused the flow coefficient to decrease, even to

below the steady-state stage stall value. The distortion
pattern is stationary. The rotor blades pass through the
spatially variant stationary pattern with each rotation,
and, from their point of reference, the flow is cyclically
unsteady. For a sinusoidal pattern, the frequency felt by a
rotor blade is

$$f = \frac{\omega}{2\pi} = \frac{N}{60} , \qquad (143)$$

where N is the mechanical rotor speed in rpm.

If the distortion pattern contained two cycles of
a sine wave instead of one (i.e., two low pressure regions),
the frequency would double. The reduced frequency for the
blade is

$$k = \frac{2\pi f C}{V_{rel}} = \frac{NC}{60 \, V_{rel}} . \qquad (144)$$

As discussed in Chapter II, the blade forces cannot instan-
taneously respond to rapid changes in angle of attack.
Therefore, as a blade passes through the low pressure region
(region of low ϕ, Fig. 39b), the blade forces, thus ψ, do
not follow the ϕ variation in a steady-state manner. Near
the stall point, if the variation is sufficiently rapid, the
lag is such that ϕ may proceed into the stalled region, and
quickly retreat, without blade stall actually occurring
[35]. The effect is more pronounced as reduced frequency
increases.

The unsteady cascade aerodynamics arising from circumferential distortion are approximated in the model following the treatment described in Chapter II, with an empirical correction added for the stalled blade region of operation. In Figs. 11 and 14, the unsteady lift magnitude is given as a function of reduced frequency. As was shown in Chapter II, Eq. (58), the dynamic response of ψ is the same as the dynamic response of C_ℓ. Therefore, the ratio of maximum dynamic ψ to the quasi-steady-state value is the same as the corresponding lift coefficient ratio. Or,

$$\frac{|\psi|_{max}}{|\psi|_{ss}} = \frac{|C_\ell|_{max}}{|C_\ell|_{ss}} = \text{DLR} . \tag{145}$$

(DLR means dynamic lift ratio.)

Referring to the upper left-hand corner of Fig. 39b, as a rotor blade begins at location $k = 1$, the value of ψ is ψ_1. As it progresses to the low pressure area, $k = 4$, $\psi = \psi_4$. The value of ψ_4 calculated on a steady flow basis in region $k = 4$ is $\psi_{4_{ss}}$, but, is incorrect because of dynamic effects. Let the actual value be $\psi_{4_{dyn}}$. A correction may be constructed as follows.

$$\frac{\psi_{4_{dyn}} - \psi_1}{\psi_{4_{ss}} - \psi_1} \approx \frac{|\psi|_{max}}{|\psi|_{ss}} = \text{DLR} . \tag{146}$$

Therefore,

$$\psi_{4_{dyn}} = DLR \ \psi_{4_{ss}} + (1 - DLR) \ \psi_1 \ . \tag{147}$$

Thus, the actual ψ_4 value depends not only on the steady-state value computed at the $k = 4$ location, but also on the blade's history as it passed from location $k = 1$.

This dynamic lag algorithm can be more generally written so as to be applied successively from one sector to the proceeding sector in the direction of rotor rotation. Or,

$$\psi_{ijk} = DLR \ \psi_{ijk_{ss}} + (1 - DLR) \ \psi_{ijkm} \ . \tag{148}$$

Thus, a lag is introduced into the stage characteristics. The value of DLR used was computed from

$$DLR = \sqrt{\frac{1}{1 + (\varepsilon k)^2}} \ , \tag{149}$$

as shown in Fig. 14. The reduced frequency, k, depended on the shape of the circumferential distortion pattern. The value of ε used followed the Goethert-Reddy analysis, but could readily be varied based on measured response of a compressor to circumferential distortion of varying pattern shape to account for additional viscous effects. This part of the unsteady correction predominates in the blade unstalled region of operation.

99

Goethert and Reddy point out in [32] that blade dynamic response should be expected to be more sluggish because of boundary layer effects not included in their inviscid analysis. This will be particularly true when the blade is operating in its stalled region. As already pointed out, the blade may transiently operate at angles of attack greater than the steady-state stall angle of attack without actually stalling. Experimental results on the degree to which this phenomenon may be present for isolated airfoils were compiled by Melick [36] and are indicated in Fig. 39c. The dynamic stall lift coefficient increment is correlated to the nondimensional time derivative of angle of attack for several different types of isolated airfoils.

This effect was incorporated in the model by computing the derivative of angle of attack from the change in flow coefficient as a blade passed through the distortion pattern using Eq. (34) to relate flow coefficient to angle of attack. A stall lift coefficient increment was then calculated using the empirical relationship of Fig. 39c. The resulting lift coefficient increment was then used to compute an equivalent increment in stage pressure and temperature coefficients using Eq. (39), neglecting the influence of the blade drag coefficient. With this infor- mation, the stage characteristic curve was translated upward, at the unstalled stage characteristic slope existing near the stage characteristic peak, in a manner analogous to the C_{ℓ} – α curve translation of Fig. 39c. This translation,

when combined with the dynamic lag effects of Eq. (149)
yields the dynamic stage characteristic behavior in the
stalled stage region depicted in Fig. 39b.

The Goethert-Reddy analysis [32] and Fig. 11
indicated less dynamic effects with a cascade of airfoils
than are experienced with a single, isolated airfoil. It
might well be anticipated that the stall region behavior of
the cascade would be less than the isolated airfoil case as
well. For that reason, the "stall overshoot" constant, m,
Fig. 39c, was chosen at four different values, and influence
on the solution determined parametrically. A value of m
between one and ten was found to be reasonable. Details of
the parametric investigation are discussed in Chapter V.

IV. METHOD OF SOLUTION

In this section, the approximation to the time
derivative of the volume integrals in the governing
equations is described. The resulting model equations,
including effects of the simplifications already described,
are written and the solution procedure described.

Volume Integral Time-Derivative Approximation

In each of the governing equations, Eqs. (119),
(120), and (125), a partial time derivative of a volume
integral exists. The general form is

$$Y = \frac{\partial}{\partial t} \int_{vol} y\ (z,r,s,t)\ d(vol)$$

$$= \int_{vol} \frac{\partial y}{\partial t}\ (z,r,s,t)\ d(vol)\ . \tag{150}$$

It is desired to approximate Y in terms of a control volume surface value of y. By the mean value theorem, there exists some point $(\bar{z},\bar{r},\bar{s})$ interior to the control volume, such that

$$\int_{vol} \frac{\partial y}{\partial t}\ (z,r,s,t)\ d(vol) = (vol)\ \frac{\partial y}{\partial t}\ (\bar{z},\bar{r},\bar{s},t)\ . \tag{151}$$

Let $\dfrac{\partial y_o}{\partial t}$ be a value of the integrand on either the forward or aft control volume face normal to the z-axis. The time derivative at the mean value point is then related to the surface time derivative by expanding around the surface point,

$$\left.\begin{aligned}
\frac{\partial y}{\partial t}\ (\bar{z},\bar{r},\bar{s},t) &= \frac{\partial y}{\partial t}\left[\ z_o,r_o,s_o,t\right] \\[2mm]
&+ \frac{\partial}{\partial z}\left[\frac{\partial y}{\partial t}\left[\ z_o+a\Delta z,r_o,s_o,t\right]\right]\Delta z \\[2mm]
&+ \frac{\partial}{\partial r}\left[\frac{\partial y}{\partial t}\left[\ z_o,r_o+b\Delta r,s_o,t\right]\right]\Delta r \\[2mm]
&+ \frac{\partial}{\partial s}\left[\frac{\partial y}{\partial t}\left[\ z_o,r_o,s_o+c\Delta s,t\right]\right]\Delta s
\end{aligned}\right\} \ , \tag{152}$$

where

$$o \leq a,\ b,\ c \leq 1\ .$$

Also,

$$\Delta z = z_o - \bar{z}$$

$$\Delta r = r_o - \bar{r}$$

and

$$\Delta s = s_o - \bar{s}$$

(153)

The approximation,

$$Y \approx (vol) \frac{\partial Y_o}{\partial t} ,$$

(154)

is chosen for use in the model. Multiplying Eq. (152) by the volume, and rearranging the order of differentiation yields an estimate for the truncation error.

$$\epsilon \approx (vol) \frac{\partial}{\partial t} \left[\frac{\partial y}{\partial z} \Delta z + \frac{\partial y}{\partial r} \Delta r + \frac{\partial y}{\partial s} \Delta s \right] .$$

(155)

The spatial derivatives are finite; therefore, as

$$\Delta z , \Delta r , \Delta s \rightarrow 0 ,$$

the error, ϵ, vanishes, thus the approximation is consistent of order one.

Numerical stability was investigated by running with different time step sizes as in the one-dimensional analysis. A time step size of approximately one-half the value indicated by the Courant-Friedrichs-Lewy criterion was used.

The actual approximations made were,

Mass

$$\frac{\partial}{\partial t} \int_{vol_{ijk}} \rho \, d(vol) \approx vol \frac{\partial}{\partial t} \rho_{ipjk} \, , \qquad (156)$$

Axial Momentum

$$\frac{\partial}{\partial t} \int_{vol_{ijk}} (\rho U) \, d(vol) \approx vol \frac{\partial}{\partial t} (\rho U)_{ijk} \, , \qquad (157)$$

Energy

$$\frac{\partial}{\partial t} \int_{vol_{ijk}} \rho \left[e + \frac{U^2 + v^2 + w^2}{2} \right] d \, (vol)$$

$$= vol \frac{\partial}{\partial t} \left[\rho \left[e + \frac{U^2 + v^2 + w^2}{2} \right] \right]_{ipjk} . \qquad (158)$$

Model Equations

Using the approximations and simplifications pre-
viously described yields the equations comprising the
distortion model.

Governing Equations

Mass, axial momentum, and energy were used. The
assumption of small v and w permits ignoring v and w terms

104

in some instances. Also, radial and circumferential flows
were determined by the crossflow approximations, thus
replacing the radial and circumferential momentum equations.
The resulting equations are as follows.

Mass

$$\frac{\partial \rho_{ipjk}}{\partial t} = \frac{1}{vol_{ijk}} \left[WZ_{ijk} + WR_{ijk} + WC_{ijk} \right.$$

$$\left. - WZ_{ipjk} - WR_{ijpk} - WC_{ijkp} \right] . \qquad (159)$$

Axial Momentum

$$\frac{\partial (\rho U)_{ijk}}{\partial t} = \frac{1}{vol_{ijk}} \left[F_{ijk} + IMP_{ijk} - IMP_{ipjk} \right] . \quad (160)$$

In Eq. (160) the contribution of the pressure integrated
over the projected areas of the radially oriented surfaces
is combined with the force term, FZ, of Eq. (120) to pro-
duce F. The force, F, is obtained from stage characteristic
information, as was done in the one-dimensional case. The
impulse terms are

$$IMP = PS \ AZ + WZ \ U . \qquad (161)$$

The momentum convected across the radial and circumferential
boundaries is negligible compared to the axial impulse terms.

Energy

$$\frac{\partial X_{ijpk}}{\partial t} = \frac{1}{(vol)_{ijk}} \left[WS_{ijk} + Q_{ijk} + HZ_{ijk} - HZ_{ipjk} \right] \quad . \quad (162)$$

In Eq. (162),

$$X = \rho \left[e + \frac{U^2}{2} \right] . \quad (163)$$

The v^2 and w^2 terms in Eq. (125) are negligible compared to U^2.

The terms neglected in Eqs. (160) and (162) are second-order terms determined by nondimensionalization and order of magnitude analysis of the equations. The terms were ignored because their influence on the solution was small. Also, inclusion of terms caused the numerical solutions to be generally less stable and to oscillate with small amplitude when a steady-state condition was reached.

Solution Procedure

The solution procedure used on the digital computer paralleled the approach used for the one-dimensional model outlined in Fig. 16. Initial values of the dependent variables, ρ, ρU, and X, were specified for every control volume location, ijk, to start the solution. For simplicity, the solution was always started from a steady, uniform flow condition, thus easing the chore of computing initial conditions.

Forward boundary conditions. Forward boundary
conditions were total pressure and total temperature,
$P_{1,j,k}$ and $T_{1,j,k}$, specified at each control volume face.
Entry plane conditions were then computed using the same
relationships as indicated in Fig. 16, but for every control
volume face instead of just one. Thus, the subscript, 1, in
Fig. 16, entry plane conditions, is replaced with subscript,
1,j,k.

Interior plane values. The same relationships
indicated in Fig. 16 are used again. Once more, the
subscript, i, must be replaced with i,j,k, and the quanti-
ties computed at each control volume face.

Crossflow values. Crossflows among the control
volumes are computed using Eqs. (127) through (136) for each
control volume. For all calculations made in this study,
crossflow across the compressor walls was zero.

Exit plane conditions. Only unchoked flow at the
exit was used for this study; thus, a uniform static
pressure was specified at every control volume aft face at
the compressor exit plane. Exit plane calculations follow-
ing the unchoked portion of the one-dimensional procedure
(Fig. 16, exit plane conditions) were therefore used with
the index, in, replaced by in,j,k, and computations made for
all control volumes.

Force and work computations. The same procedure used in the one-dimensional procedure was used again, but individually at each control volume. Local values of flow coefficient were computed and adjusted for distortion effects according to Eqs. (141) and (142). Further corrections to stage characteristics for radial variations and for unsteady effects were also made.

Time-derivative computations. The derivatives of the dependent variables, ρ, ρU, and X, are computed from Eqs. (159), (160), and (162) for every control volume. The values are then integrated to provide values of the variables at the next time step. The sequence is then repeated, with the boundary conditions changing in accordance with the specified problem under investigation and the computations continued until the desired solution is obtained.

Additional numerical stability considerations. To prevent numerical instabilities in the model solution caused by error buildup in the crossflow calculations when the driving pressure differences from control volume to control volume are very small, the pressure differences are tested to assure a significant pressure gradient exists. If a significant difference exists, crossflow is calculated; if not, crossflow is set to zero.

CHAPTER V

EXAMPLE PROBLEMS WITH COMPARISON TO EXPERIMENTS,

DISTORTION MODEL

One steady-state combined radial and circumfer-
ential distortion case for the XC-1 compressor is given.
Detailed experimental data were available for this case and
comparisons between model computations and experimental
measurements are presented. An example of time-variant
distortion for the XC-1 compressor is given. Pure radial
and pure circumferential distortion effects are computed.
A pure circumferential temperature distortion case is also
presented. Specific experimental data were not available
for the time-variant distortion, pure radial and pure
circumferential distortion patterns for the XC-1 compressor.
Data from other compressor tests were used, therefore, to
check the model results for proper trend and order of
magnitude.

In all cases discussed in this chapter, the
nominal compressor entry conditions were one atmosphere
pressure and 518.7°R temperature.

I. COMBINED DISTORTION PATTERN, XC-1 COMPRESSOR

Figure 40 shows a contour map of the combined
circumferential and radial total pressure distortion pattern
to which the XC-1 compressor was subjected. The pattern was

generated using a distortion screen to simulate a distortion
pattern present in the inlet of a VTOL aircraft [43]. The
pattern of Fig. 40 is for a corrected rotor speed of 90%.
The pattern amplitude was 10.2%. The lowest pressure region
was centered at approximately 210 degrees, in the tip region.

The distortion pattern was input to the model by
dividing the compressor annulus as indicated in Fig. 41.
Each stage was divided into 30 control volumes. The total
pressure at the compressor entry plane was averaged over
each control volume face to obtain the values indicated in
Fig. 41. The averaging resulted in reduction in the
apparent distortion pattern amplitude of approximately 1.0%.
The compressor was divided axially into four stages (five
axial locations) as shown in Fig. 34. Inlet total tempera-
ture was constant.

The compressor discharge static pressure was
specified as the aft boundary condition and was ramped
upward to load the compressor to the stability limit. The
process was conducted with and without distortion. The
results are shown in Fig. 42, and are compared to experi-
mental measurements. A reduction of 5.3% in stability limit
pressure ratio caused by distortion was computed. The
results agreed well with experimental measurements.

Figure 43a presents a detailed comparison of the
circumferential total pressure profiles in the tip region of
the compressor at each stage entry and exit. The distortion
pattern is seen to attenuate until, at the compressor

110

discharge, the variation is within 1% of the average value.
The agreement between the model and experiment is reasonably
good, usually within 1%, but occasionally different by as
much as 2%.

Two mechanisms serve to attenuate the circumfer-
ential distortion. The first stems from the fact that in
the low pressure region, the flow coefficient is lower;
thus, if the stage is not stalled, it will work harder
(produce a higher pressure and temperature coefficient) than
the high pressure regions. This effect tends to drive the
stage discharge pressures of the low and high pressure
regions toward equality. Figure 43b shows the corresponding
total temperature profiles and indicates the transposition
of the pressure distortion to temperature distortion. The
second mechanism working to smooth out the circumferential
pressure profile is circumferential crossflow, which was
discussed in Chapter IV. The slight phase shift between the
experimental and computed profiles may be caused in part by
slightly different crossflow in the actual compressor than
that allowed for in the model. (Crossflow effects are dis-
cussed in more detail later in this chapter.)

Another reason for the apparent phase shift is the
finite size of the control volumes. A finer circumferential
division would reduce any skew of the computed profile
waveform caused by averaging. The profile waveform ampli-
tude is also reduced by the averaging effect of the finite
control volume, just as occurred between Figs. 40 and 41.

Thus, the model profile amplitudes should be expected to be
1% or so less than the experimentally observed profiles.

Figure 44 shows the attenuation of the distortion
pattern through the compressor for the tip (Fig. 44a),
mid-span (Fig. 44b), and hub (Fig. 44c) regions. Agreement
between the computed and experimental results is generally
within 1% when allowance is made for the averaging effects
of the finite control volumes of the model. Pressure dis-
tortion reduction and temperature distortion production are
similar for the tip and mid-span regions. In the hub
region, however, both the computed and experimental measure-
ments indicate amplification of the distortion across the
first stage. This occurs because of the shallower stage
characteristics which exist in the hub region. The agree-
ment is not as good in the hub region as in the tip and
mid-span regions, indicating some inaccuracy in the
estimation of the hub region stage characteristics.

Figure 45 presents a comparison of radial total
pressure and temperature profiles in the region of maximum
radial distortion (at 210 degrees). Figure 45a shows agree-
ment within 1 to 2% except in the hub region at the second
stage entry. Once more, this indicates some inaccuracy in
the hub region stage characteristic. Figure 45b shows the
total temperature radial profiles. Agreement within 1% was
generally achieved.

Figure 46 presents similar profiles for the
compressor operating without distortion. Agreement between

computed and experimental results was generally within 1%.
Comparing Figs. 45 and 46 indicates that the radial dis-
tortion with low pressure in the hub decays rapidly in the
compressor, but some modification to the profiles does
occur.

Computation of proper distributions within the
compressor is important to stability limit determination
because it determines the local stage flow coefficient
distribution which in turn controls stability. Figure 47
presents the approximate flow coefficient distribution
computed for each stage just prior to reaching the com-
pressor stability limit. The flow coefficient values are
normalized by the stage stall value. As should be expected,
the distribution approximates the shape of the total
pressure distortion pattern. Stage 1, Fig. 47a, is almost
stalled in a small region at the tip. Stage 2, Fig. 47b, is
actually operating with the tip stalled in the distorted
region. Figure 47c shows a similar pattern for stage 3, but
it is not stalled. Stage 4, Fig. 47d, is stalled over a
wide arc from hub to tip, and, along with stage 2, is indi-
cated by the model to cause the flow breakdown leading to
total compressor instability.

The stalled region in stage 4 is seen to extend
beyond the concentrated low pressure region of the imposed
distortion pattern. The "pattern spreading" is caused by

the attenuation mechanisms discussed previously. When a
sufficiently large region becomes affected, total insta-
bility will occur.

Control Volume Size Selection

The example problem discussed in this section
illustrates the division of the compressor into finite
control volumes. The circumferential division (60-degree
arc sectors) was made because, as Goethert and Reddy point
out in [32], it is at approximately 60 degrees that each arc
sector acts very much as a separate compressor (as parallel
compressor theory would suggest); thus, the effects of the
unsteady cascade aerodynamic and crossflow approximations
are less crucial to achieving an accurate representation of
the compressor with regard to circumferential distortion.
As already noted, some error is introduced into the model
results because of local distortion pattern variations
within a 60-degree arc sector which are averaged out by the
approximating process.

The radial division selection (five rings) was
made based on the number of radial locations at which
experimental total temperature and total pressure profile
data were available for approximation of the radial vari-
ation of stage characteristics. In general, the selection
of the radial division must depend on the strength of the
radial gradients of the distortion pattern and the internal
radial profiles within the compressor. Divisions which

hold averaging error to within 1 or 2% should be quite
sufficient. Also, the radial crossflow representation in
the model is relatively crude. Therefore, it should not be
expected that finer and finer radial division of the com-
pressor would yield greater and greater accuracy of the
computed results. Additionally, the stage characteristic
data are based on one-dimensional (or, at best, averaged
over a radial distance) data, thus, a very fine division
radially would not be consistent with the resolution of the
input empirical information.

II. TIME-VARIANT DISTORTION

Figure 48 illustrates time-variant distortion.
The total pressure at the engine entry plane fluctuates with
time and also varies spatially across the compressor face.
The fluctuations are caused by unsteady flow processes in
the inlet, such as unsteady shock wave-boundary layer
separation [6, 13, 15]. The unsteady, nonuniform flow
causes distortion patterns at the engine entry which vary
with time, as illustrated in Fig. 48. The spatially
averaged pressure also oscillates.

The XC-1 compressor model was subjected to time-
variant distortion by superimposing a time-dependent
waveform on the distortion pattern of Fig. 40. Figure 49
shows the frequency spectrum of the superimposed fluctu-
ations. The spectrum is representative of those measured
experimentally in aircraft inlets [15]. The waveform was

applied in two parts. One part was phase shifted over the compressor face so as to alternately stretch and shrink the steady-state distortion pattern. The other part was added uniformly to produce timewise fluctuation in the spatial average. (Details of time-variant distortion pattern analysis and synthesis are discussed in [42].)

Two cases were computed for the XC-1 compressor with time-variant distortion. One was for an overall root-mean-square (rms) amplitude of 2% and the other was for 4%. With these inlet flow fields present, the compressor exit pressure was ramped upward until instability occured. Figure 50a shows the loss in stability limit pressure ratio correlated with the rms amplitude. A reduction results, as should be expected, and is of similar magnitude as the experimental results of [7] for a different compressor.

The model computed results were also correlated to the amplitude of the instantaneous distortion pattern existing just prior to compressor instability, as shown in Fig. 50b. All pattern shapes were similar, thereby per-mitting use of the simple distortion pattern magnitude descriptor. The results generalize well with steady-state distortion results, thus providing a degree of analytical conformation to the quasi-steady-state distortion approach currently used in experimental stability analysis. (See Chapter I and [7] for further details on that approach.)

The results shown in Fig. 50 should not be sur-prising because the XC-1 compressor is very small (about

17 inches in diameter and 8 inches long) and has high rotor speed (about 16,230 rpm at 90% speed). Therefore, fluctuations in the frequency range considered are sufficiently low to permit the instantaneous distortion pattern to dwell at the entry, and penetrate through the compressor in a quasi-steady manner. For example, in this case, approximately 0.0037 second is required for one rotor revolution, and 0.0017 second is required to convect a particle through the compressor (average axial velocity of 400 ft/sec). The period of the highest frequency component in the spectrum is 0.0038 second. Thus, the distortion effects will be much like steady-state distortion.

If larger amplitude timewise fluctuations are considered, particularly if the compressor is combined with upstream ducting and a combustor, planar oscillation effects similar to those discussed in Chapter III would show an effect also.

III. PURE RADIAL AND CIRCUMFERENTIAL DISTORTION PATTERNS

Three additional types of distortion patterns were computed to gain some insight into the influence of pattern severity and shape variations. The patterns considered are pure radial pressure distortion, pure circumferential pressure distortion, and pure circumferential temperature distortion. No specific experimental data for the XC-1

compressor were available for these cases. Comparisons to
experimental results from other compressors are made
therefore.

Radial Pressure Distortion

Figure 51a illustrates the results of loading the
XC-1 compressor model to the stability limit with tip radial
distortion (low pressure in the tip region). Pattern
severities of 5, 10, and 20% were considered. Because of
the relatively high tip loading of this compressor, Fig. 46,
it appears to be more sensitive to tip radial distortion.
Figure 51b shows the results for the hub radial case and
indicates the compressor to be more tolerant. Figure 52
shows comparisons of the XC-1 model results with experi-
mental data from a J85-13 test [16]. Similar results were
obtained, except that the J85-13 was even more tolerant of
hub radial distortion than the XC-1 was computed to be.

Circumferential Pressure Distortion

Figure 53 shows the effect of increasing the
severity of a 60-degree-arc circumferential distortion
pattern. Pattern magnitudes of 5, 10, 15, and 20% were
computed. Increasing loss of stability limit pressure ratio
and airflow was computed. Figure 54 shows the model
results compared to a range of experimental data from other
compressors. The model results appear reasonable.

Figure 55a depicts the variation of airflow in the
distorted region. Crossflow into the distorted region

rapidly increases the flow in that sector. Also shown in
Fig. 55a is the crossflow into an approximately 90-degree
distorted region computed for the XC-1 compressor from
experimental measurements [43].

Two different crossflow distribution cases were
computed to check the influence of crossflow on computed
compressor behavior. In one case, the first stage cross-
flow was increased. The increase was accomplished by
increasing the first stage crossflow area. Figure 55b indi-
cates the effect of the crossflow change on compressor
stability. The increased first stage crossflow case
matched the experimental distribution better, and caused a
higher stability limit pressure ratio with distortion
present. The improved performance comes about by allowing
crossflow to relieve downstream stage loading in the dis-
torted region. The crossflow distribution more closely
matching the experimental case was used in the previously
discussed combined distortion case.

Figure 56 shows the influence on stability of
varying the angular extent of the circumferential low
pressure area while holding the distortion pattern magnitude
constant. Three different cases, $\bar{\theta}$ = 30, 60, and 180
degrees are shown. The 30-degree case has the least loss in
stability. The 60- and 180-degree cases have approximately
the same percentage loss in stability limit pressure ratio
(taken at constant corrected airflow through each stability
limit point). However, the flow and pressure ratio

119

reduction for the 180-degree case was more than that of the 60-degree case. Figure 57 shows the loss in stability limit pressure ratio as a function of distortion pattern angular extent. Computations were made for four different values of dynamic lift coefficient "stall overshoot" constant, m, Fig. 39c. Also shown in Fig. 57 are experimental data from a J85-13 compressor subjected to distortion of varying angular extent. The experimental results fall between the m = 1 and m = 10 model computation results. The m = 40 results, corresponding to the center of the isolated airfoil correlation curve, Fig. 39c, produce virtual insensitivity to circumferential distortion up to 60 degrees, which is an unrealistic result. A value of m between 1 and 10 is a more realistic value. The results shown in Fig. 56 are for m = 10.

The analysis presented in Fig. 57 indicates that the unsteady cascade aerodynamic effects predominate in determining the response of the compressor to circumferential distortion below approximately 60 degrees angular extent.

Circumferential Temperature Distortion

Figure 58 shows the effect of varying the severity of total temperature distortion on compressor stability. Temperature distortion destabilizes the compressor in much the same manner as does pressure distortion. The distorted region, which is hotter than the rest of the compressor,

operates at reduced airflow, thus at reduced flow coefficients compared to the rest of the compressor. Therefore, as the load on the compressor is increased, the hot region stalls first, eventually causing the entire compressor to become unstable.

Mechanical rotor speed was constant during the loading. Corrected rotor speed, indicated in Fig. 58, decreased as much as 1.1% because of the increased average temperature over the face of the compressor.

Little influence of crossflow was found, indicating that basic parallel compressor theory (with appropriate unsteady cascade corrections) should give reasonable predictions for temperature distortion.

Figure 59 shows a comparison of model computed stability limit pressure ratio reduction to experimental results from other compressors. The predicted trend is reasonable, although more pressure ratio reduction is computed than was experienced on the other compressors.

CHAPTER VI

SUMMARY OF RESULTS AND RECOMMENDATIONS

FOR FURTHER WORK

The overall objective of this work was to develop an improved analytical method for the computation of turbine engine compressor stability loss caused by a wide range of different types of external flow disturbances. Another objective was to gain understanding of the physical processes leading up to instability as induced by external disturbances. The understanding was provided by the development of an analytical model and by application of the model to example problems with comparisons to experimental results. The objectives were accomplished in two major steps. In the first step, a one-dimensional, time-dependent math model was developed and applied to a variety of steady and time-dependent planar disturbances which are destabilizing to the compressor. In the second step, the concepts of the one-dimensional model were extended to three dimensions to allow the development of a time-dependent model for computation of radial, circumferential and combined distortion effects on stability. The distortion model was then applied to the computation of distortion cases with comparisons to experimental results. The results of those two steps are summarized as follows.

I. ONE-DIMENSIONAL, TIME-DEPENDENT ANALYSIS

Model Description

The one-dimensional model satisfies the time-dependent mass, momentum and energy equations. The full, nonlinear form of the equations, not used in earlier works, was used. The compressor is divided into control volumes on a stage-by-stage basis. The force and shaft work applied to the fluid is determined from empirical steady-state stage characteristics modified for unsteady cascade airfoil effects. The solution of the model governing equations is obtained through finite difference approximation of the governing differential equations. The resulting system of equations was solved on a digital computer.

Example Problems

Steady-state stability limit. Three different compressors were modeled. They were, an Allison XC-1 lift engine four-stage compressor, a NACA eight-stage research compressor, and the General Electric J85-13 turbojet engine compressor. The model was shown to be able to generally compute the steady-state stability limit pressure ratio and corrected airflow to within 1 to 2% of experimentally determined values. Compressor internal steady-state flow conditions in agreement with experimental values were also shown to be computed by the model. The initial flow

breakdown process in the compressor at the stability limit
was shown to be reasonably well reproduced by the model.

Dynamic stability limits (oscillating inflow
loading), NACA eight-stage compressor. The NACA eight-stage
compressor model was driven to its stability limit by planar
oscillation of the compressor inlet pressure at frequencies
from 20 to 320 Hz. The model results indicated that, as
frequency increased, the amplitude required to cause insta-
bility decreased. It also showed that the individual stages
transiently enter and retreat from their stalled regions
during the oscillations without total compressor instability
occurring. As the oscillation amplitude increased, however,
the time period during which the stage is in the stalled
region is increased, and a point is eventually reached where
total compressor instability occurs. The analysis showed
further that, for planar oscillations in the frequency range
analyzed, the influence on stability of the unsteady cascade
correction to the steady-state stage characteristics was
small.

The ability of the model to compute dynamic
stability limits was shown to depend strongly on the model's
ability to properly compute the dynamic response of the
compressor to imposed disturbances.

Oscillating inflow dynamic response, J85-13
compressor. The unstalled, dynamic response to planar entry
pressure oscillations in terms of amplitude ratio and phase

angle were computed and compared to experimental data. The
experimental data were obtained by NASA in a wind tunnel at
Mach 2.5 with the engine operating behind a supersonic
inlet. The compressor entry pressure oscillations were pro-
duced by forced oscillations of the inlet bypass doors.
Data were acquired from 1 to 50 Hz. Amplitude ratios and
phase angles computed by the model agreed with experimental
values to within 10% and five degrees, respectively. An
additional set of experimental oscillating entry pressure
data obtained by NASA was compared to the inlet data and
model computations. The additional set was obtained in a
test cell with an array of small airjets blowing against the
primary engine flow in an oscillatory manner to produce the
pulsations. The results differed markedly from the inlet-
engine results, probably because of differences in the
boundaries of the dynamic system under consideration.

Oscillating compressor discharge pressure, J85-13
compressor. The unstalled, dynamic response of the J85-13
compressor to oscillations in discharge pressure caused by
engine fuel flow oscillations was computed using the model
and compared to experimental results. A frequency range of
1 to 60 Hz was considered. Agreement between model compu-
tations and experimental results was 10 to 20% and 5 to 10
degrees on amplitude ratio and phase angle, respectively, at
40 Hz. The experiment was conducted in a wind tunnel at
Mach 2.5 with the engine installed behind a supersonic inlet.

Three dynamic disturbance paths were discovered to exist at frequencies below 20 Hz and were included in the model analysis. The three paths are: (1) the direct upstream propagation of the pressure disturbances, (2) oscillation of stage pumping because of rotor speed oscillations, and (3) oscillation of compressor entry pressure caused by the supersonic inlet shock wave oscillations resulting from the engine airflow oscillation. The example illustrated the influence of multiple disturbance paths on dynamic behavior and stability.

Rapid inlet temperature ramp, NACA eight-stage compressor. The NACA eight-stage compressor model was driven to instability by ramping inlet temperature at a rate of 3600°R per second to simulate hot gas ingestion from rocket or gun fire. Ramp heights of 100°R or over caused instability. The results were compared to a band of experimental data from other compressors. The model computations were within the band.

II. DISTORTION ANALYSIS

Model Description

The concepts of the one-dimensional model were extended to allow computation of the effects on stability of distorted flow at the compressor entry plane. The compressor was divided radially and circumferentially as well as axially into control volumes, and crossflow between the

control volumes caused by distortion was approximated. The governing equations were developed from the three-dimensional, time-dependent mass, momentum and energy equations for a finite control volume. Empirical crossflow relationships were used to replace the radial and circumferential momentum equations for purposes of simplification. The radial work distribution variation effect necessary for treatment of radial distortion was approximated using average stage characteristics modified as a function of radius by an empirical total pressure and total temperature profile correction. Crossflow and unsteady cascade effects for circumferential distortion were built into the model also. The resulting set of equations was solved using a digital computer.

Example Problems

Steady-state combined radial and circumferential distortion. The four-stage, XC-1 compressor was modeled for distortion by dividing each stage into five radial and six circumferential divisions. This produced 30 control volumes per stage, or 120 control volumes for the entire compressor. The model was subjected to a combined distortion pattern and loaded to the stability limit using compressor discharge static pressure as the aft boundary condition. Detailed experimental data were available for this case and comparisons were made. The stability limit pressure ratio and corrected airflow were computed to within 1.3 to 0.8% of the

experimental values, respectively. Detailed circumferential
and radial profile comparisons of total pressure and total
temperature were made. Agreement with experimental results
was reasonable.

Time-variant distortion. A timewise fluctuating
total pressure was superimposed on the steady-state combined
radial and circumferential distortion pattern to which the
XC-1 compressor model was subjected to simulate time-variant
distortion. The reduction in stability limit pressure ratio
was shown to correlate well with the severity of the instan-
taneous distortion pattern existing just prior to compressor
instability. The correlation also agreed with results
obtained by imposing steady-state distortion of increased
severity on the model. This result provides an analytical
confirmation of the quasi-steady-state distortion method of
analysis currently used in experimental stability test and
analysis.

Pure Radial and Circumferential Distortion

The XC-1 compressor model was subjected to pure
radial pressure distortion, pure circumferential pressure
distortion, and pure circumferential temperature distortion
patterns of varying severity and their influences on
stability were computed. No specific experimental data for
the XC-1 compressor subjected to these specific distortion
patterns were available. Therefore, comparisons were made

128

to experimental results from other compressors. Trends and general magnitudes computed by the model were in agreement with the experimental results.

The response of the compressor to pure radial distortion was indicated by the model analysis to depend most strongly on the radial work distribution (radial stage characteristic variations) built into the compressor. Response to pure circumferential pressure distortion and attenuation of the distortion pattern through the compressor depended on a combination of stage characteristic curve slope (steepness), and mildly on crossflow distribution. Response to circumferential distortion patterns with low pressure region angular extent less than 60 degrees was indicated to depend strongly on the blading unsteady aerodynamic response.

III. RECOMMENDATIONS FOR FURTHER WORK

The modeling technique developed in this work can be used beneficially in turbine engine compressor design and development and to assist in solving operational problems which may arise in field use. There are both improvements and an extension which can potentially increase its value further.

Improvements

Stage characteristics. Stage characteristic information is at the heart of this modeling method.

Efforts should be made to obtain improved stage character-
istic information. More attention should be given to
acquiring accurate stage characteristic data during com-
pressor tests. Theoretical methods for computing (or at
least extending the experimental results) should be
developed.

Unsteady cascade aerodynamics. Continued work is
necessary in this area to define the unsteady aerodynamics
of cascades, particularly near and in the stalled operating
regime.

Crossflows. The approximate methods used for
crossflow in the model are somewhat crude. Specific atten-
tion should be given to improving the crossflow represen-
tation. A possible approach is the determination of a
different solution method to solve the governing equations,
including the radial and circumferential momentum equations.
The method would have to be reasonably economic in terms of
computer storage and time requirements. This would also
require determination of a proper representation for the
radial and circumferential forces present in the compressor.

Extension

Post-stall behavior. The model could be extended
to compute the behavior of the compressor after an insta-
bility was entered by incorporation of unsteady aerodynamic
cascade behavior in the deeply stalled regime. Because of

the highly inefficient processes present in the compressor
in deep stall, consideration should also be given to the
metal-to-gas unsteady heat transfer processes. Such an
extension would be valuable for determining methods for
returning the compressor from an unstable to a stable
condition.

BIBLIOGRAPHY

1. Kimzey, W. F., and C. W. Edmunds. "An Investigation of
   the Effects of Inlet Flow Density on Compressor
   Blade Dynamic Stress During Compressor Stall of a
   YJ93-GE-3 Turbojet Engine in an Altitude Test
   Cell," Arnold Engineering Development Center
   TR-66-101, Arnold Air Force Station, Tennessee,
   June, 1966.

2. Montgomery, J. Franklin, III. "The Need for Air Force
   Engine Stability Margin Testing for Inlet-Engine
   Interface Definition," Air Force Aero Propulsion
   Laboratory TR-71-84, Wright-Patterson Air Force
   Base, Ohio, December, 1971.

3. Turner, C. E., and M. K. Lake. "Stall Line Determi-
   nation of a Modified J85-GE-5 Turbojet Compressor,"
   Arnold Engineering Development Center TR-62-150,
   Arnold Air Force Station, Tennessee, September,
   1962.

4. Calogeras, James E., Charles M. Mehalic, and
   Paul L. Burstadt. "Experimental Investigation of
   the Effects of Screen-Induced Total Pressure Dis-
   tortion on Turbojet Stall Margin," National
   Aeronautics and Space Administration TMX-2239,
   Lewis Research Center, Cleveland, Ohio, March,
   1971.

5. Reynolds, G. G., W. F. Vier, and T. P. Collins. "An
   Experimental Evaluation of Unsteady Flow Effects on
   an Axial Compressor," Air Force Aero Propulsion
   Laboratory TR-73-43, Wright-Patterson Air Force
   Base, Ohio, July, 1973.

6. Kimzey, W. F., and R. J. Lewis. "An Experimental
   Investigation of the Effects of Shock-Induced
   Turbulent In-Flow on a Turbojet Engine." Paper
   presented at the AIAA Second Propulsion Joint
   Specialist Conference, Air Force Academy, Colorado
   Springs, Colorado, June 13-17, 1966.

7. Plourde, G. A., and B. Brimlow. "Pressure Fluctuations
   Cause Compressor Instability," Proceedings of the
   Air Force Airframe-Propulsion Compatibility
   Symposium. Wright-Patterson Air Force Base, Ohio:
   Air Force Aero Propulsion Laboratory, 1970.
   Pp. 576-604.

8. Ward, G. G. "Compressor Stability Assessment Program,
        Volume I--Dual Spool Compression System Test and
        Data Analysis," Air Force Aero Propulsion Labora-
        tory TR-74-107, Wright-Patterson Air Force Base,
        Ohio, December, 1974.

9. Mehalic, Charles M., and Ray A. Lottig. "Steady-State
        Inlet Temperature Distortion Effects on the Stall
        Limits of a J85-GE-13 Turbojet Engine," National
        Aeronautics and Space Administration TMX-2990,
        Lewis Research Center, Cleveland, Ohio, February,
        1974.

10. Rich, William A., and Robert A. Reale. "Specification
        Rocket Test for Turbojet/Turbofan Missile Gas
        Ingestion," Naval Air Propulsion Test Center
        ATD-197, Naval Air Propulsion Test Center, Trenton,
        New Jersey, February, 1971.

11. Boyd, H. E., Jr. "Propulsion System Integration and
        Test Program (Steady-State), Part VI, YTF-33
        Turbofan Engine Tests," Air Force Aero Propulsion
        Laboratory TR-69-44, Part VI, Wright-Patterson Air
        Force Base, Ohio, June, 1969.

12. Gas Turbine Engine Flow Distortion Methodology.
        Warrendale, Pennsylvania: Society of Automotive
        Engineers, 1976.

13. Proceedings of the Air Force Airframe-Propulsion
        Compatibility Symposium. Wright-Patterson Air
        Force Base, Ohio: Air Force Aero Propulsion
        Laboratory, 1970.

14. Aircraft Propulsion. Washington, D. C.: National
        Aeronautics and Space Administration, 1970.

15. Kimzey, W. F., and S. H. Ellis. "Supersonic Inlet
        Simulator--A Tool for Simulation of Realistic
        Engine Entry Flow Conditions." Society of Auto-
        motive Engineers Paper 740824, Warrendale,
        Pennsylvania, October, 1974.

16. Distortion Induced Engine Instability. Neuilly sur
        Seine, France: Advisory Group for Aerospace
        Research and Development, 1974.

17. Whittle, F. "The Turbo-Compressor and the Super-
        charging of Aero Engines," Royal Aeronautical
        Society Journal, 35:1047-1074, November, 1931.

18. Kearton, W. J. Turbo-Blowers and Compressors. London: Sir Isaac Pitman and Sons, Ltd., 1926.

19. Den Hartog, J. P. Mechanical Vibrations. New York: McGraw-Hill Book Company, Inc., 1940.

20. Horlock, J. H. Axial Flow Compressors. Huntington, New York: Robert E. Krieger Publishing Company, 1973.

21. Pearson, H., and T. Bowmer. "Surging of Axial Compressors," The Aeronautical Quarterly, 1:195-210, November, 1949.

22. Bullock, Robert O., Ward W. Wilcox, and Jason J. Moses. "Experimental and Theoretical Studies of Surging in Continuous-Flow Compressors," National Advisory Committee for Aeronautics Report 861, Aircraft Engine Research Laboratory, Cleveland, Ohio, April, 1946.

23. Howell, W. T. "Stability of Multi-stage Axial Flow Compressors," The Aeronautical Quarterly, 15:328-356, November, 1964.

24. Goethert, B. H. "Research and Engineering Studies and Analysis of Fan Engine Stall, Dynamic Interaction with Other Subsystems and Systems Performance," Air Force Aero Propulsion Laboratory TR-70-51, Wright-Patterson Air Force Base, Ohio, July, 1970.

25. Daniele, C. J., R. J. Blaha, and K. Seldner. "Prediction of Axial Flow Instabilities in a Turbojet Engine by Use of a Multistage Compressor Simulation on the Digital Computer," National Aeronautics and Space Administration TMX-3134, Lewis Research Center, Cleveland, Ohio, January, 1975.

26. Alford, J. S. "Inlet Flow Distortion Index." Paper presented at the International Days of Aeronautical Sciences Meeting, Paris, France, May 27-29, 1957.

27. Pearson, J. "Wakes in Axial Compressors," Journal of the Royal Aeronautical Society, 63:415-416, July, 1963.

28. Hercock, R. G., and D. D. Williams. "Aerodynamic Response," Distortion Induced Engine Instability. AGARD Lecture Series No. 72. Neuilly sur Seine, France: Advisory Group for Aerospace Research and Development, 1974. Pp. 3-1 - 3-37.

29. Goethert, B. H., and W. F. Kimzey. "Effect of High Frequency Fluctuations of Inlet Flow on Compressor Stall." Paper presented at the 32nd Meeting of the Propulsion and Energetics Panel of AGARD, Toulouse, France, September 9-13, 1968.

30. Reid, C. "The Response of Axial Flow Compressors to Intake Flow Distortion." American Society of Mechanical Engineers Paper No. 69-GT-29, presented at the Gas Turbine Conference and Products Show, Cleveland, Ohio, March, 1969.

31. Calogeras, James E., Charles M. Mehalic, and Paul L. Burstadt. "Experimental Investigation of the Effect of Screen-Induced Total Pressure Distortion on Turbojet Stall Margin," National Aeronautics and Space Administration TMX-2239, Lewis Research Center, Cleveland, Ohio, March, 1971.

32. Goethert, B. H., and K. C. Reddy. "Unsteady Aerodynamics of Rotor Blades of a Compressor Under Distorted Flow Conditions." Paper presented at AGARD Fluid Dynamics Panel Specialist Meeting on Aerodynamic Interference, Silver Springs, Maryland, September 28-30, 1970.

33. Peacock, R. E. "Unsteady Response of Compressor Rotors at a 90° Circumferential Pressure Distortion," Proceedings of a Workshop on Unsteady Flows in Jet Engines Held at United Aircraft Research Laboratories, F. O. Carta, editor. West Lafayette, Indiana: Purdue University, Project Squid Headquarters, 1974. Pp. 193-210.

34. Korn, J. A. "Estimated Effect of Circumferential Distortion on Axial Compressors Using Parallel Compressor Theory and Dynamic Stall Delay." American Institute of Aeronautics and Astronautics Paper No. 74-33, presented at 1974 AIAA Aerospace Sciences Meeting, Washington, D. C., January-February, 1974.

35. Carta, F. O. "An Experimental Study on the Aerodynamic Response of a Subsonic Cascade Oscillating Near Stall," Project Squid Headquarters TR-UTRC-2-PU, West Lafayette, Indiana, July, 1976.

36. Melick, H. C. "Analysis of Inlet Flow Distortion and Turbulence Effects on Compressor Stability," National Aeronautics and Space Administration CR-114577, Moffett Field, California, March, 1973.

37. Gabricl, David S., Lewis E. Wallner, and
    Robert J. Lubick. "Some Effects of Transients in
    Inlet Pressure and Temperature on Turbojet
    Engines." Paper presented at the 25th Annual
    Meeting of the Institute of the Aeronautical
    Sciences, New York, January 28-31, 1957.

38. Kimzey, William F. "The Effects of Unsteady, Non-
    uniform Flow on Axial Flow Compressor Stall
    Characteristics." Unpublished Master's thesis,
    The University of Tennessee, Knoxville, 1966.

39. Kuhlberg, J. F., D. E. Sheppard, and E. O. King.
    "The Dynamic Simulation of Turbine Engine Com-
    pressors." American Institute of Aeronautics and
    Astronautics Paper No. 69-486, presented at the
    AIAA/SAE Joint Propulsion Specialist Conference,
    Cleveland, Ohio, June, 1969.

40. Willoh, Ross G., and Kurt Seldner. "Multistage
    Compressor Simulation Applied to the Prediction of
    Axial Flow Instabilities," National Aeronautics
    and Space Administration TMX-1880, Lewis Research
    Center, Cleveland, Ohio, September, 1969.

41. Jacocks, J. L. "Prediction of Maximum Time Variant
    Inlet Distortion Levels," Proceedings of a Workshop
    on Unsteady Flow in Jet Engines Held at United
    Aircraft Research Laboratories, F. O. Carta, editor.
    West Lafayette, Indiana: Purdue University,
    Project Squid Headquarters, 1974. Pp. 377-390.

42. Kimzey, William F., and Milton W. McIlveen. "Analysis
    and Synthesis of Distorted and Unsteady Turboengine
    Inlet Flow Fields." American Institute of Aero-
    nautics and Astronautics Paper No. 71-668,
    presented at the AIAA Seventh Propulsion Joint
    Specialist Conference, Salt Lake City, Utah,
    June 14-18, 1971.

43. Korn, James A. "Propulsion System Flow Stability
    Program (Dynamic) Part XI, Lift Engine Compressor
    Tests and Response to Steady-State Distortion,"
    Air Force Aero Propulsion Laboratory TR-68-142,
    Part XI, Air Force Systems Command, Wright-
    Patterson Air Force Base, Ohio, December, 1968.

44. Voit, Charles H. "Investigation of a High-Pressure
    Ratio Eight-Stage Axial-Flow Research Compressor
    with Two Transonic Inlet Stages, I--Aerodynamic
    Design," National Advisory Committee for Aero-
    nautics Report RM-E53124, Lewis Flight Propulsion
    Laboratory, Cleveland, Ohio, December, 1953.

45. Geye, Richard P., Ray E. Budinger, and Charles H. Voit. "Investigation of High-Pressure-Ratio Eight-Stage Axial-Flow Research Compressor with Two Transonic Inlet Stages, II--Preliminary Analysis of Overall Performance," National Advisory Committee for Aeronautics Report RM-E53J06, Lewis Flight Propulsion Laboratory, Cleveland, Ohio, December, 1953.

46. Voit, Charles H., and Richard P. Geye. "Investigation of a High-Pressure-Ratio Eight-Stage Axial-Flow Research Compressor with Two Transonic Inlet Stages, III--Individual Stage Performance Characteristics," National Advisory Committee for Aeronautics Report RM-E54H17, Lewis Flight Propulsion Laboratory, Cleveland, Ohio, November, 1954.

47. Milner, Edward J., and Leon M. Wenzel. "Performance of a J85-13 Compressor with Clean and Distorted Inlet Flow," National Aeronautics and Space Administration TMX-3304, Lewis Research Center, Cleveland, Ohio, December, 1975.

48. Bruce, E. P., and R. E. Henderson. "Axial Flow Rotor Unsteady Response to Circumferential Inflow Distortions," Project Squid Headquarters TR-PSU-13-PU, West Lafayette, Indiana, September, 1975.

49. Ostdiek, Francis Richard. "A Cascade in Unsteady Flow." Ph.D. dissertation, Ohio State University, Columbus, 1975.

50. Carnahan, Brice, H. A. Luther, and James O. Wilkes. Applied Numerical Methods. New York: John Wiley and Sons, Inc., 1969.

51. Roache, Patrick J. Computational Fluid Dynamics. Albuquerque, New Mexico: Hermosa Publishers, 1972.

52. Wallhagen, Robert E., Francis J. Paulovich, and Lucille C. Geyser. "Dynamics of a Supersonic Inlet Engine Combination Subjected to Disturbances in Fuel Flow and Inlet Overboard Bypass Airflow," National Aeronautics and Space Administration TMX-2558, Lewis Research Center, Cleveland, Ohio, May, 1972.

53. Milner, Edward J., Leon M. Wenzel, and Francis J. Paulovich. "Frequency Response of an Axial-Flow Compressor Exposed to Inlet Pressure Perturbations," National Aeronautics and Space Administration TMX-3012, Lewis Research Center, Cleveland, Ohio, April, 1974.

54. Plourde, G. A., and A. II. Stenning. "The Attenuation
        of Circumferential Inlet Distortion in Multistage
        Compressors." American Institute of Aeronautics
        and Astronautics Paper No. 67-415, presented at the
        AIAA Third Joint Propulsion Specialist Conference,
        Washington, D. C., June, 1967.

55. Aerodynamic Design of Axial-Flow Compressors. Revised.
        Washington, D. C.: National Aeronautics and Space
        Administration, 1965.

56. Langston, C. E. "Distortion Tolerance - By Design
        Instead of By Accident." Paper presented at the
        International Gas Turbine Conference and Products
        Show, Cleveland, Ohio, March 10-13, 1969.

APPENDIX A

FIGURES FOR CHAPTERS I THROUGH VI
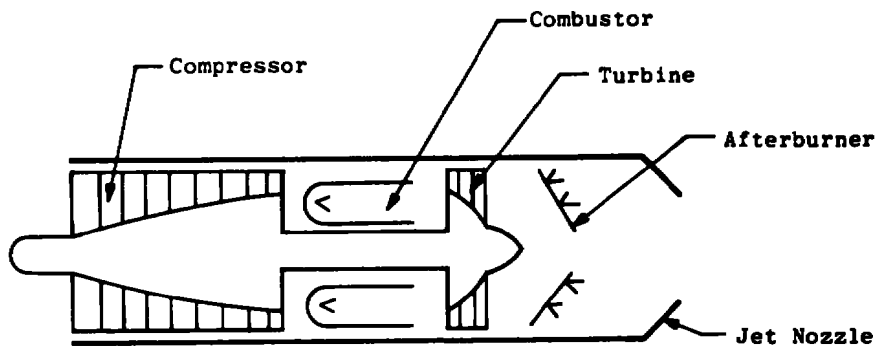
a. Single-spool afterburning turbojet
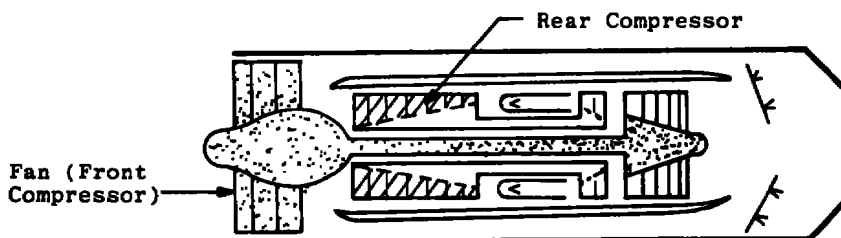
b. Dual-spool augmented (afterburning) turbofan,
bypass ratio ~ 1:1
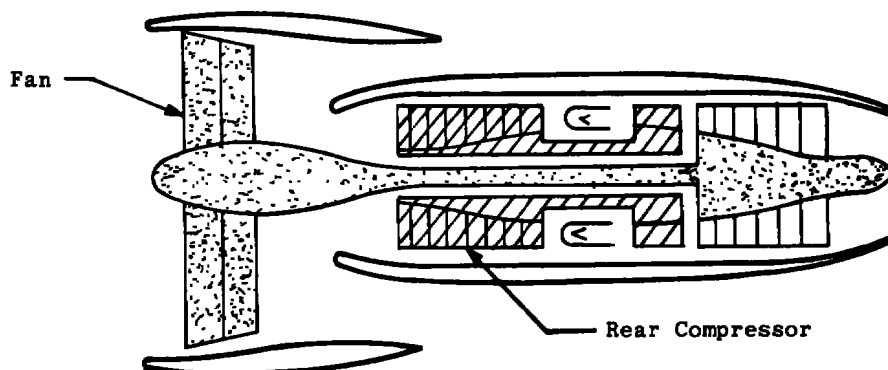
c. Dual-spool high bypass ratio turbofan,
bypass ratio ~ 6:1

Figure 1. Typical aircraft gas turbine compression system
configurations.

142
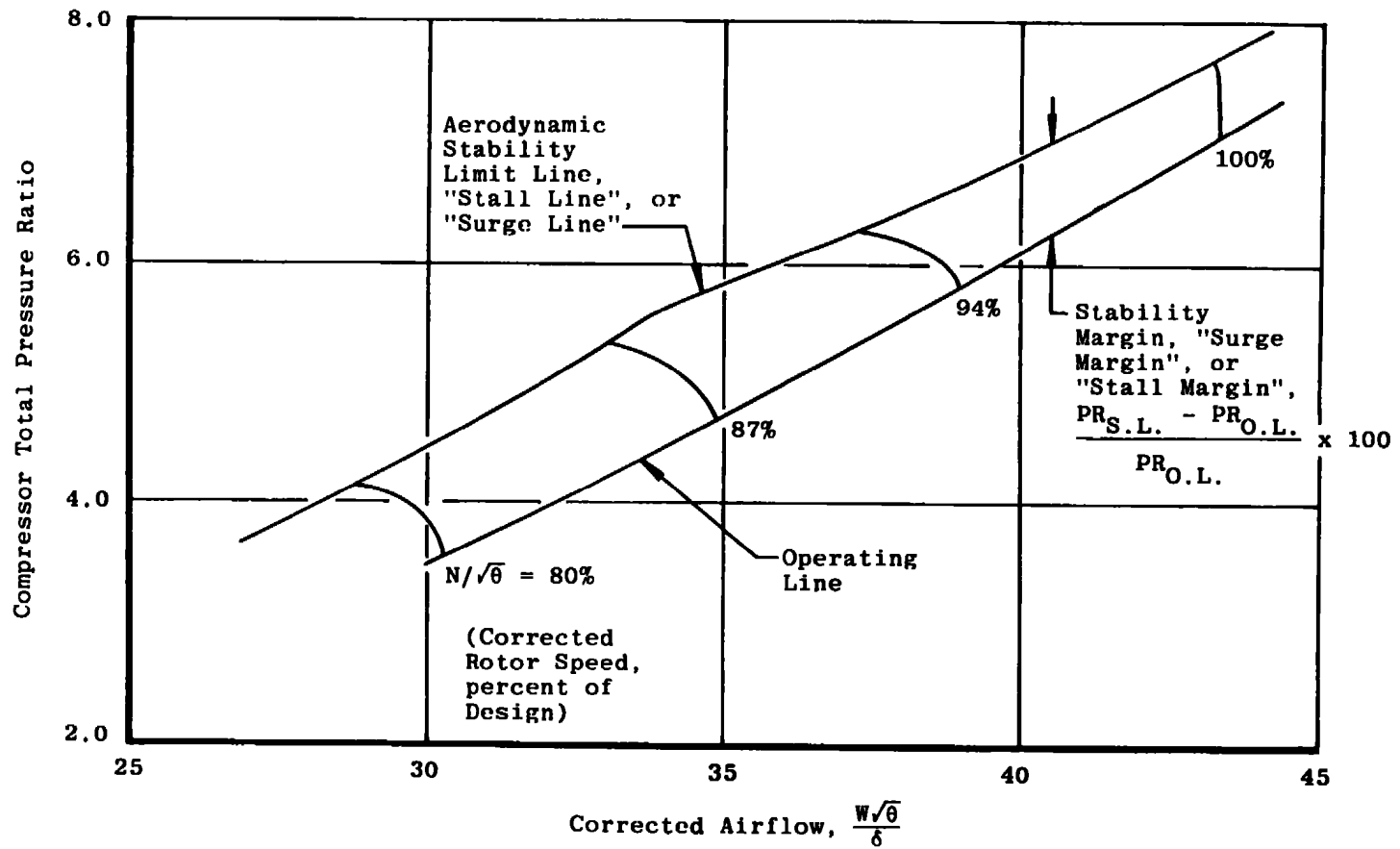
Figure 2. Typical compressor map.
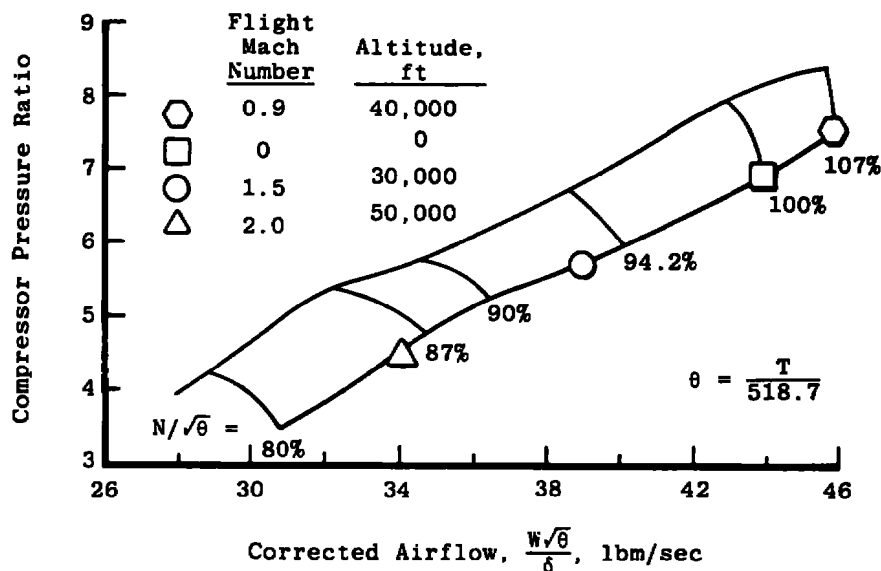
a. Compressor map operating regions for a single-spool
    turbojet engine operating at constant mechanical speed
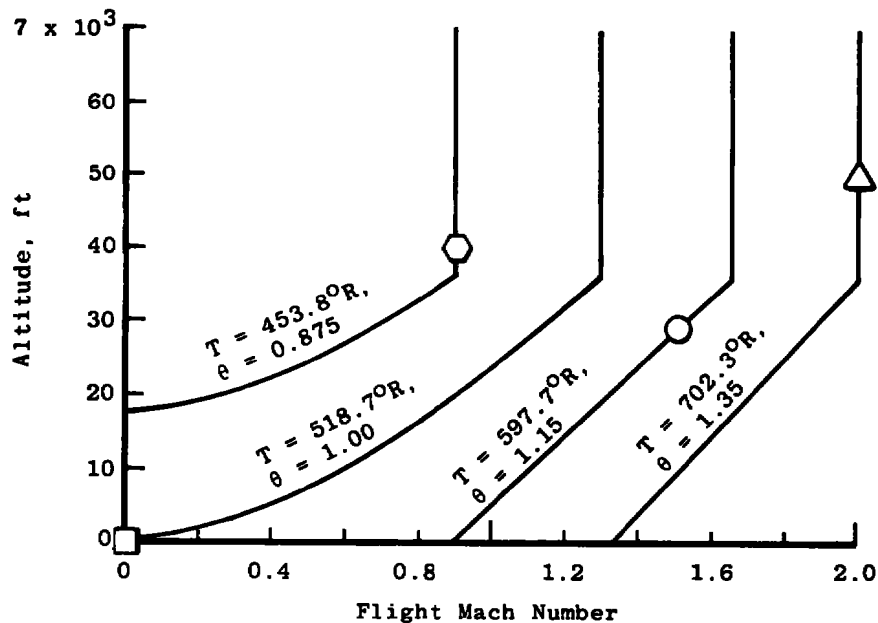
b. Variation of engine inlet total temperature
    with flight condition

Figure 3.   Effect of flight altitude and Mach number on
            compressor operating region.
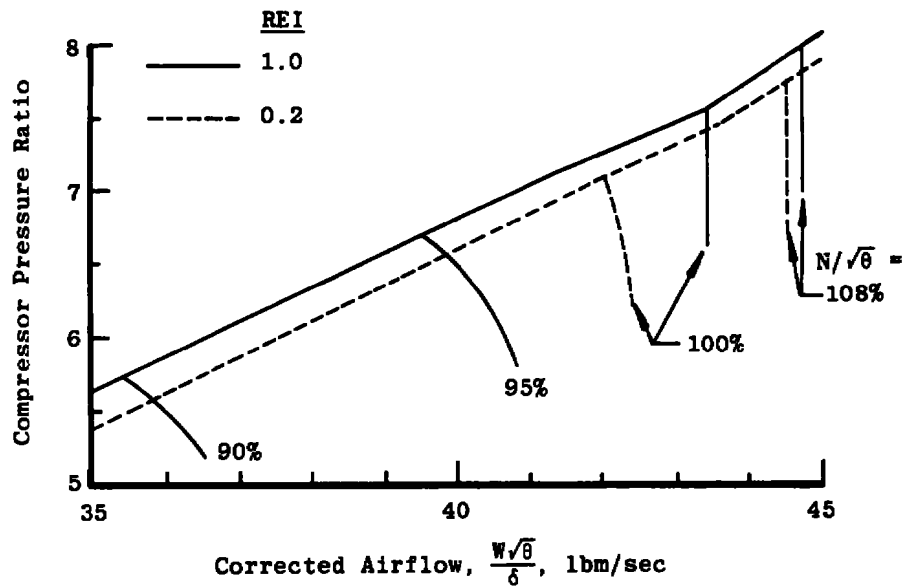
c. Influence of Reynolds number on compressor
    stability limit [3]
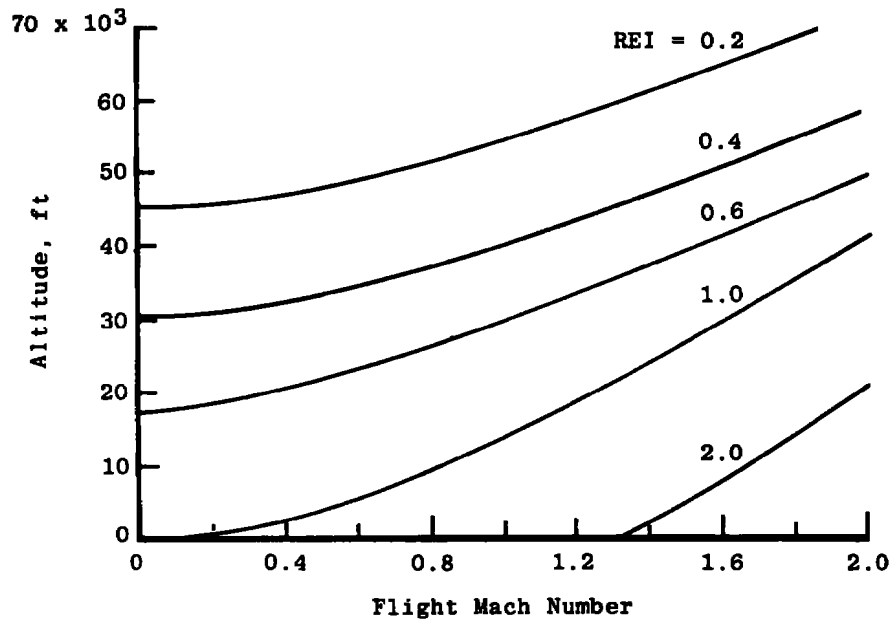
d. Variation of Reynolds number with flight
    condition

Figure 3. (Continued).
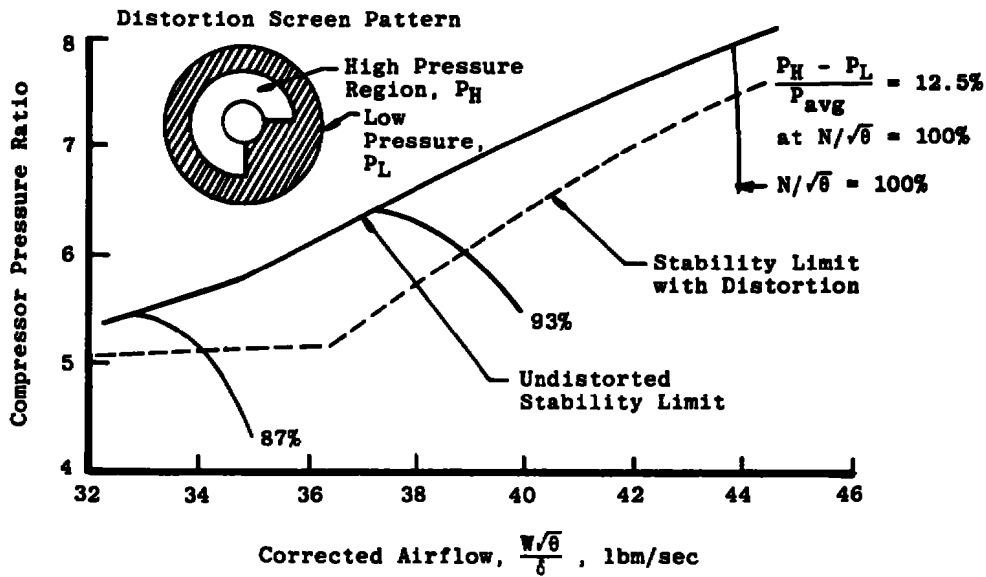
a. Influence of steady, screen generated distortion on turbojet compressor stability limit [4]
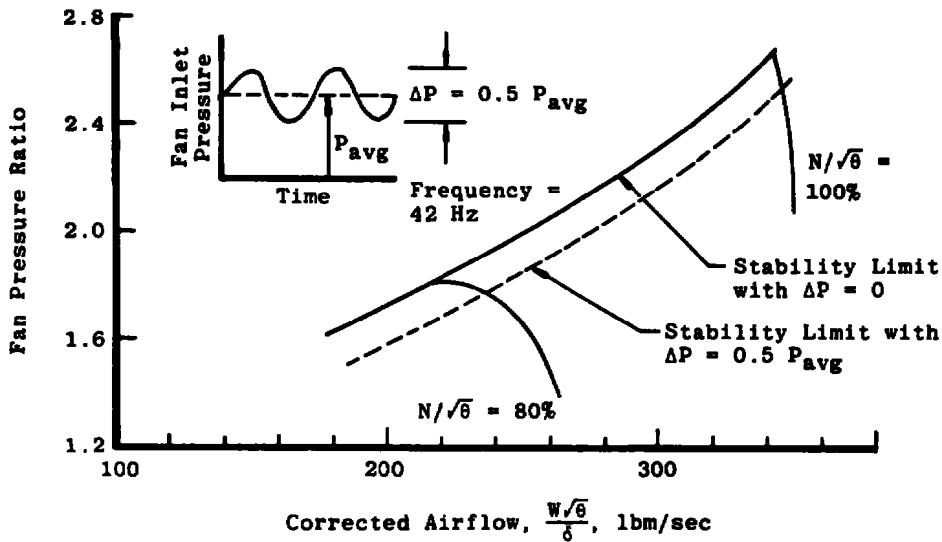
b. Influence of uniform time varying flow at the inlet of a turbofan engine [5]

Figure 4. Typical influences of external disturbances on compressor stability.
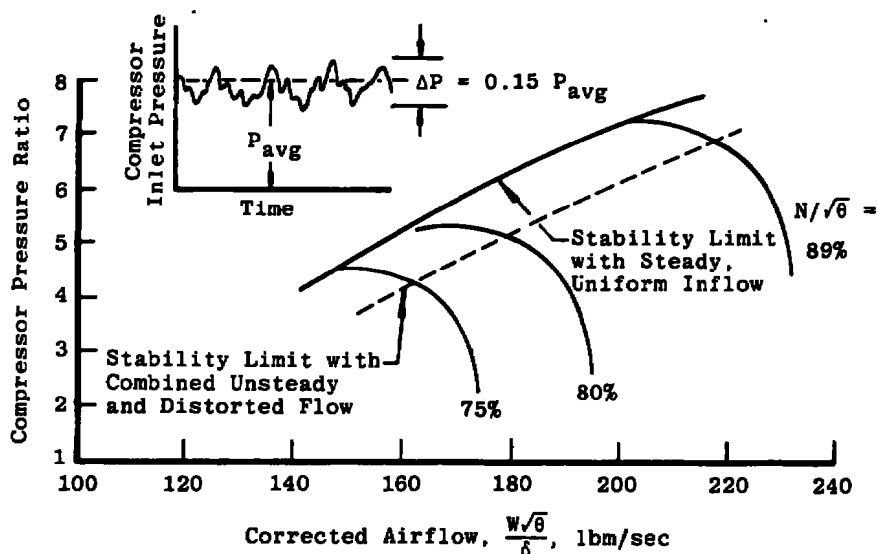
c. Influence of time-variant distortion on
turbojet engine compressor stability limit [6]
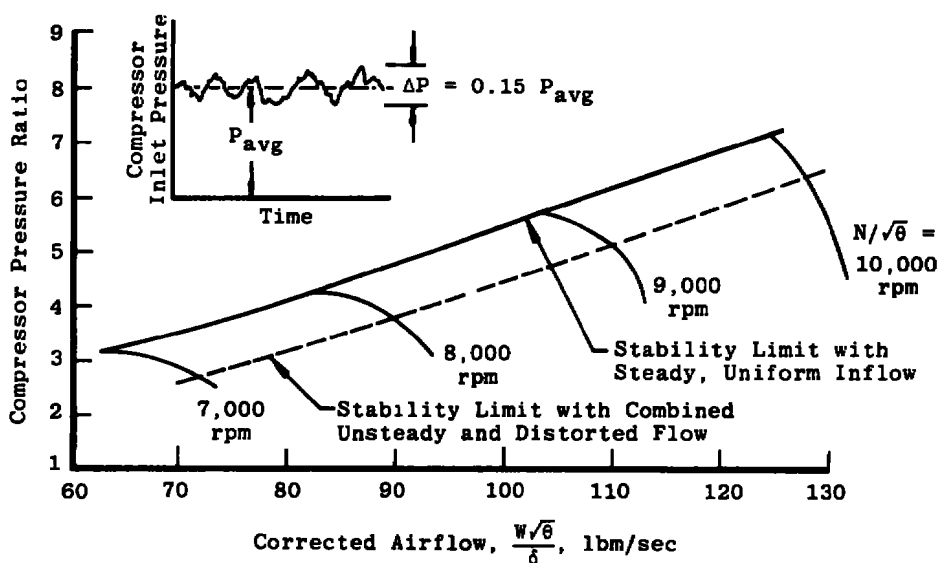
d. Influence of time-variant distortion on the
low-pressure compressor of a turbofan engine [7, 8]

Figure 4. (Continued).
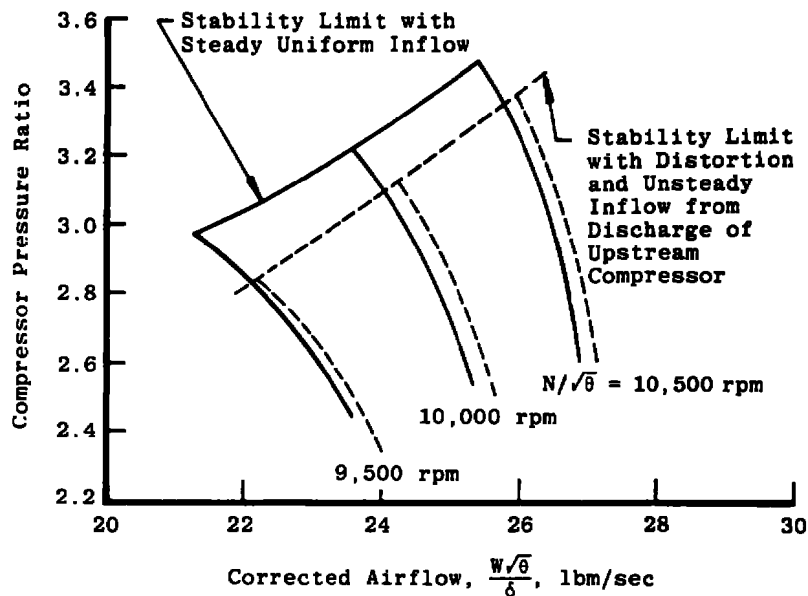
e. Influence of unsteady and nonuniform flow from the low-pressure compressor on high-pressure compressor stability limit in a turbofan engine [8]
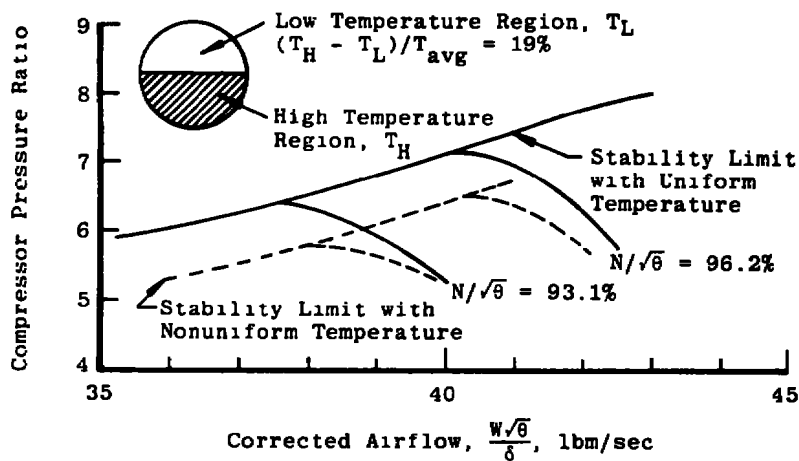
f. Influence of nonuniform total temperature on a turbojet engine compressor [9]

Figure 4. (Continued).
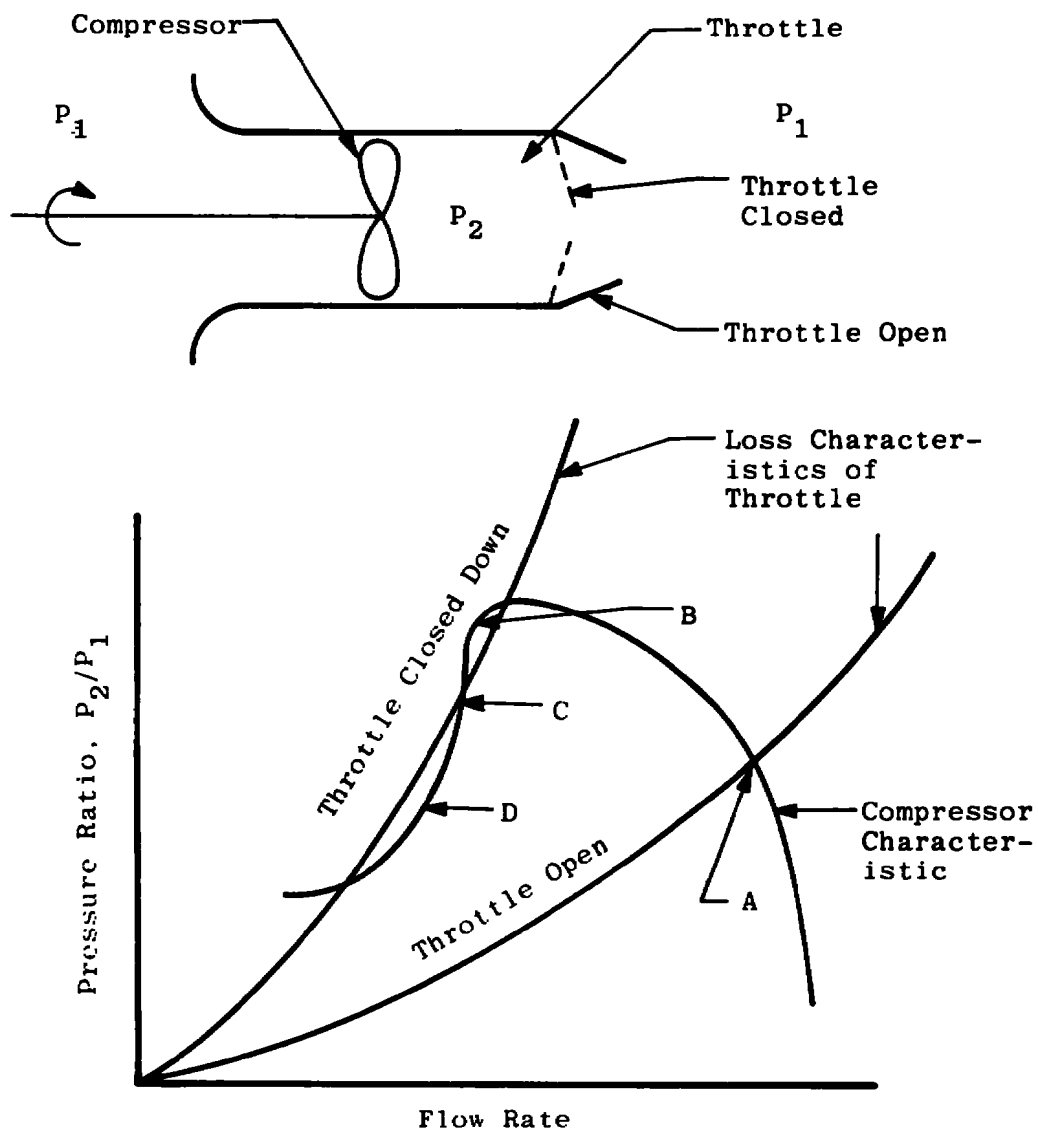
Figure 5.   Surge analysis based on compressor and throttle
curve shapes.
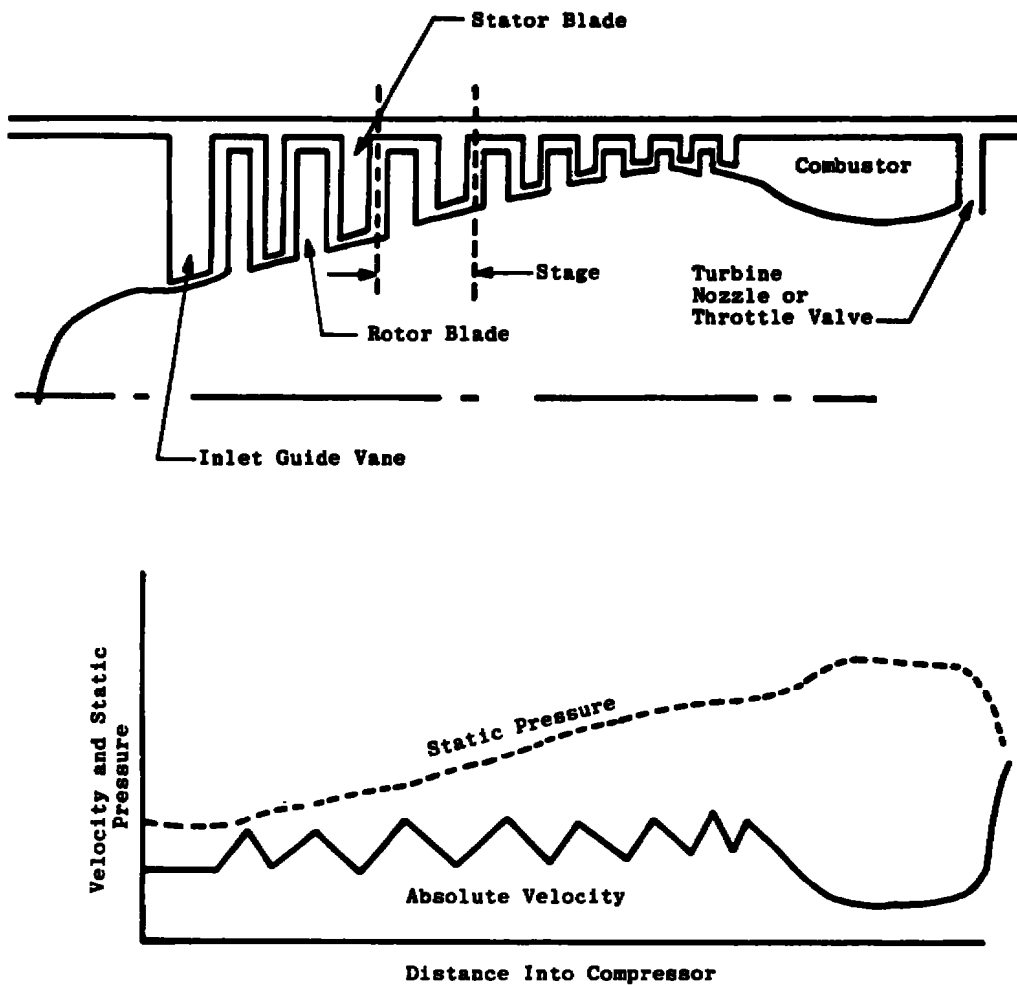
Figure 6. Representative axial flow compressor arrangement and operation.

a. Physical system modeled

b. Overall system control volume

c. Elemental control volume

Figure 7. Physical system modeled and control volumes.
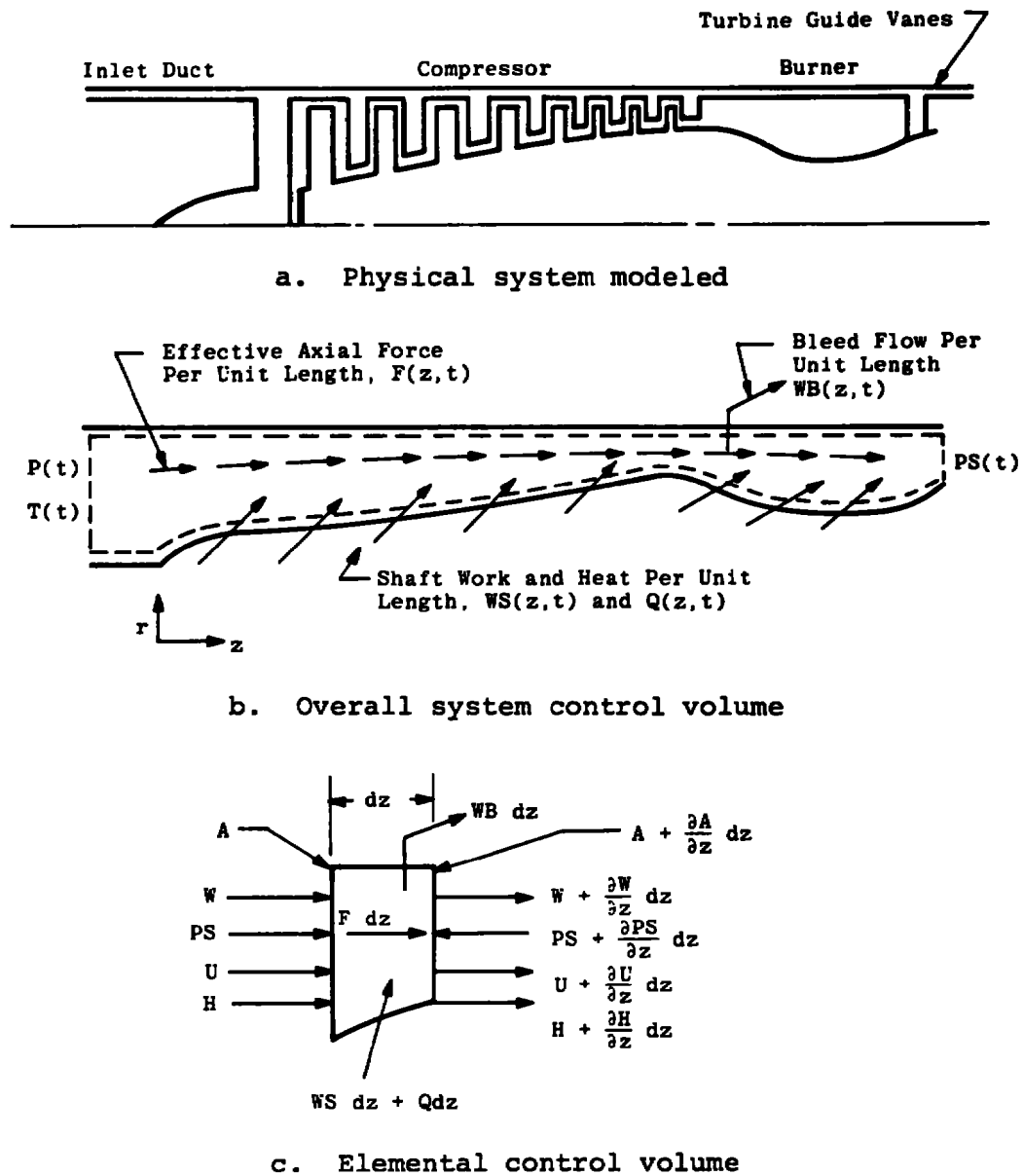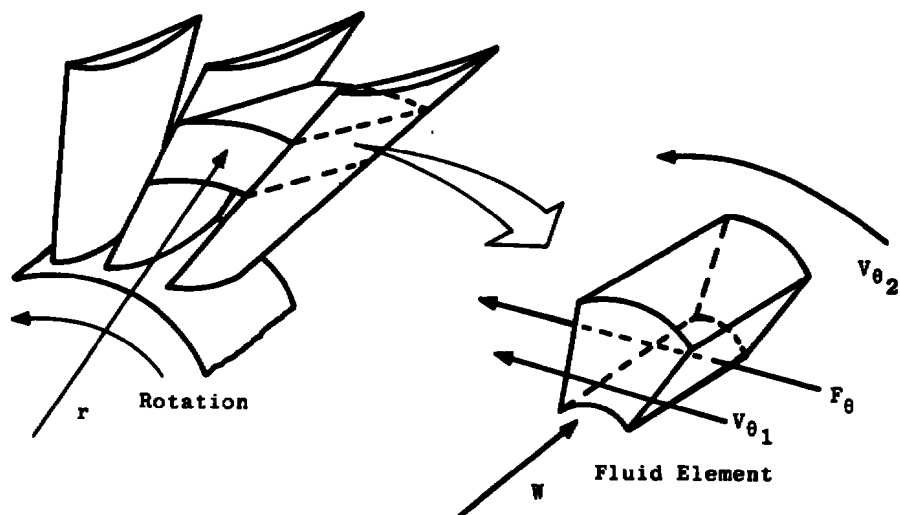
a. Rotating fluid element

$$\omega r = U_{wh}$$

$$V_\theta = U_{wh} + V_{sw}$$

$$F_\theta = L \cos(\alpha + \lambda) + D \sin(\alpha + \lambda)$$
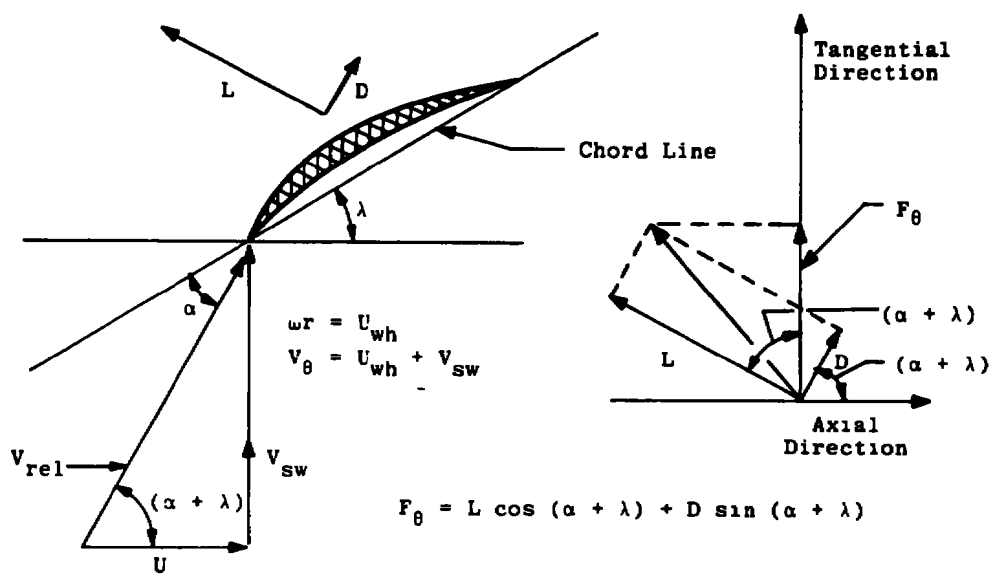
b. Blade element velocities and forces

Figure 8. Rotor fluid element velocities and forces.
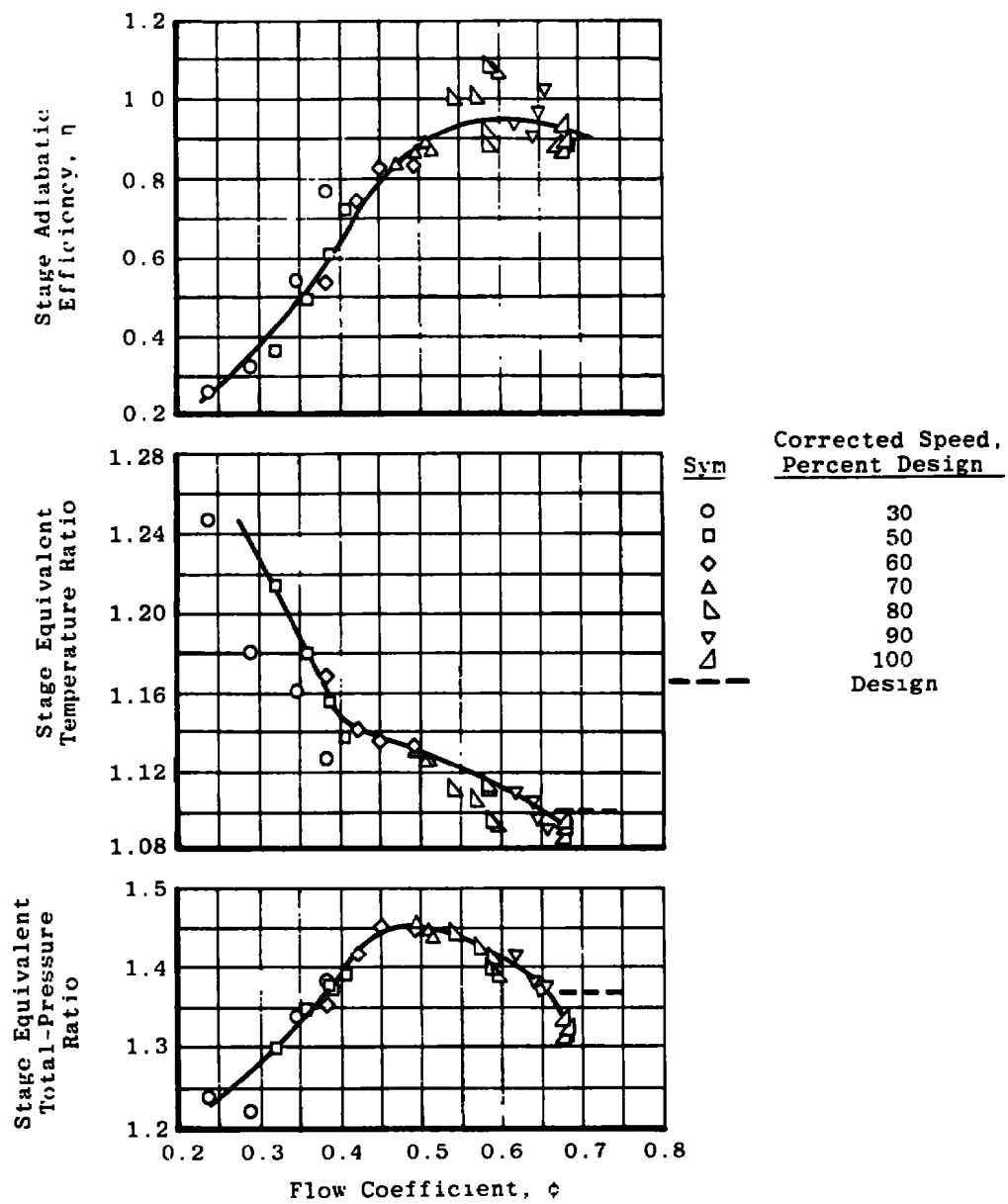
Figure 9. Representative stage characteristics [46].

Steady Flow   Unsteady Flow

Stage Characteristic Curves
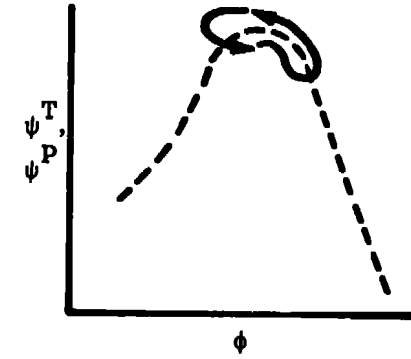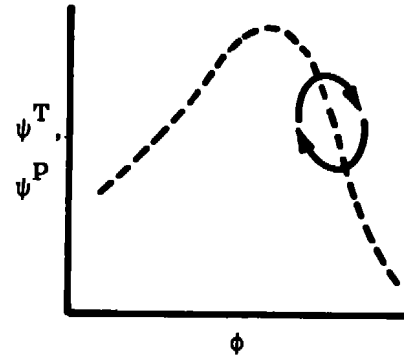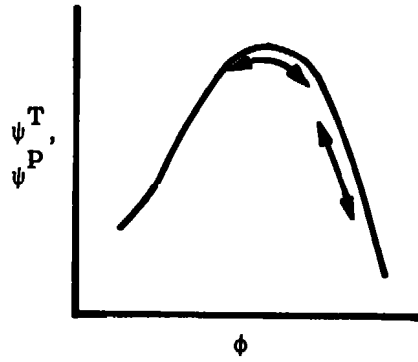
Equivalent Lift Coefficient Curves
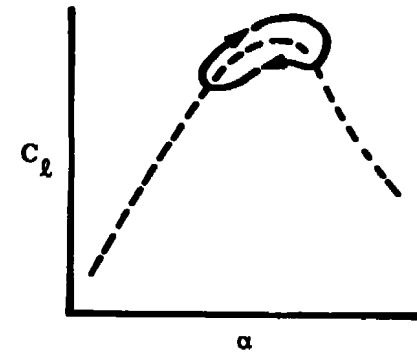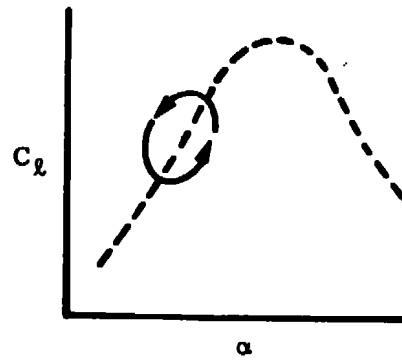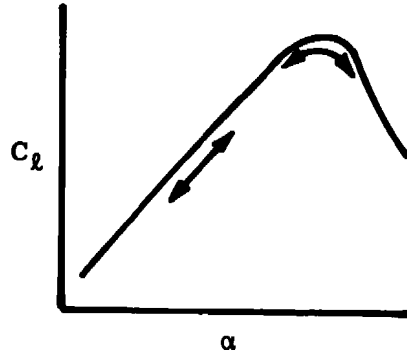
Figure 10.   Steady-state and unsteady stage characteristic behavior.

$$k = \frac{2\pi fC}{V_{rel}} \qquad \frac{|C_\ell|_{max}}{|C_\ell|_{ss}}$$

Stagger $\lambda = 50^{\circ}$
Cascade a/c:

0.8
1.0
1.3

Single Airfoil
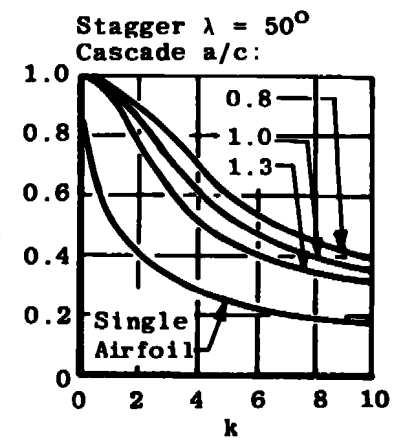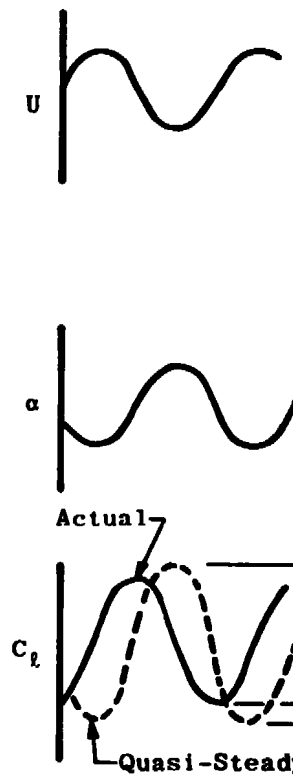
Oscillating Stream, Stationary Foils

U

α

Actual

C_ℓ

$C_{\ell_{max}}$ $C_{\ell_{ss}}$

$\frac{|C_\ell|_{max}}{|C_\ell|_{ss}}$

Quasi-Steady State

λ

C

a

$V_\theta = \omega r$

α

U

Cascade

a/c = 1

Single Airfoil a/c = ∞
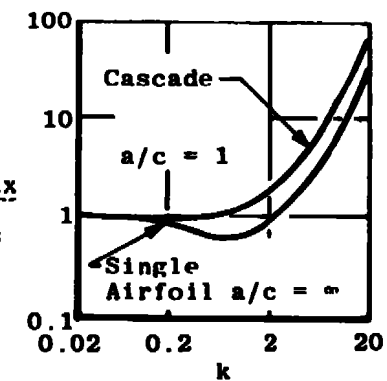
Oscillating Foils, Steady Stream

Figure 11. Unsteady airfoil and cascade aerodynamics.
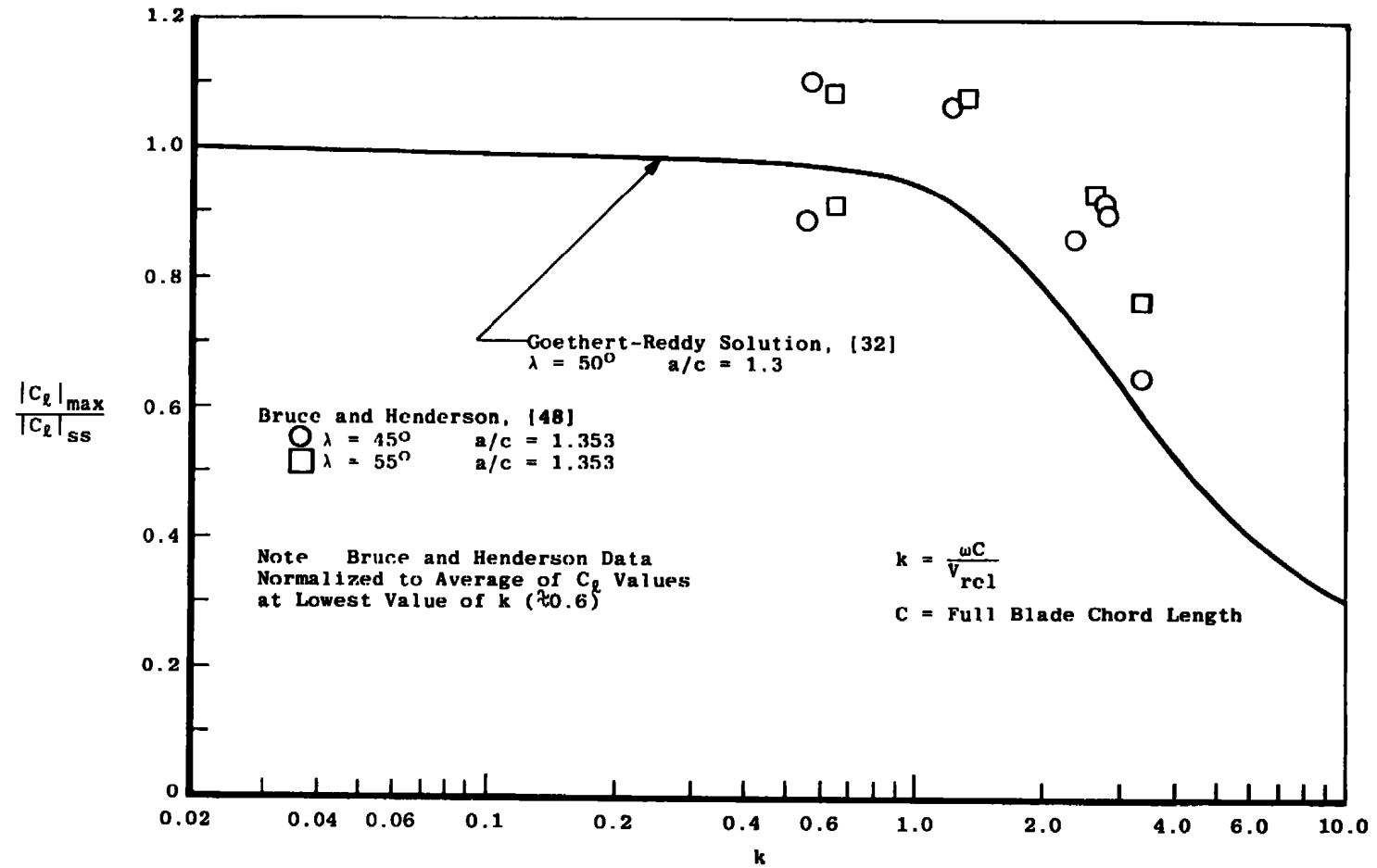
Figure 12.   Comparison of theoretical and experimental unsteady
cascade lift coefficients.
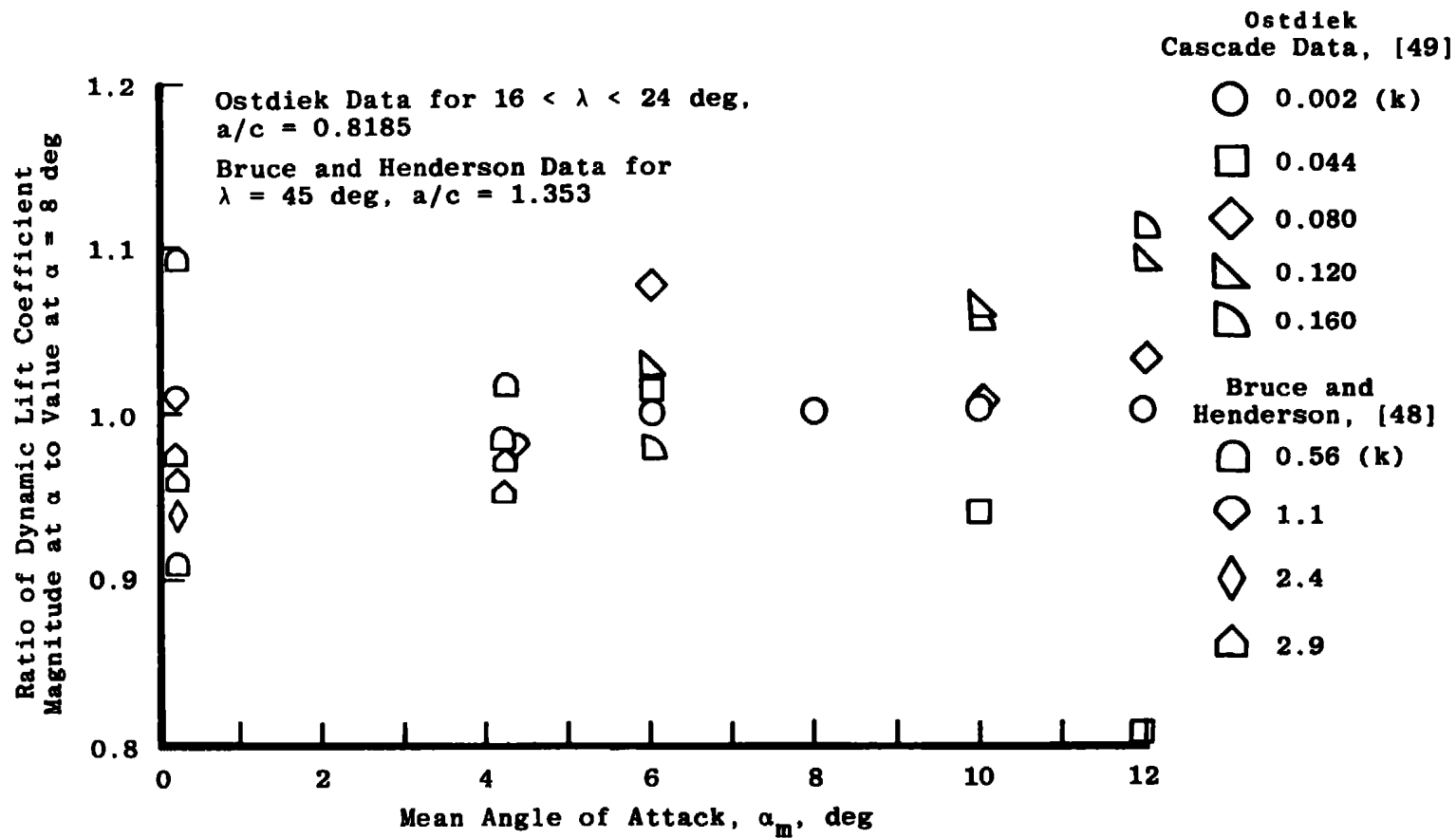
Figure 13. Variation of dynamic lift coefficient ratio with mean angle of attack.
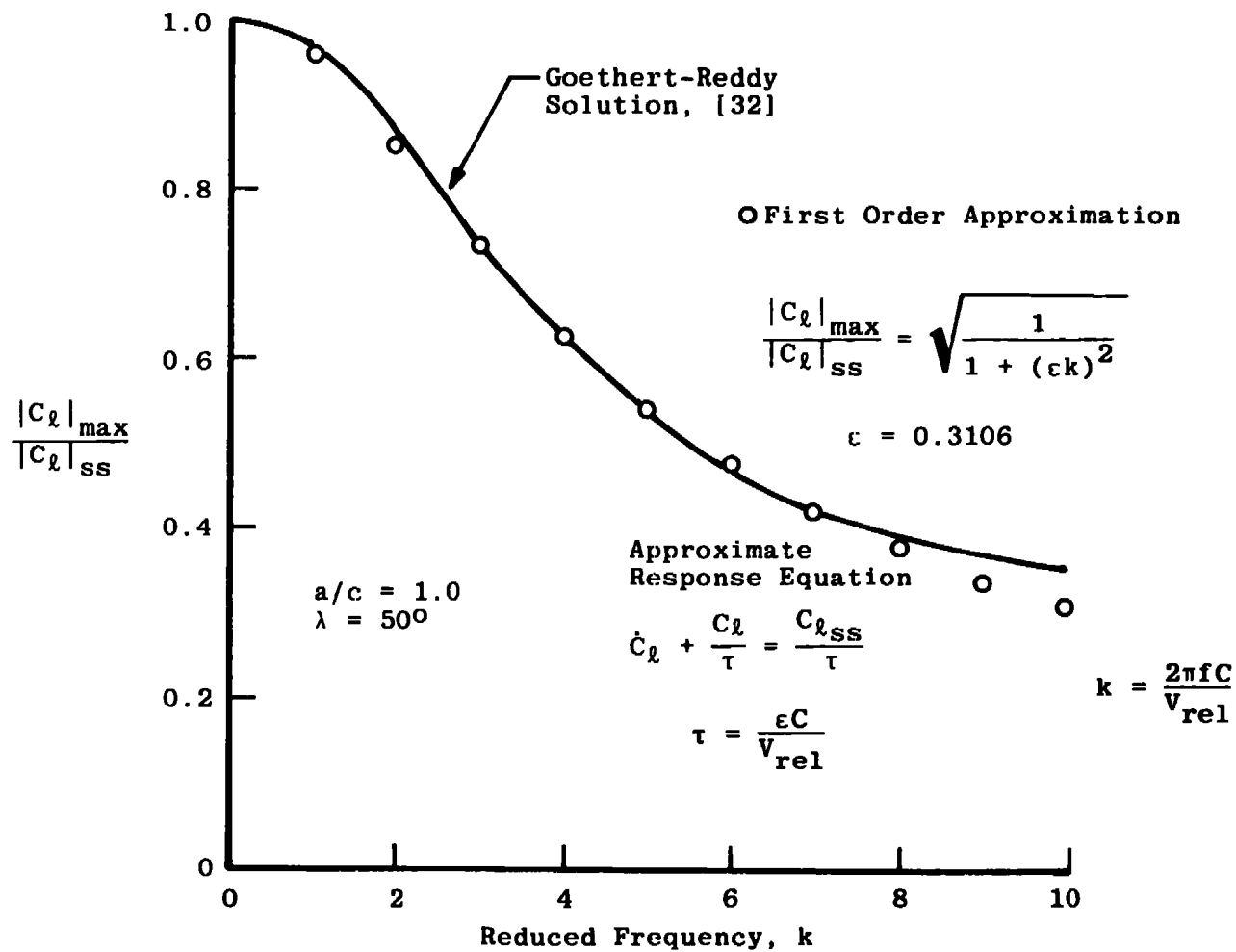
Figure 14. Unsteady lift coefficient magnitude ratio.

Plane Location Designations
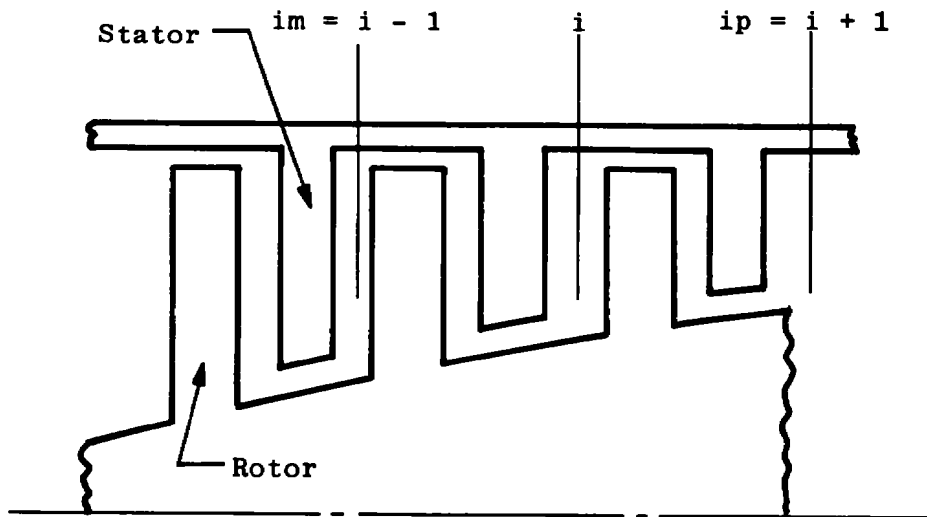
a. Physical system
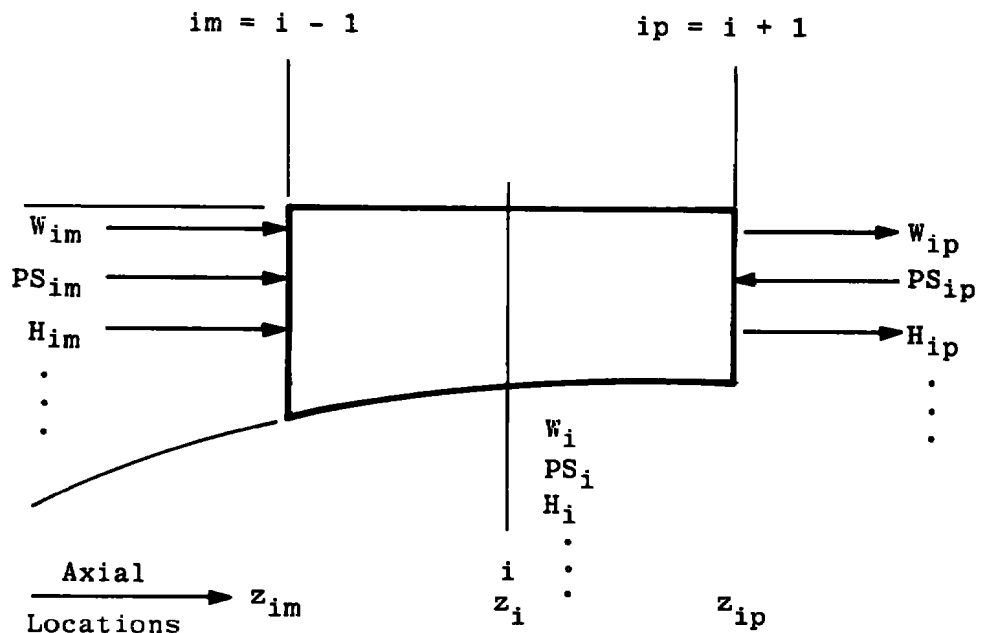
b. Computational planes

Figure 15. Computational plane designations for finite
difference solutions.

159

Initial Conditions

At t = 0

$(\rho A)_i(t = 0)$, $W_i(t = 0)$, $(XA)_i(t = 0)$, $\psi_i(t = 0)$ = Inputs

Compute Variables at Each Plane

Entry Plane Conditions

$M_1 = M(P_1, T_1, W_1, A_1)$	Eq. (75)
$TS_1 = TS(T_1, M_1)$	Eq. (76)
$PS_1 = PS(P_1, M_1)$	Eq. (77)
$\rho_1 = \rho(PS_1, TS_1)$	Eq. (78)
$X_1 = X(PS_1, M_1)$	Eq. (79)

Interior Plane Values

$U_i = U(W_i, \rho_i A_i)$	Eq. (80)
$TS_i = TS(X_i, \rho_i, U_i)$	Eq. (81)
$PS_i = PS(\rho_i, TS_i)$	Eq. (82)
$T_i = T(TS_i, U_i)$	Eq. (83)
$P_i = P_i(T_i, TS_i)$	Eq. (84)
$M_i = M(U_i, TS_i)$	Eq. (86)
$IMP_i = IMP(PS_i, A_i, M_i)$	Eq. (87)
$H_i = H(W_i, T_i, c_p)$	Eq. (88)

Exit Plane Conditions

If $P_{in}/P_{exit} \geq (P/PS)_{crit}$	Eq. (89)
$M_{in} = 1.0$	
If $P_{in}/P_{exit} < (P/PS)_{crit}$	Eq. (90)
$PS_{in} = P_{exit}$	
$M_{in} = M_{in}(X, P_{exit})$	Eq. (91)
$TS_{in} = TS(PS_{in}, \rho_{in})$	Eq. (92)
$U_{in} = U(M_{in}, TS_{in})$	Eq. (93)
$W_{in} = W_{in}(\rho_{in}, U_{in}, A_{exit})$	Eq. (94)

Runge-Kutta Integration

At t ≠ 0

$(\rho A)_i(t + \Delta t) = g(\partial(\rho A)_i/\partial t, (\rho A)_i(t))$

$W_i(t + \Delta t) = g(\partial W_i/\partial t, W_i(t))$

$(XA)_i(t + \Delta t) = g(\partial(XA)_i/\partial t, (XA)_i(t))$

$\psi_i(t + \Delta t) = g(\partial\psi_i/\partial t, \psi_i(t))$

Compute Time Derivatives

$\partial(\rho A)_i/\partial t = f_1(W_{im}, W_i, W_{ip}, WB_i)$	Eq. (63), Eq. (104)
$\partial W_i/\partial t = f_2(IMP_{im}, IMP_i, IMP_{ip}, F_i)$	Eq. (64), Eq. (105)
$\partial(XA)_i/\partial t = f_3(H_{im}, H_i, H_{ip}, WS_i)$	Eq. (65), Eq. (106)
$\partial\psi_i/\partial t = f_4(\psi_i, \psi_{ss_i})$	Eq. (58)

Compute Forces and Work

Compressor

$\phi_i = \phi_i(U_i, V_{\theta_i})$	Eq. (66)
$\psi_i = \psi_i(\phi_i)$	
$n_i = n_i(\phi_i)$ Curve Fits	
$PR_i = PR(\psi_i, N_i, T_i)$	Eq. (67)
$TR_i = TR(PR_i, n_i)$	Eq. (68)
$F_i = F_i(PR_i, M_i, A_{ip})$	Eq. (70)
$WS_i = WS_i(TR_i, H_i)$	Eq. (69)

Duct

$F_i = F_i(PS_i, M_i, A_i)$	Eq. (111)

Inputs (Boundary Conditions)

P_1 = Input	P_{exit} = Input
T_1 = Input	A_{exit} = Input
Q_i = Input	N_i = Input

Figure 16. Solution procedure for one-dimensional, time-dependent model.
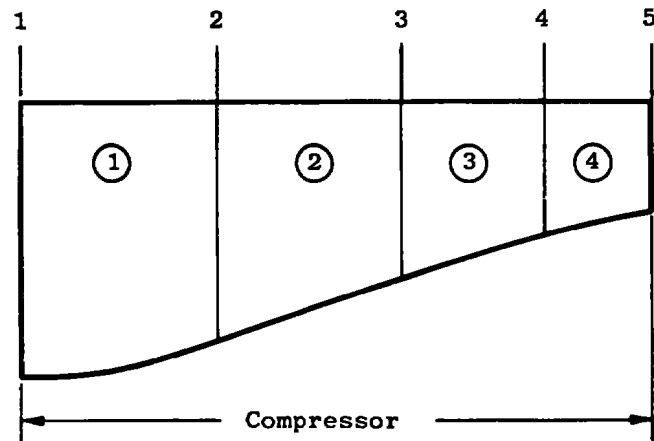
a. Allison XC-1 compressor
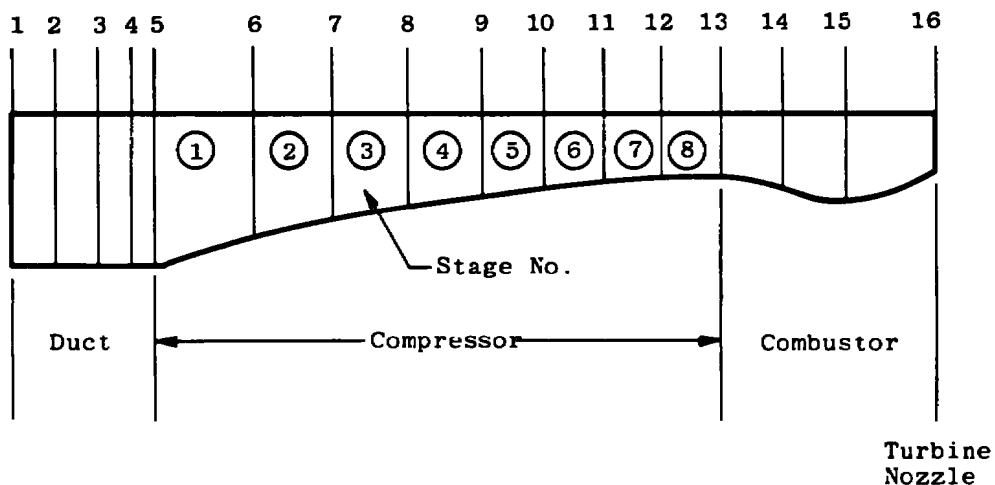
b. NACA-8 and J85-13 compressors

Figure 17. Station locations (computation planes) for one-dimensional, time-dependent models.
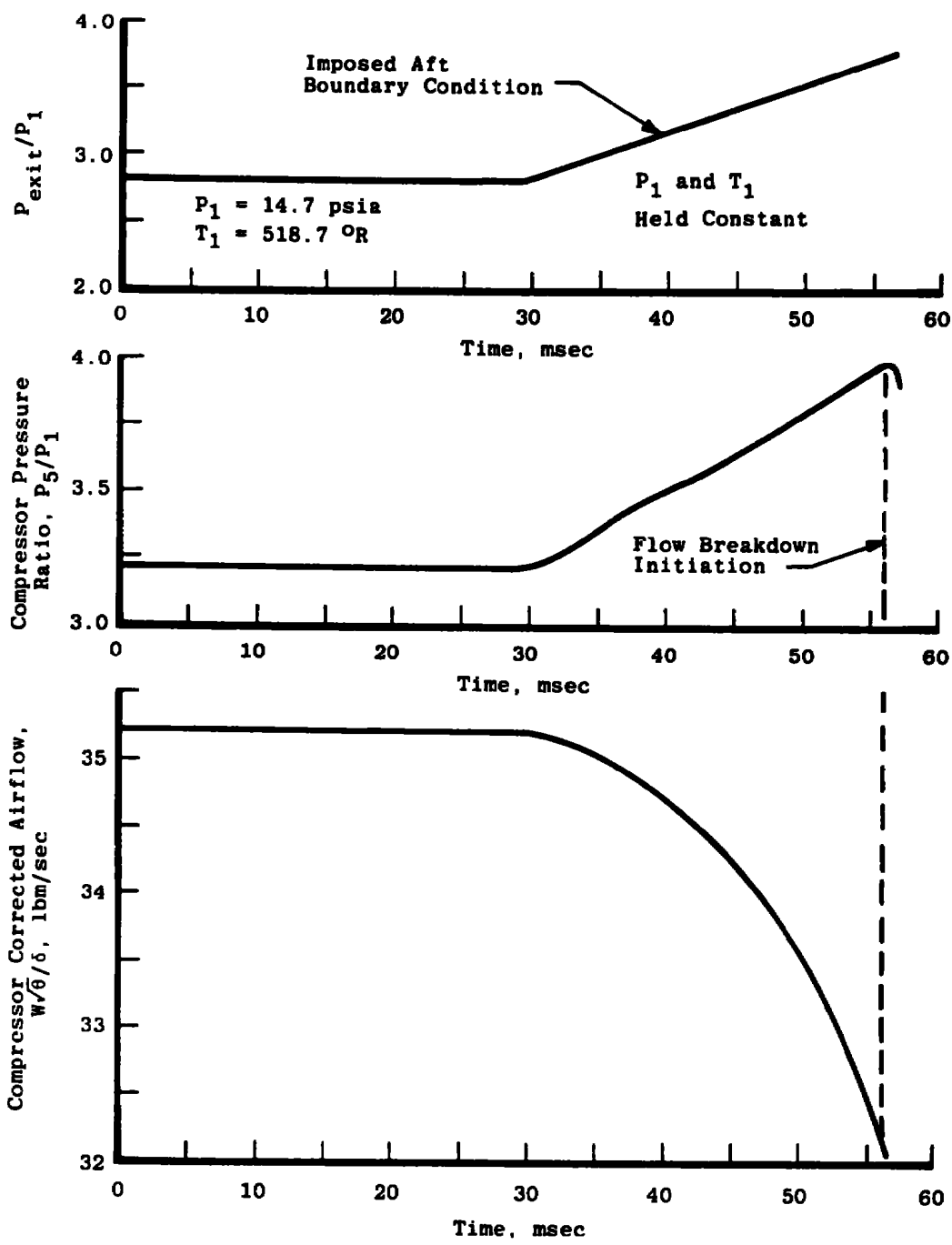
Figure 18. XC-1 compressor model loaded to stall,
$N/\sqrt{\theta} = 90\%$.
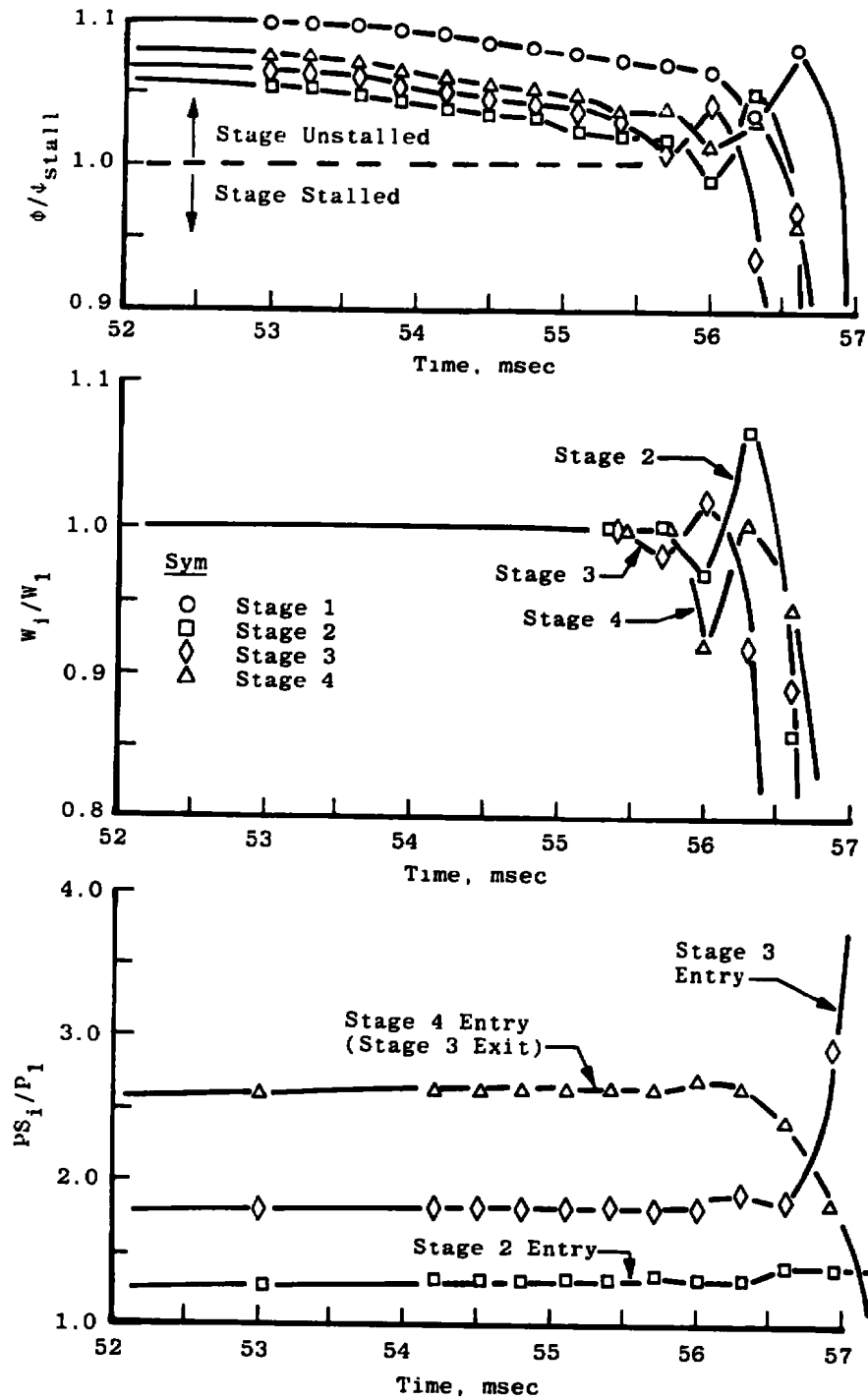
Figure 19. Flow breakdown process leading to instability,
XC-1 compressor, $N/\sqrt{\theta}$ = 90%.
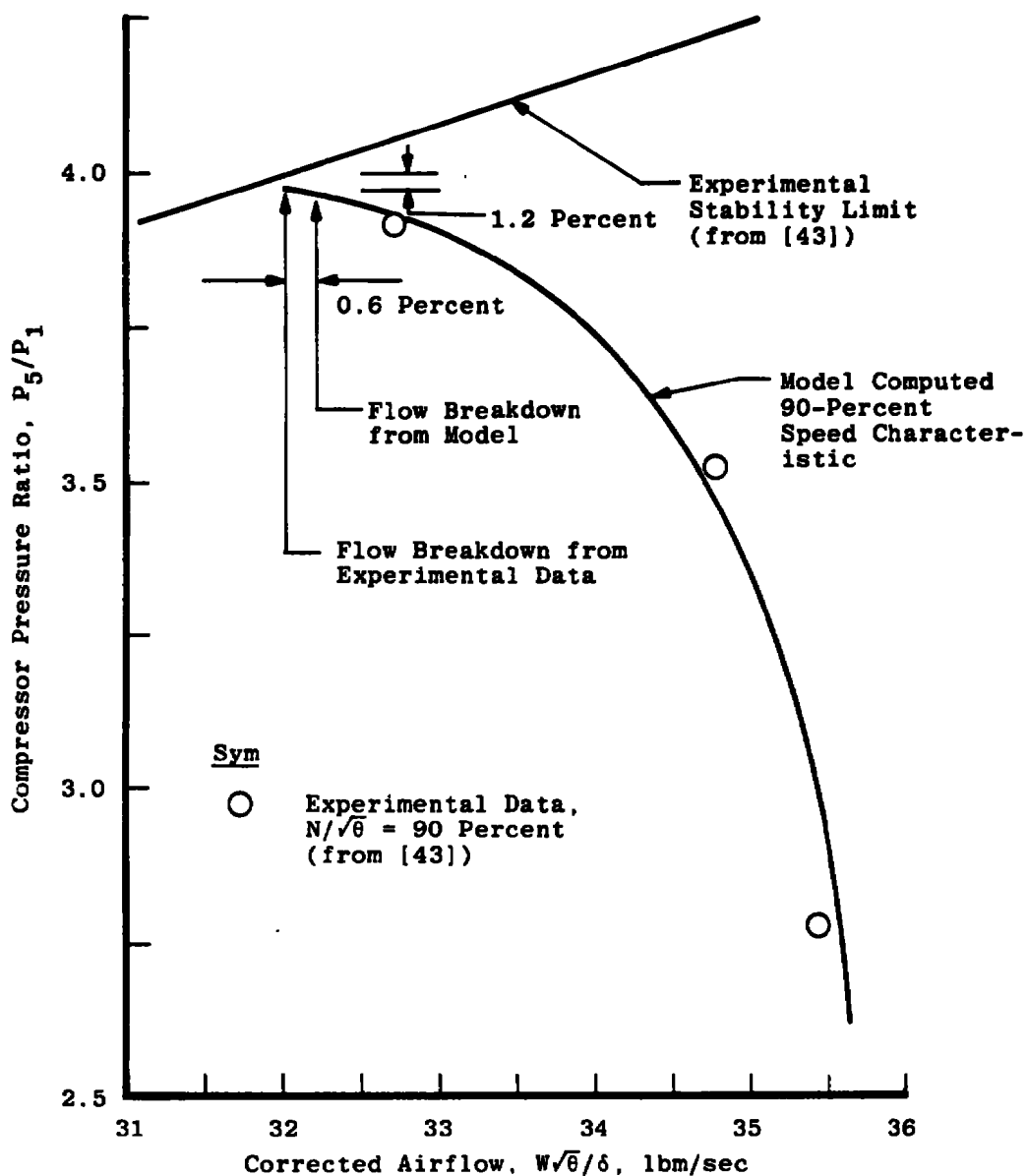
Figure 20. Comparison of model computed 90% speed charac-
teristic and stability limit with experimental
measurements, XC-1 compressor.
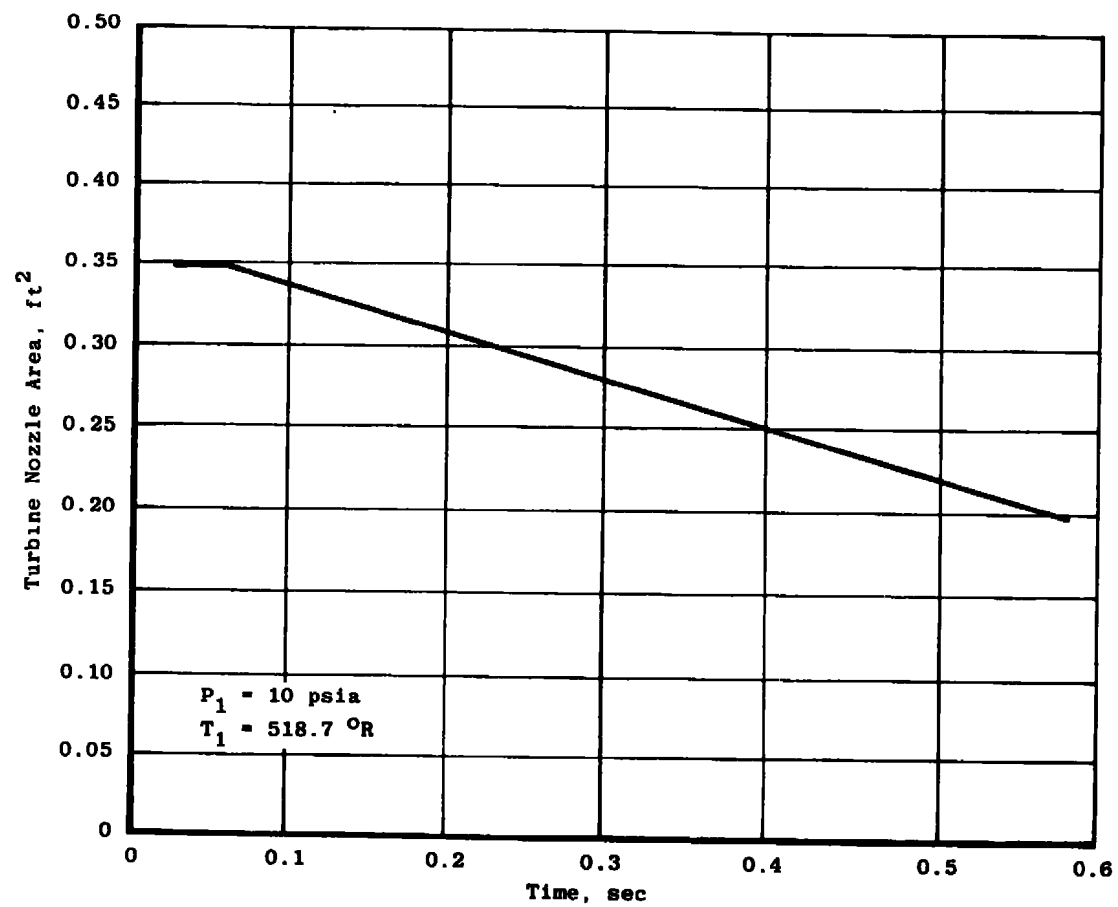
a. Imposed nozzle area reduction.

Figure 21. NACA-8 compressor model loaded to stall, $N/\sqrt{\theta} = 90\%$.
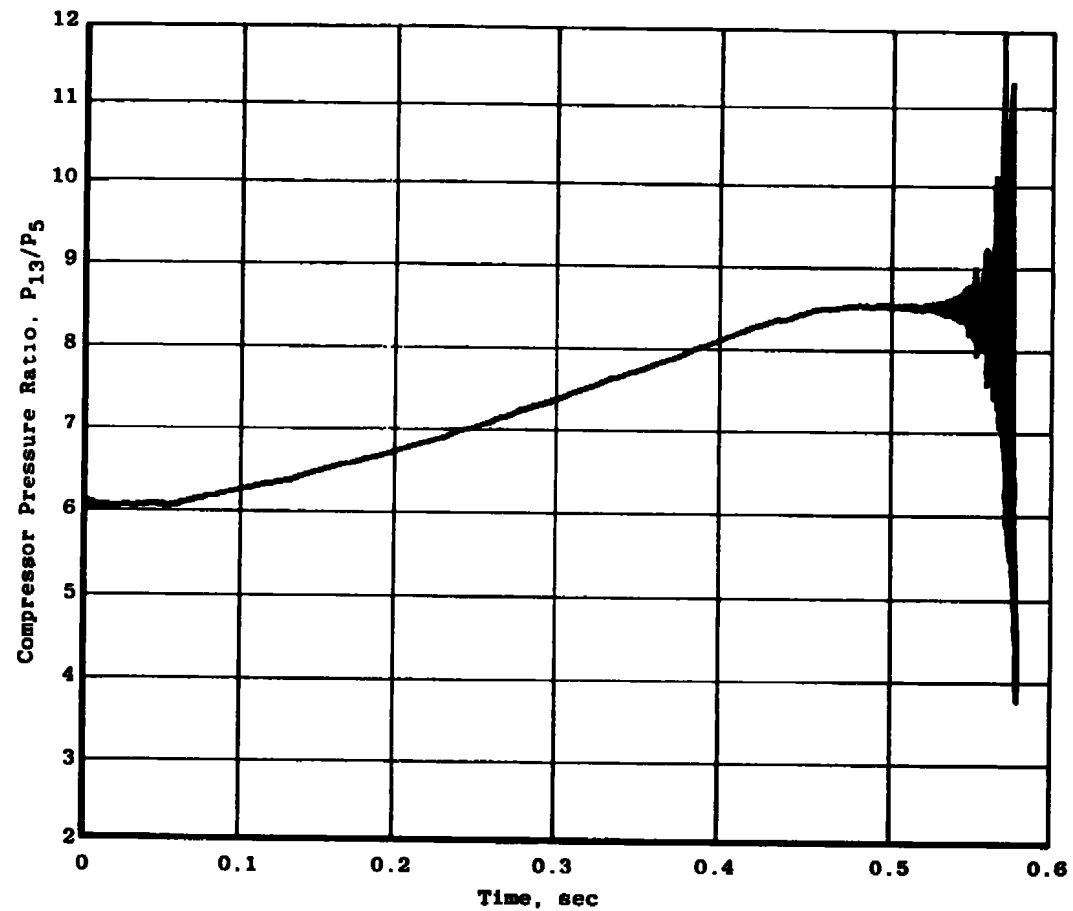
b.   Compressor pressure ratio

Figure 21.   (Continued).
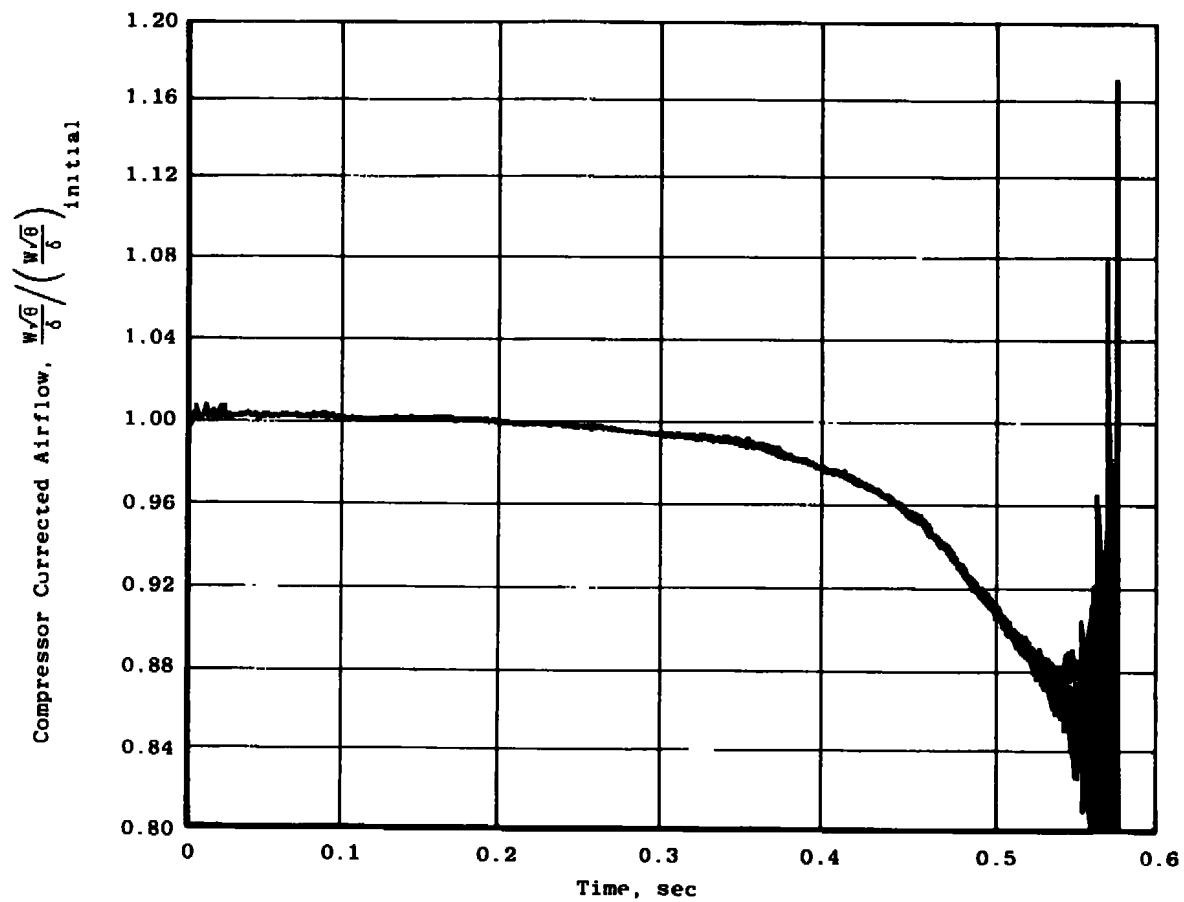
c. Corrected airflow.

Figure 21. (Continued).
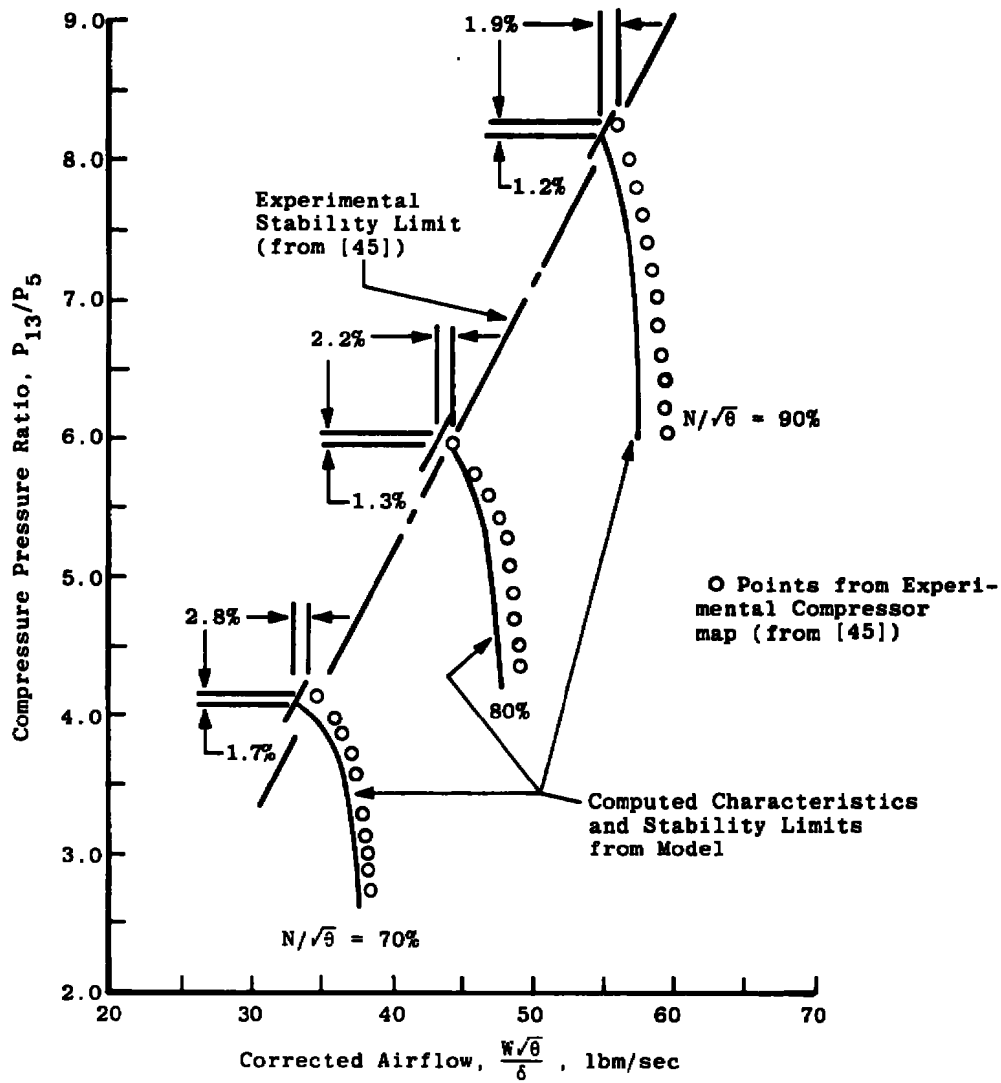
Figure 22. Comparison of model computed speed character-
istics and stability limits with experimental
measurements, NACA-8 compressor.
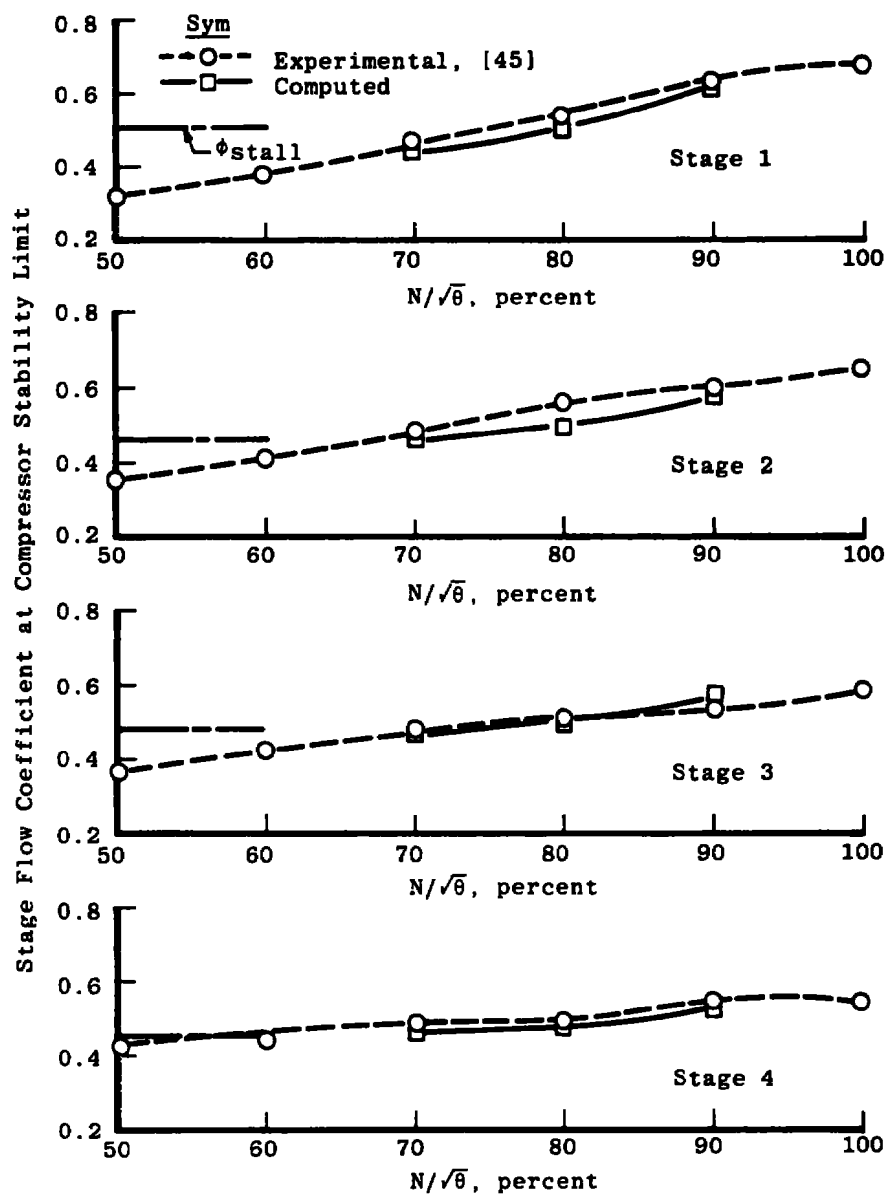
a. Stages 1 through 4

Figure 23. Comparison of model computed flow coefficients at compressor stability limit with experimental measurements, NACA-8 compressor.
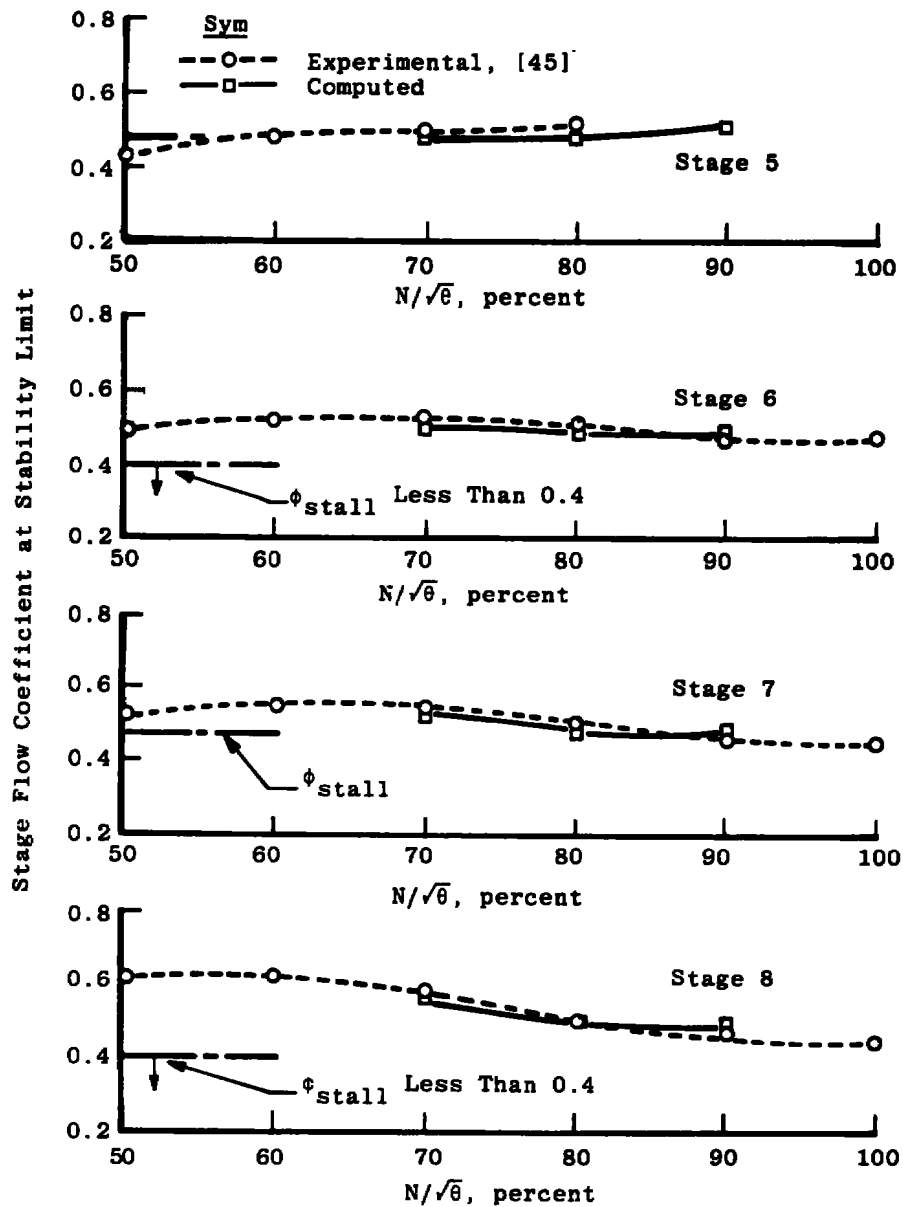
b. Stages 5 through 8

Figure 23. (Continued).
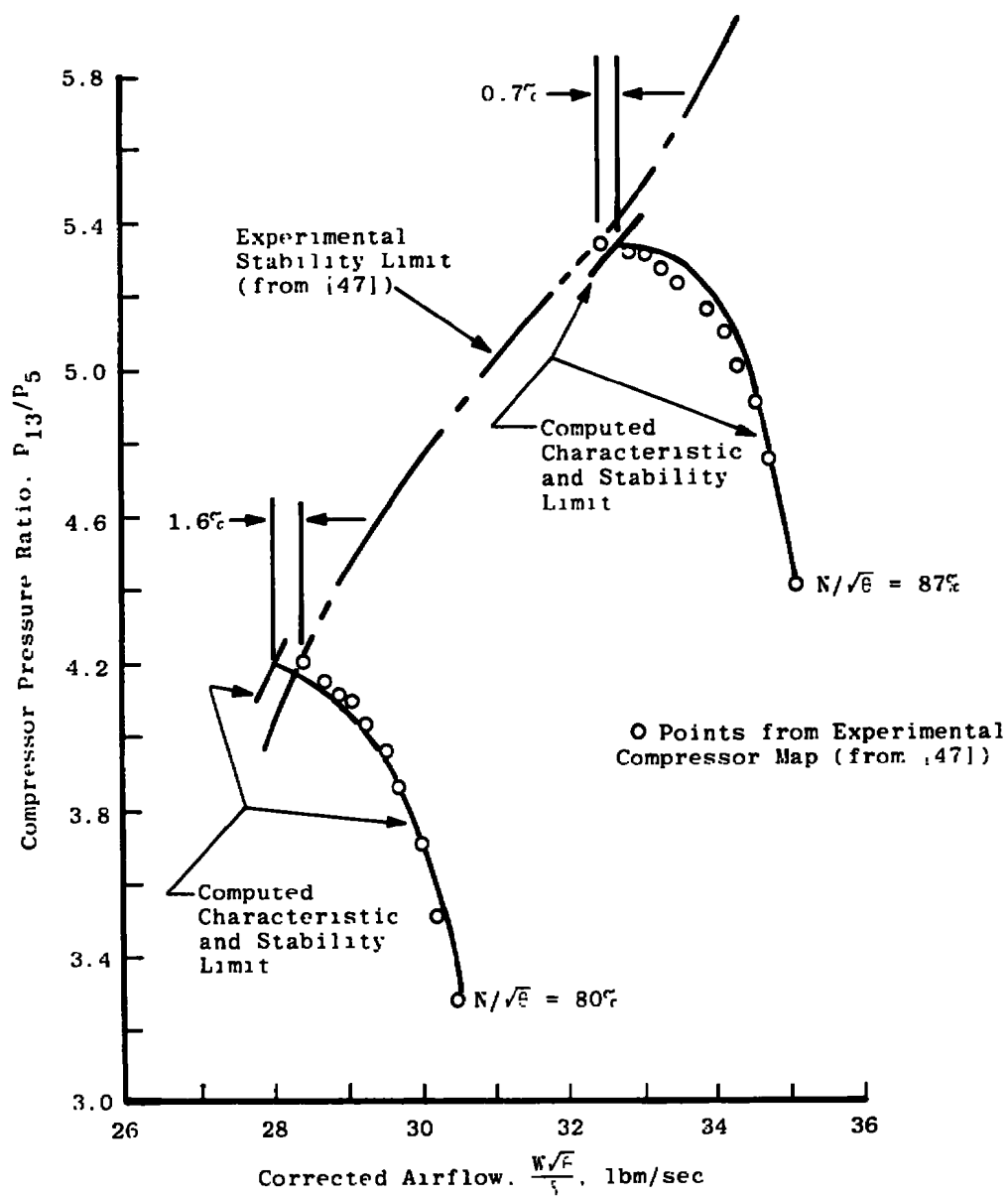
Figure 24. Comparison of model computed speed character-
istics and stability limits with experimental
measurements, J85-13 compressor.

171
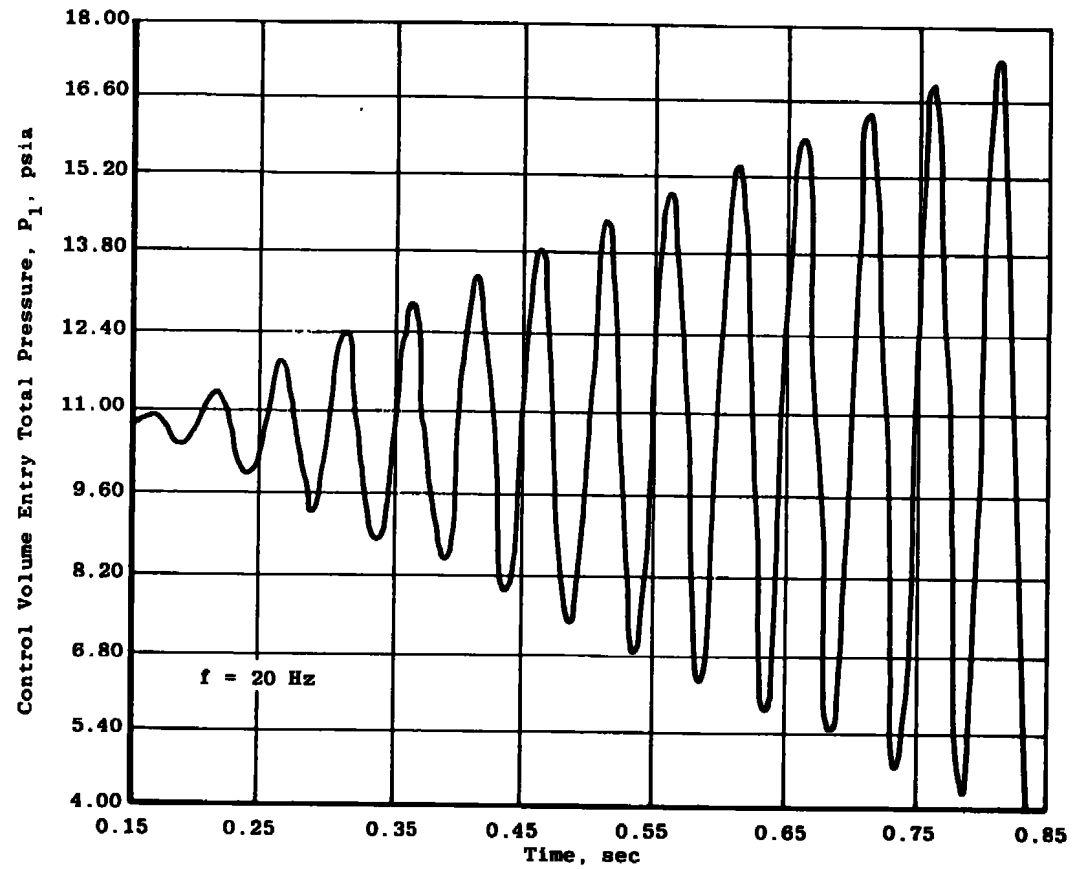
a.   Inlet total pressure

Figure 25.   Oscillating inflow loading to stall, NACA-8 compressor,
N/√θ = 70%.
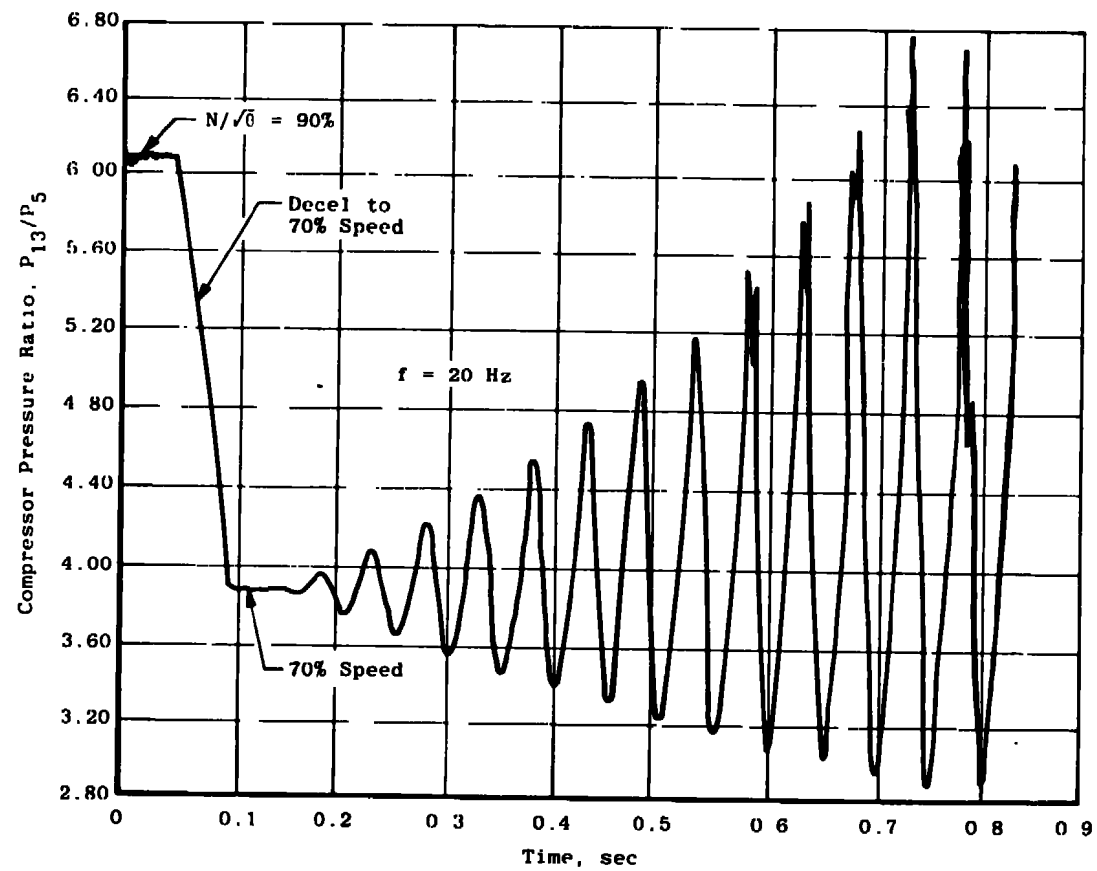
b. Compressor pressure ratio

Figure 25. (Continued).
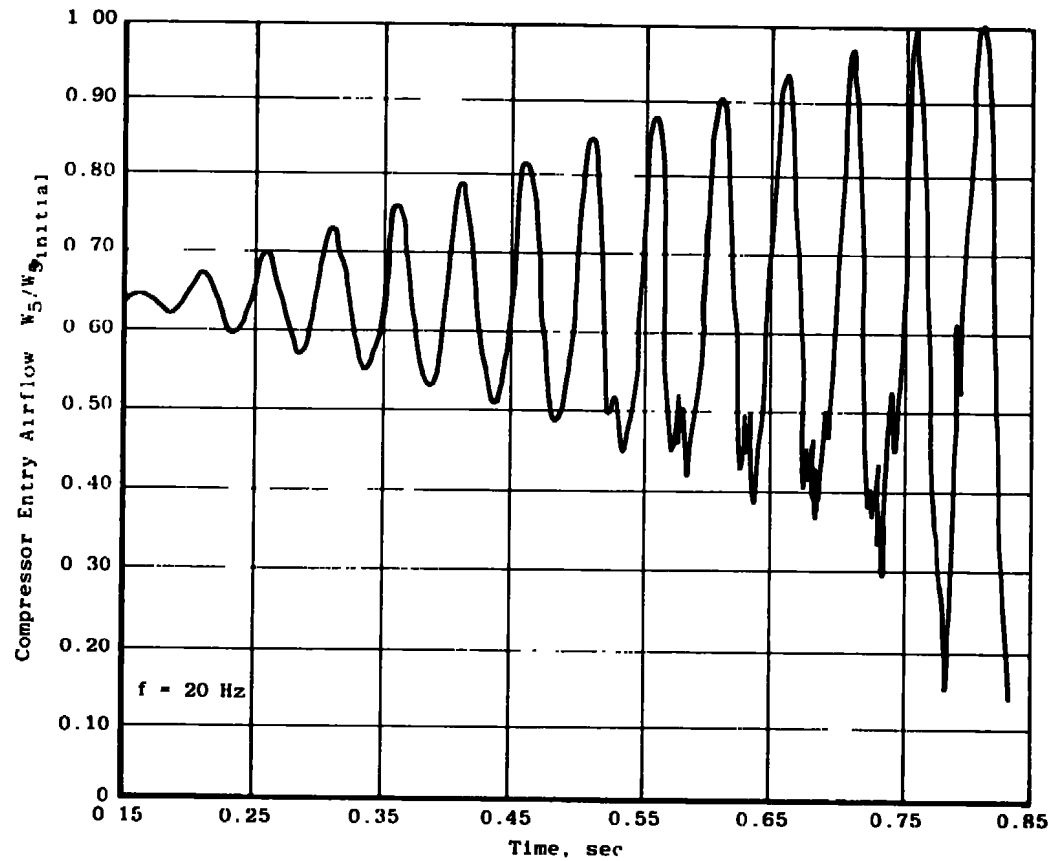
c. Compressor entry airflow

Figure 25. (Continued).
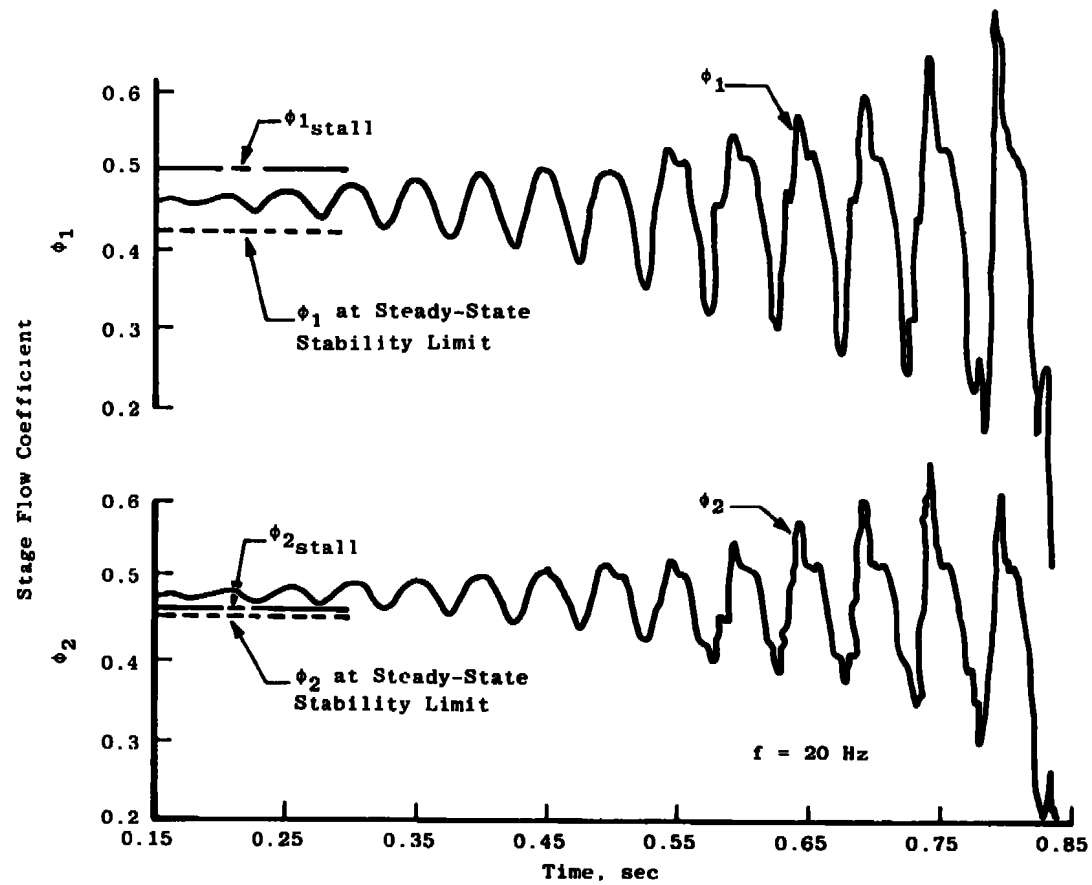
d. Flow coefficients, stages 1 and 2

Figure 25. (Continued).
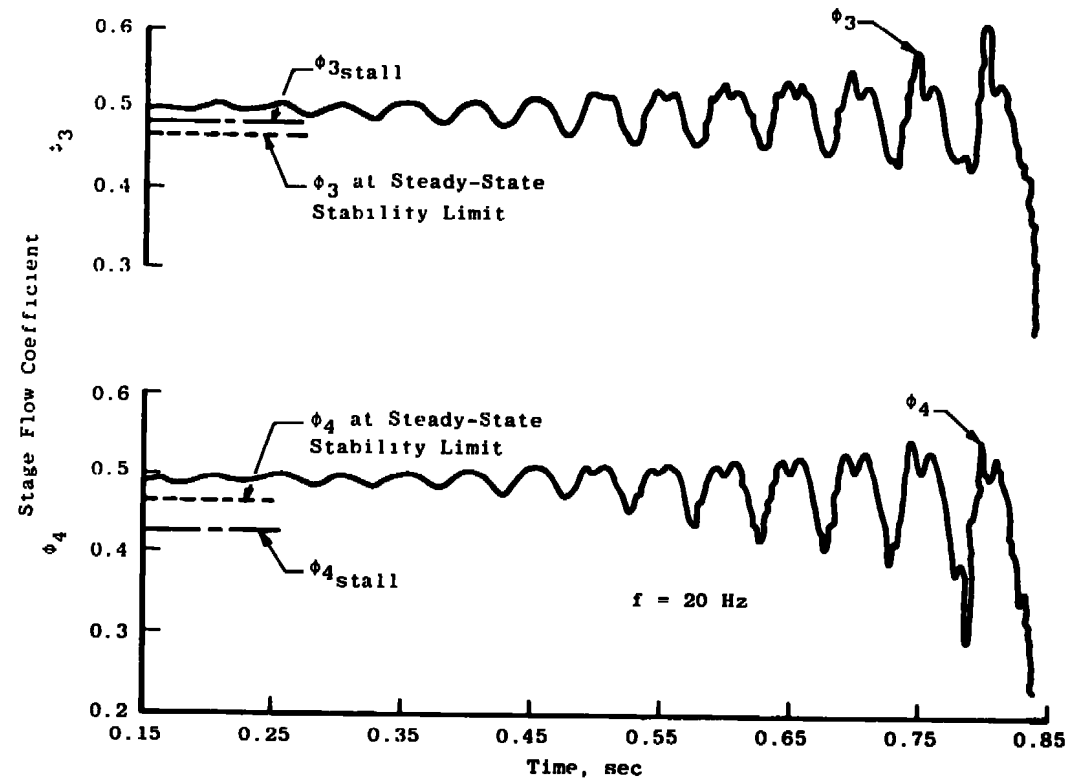
e. Flow coefficients, stages 3 and 4

Figure 25. (Continued).
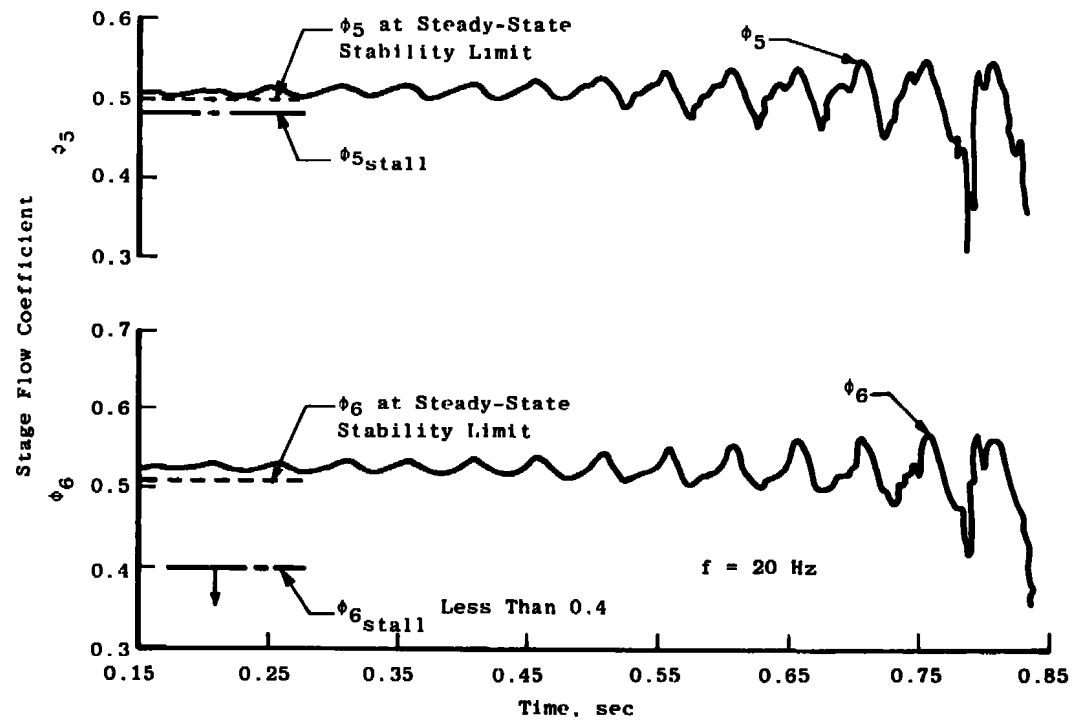
f. Flow coefficients, stages 5 and 6

Figure 25. (Continued).
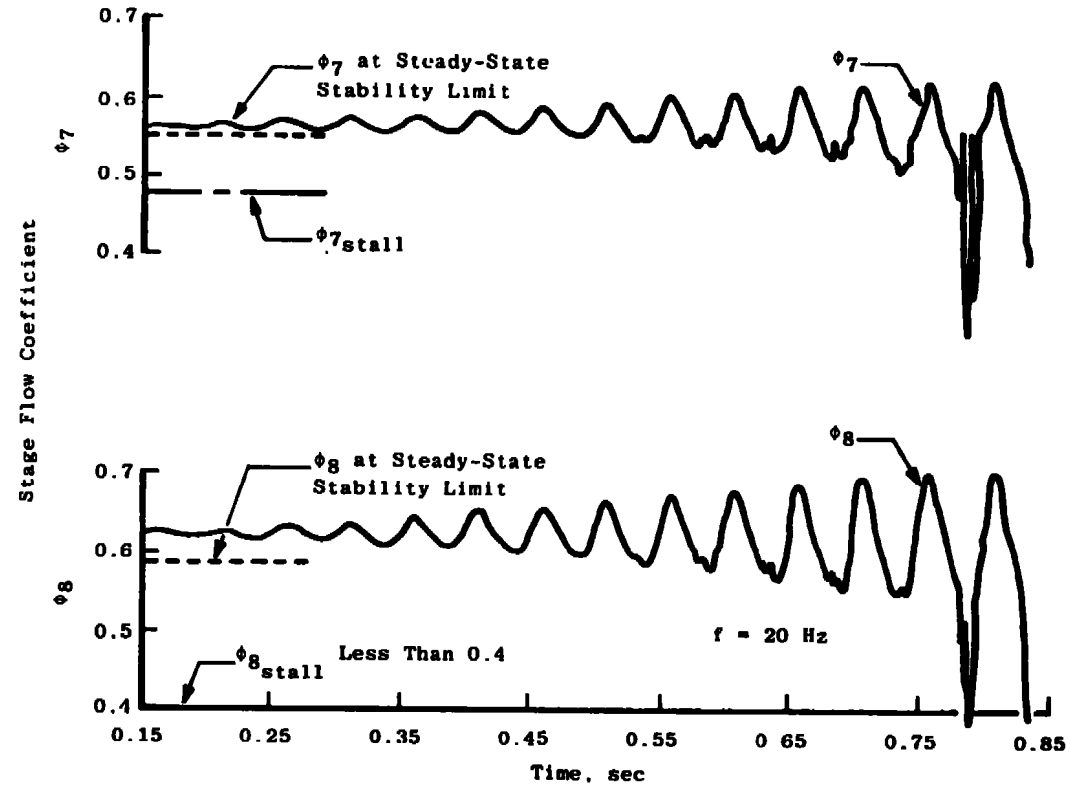
g. Flow coefficients, stages 7 and 8

Figure 25. (Continued).
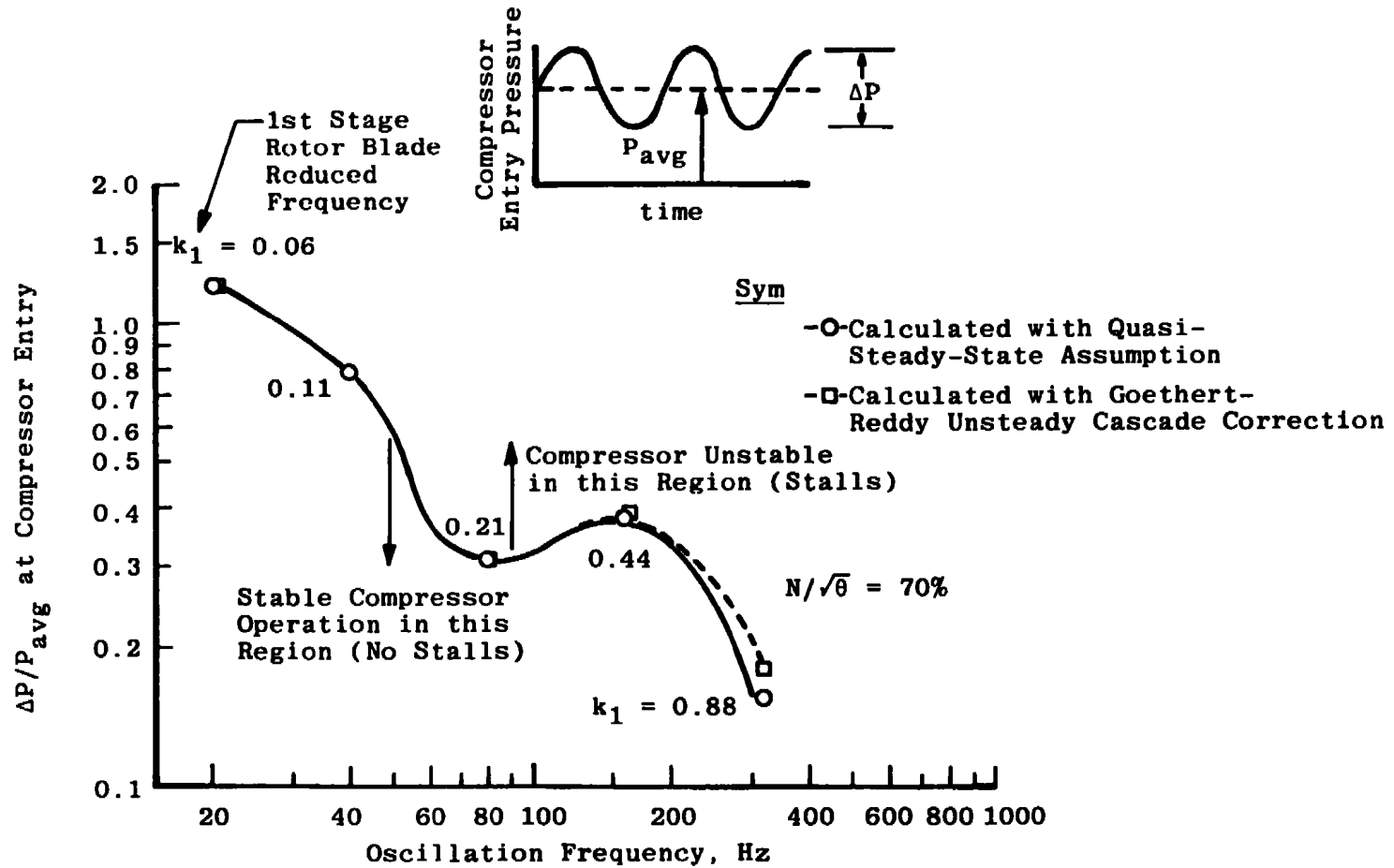
Figure 26. Stability limits for planar oscillating inflow, NACA-8 compressor.
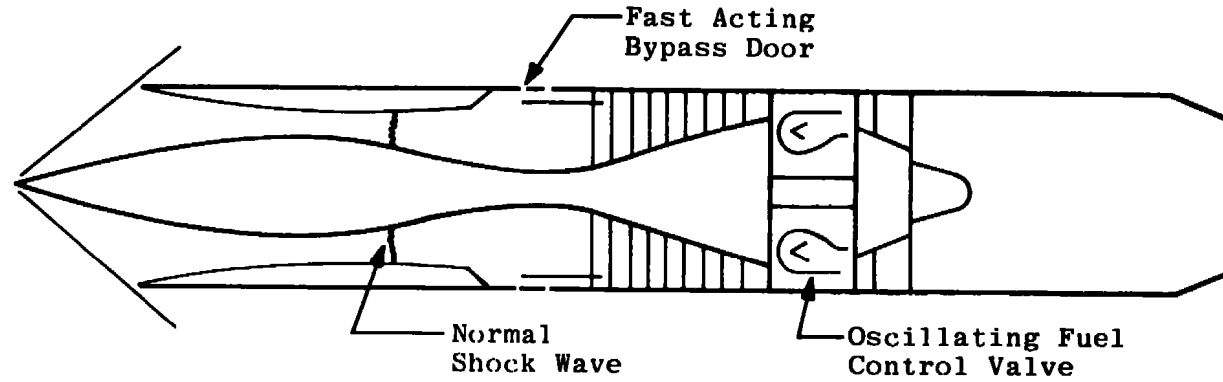
a. With supersonic inlet in wind tunnel, Mach = 2.5 [52]
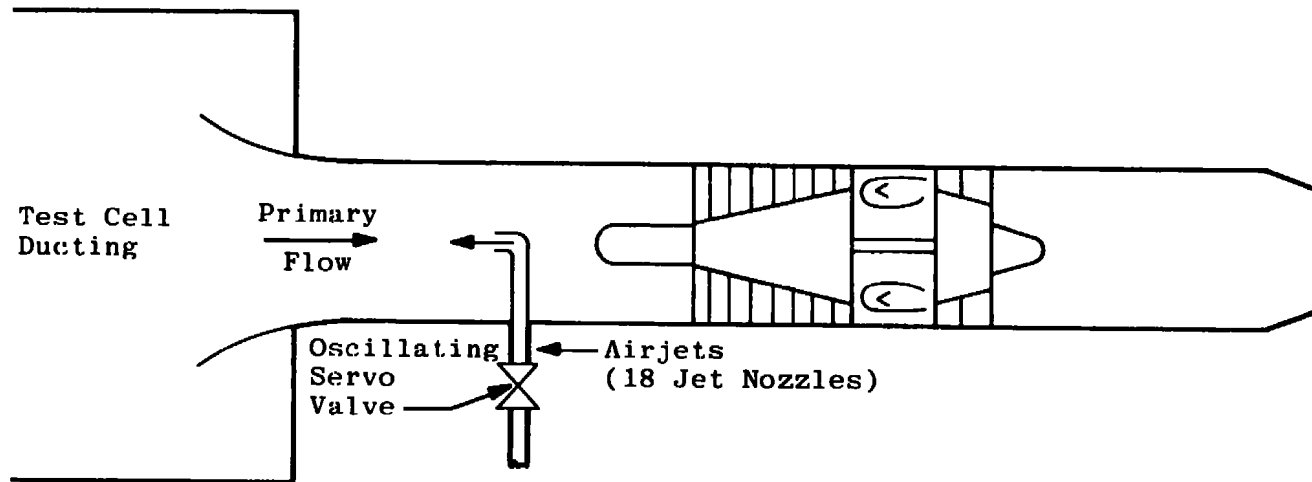
b. With airjet system [53]

Figure 27. Test arrangements for NASA J85-13 dynamic response experiments.
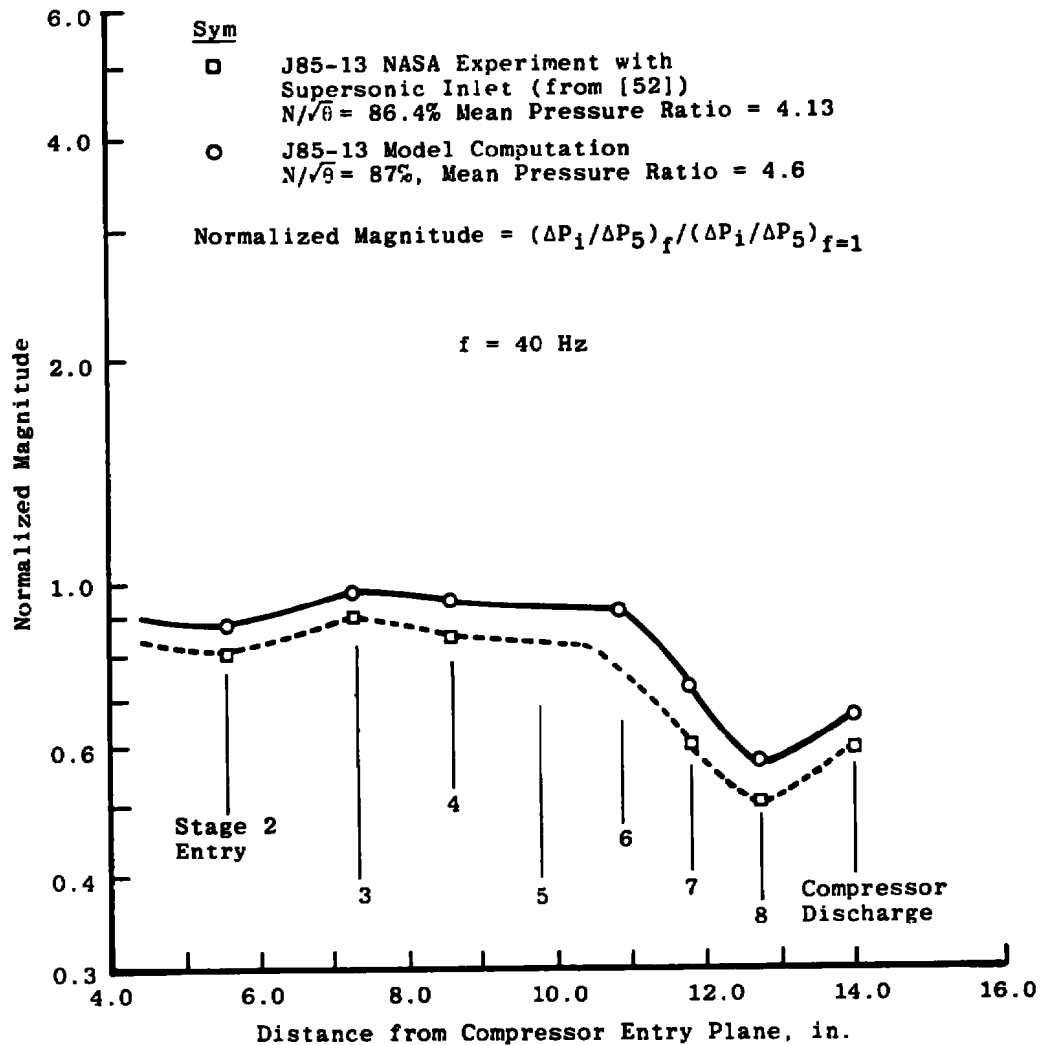
a. Amplitude ratio

Figure 28. Variation of amplitude ratio and phase angle through the J85-13 compressor with oscillating compressor entry pressure at 40 Hz.
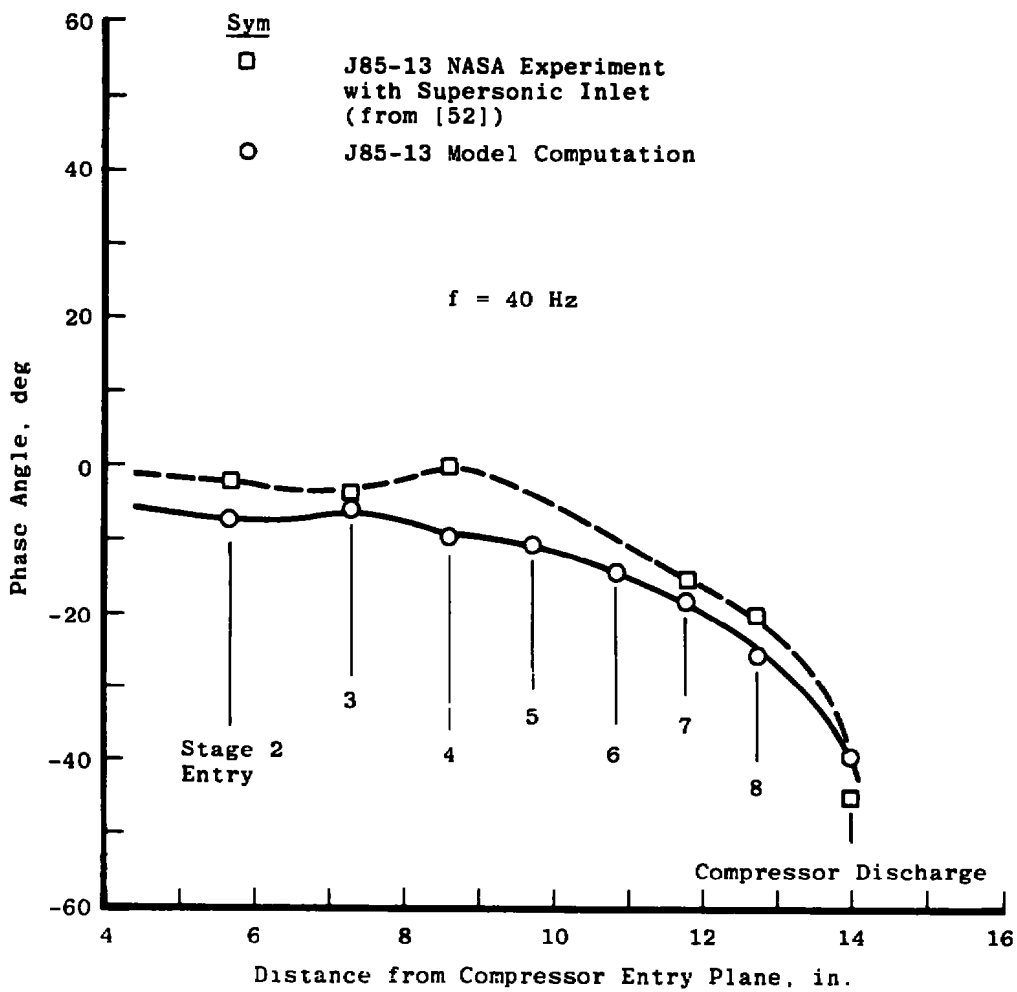
b. Phase angle

Figure 28. (Continued).
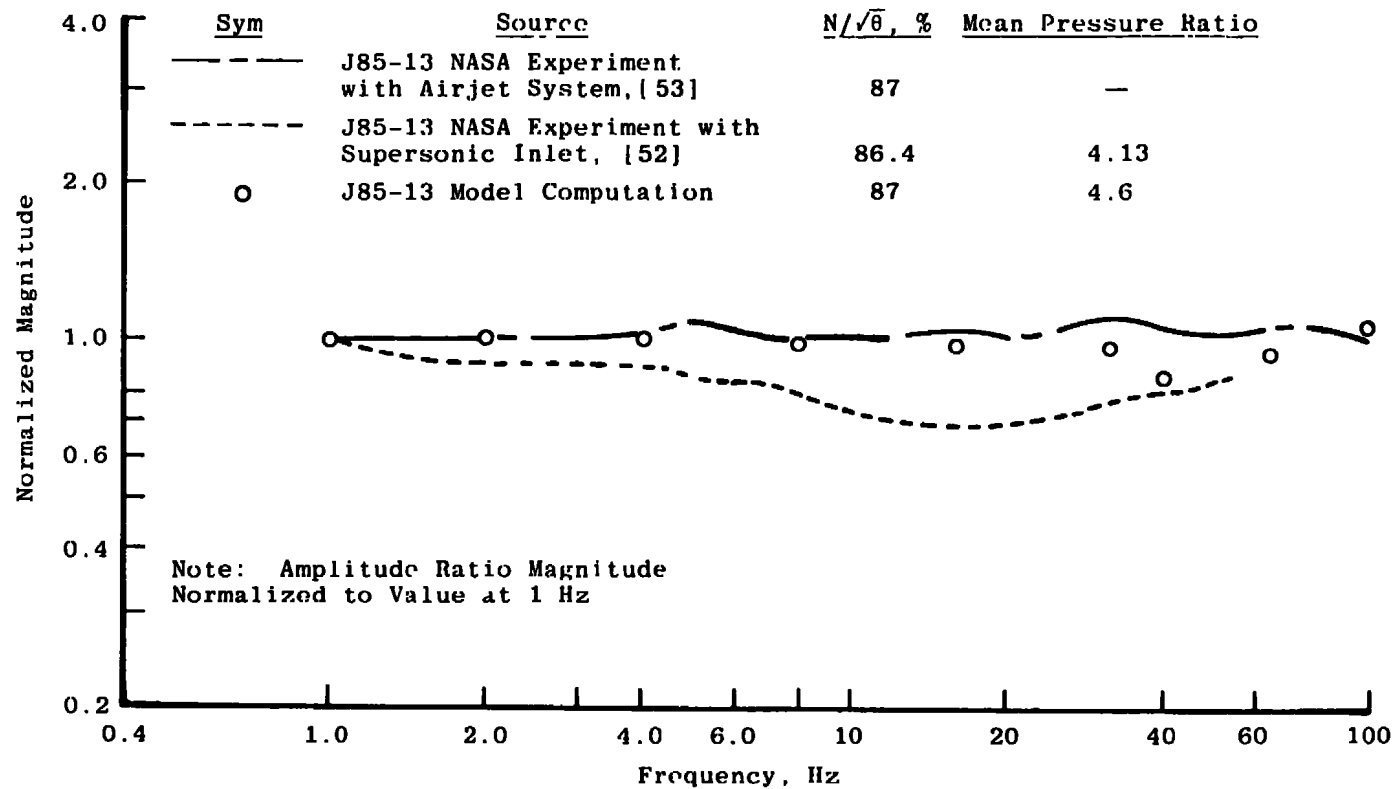
a. Stage 2 entry (amplitude ratio)

Figure 29. Dynamic response to oscillating compressor entry pressure, J85-13 compressor.
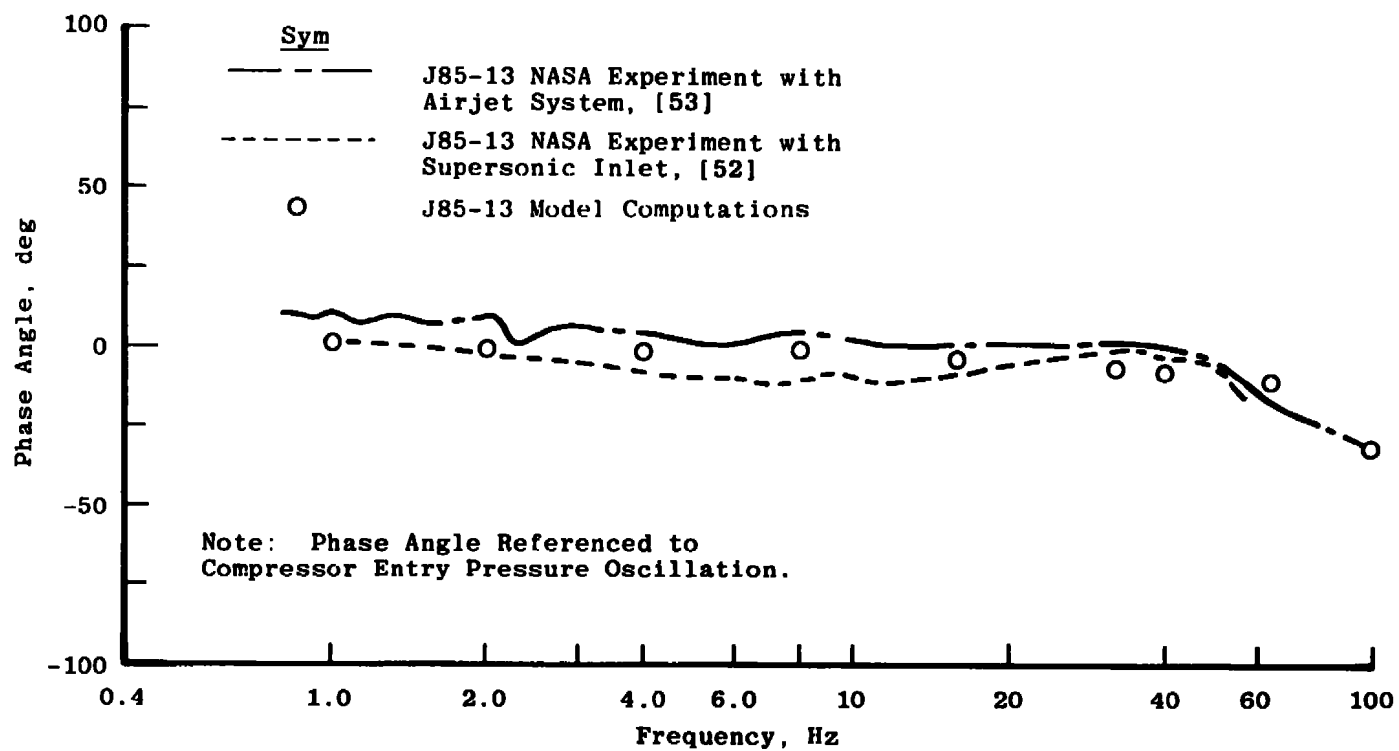
b. Stage 2 entry (phase angle)

Figure 29. (Continued).
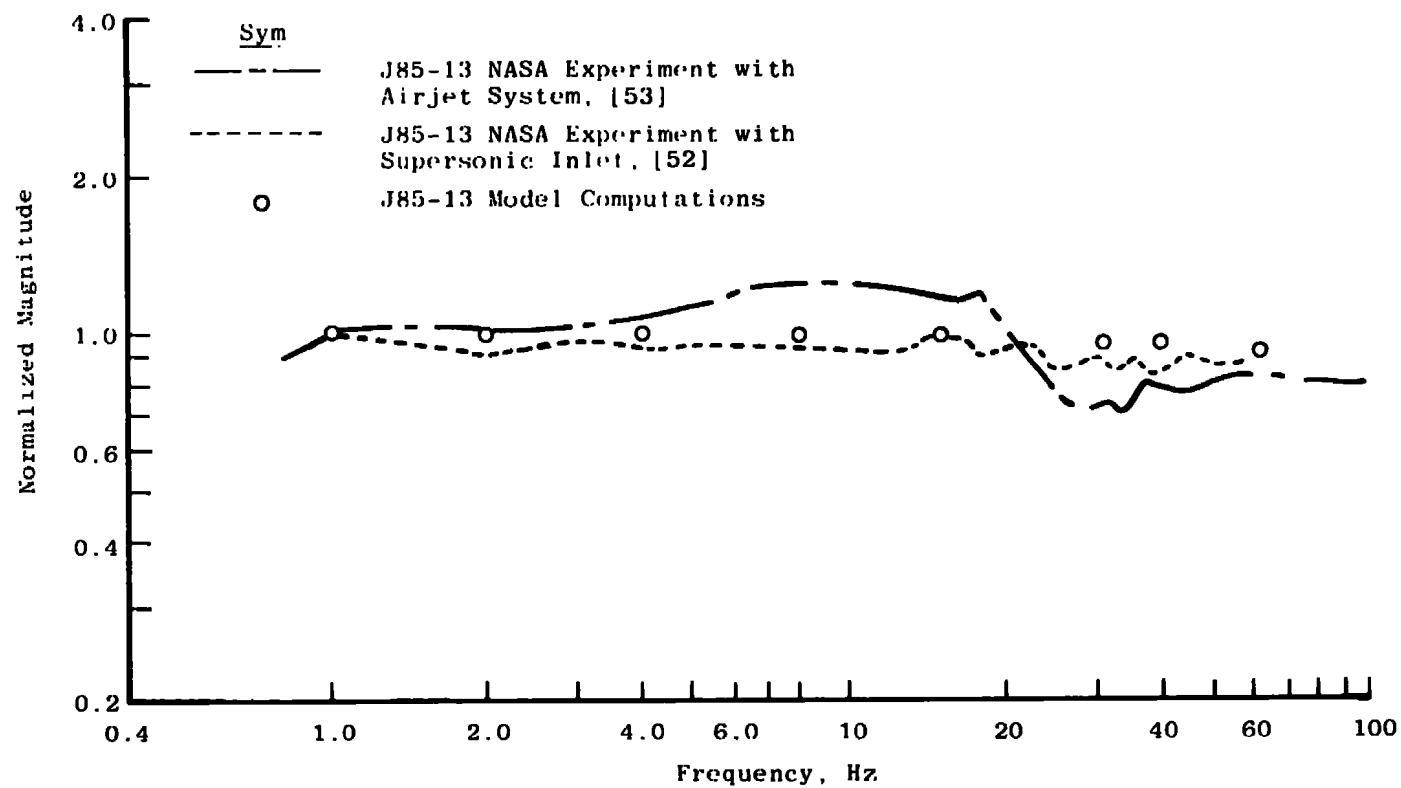
c. Stage 4 entry (amplitude ratio)

Figure 29. (Continued).
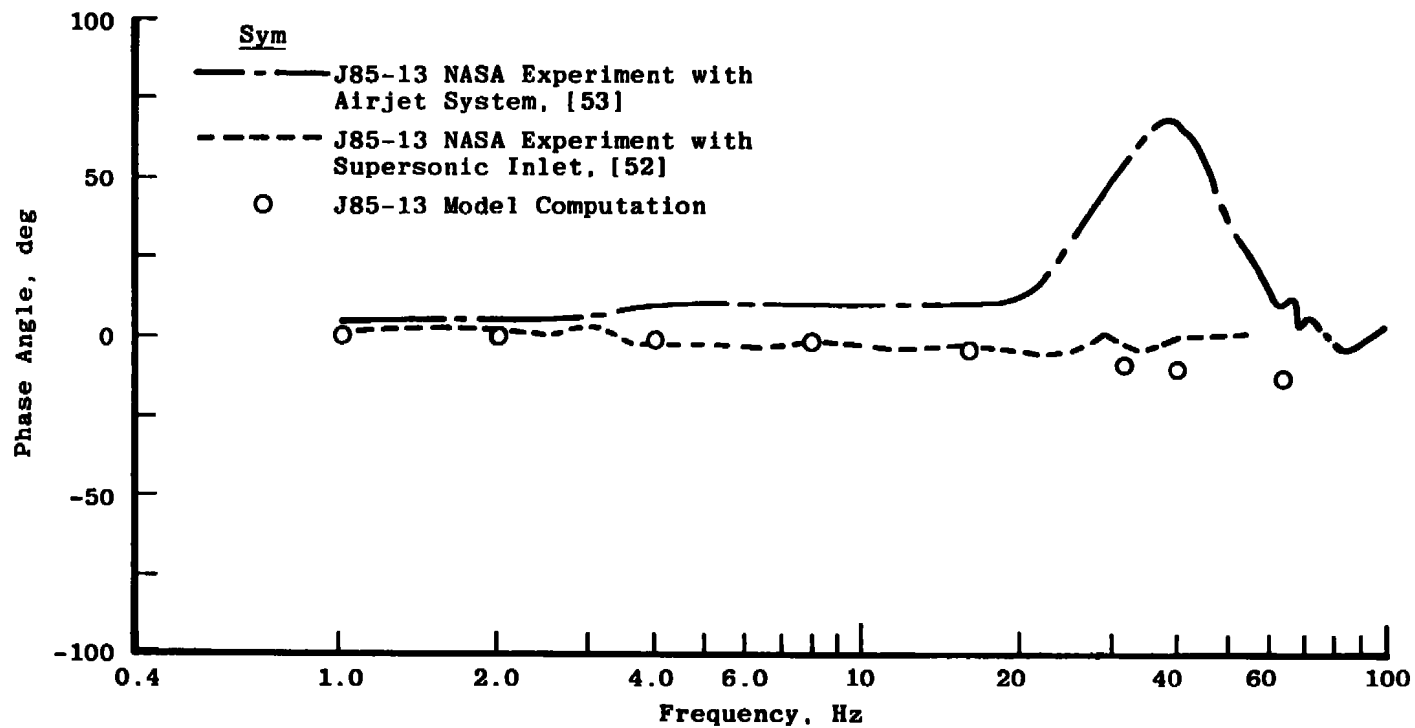
d.   Stage 4 entry (phase angle)

Figure 29.   (Continued).
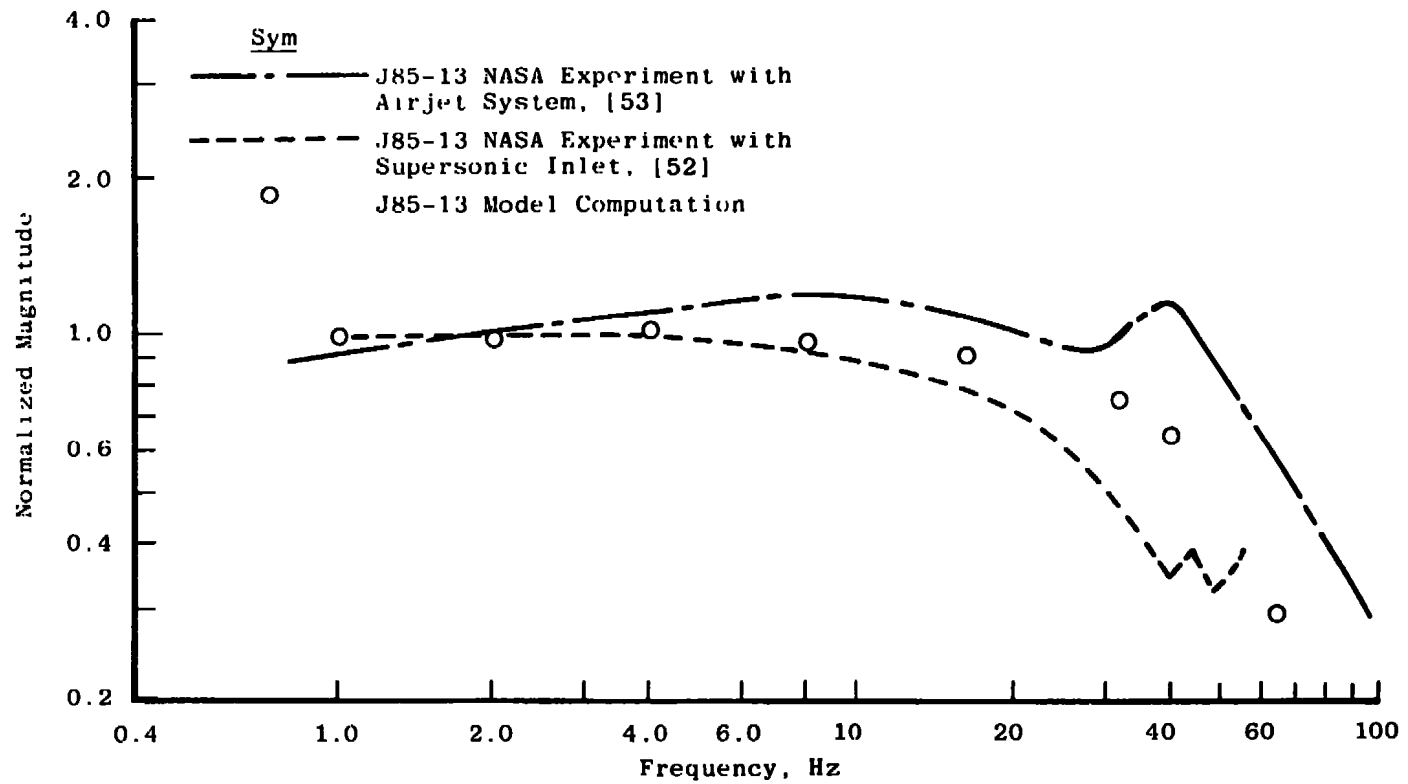
e. Compressor discharge (amplitude ratio)

Figure 29. (Continued).
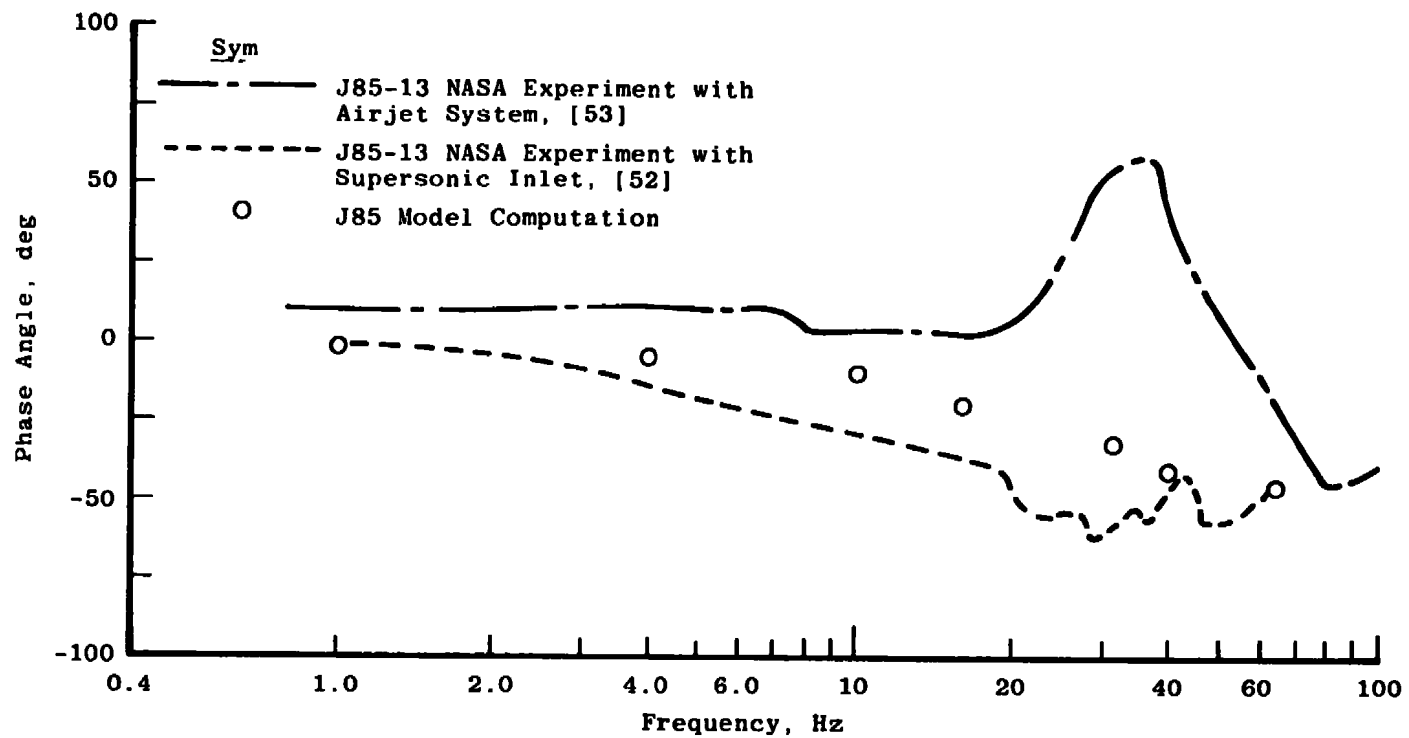
f.   Compressor discharge (phase angle)

Figure 29.   (Continued).
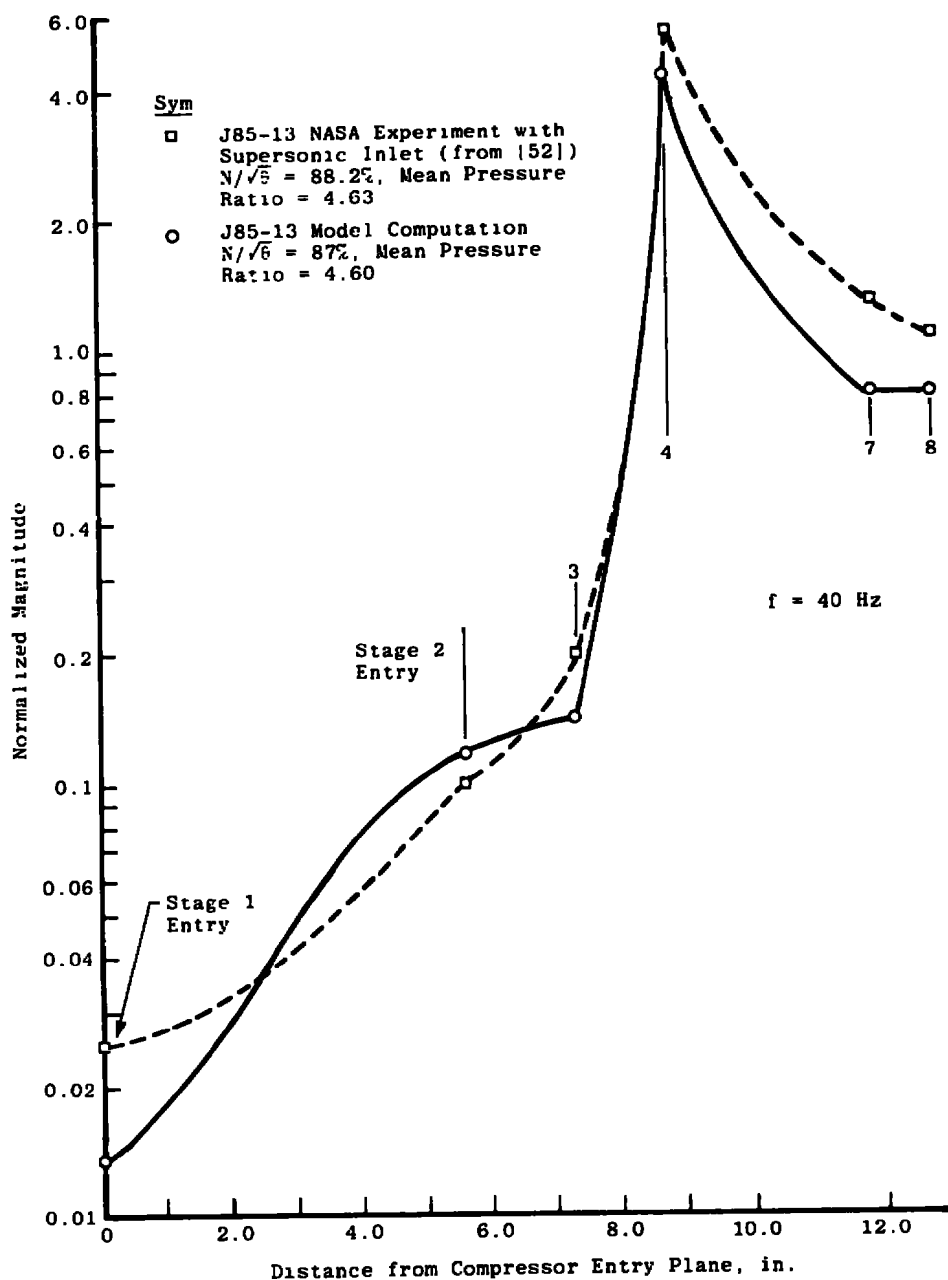
a. Amplitude ratio

Figure 30. Variation of amplitude ratio and phase angle through the J85-13 compressor with oscillating engine fuel flow at 40 Hz.

189
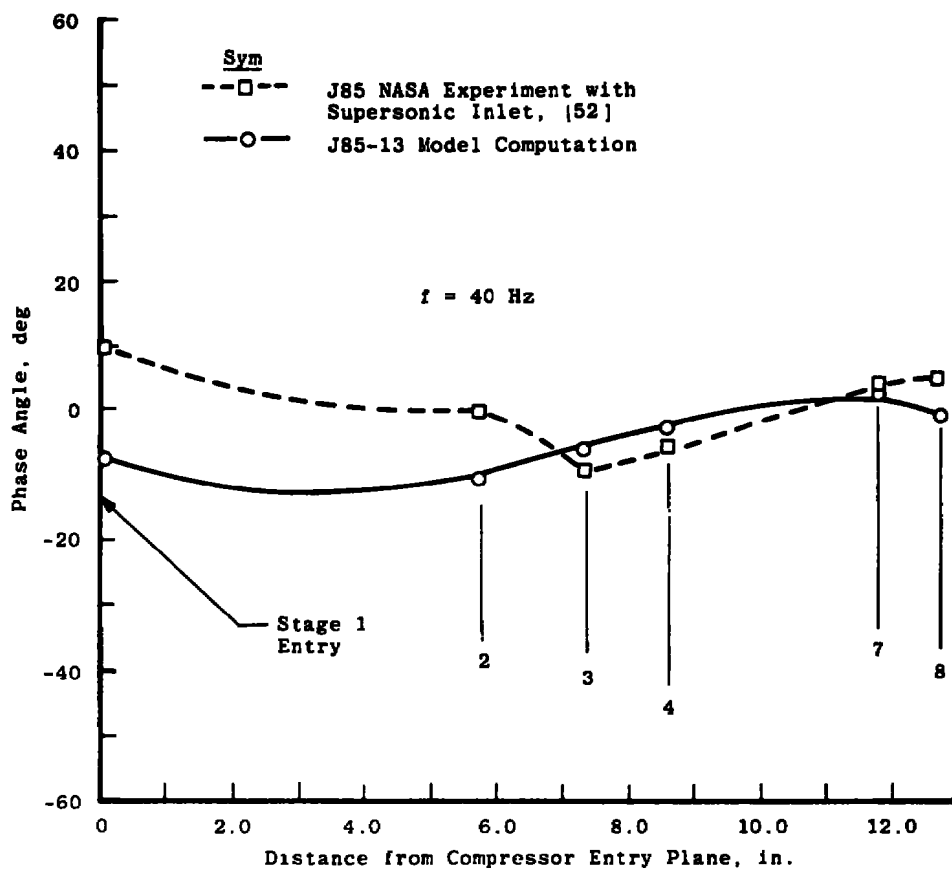
b. Phase angle

Figure 30. (Continued).
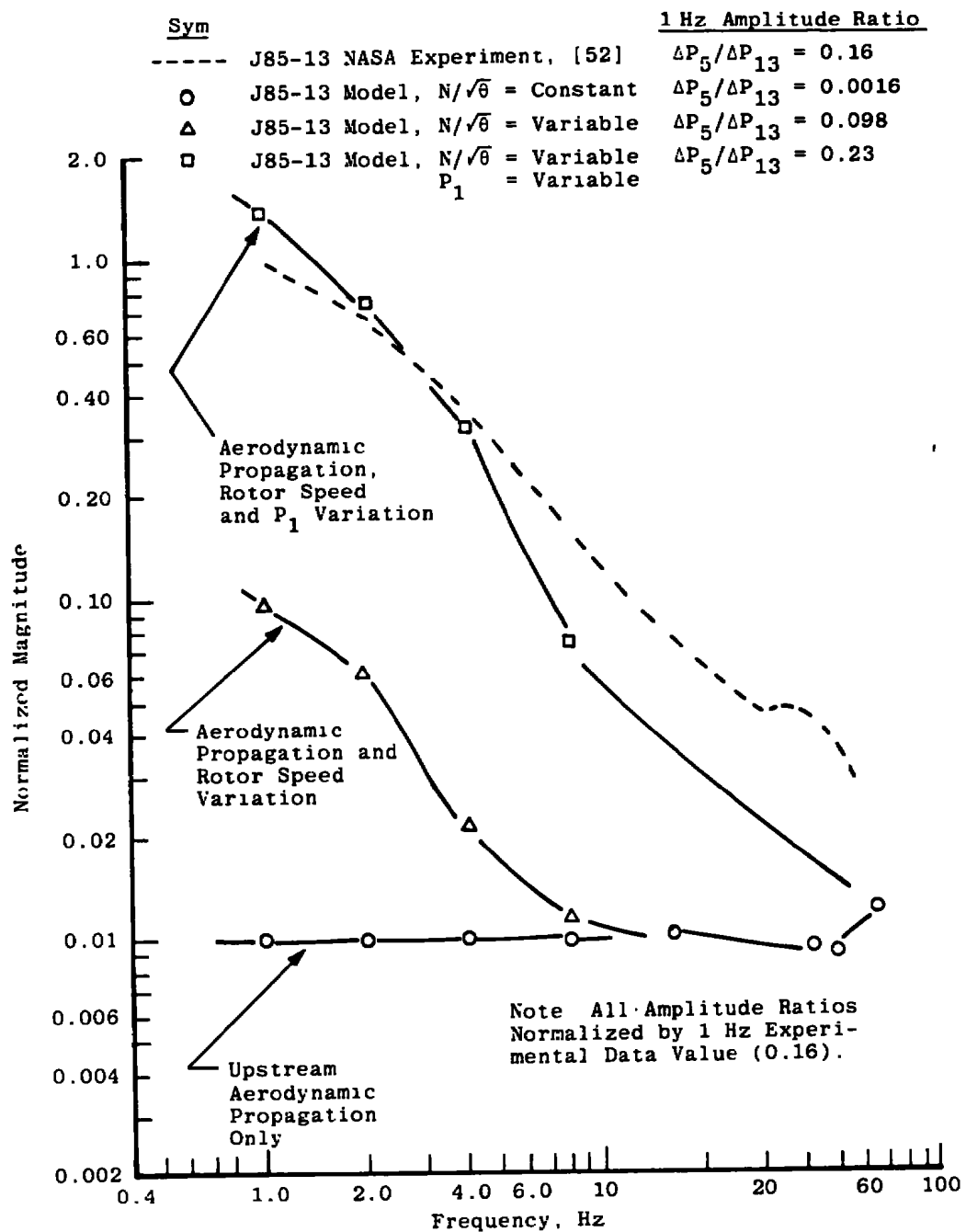
a. Compressor entry (amplitude ratio)

Figure 31. Dynamic response to oscillating fuel flow, J85-13 compressor.
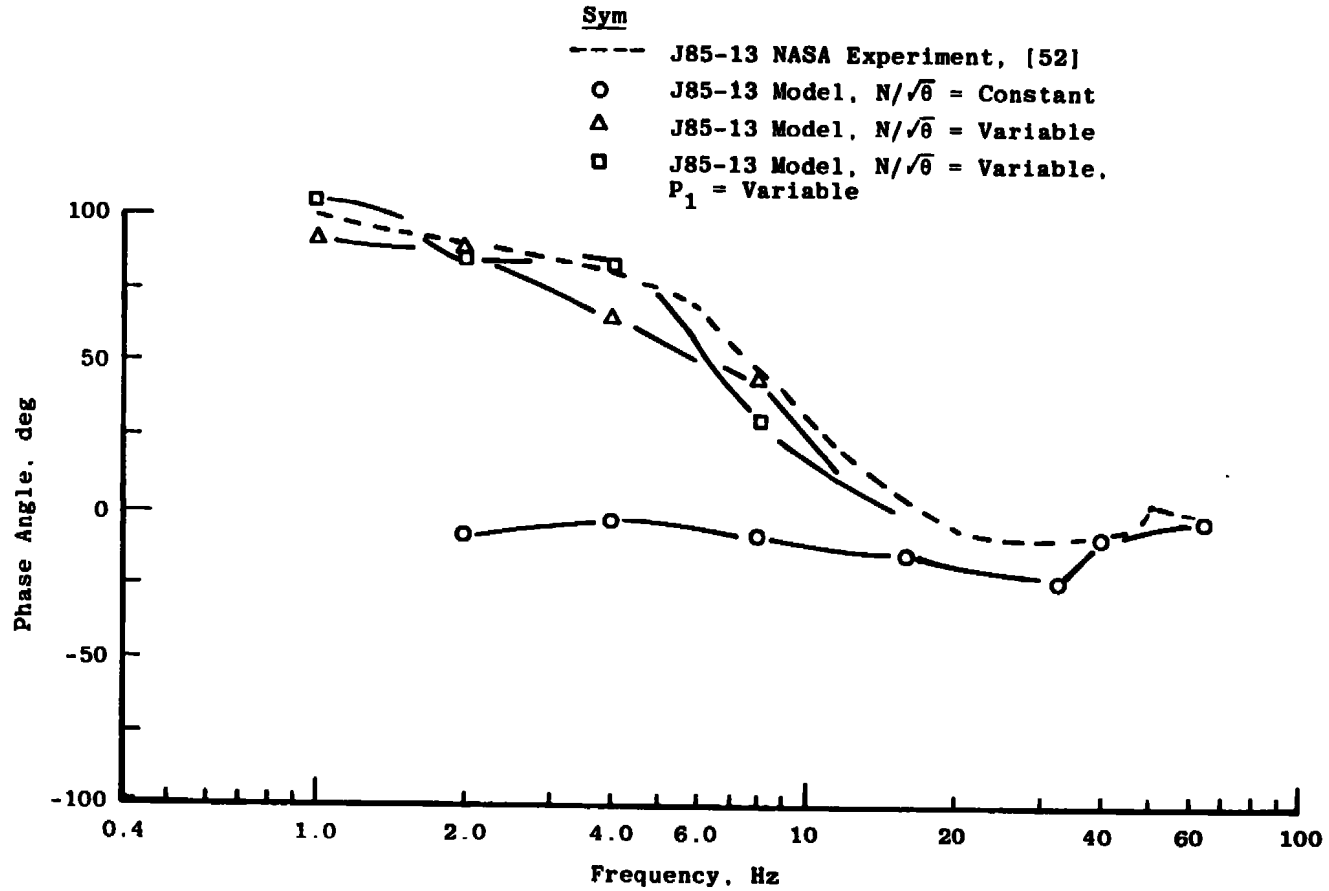
b.   Compressor entry (phase angle)

Figure 31.   (Continued).
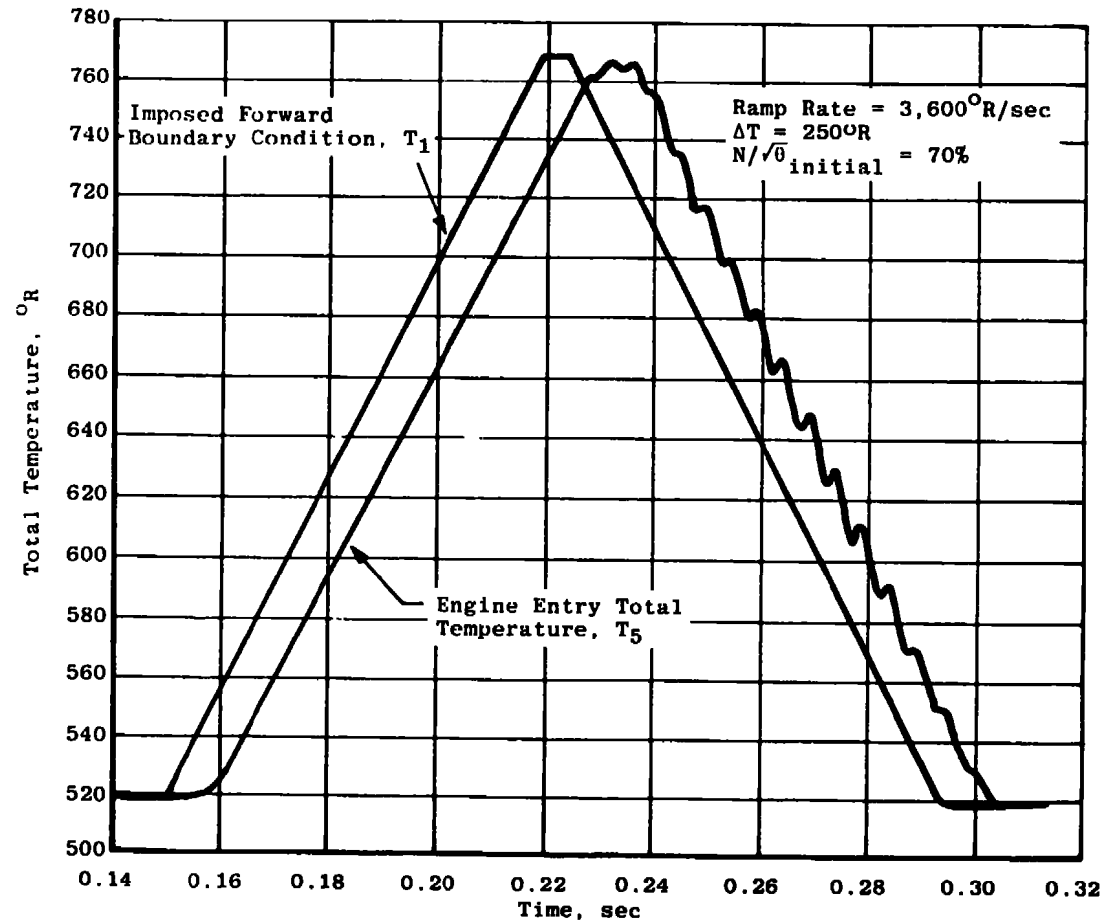
a. Inlet temperature

Figure 32. Rapid inlet temperature ramp to stall, NACA-8 compressor.
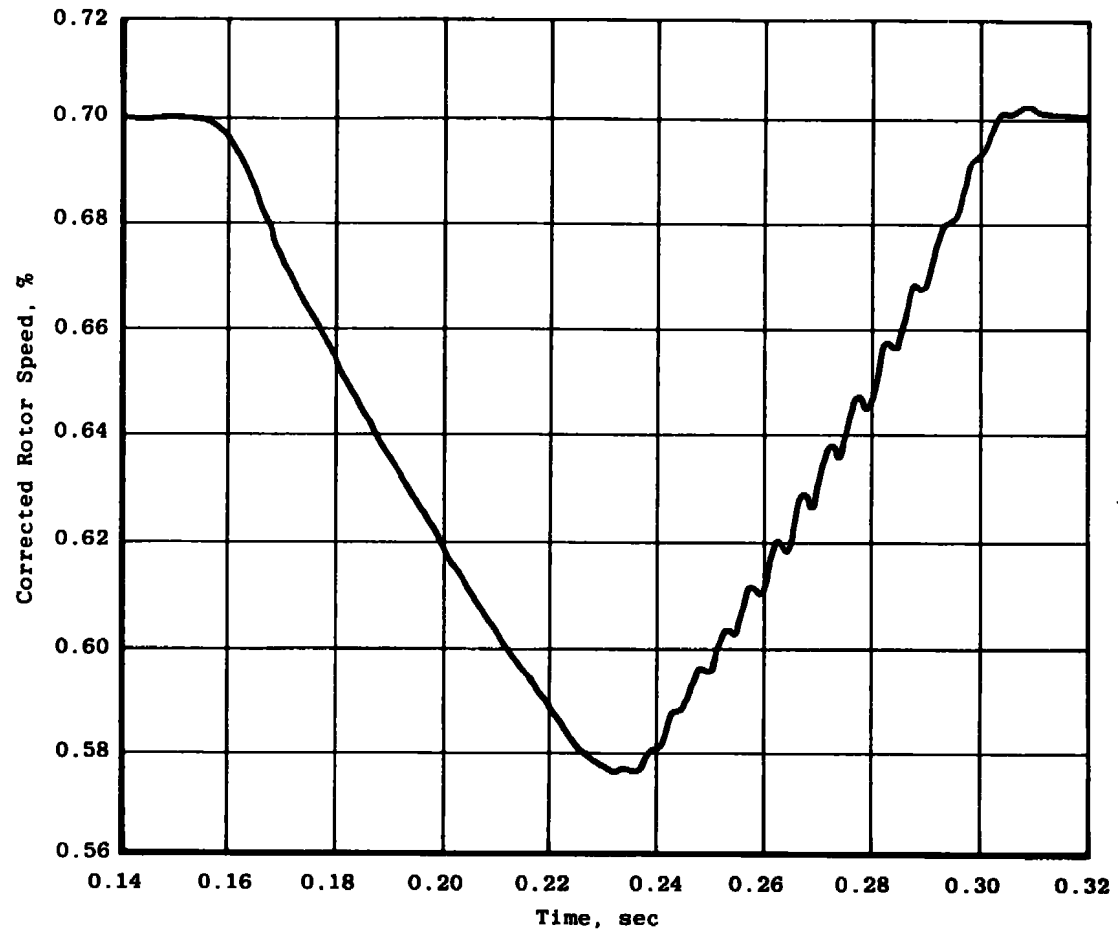
b. Corrected rotor speed

Figure 32. (Continued).
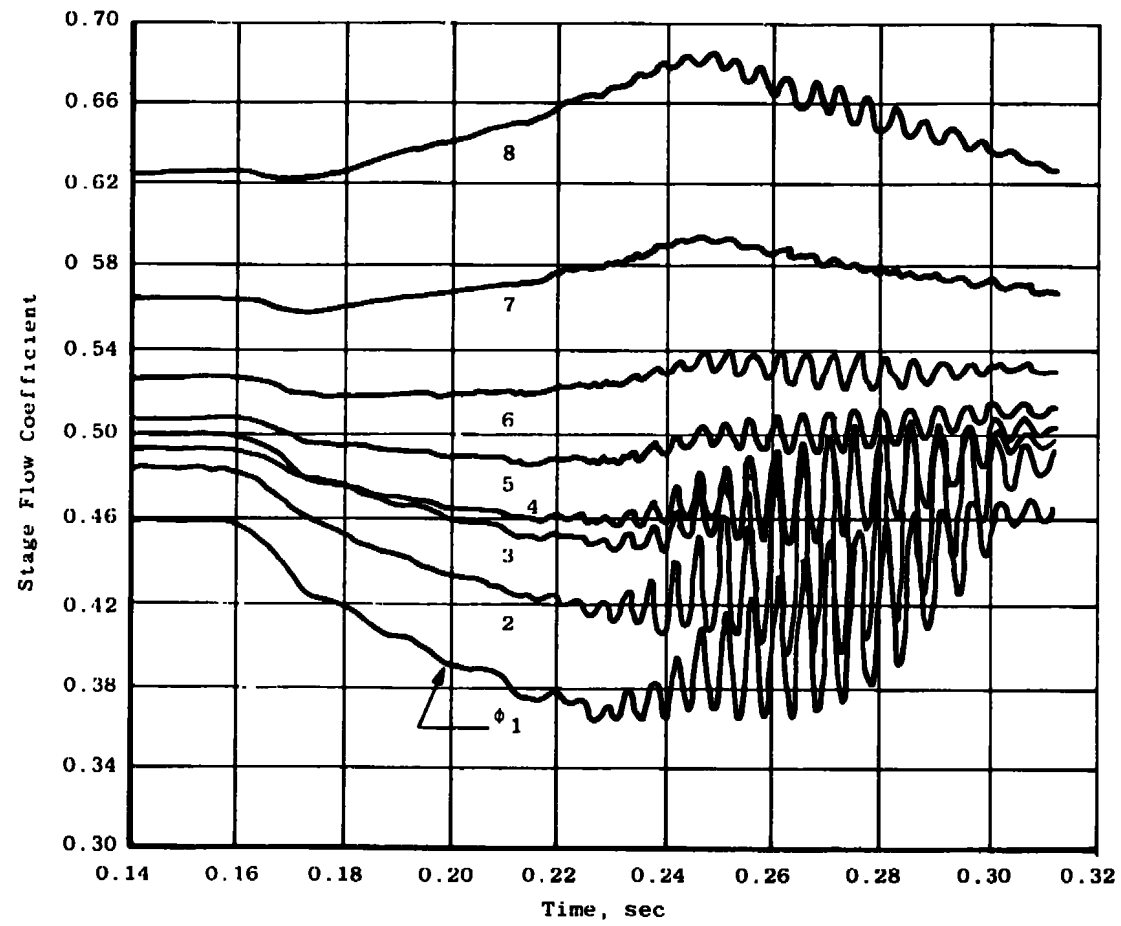
c. Stage flow coefficients

Figure 32. (Continued).
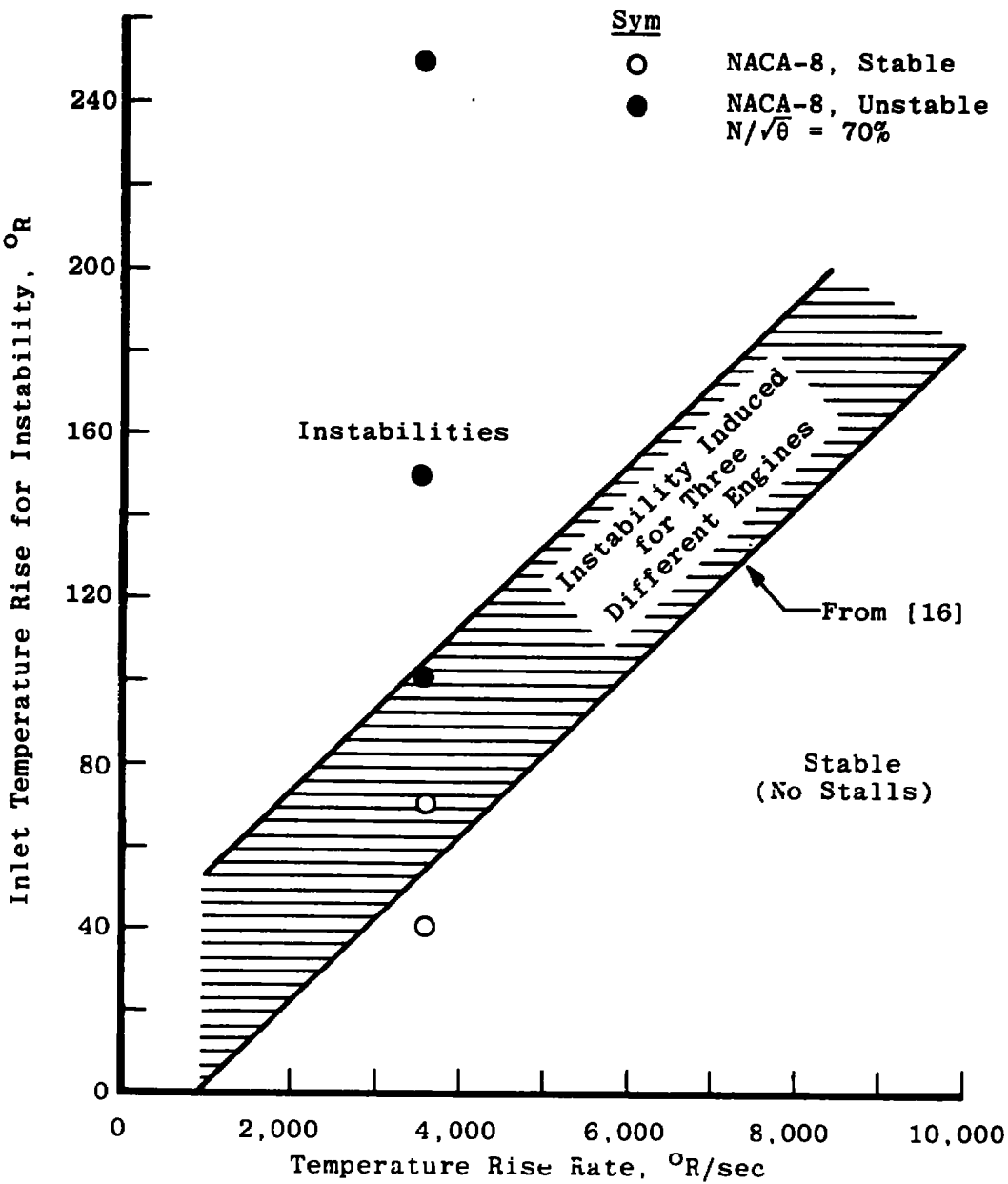
Figure 33. Compressor instability caused by rapid inlet temperature ramps.

Control Volume i,j,k
p Denotes + 1
m Denoted - 1
ip = i + 1, im = i - 1 ...

Control
Volume

k = 1   J =

jn = 4

kn = 6

Front View

Control Volume
(i,j,k) = (1,2,1)

jn = 4

j = 1

in = 5

Side View
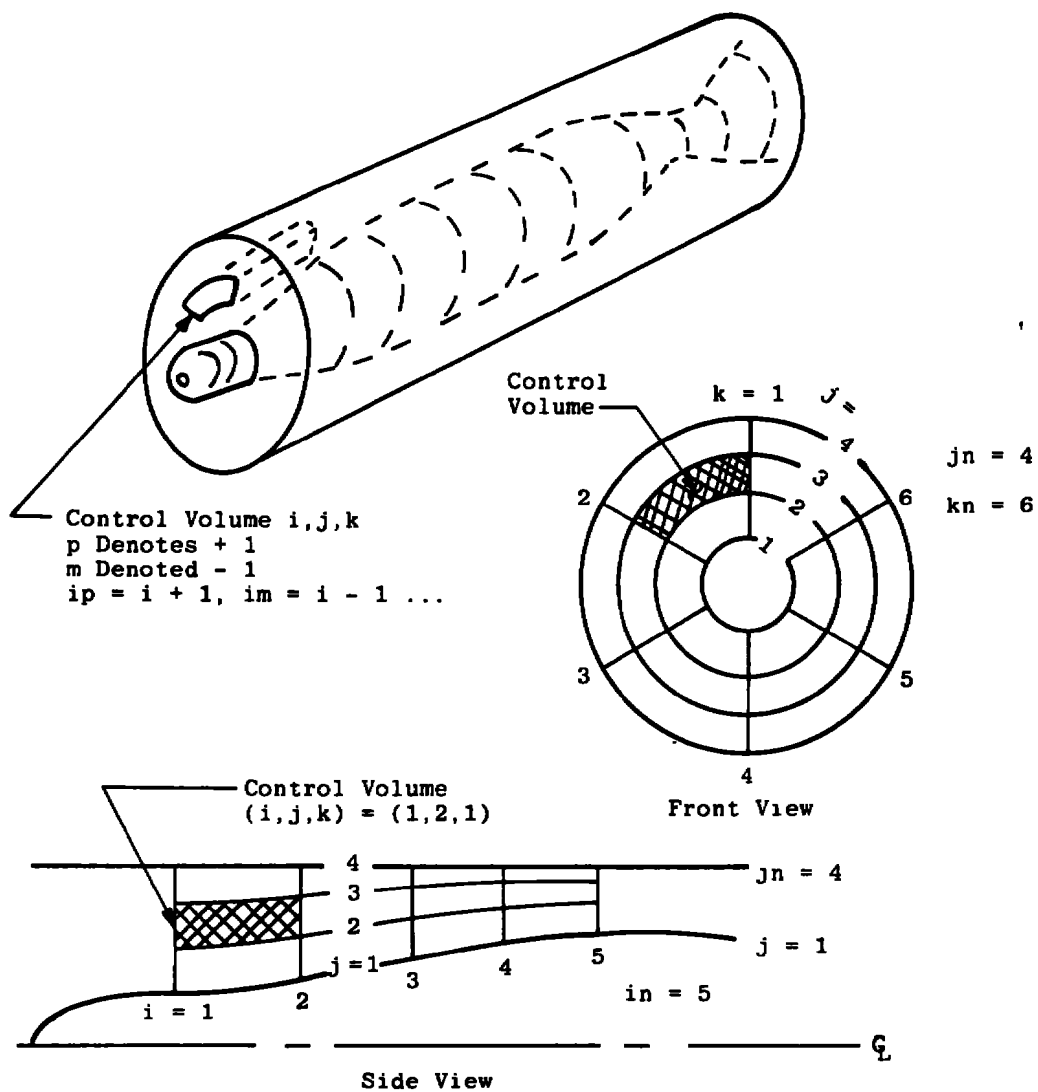
Figure 34.   Division of compressor into control volumes.
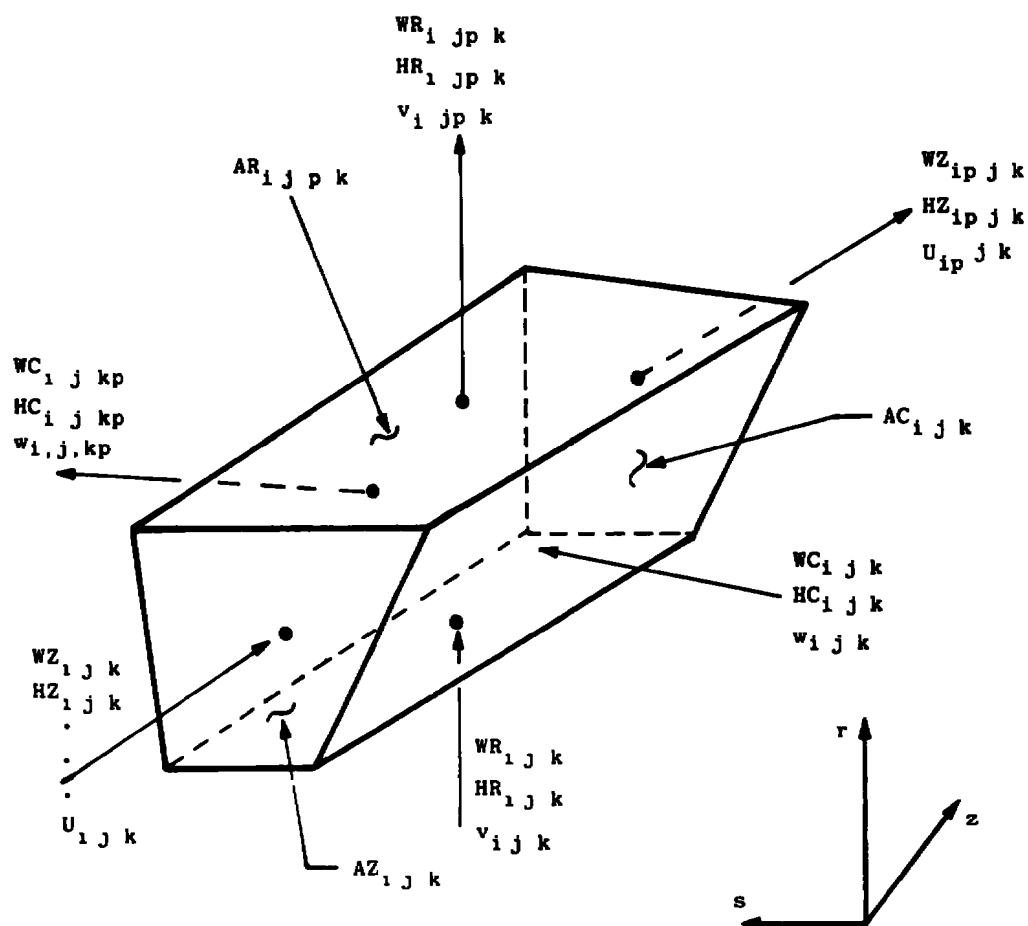
Figure 35. Control volume velocities and fluxes.

Control Volume i j k

WC

PS_{high}

PS_{low}

Control
Volume
i j kp

Rotor Gap Stator

Orifice Flow
Analogy

PS_{high}

WC

WC

WC

PS_{low}

Flow

Rotation

PS_{high}

WC

PS_{low}
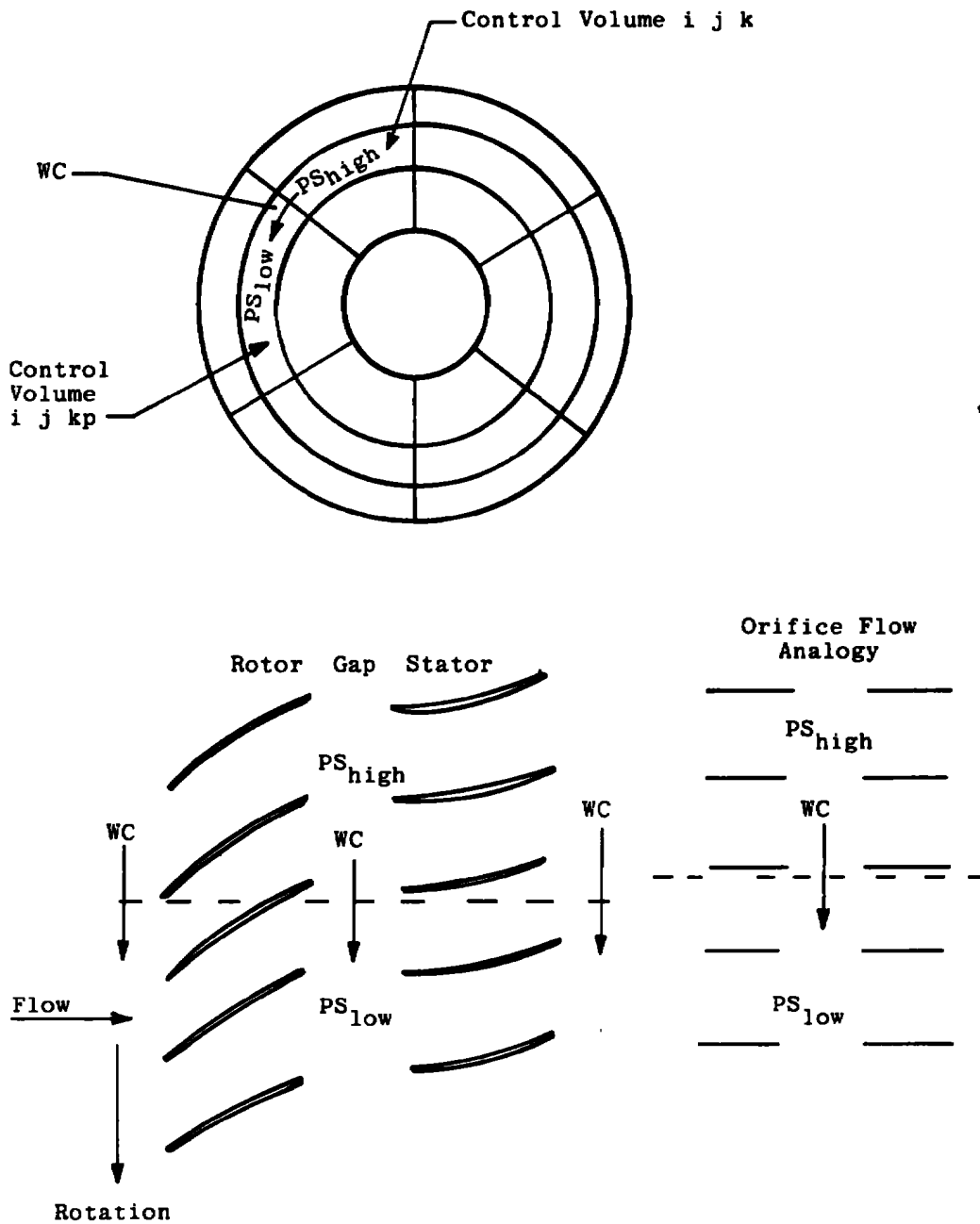
Figure 36. Circumferential crossflow.
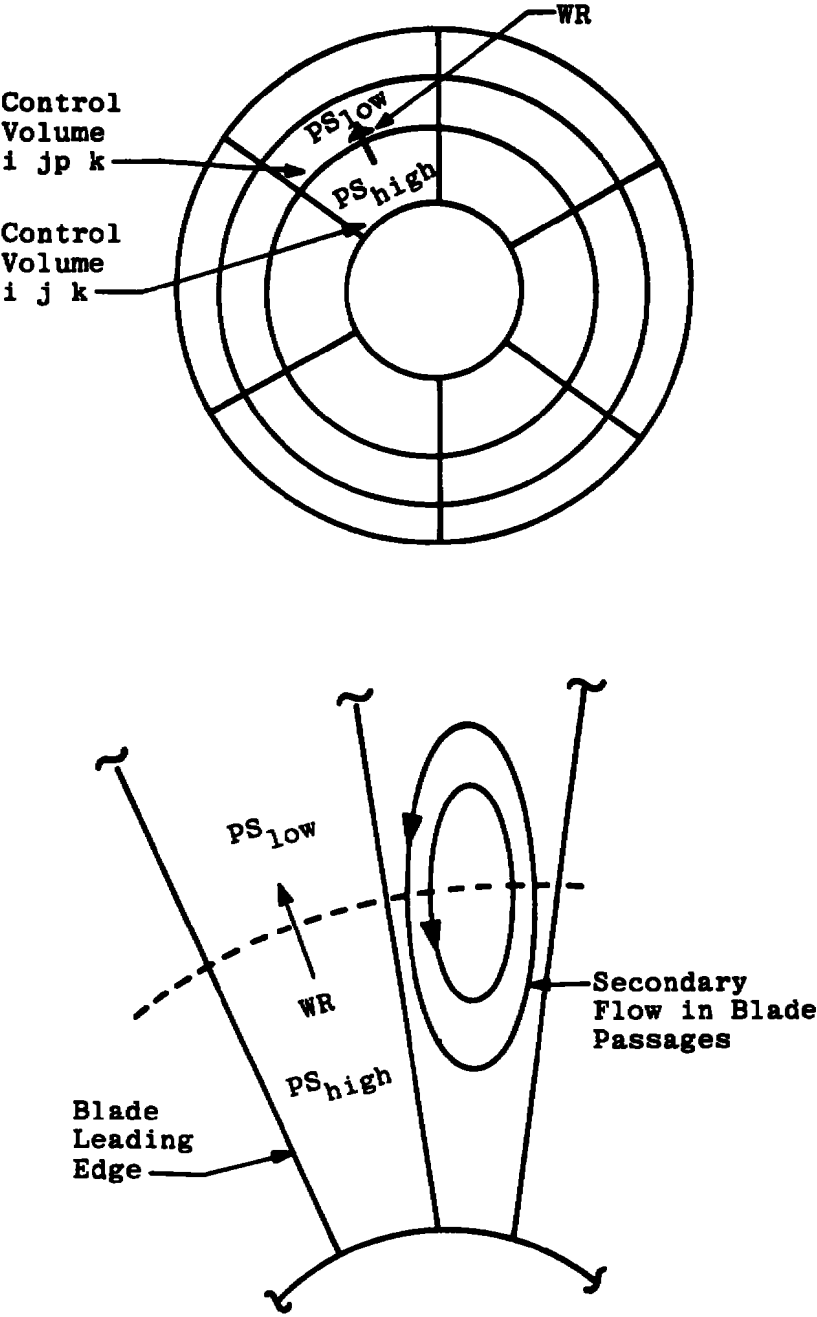
Figure 37. Radial crossflow.

Uniform Flow

Radially Distorted Flow

Velocity Triangles for Case A
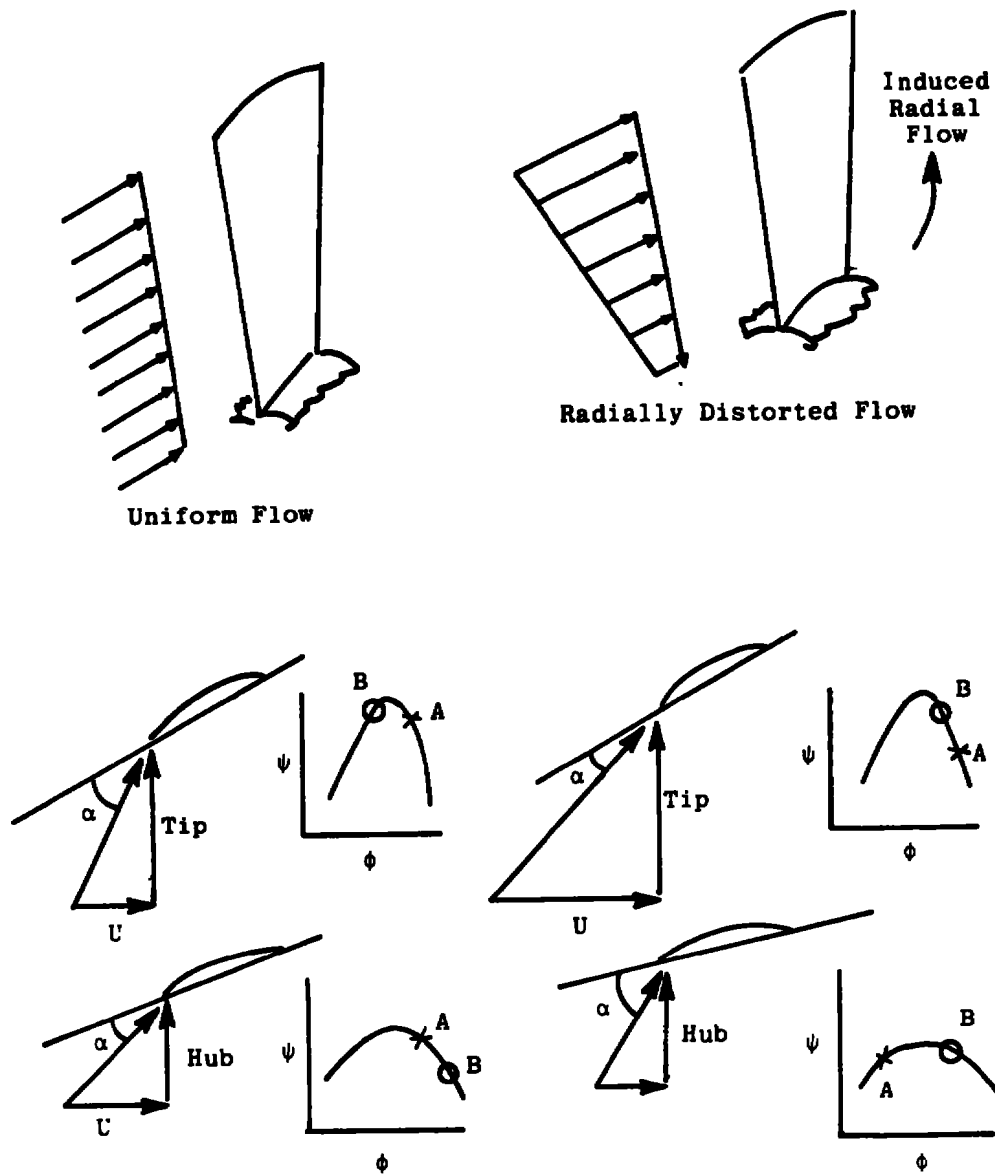
Figure 38.   Radial distortion effects.
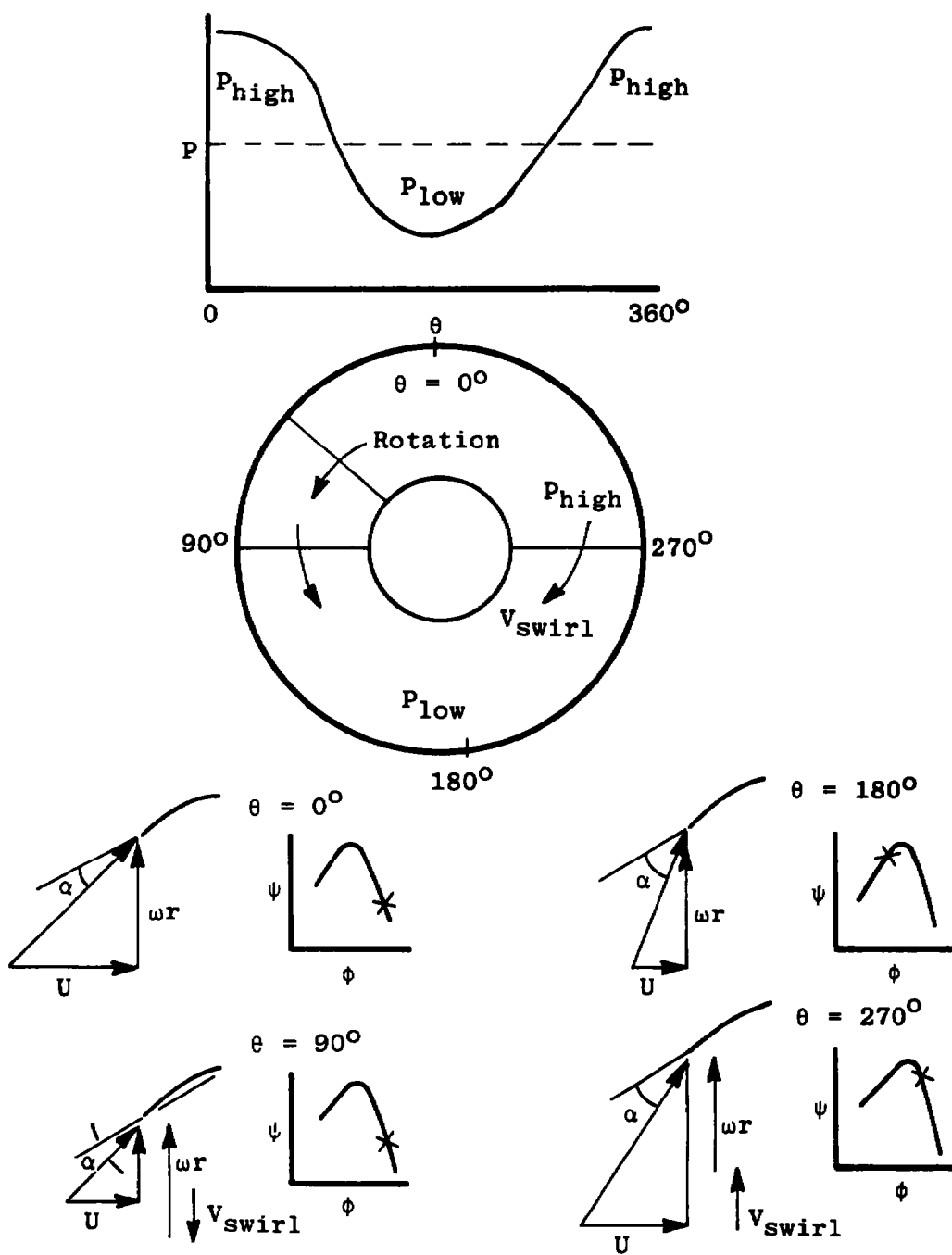
a. Steady flow effects

Figure 39. Circumferential distortion effects.

b. Unsteady flow effects

Figure 39. (Continued).

203

$$\Delta C_\ell = m \frac{C}{V_{ref}} \frac{d\alpha}{dt}$$

Angle of Attack, α
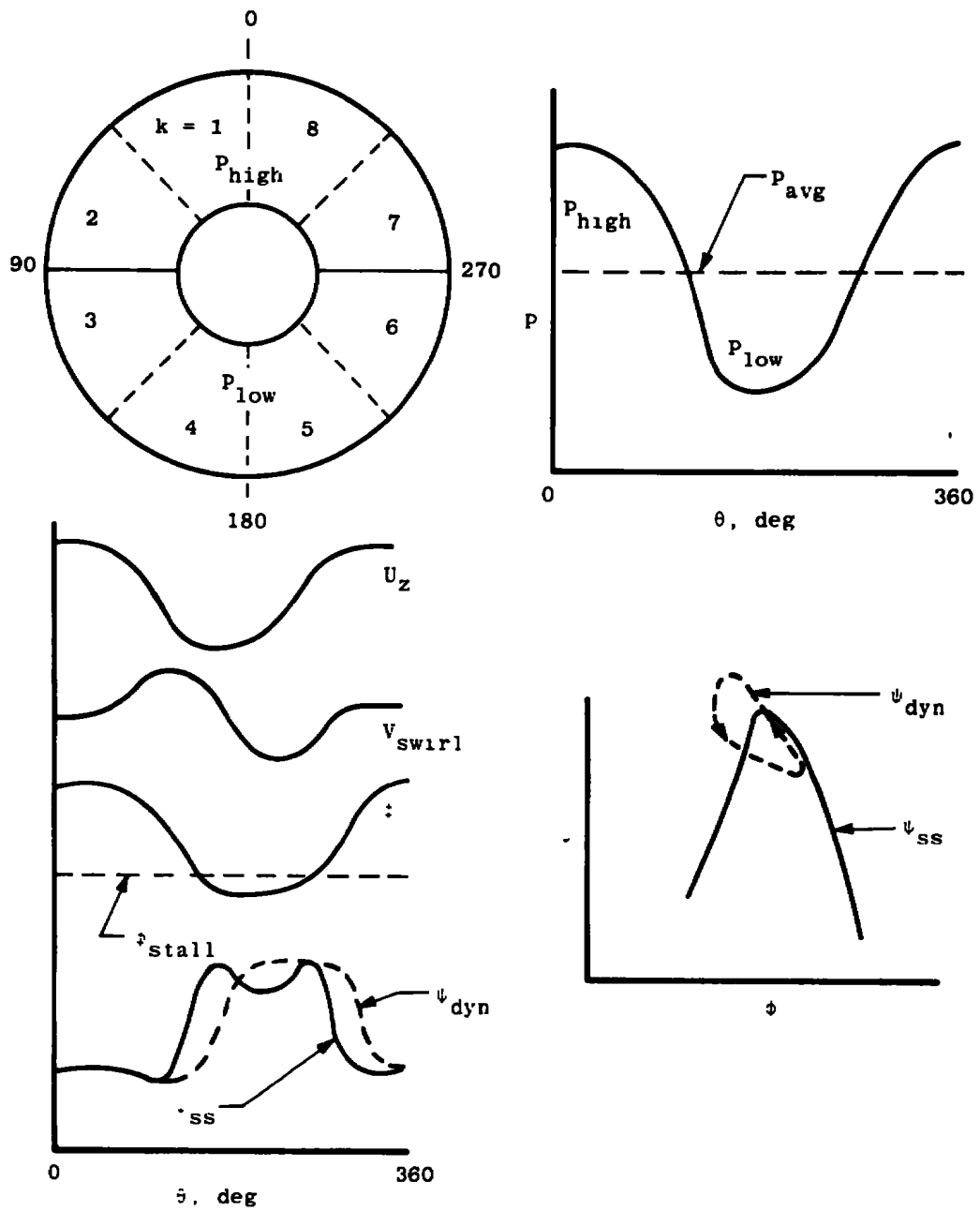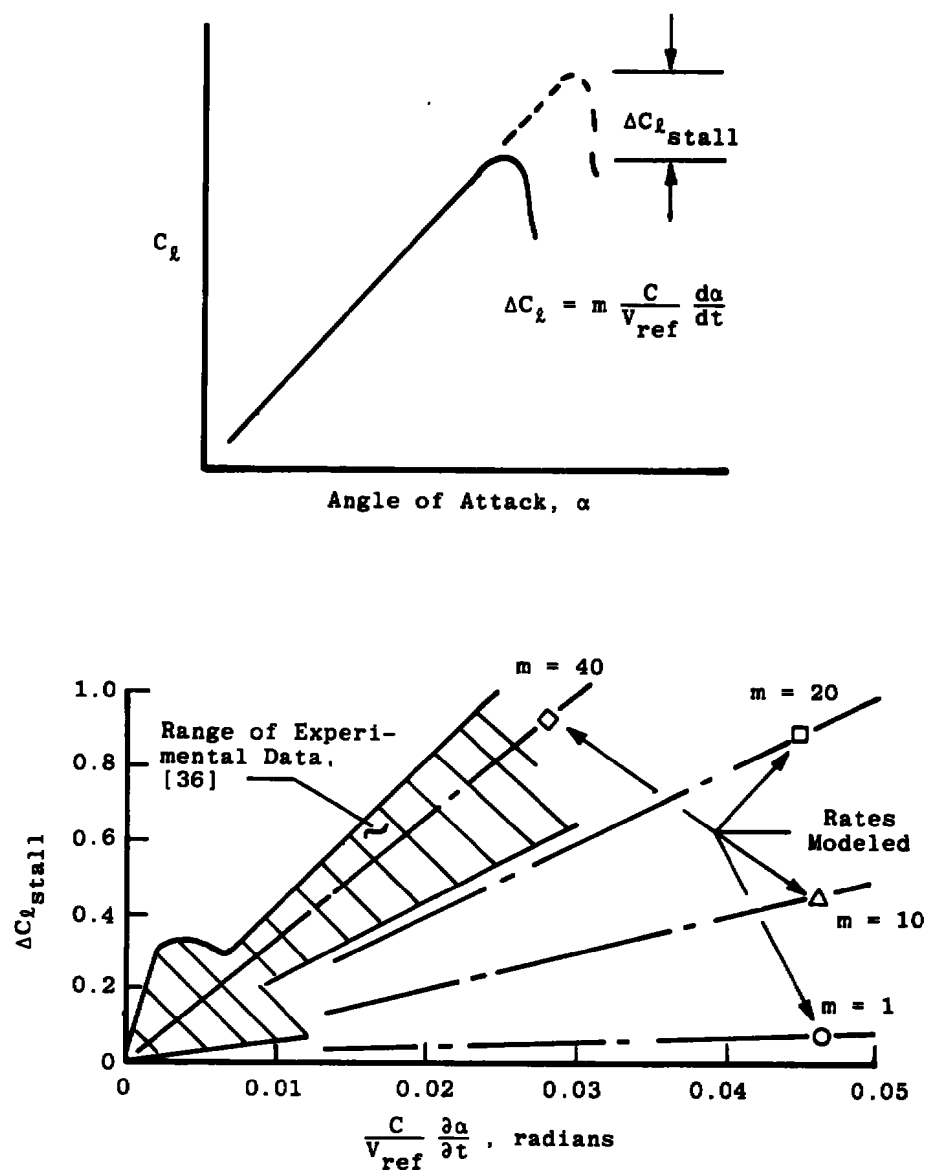
c. Unsteady stall effects

Figure 39.   (Continued).
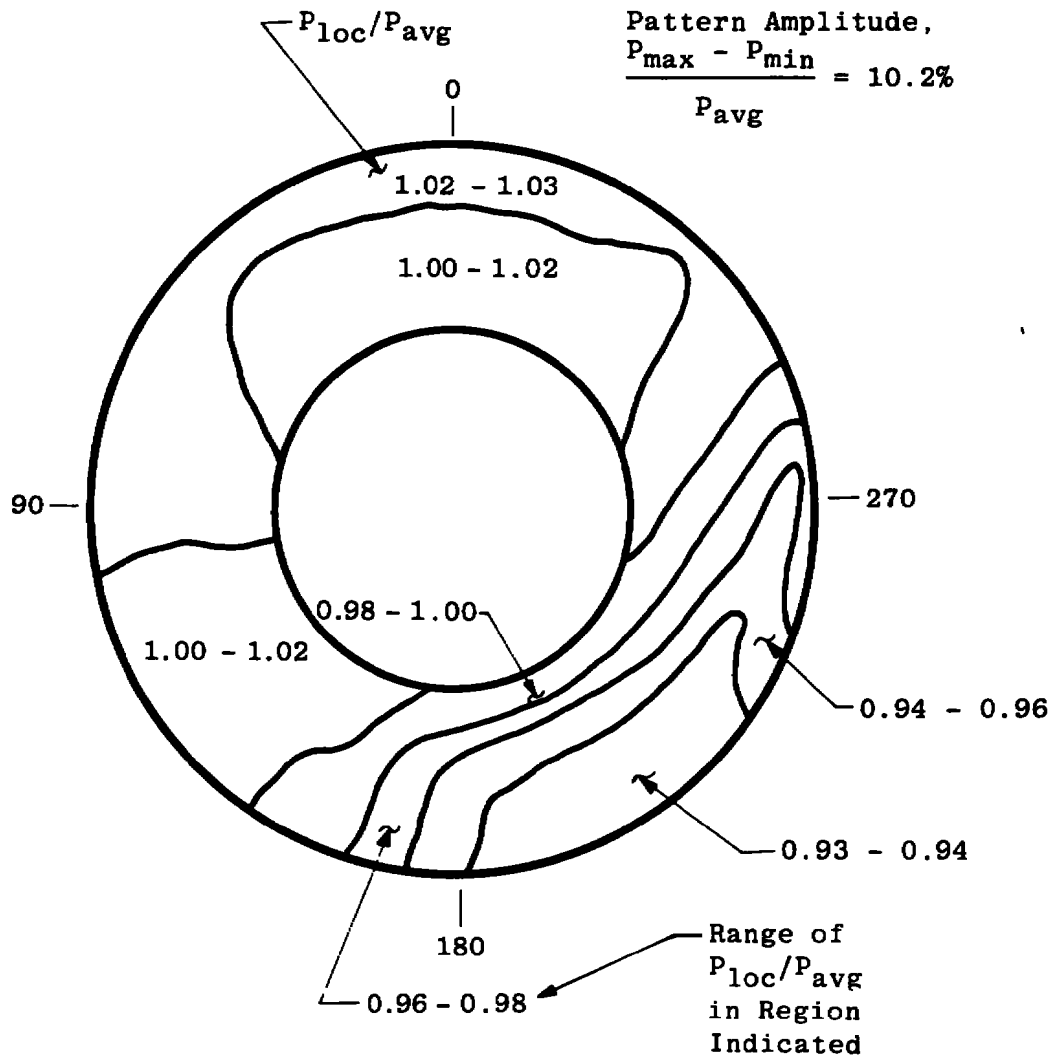
Figure 40. Compressor entry total pressure distribution for combined distortion pattern.
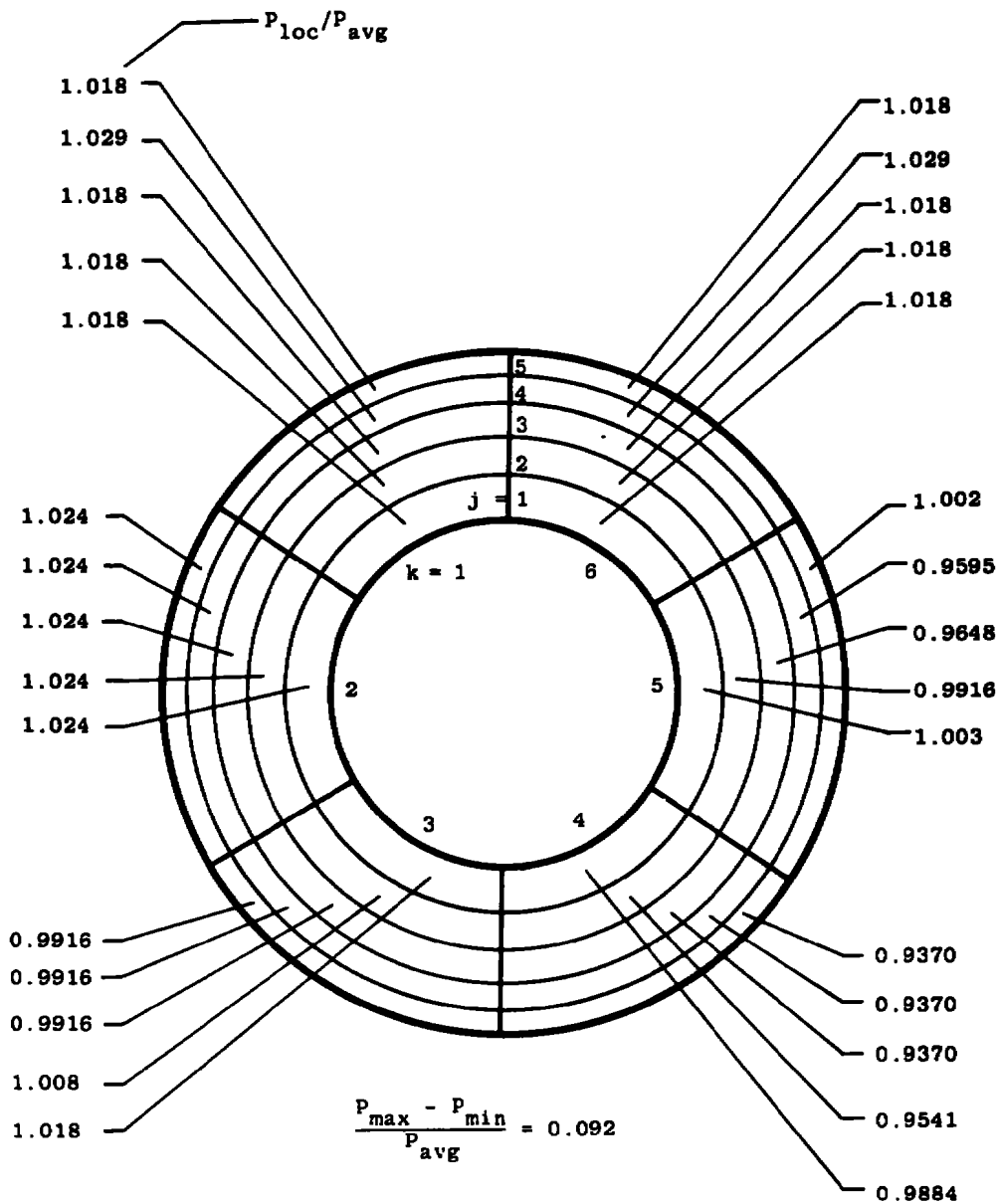
Figure 41.   Compressor entry pressure input values for combined distortion pattern.
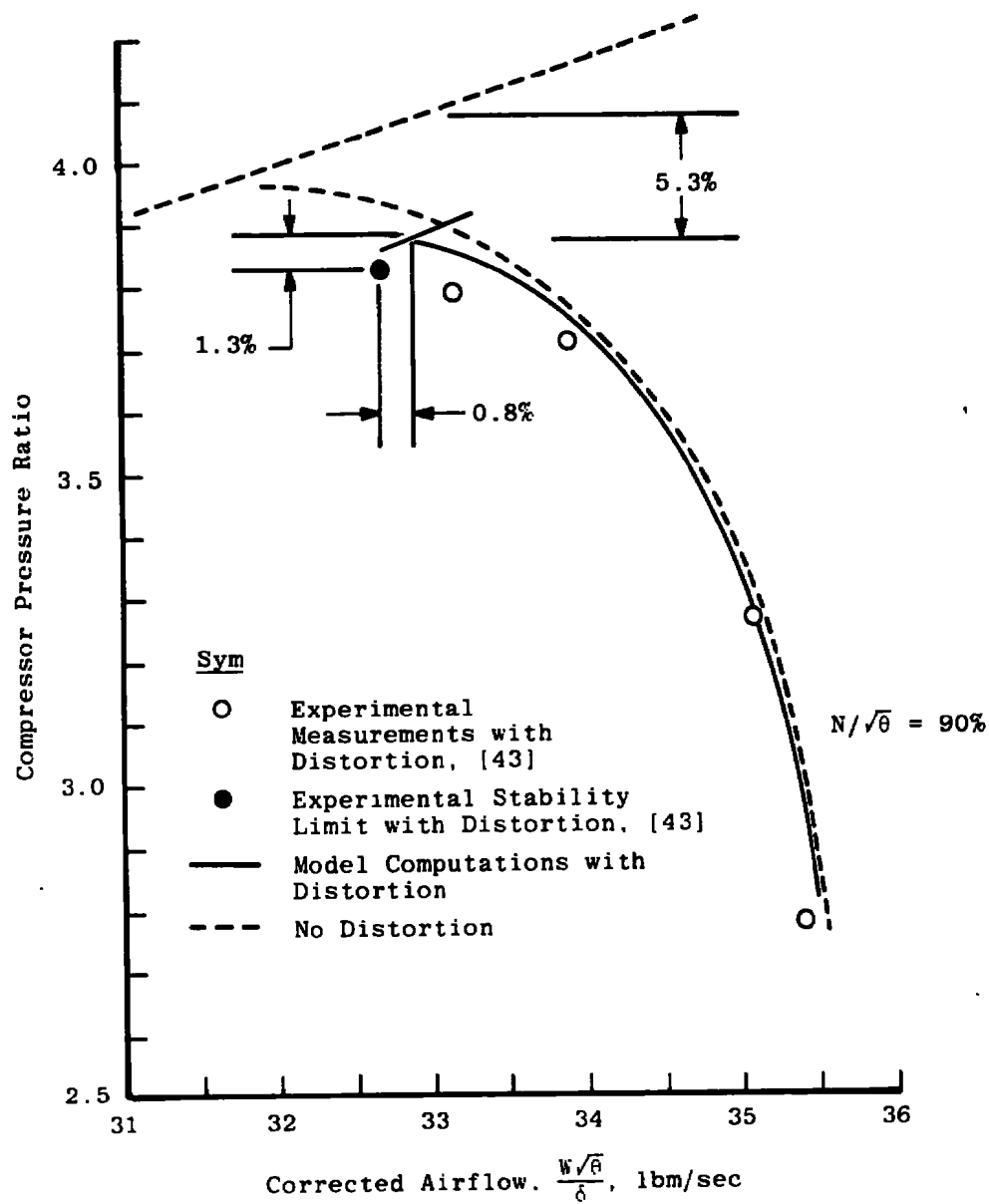
Figure 42. Comparison of computed and experimental
stability limits with combined distortion
pattern, XC-1 compressor.
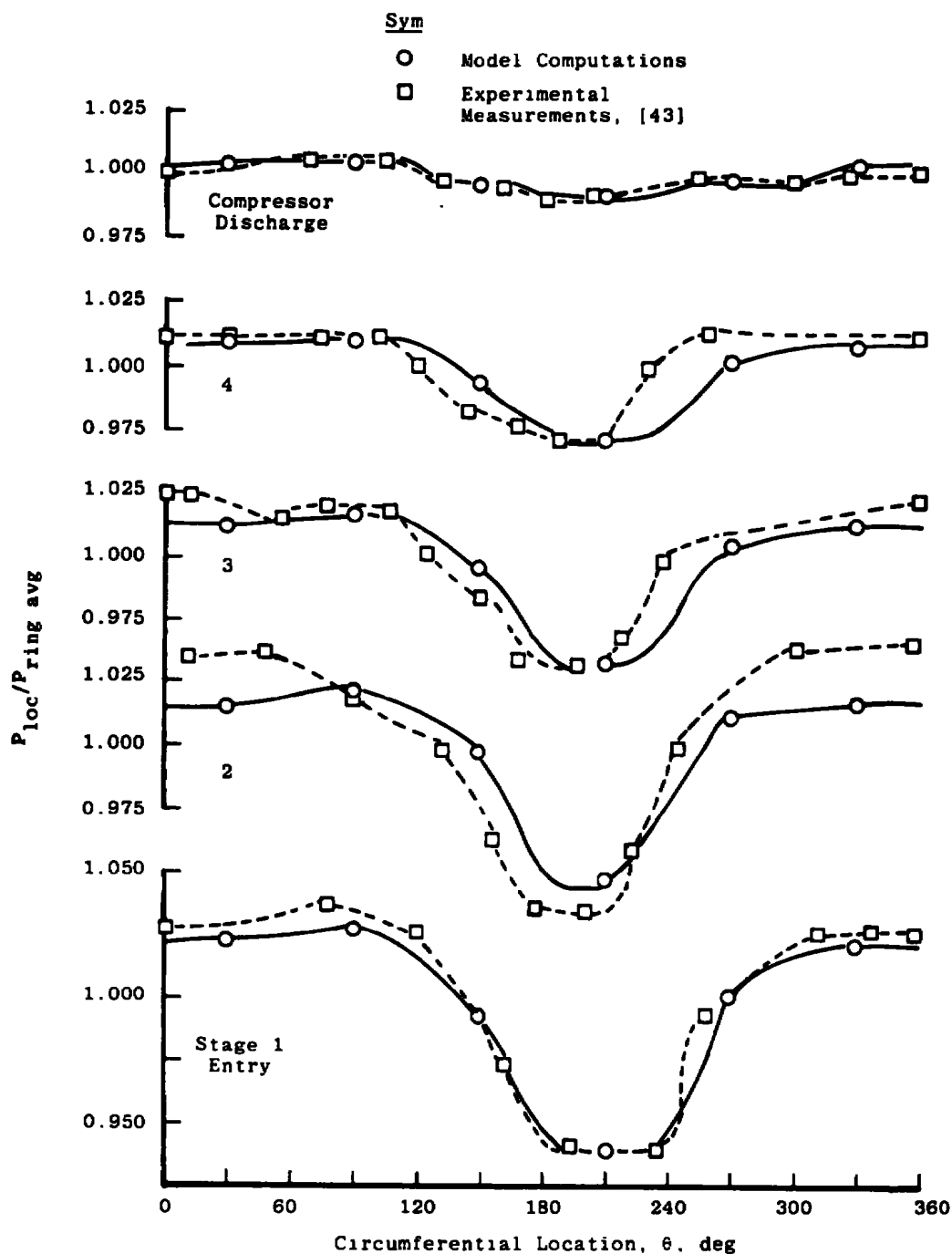
a. Total pressure

Figure 43. Circumferential profiles in tip region with
combined distortion pattern, XC-1 compressor.
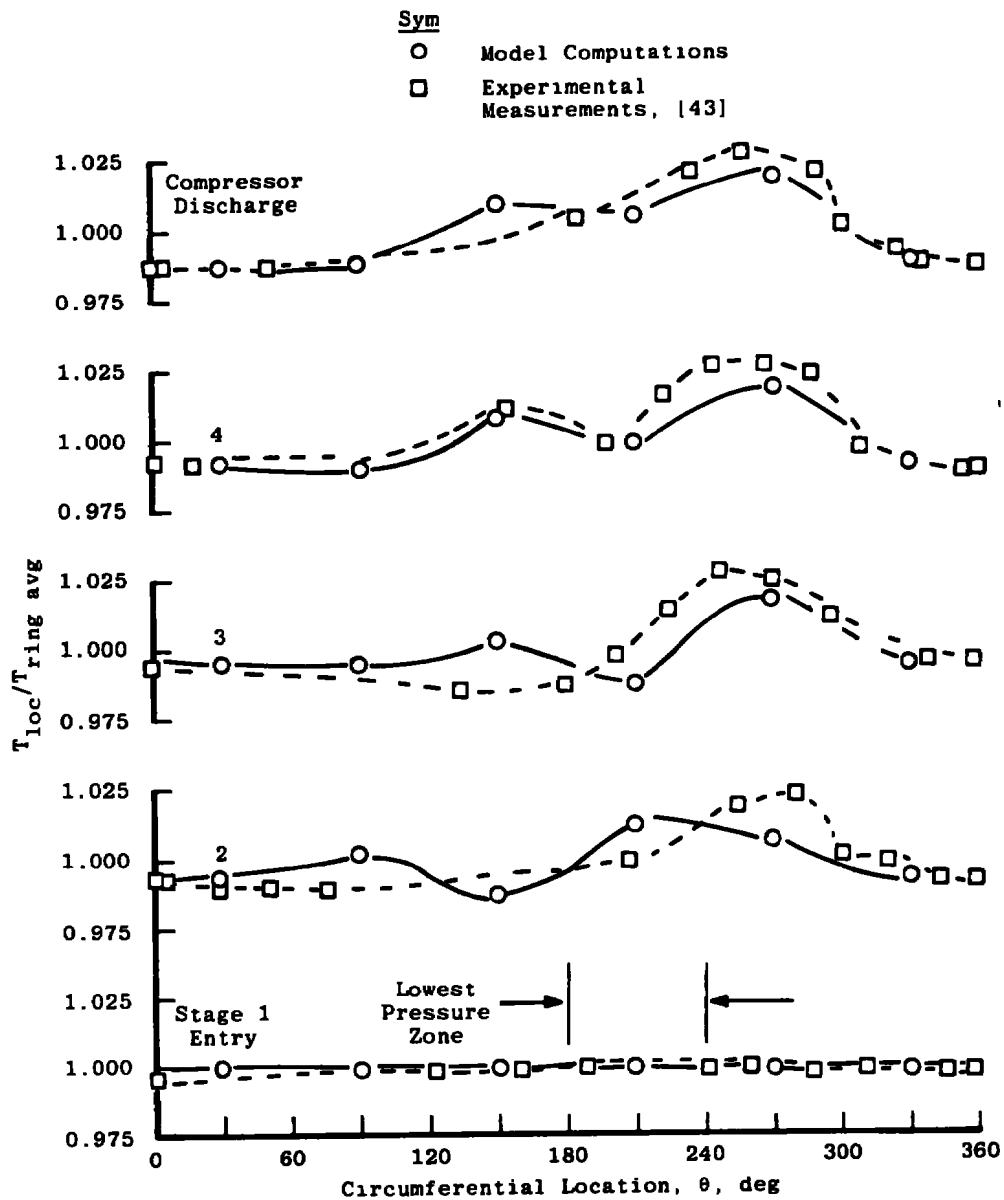
b. Total temperature

Figure 43. (Continued).
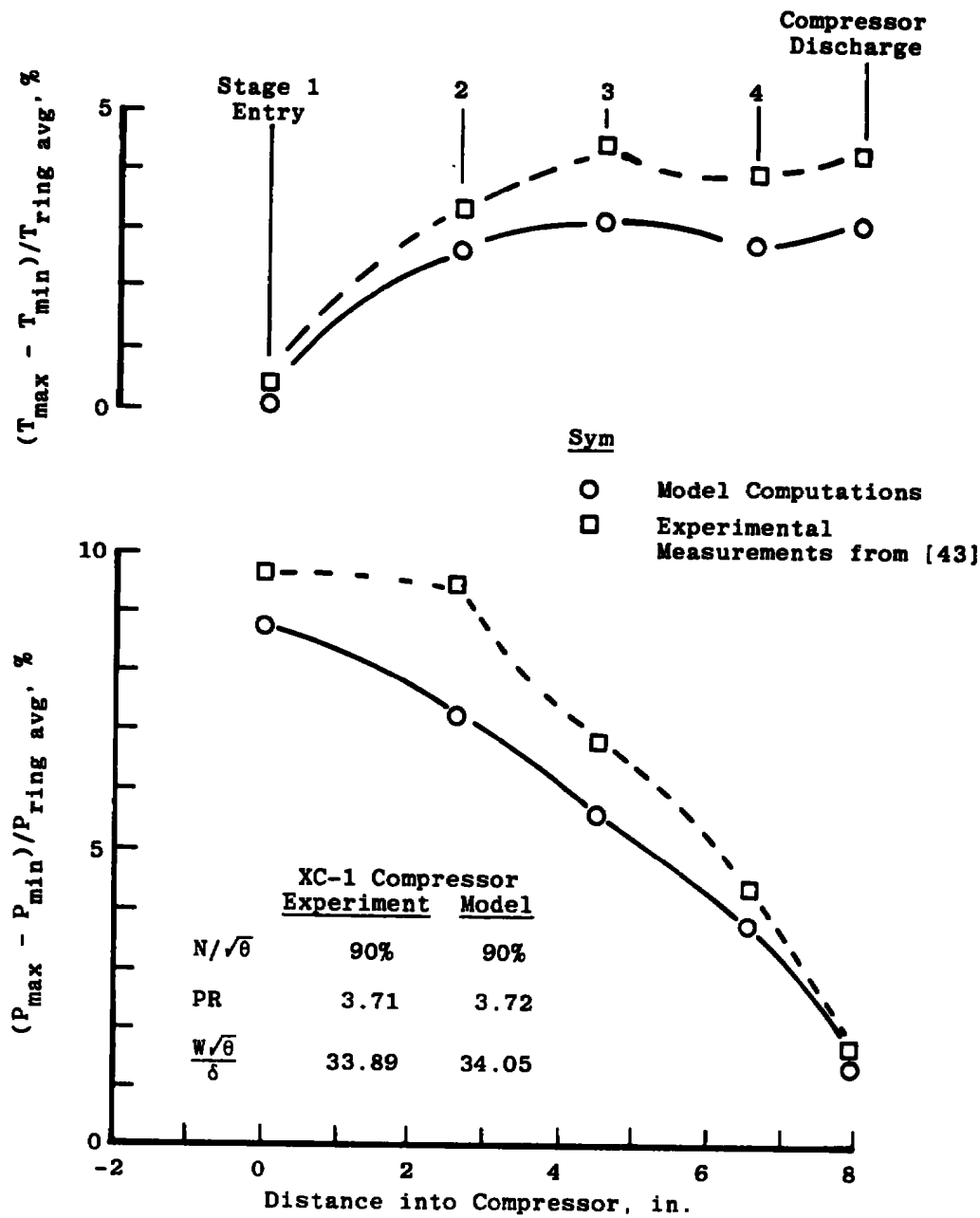
a. Tip region

Figure 44. Comparison of computed and measured circumfer-
ential distortion attenuation for combined
pattern.
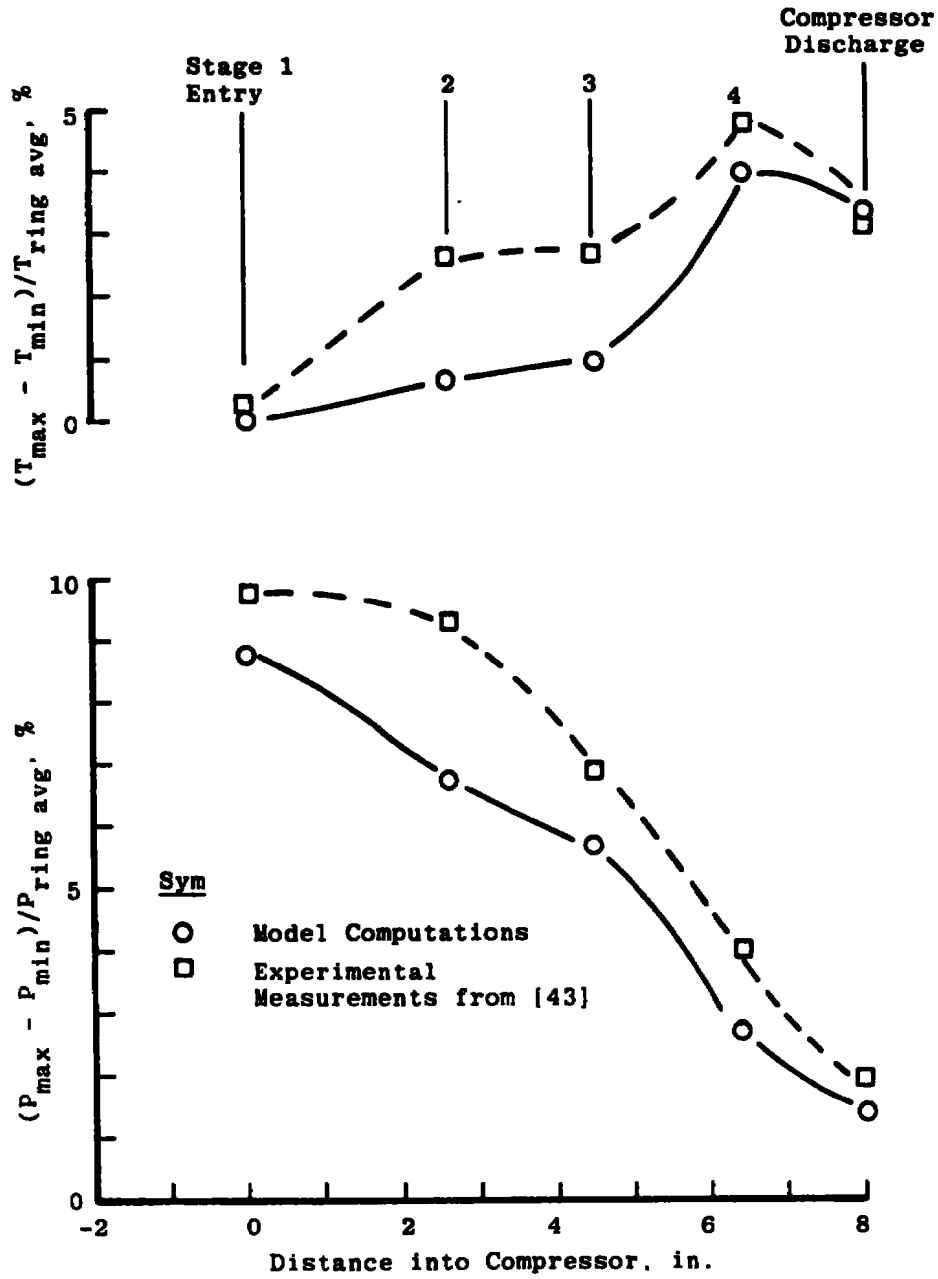
b. Mid-span region

Figure 44. (Continued).
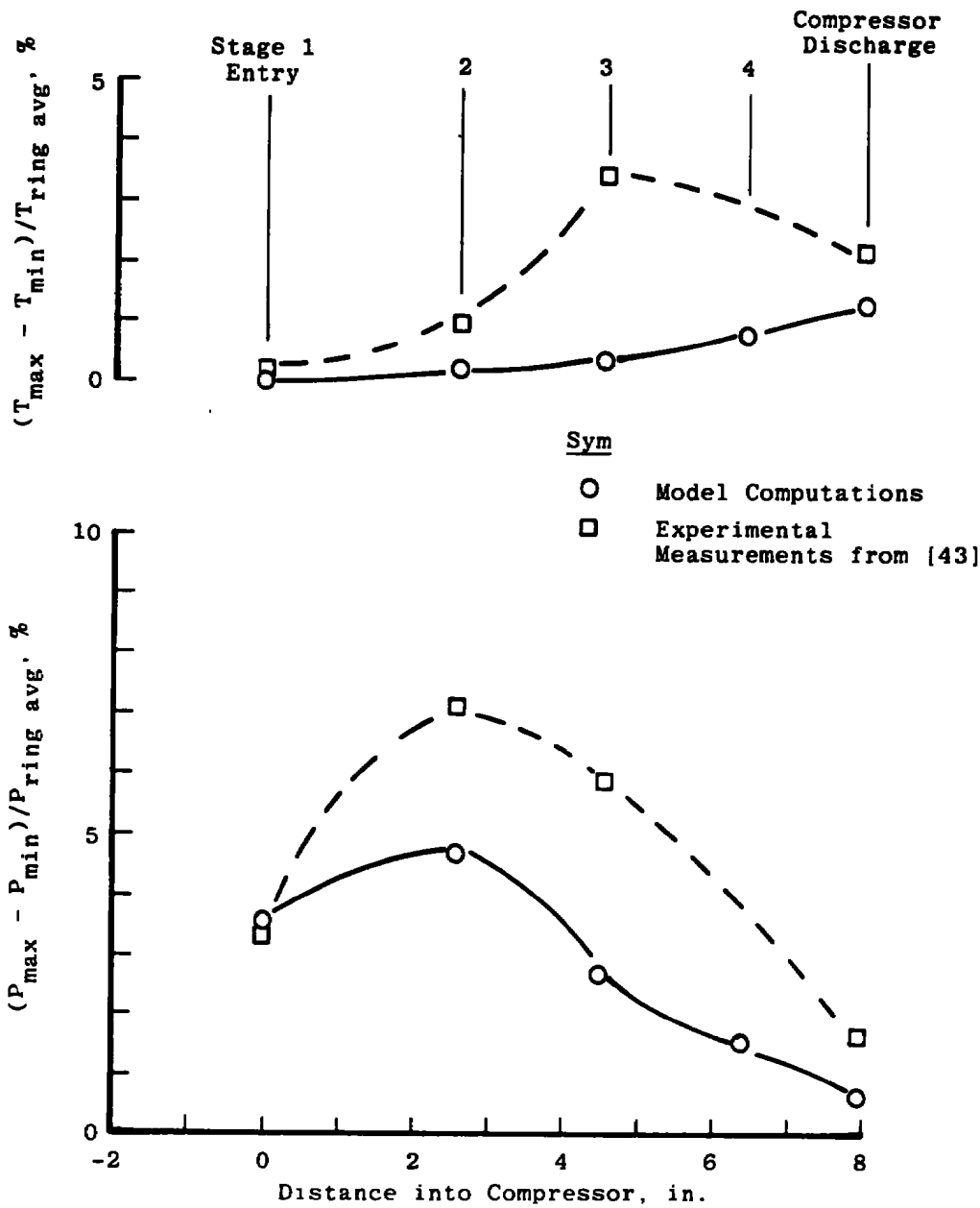
c. Hub region

Figure 44. (Continued).
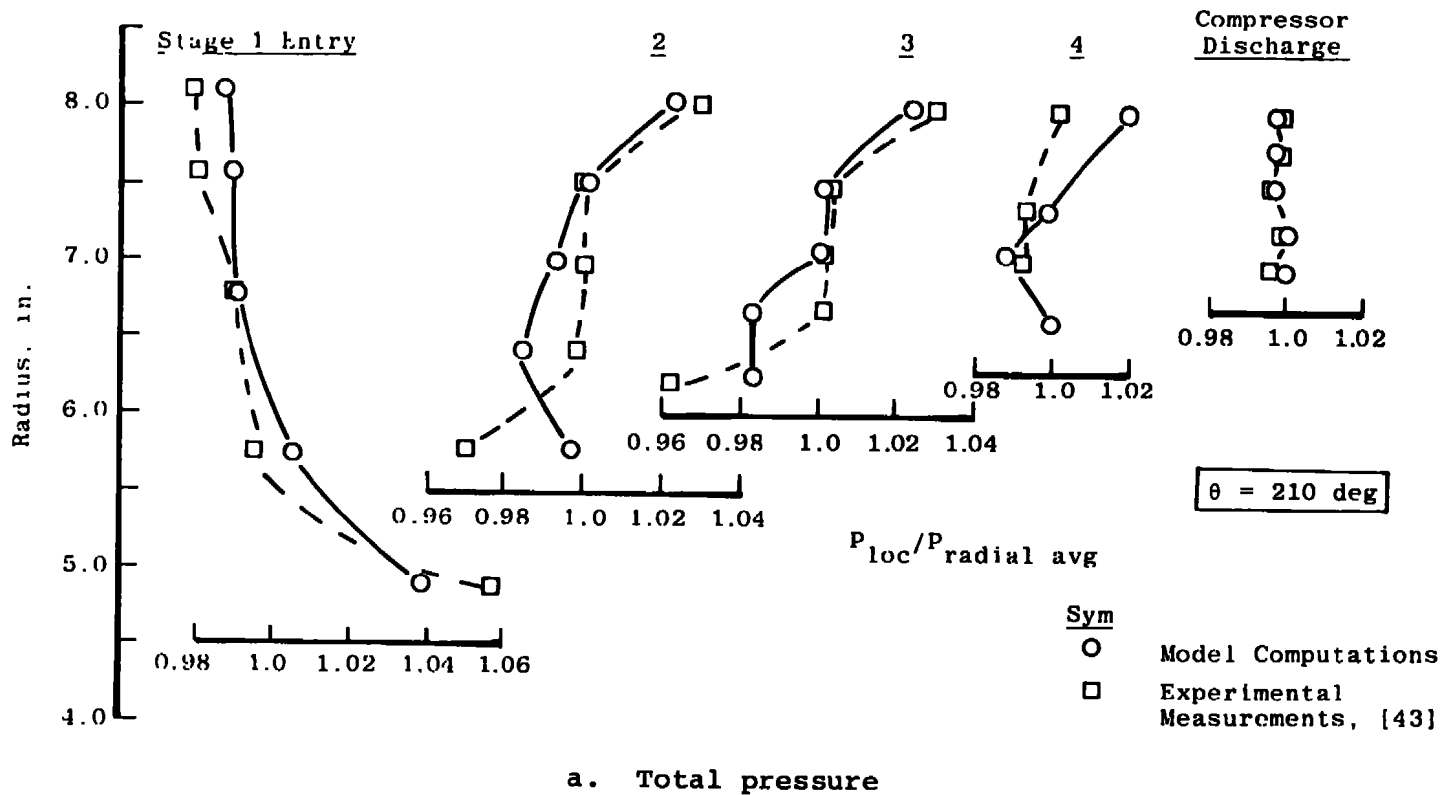
a. Total pressure

Figure 45. Radial profiles with combined distortion pattern.
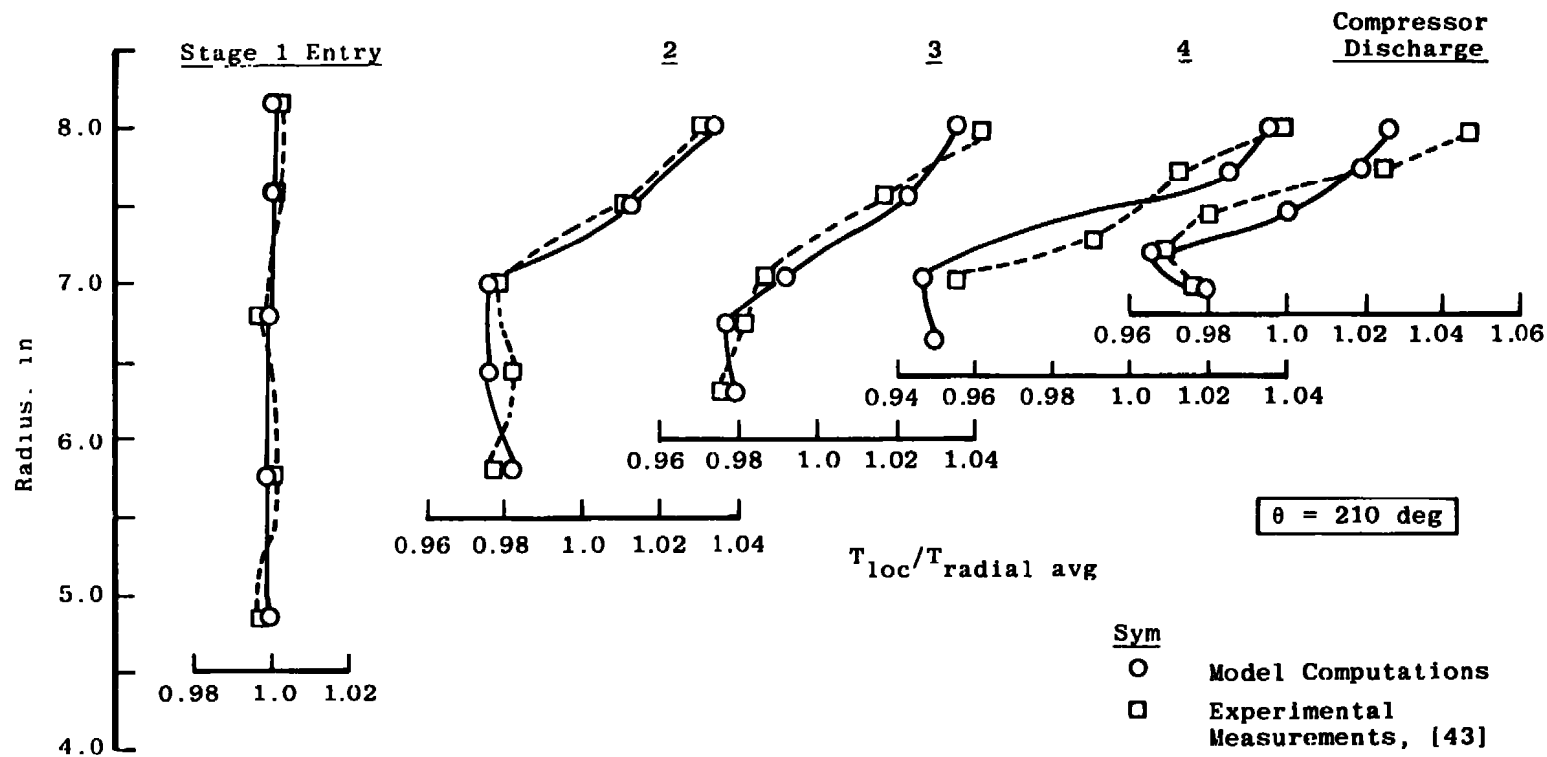
b. Total temperature

Figure 45. (Continued).

Stage 1 Entry   2   3   4   Compressor Discharge

Radius in.

8.0

7.0

6.0

5.0

4.0

0.98 1.0 1.02 1.04 1.06

0.96 0.98 1.0 1.02 1.04

0.96 0.98 1.0 1.02 1.04

0.98 1.0 1.02

0.98 1.0 1.02

$P_{loc}/P_{radial\ avg}$

Sym

O   Model Computations

□   Experimental Measurements, [43]
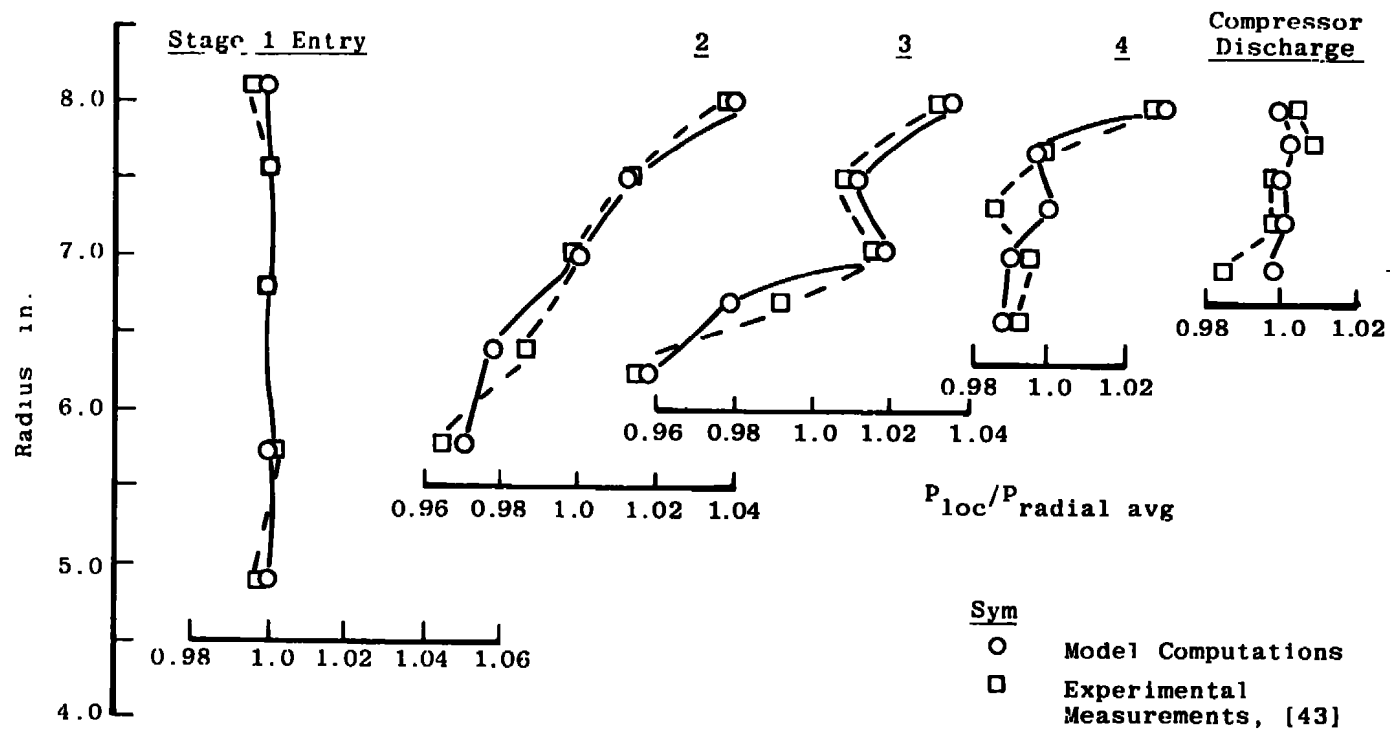
a.   Total pressure

Figure 46.   Radial profiles with uniform entry flow.
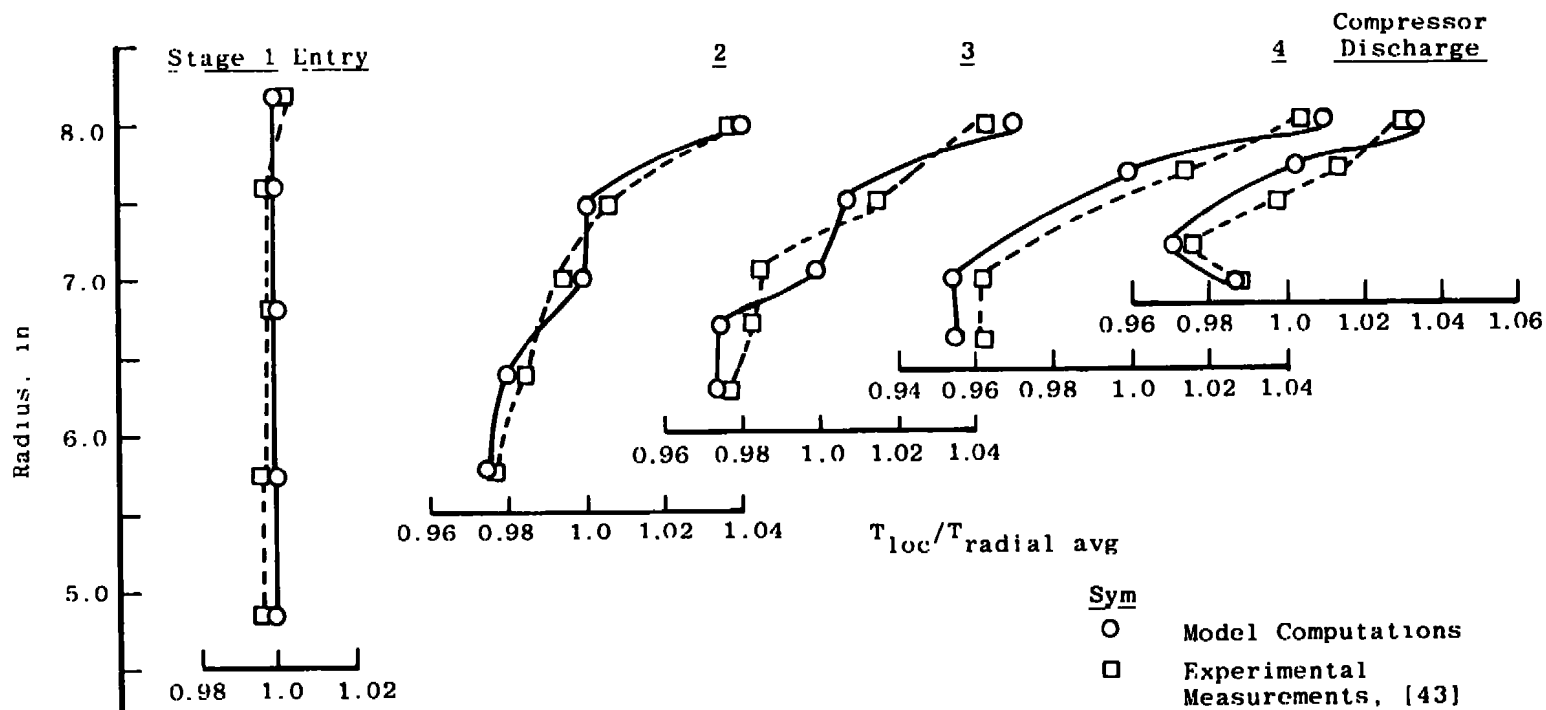
b.   Total temperature

Figure 46.   (Continued).

1.16 - 1.20

1.08 - 1.16

1.04 - 1.08

1.02 - 1.04

1.01 - 1.02

1.00 - 1.01

ϕ/ϕ_{stall}
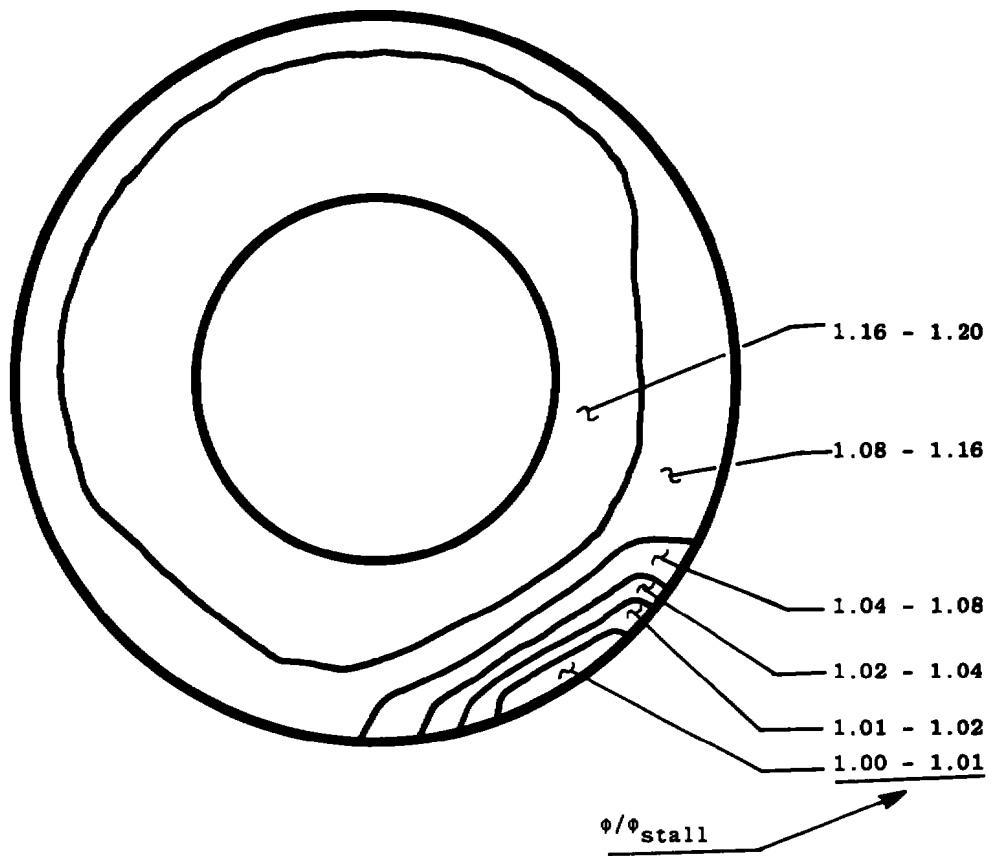
a.   Stage 1

Figure 47.   Flow coefficient distribution just prior to
instability with combined distortion pattern.

217
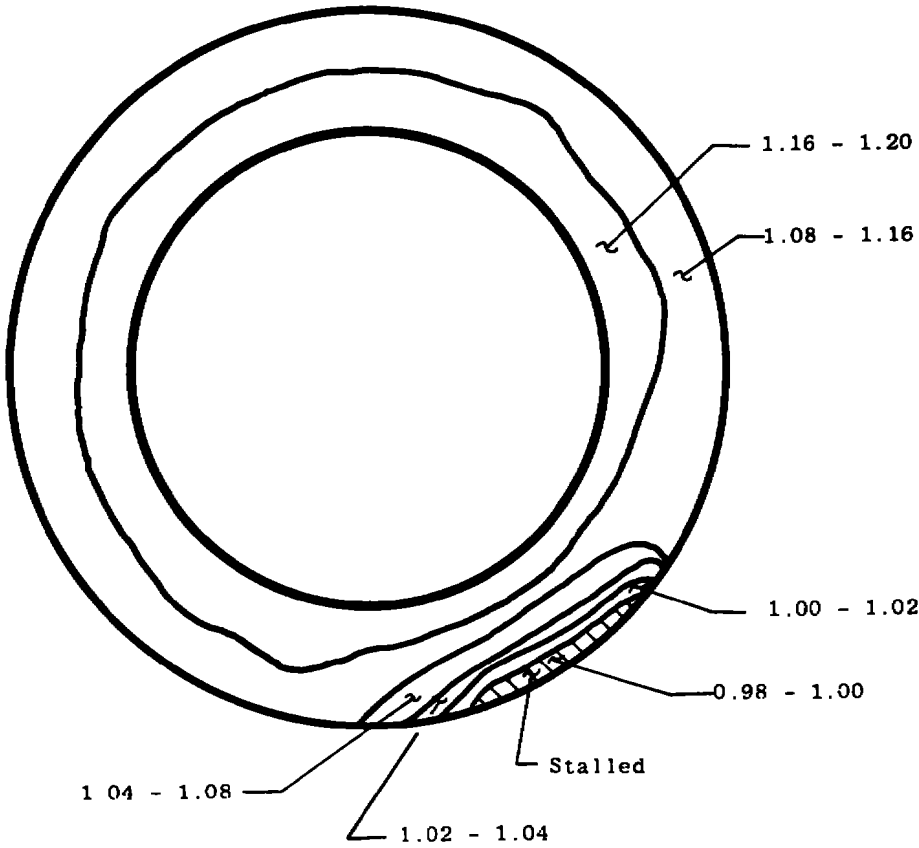
b. Stage 2

Figure 47. (Continued).

1.16 - 1.20

1.08 - 1.16

1.04 - 1.08

1.02 - 1.04
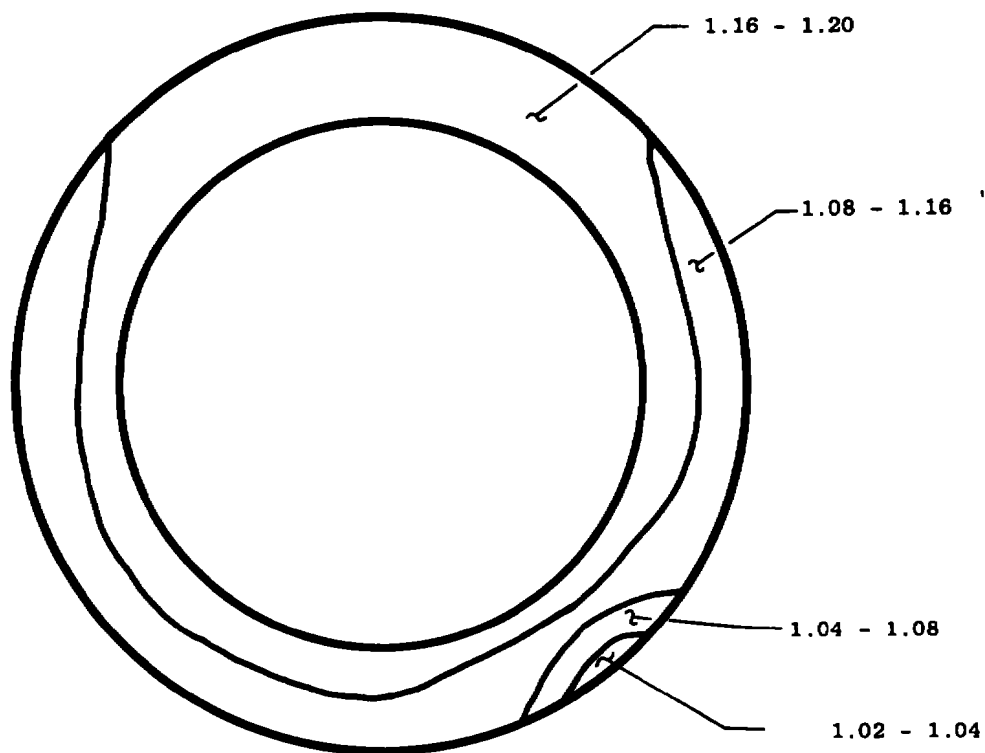
c.   Stage 3

Figure 47.   (Continued).
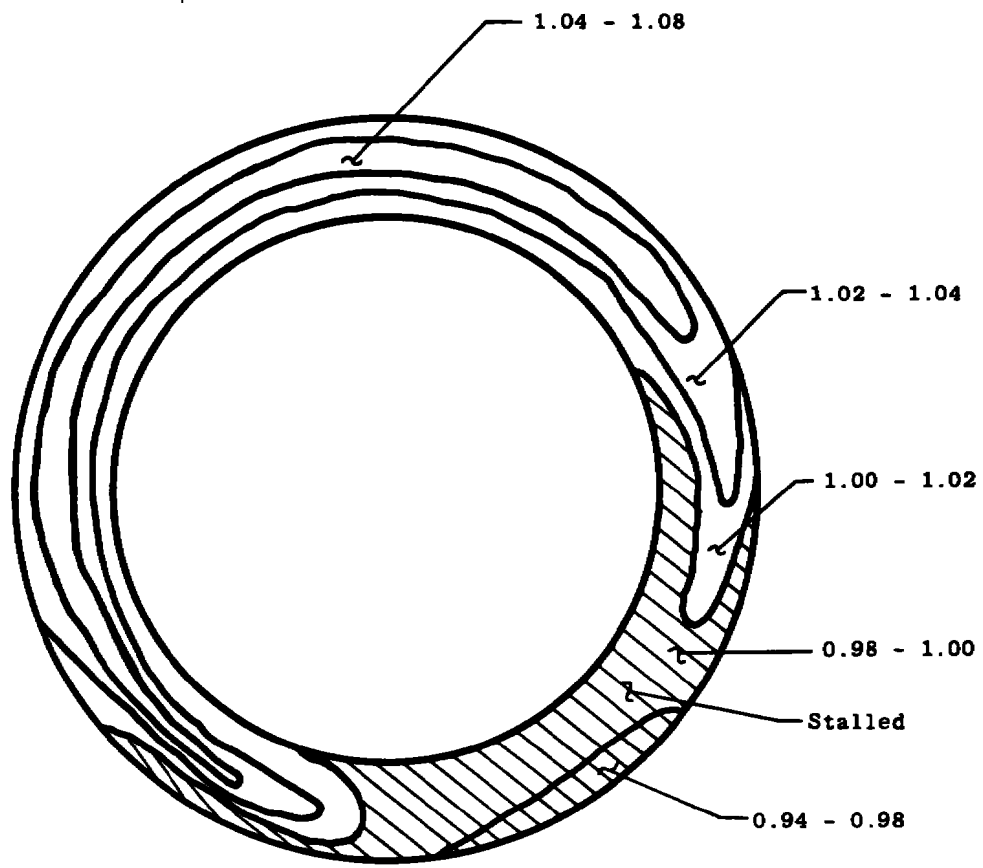
d.   Stage 4

Figure 47.   (Continued).
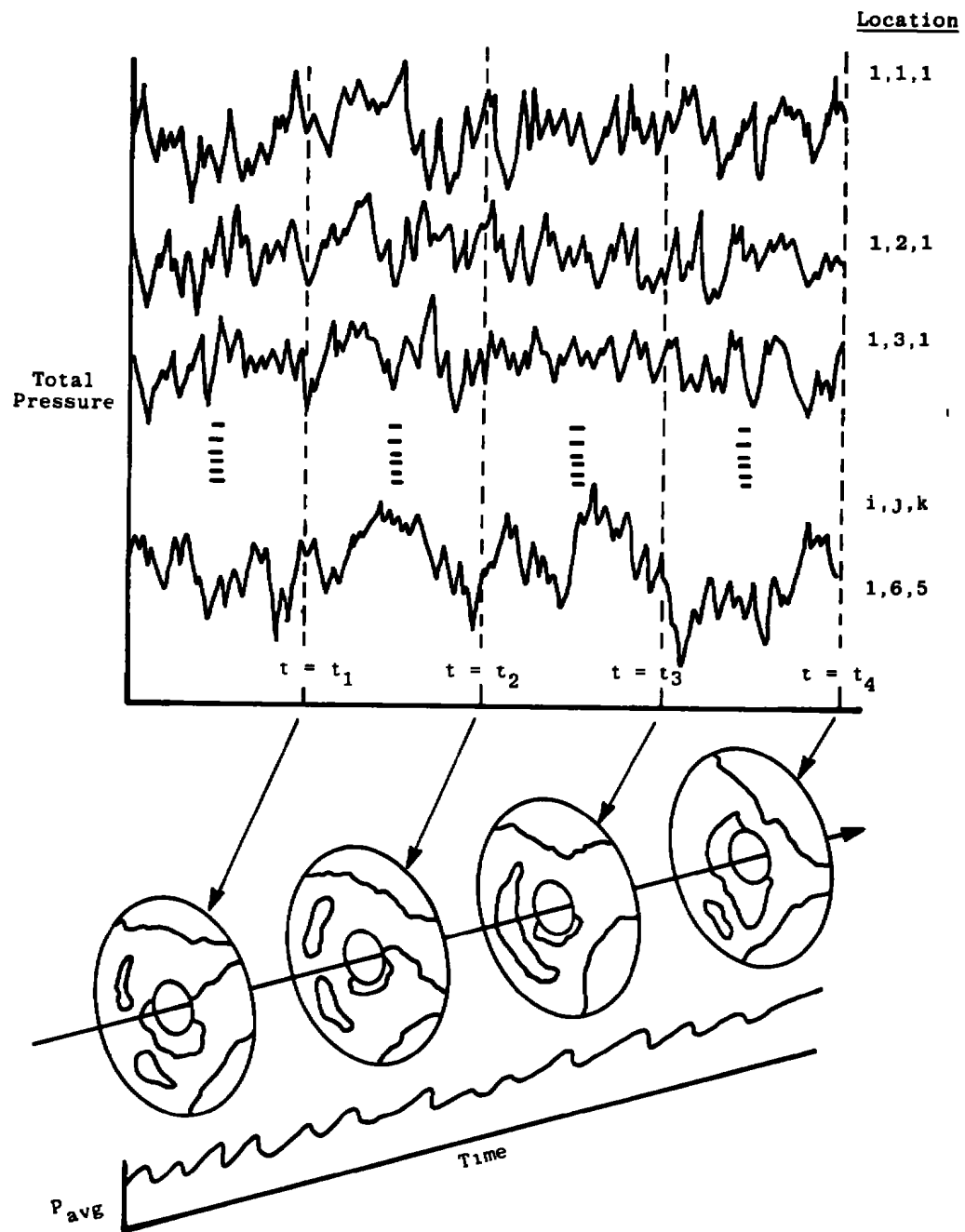
Figure 48. Time-variant distortion.
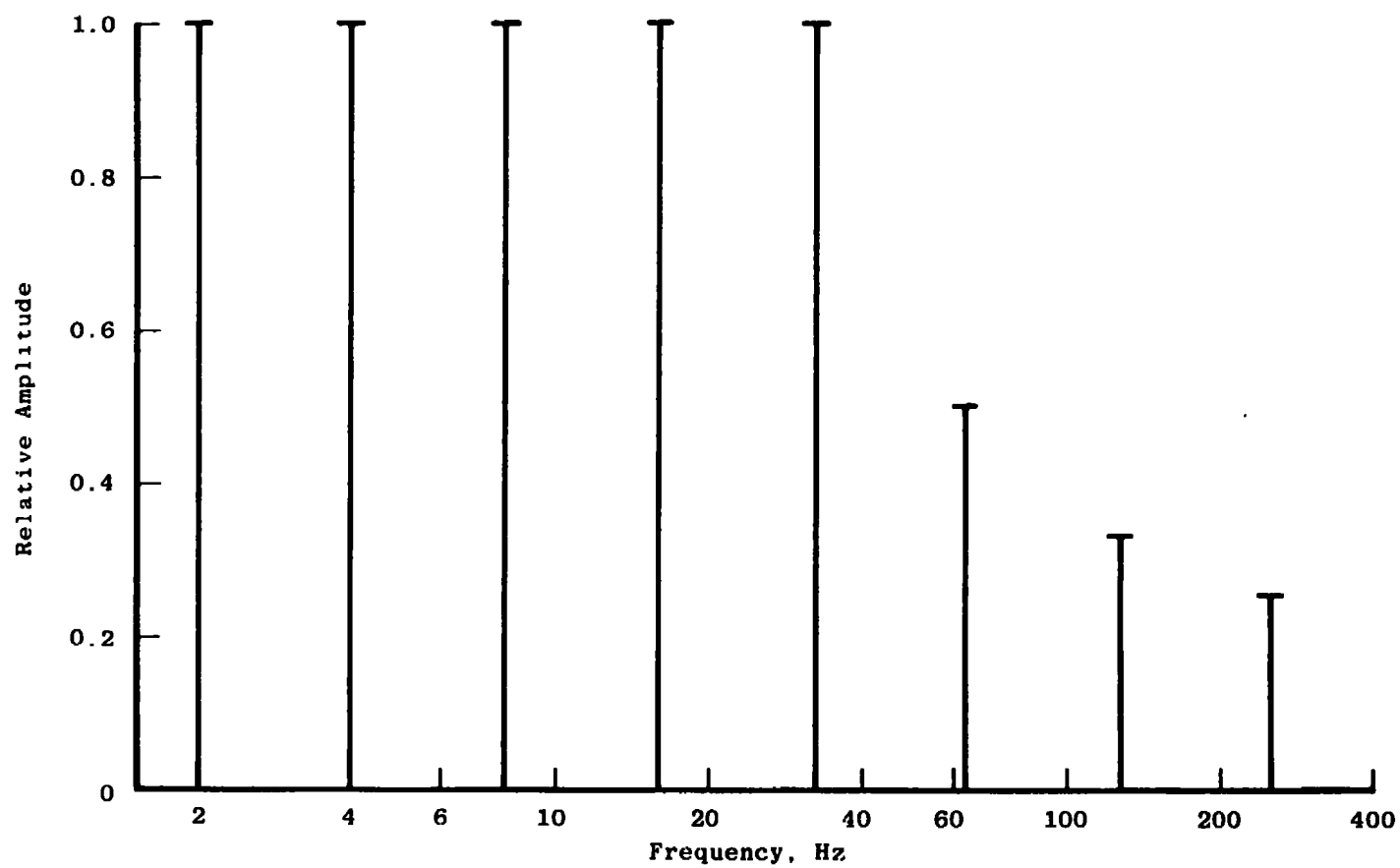
Figure 49. Relative frequency spectrum for time-variant distortion pattern.
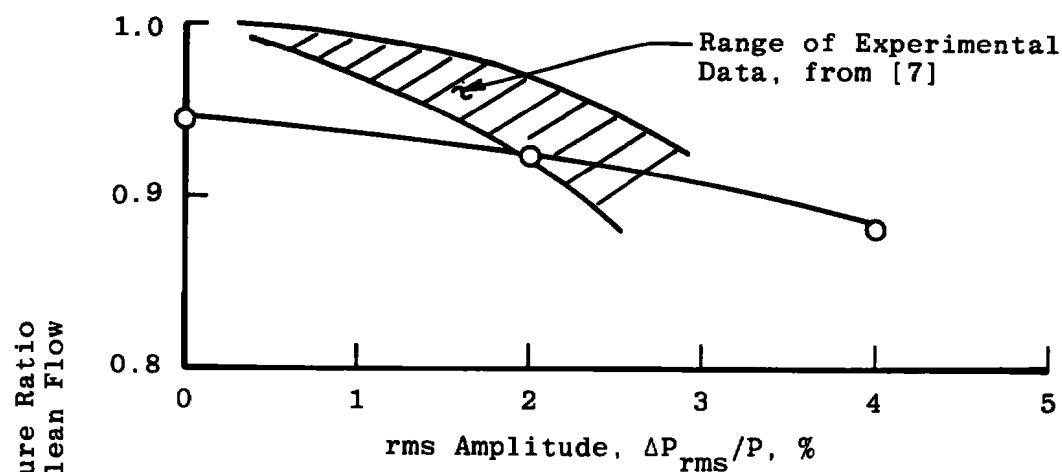
a. Correlation with fluctuation amplitude
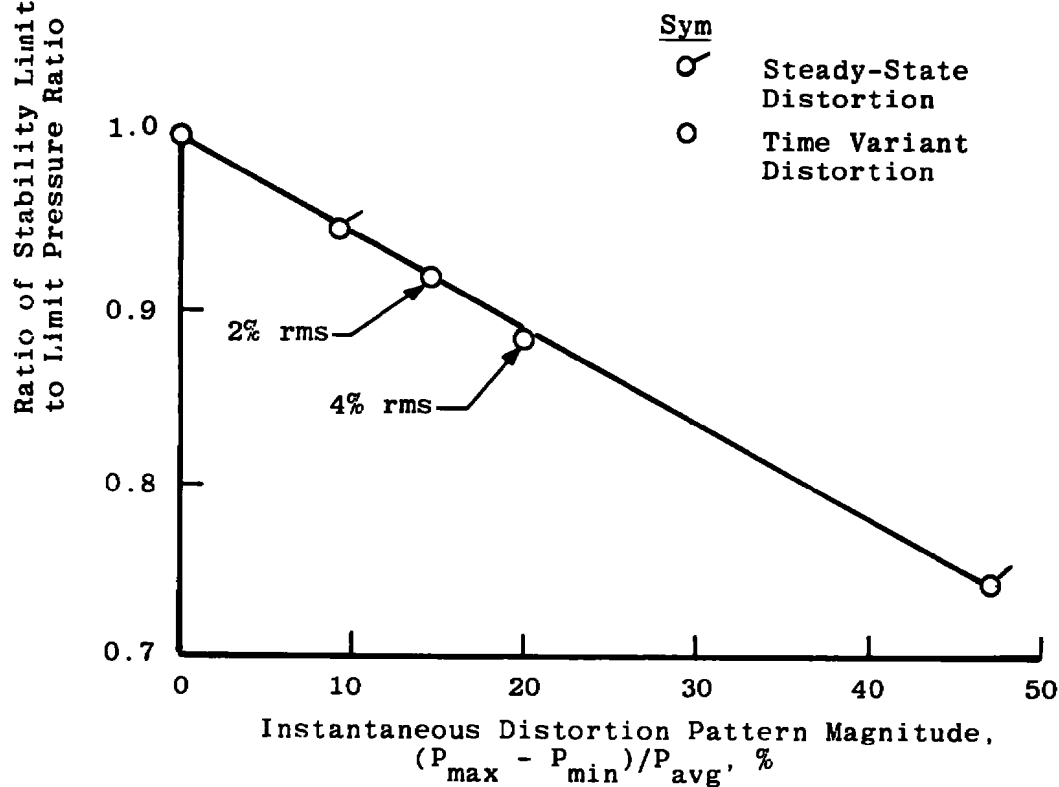
b. Correlation with instantaneous distortion magnitude

Figure 50. Loss in stability limit pressure ratio with time-variant distortion
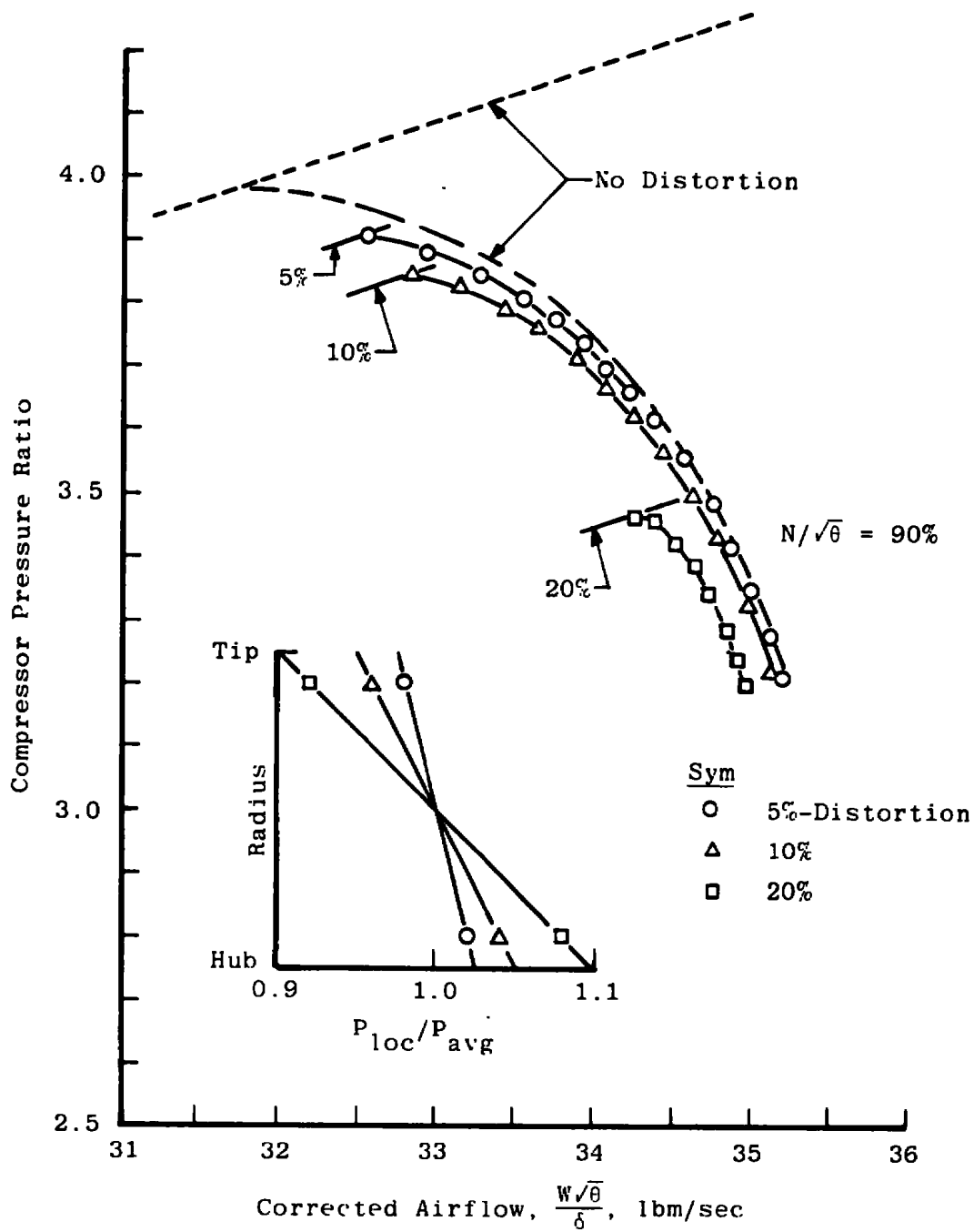
a. Tip radial distortion

Figure 51. Computed radial distortion influences on stability.
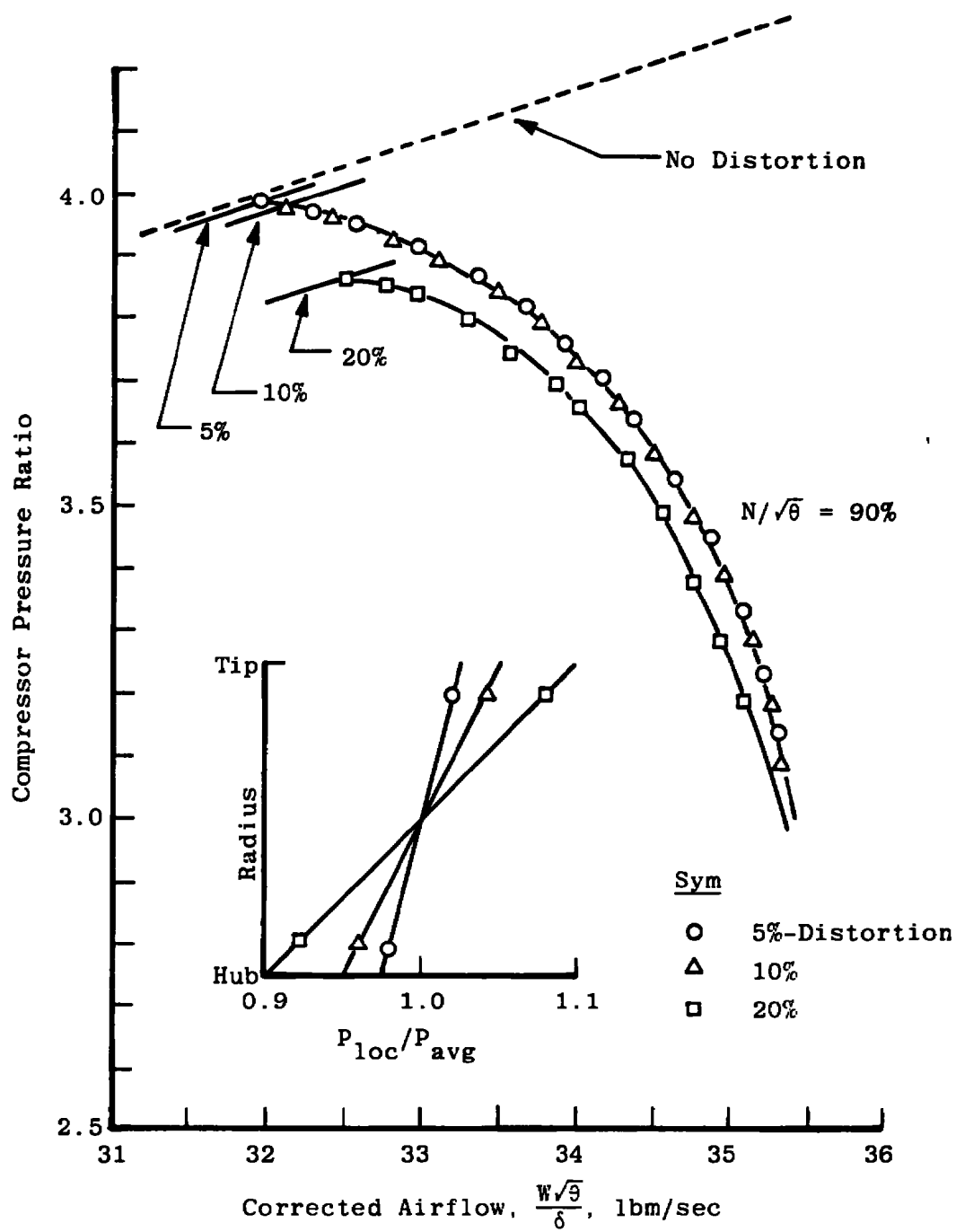
b. Hub radial distortion

Figure 51. (Continued).

Figure 52. Comparison of radial distortion model compu-
tations with experimental results.
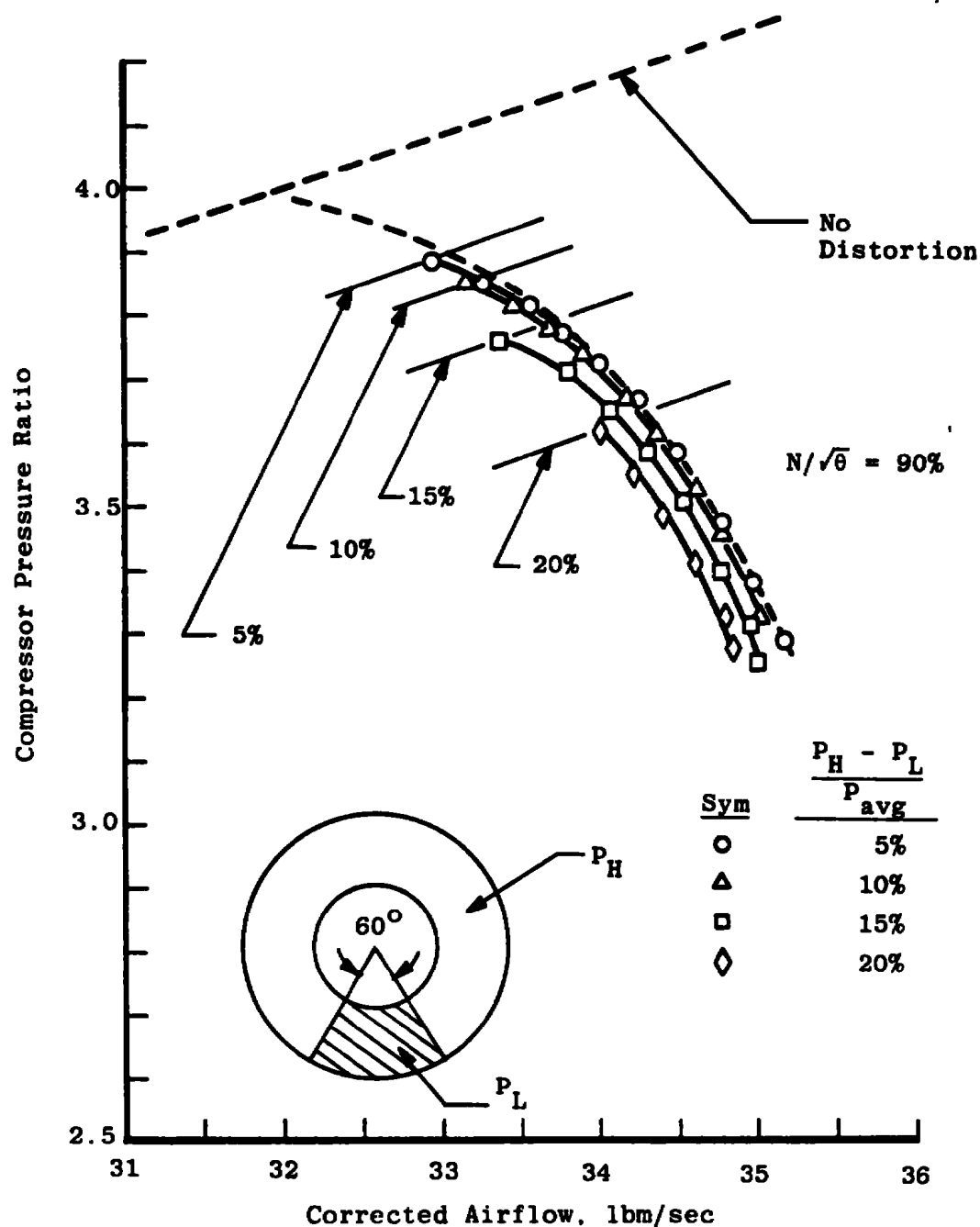
Figure 53. Model computed influence of circumferential
pressure distortion on stability,
XC-1 compressor.
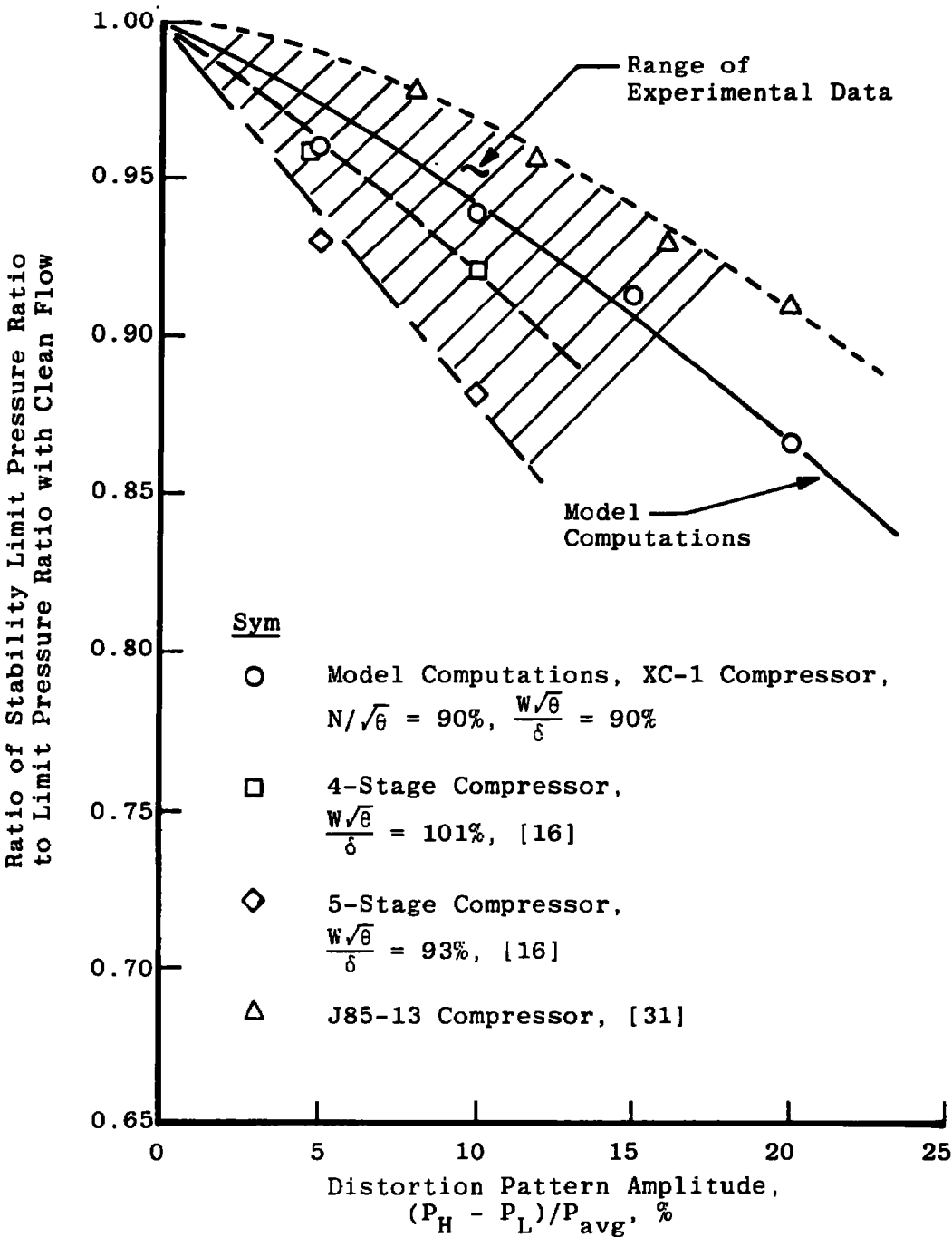
Figure 54. Comparison of circumferential distortion model computations with experimental results.
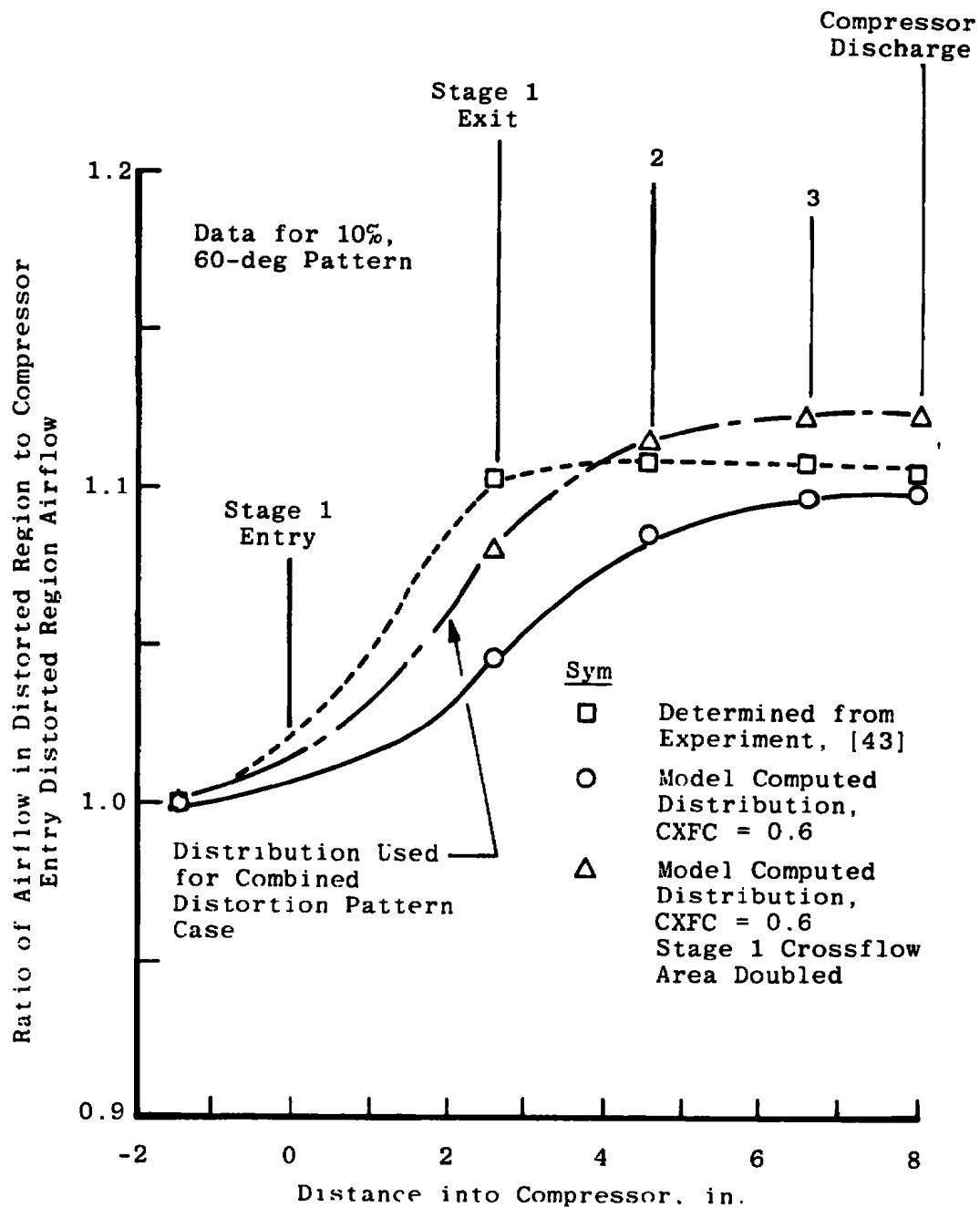
a. Circumferential crossflow distribution

Figure 55. Circumferential crossflow magnitudes and
effects.
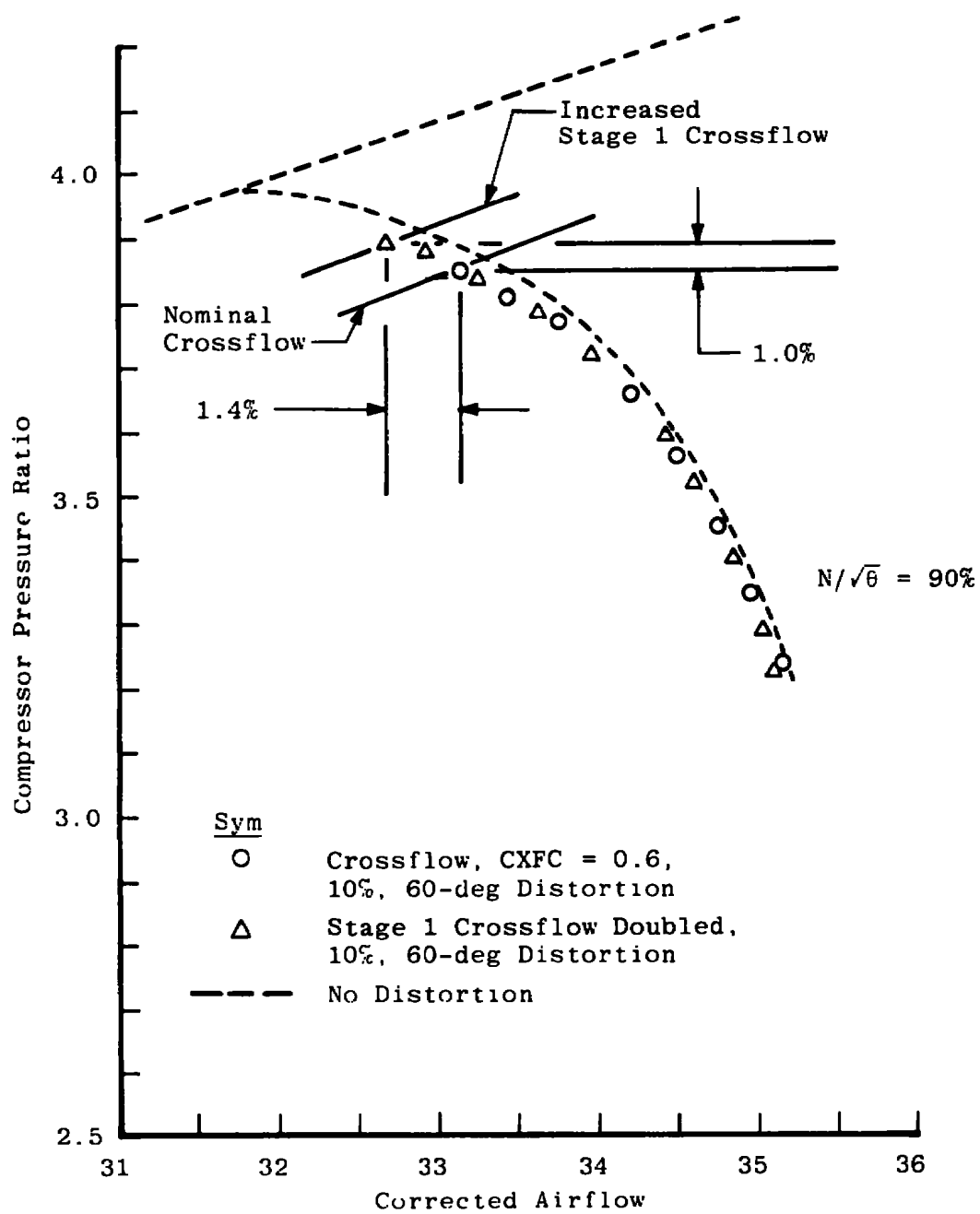
b. Effect on stability limit

Figure 55. (Continued).
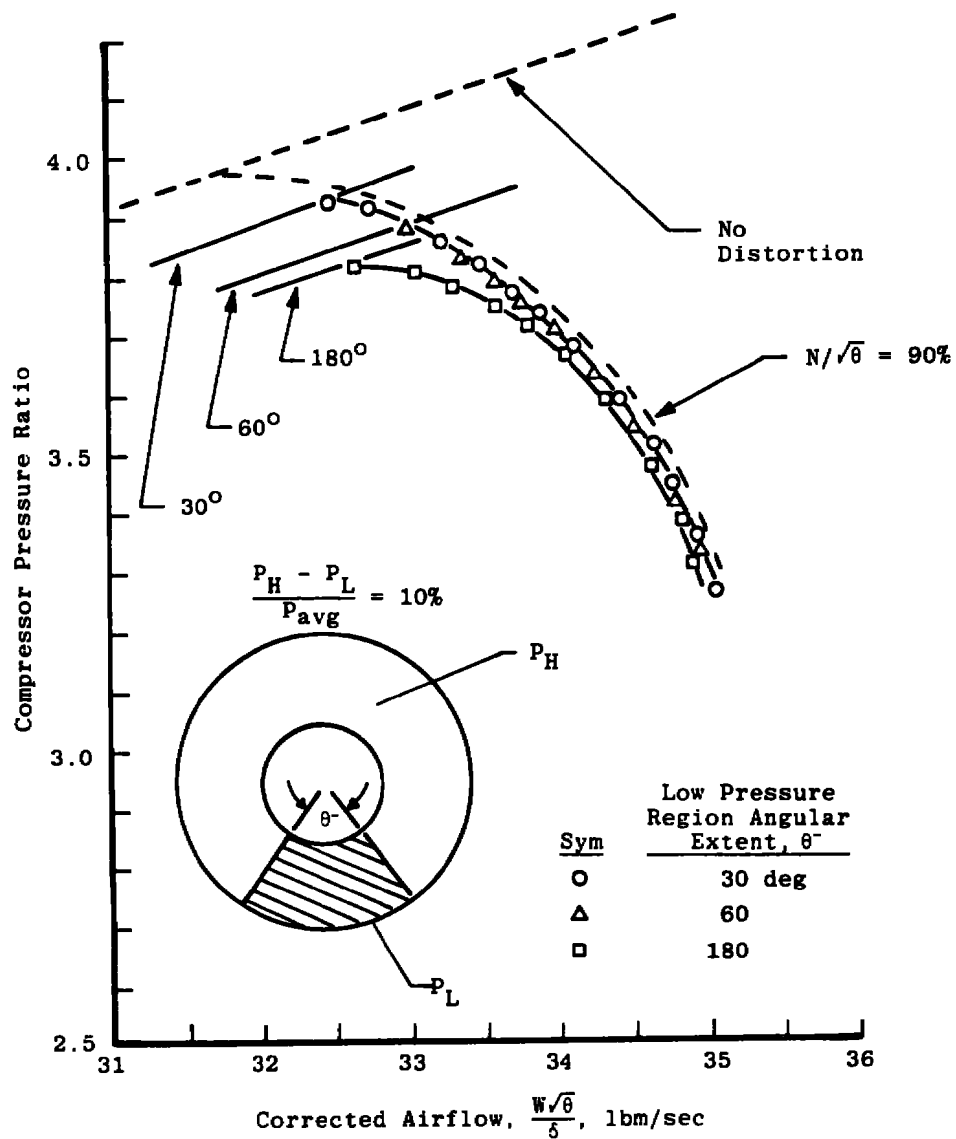
Figure 56. Model computed influence of circumferential distortion angular extent on stability, XC-1 compressor.
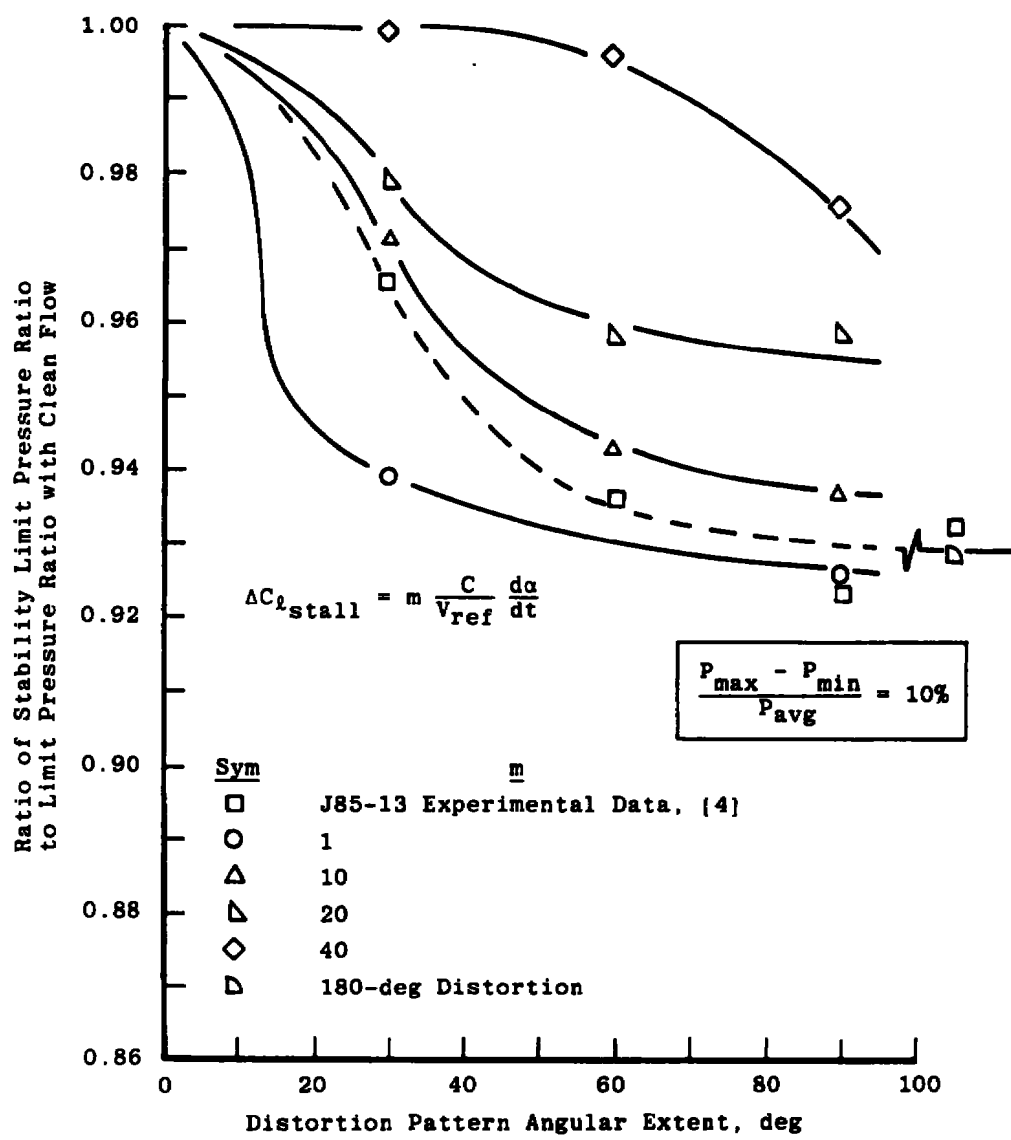
Figure 57.   Effect of unsteady airfoil stall properties
on stability margin.
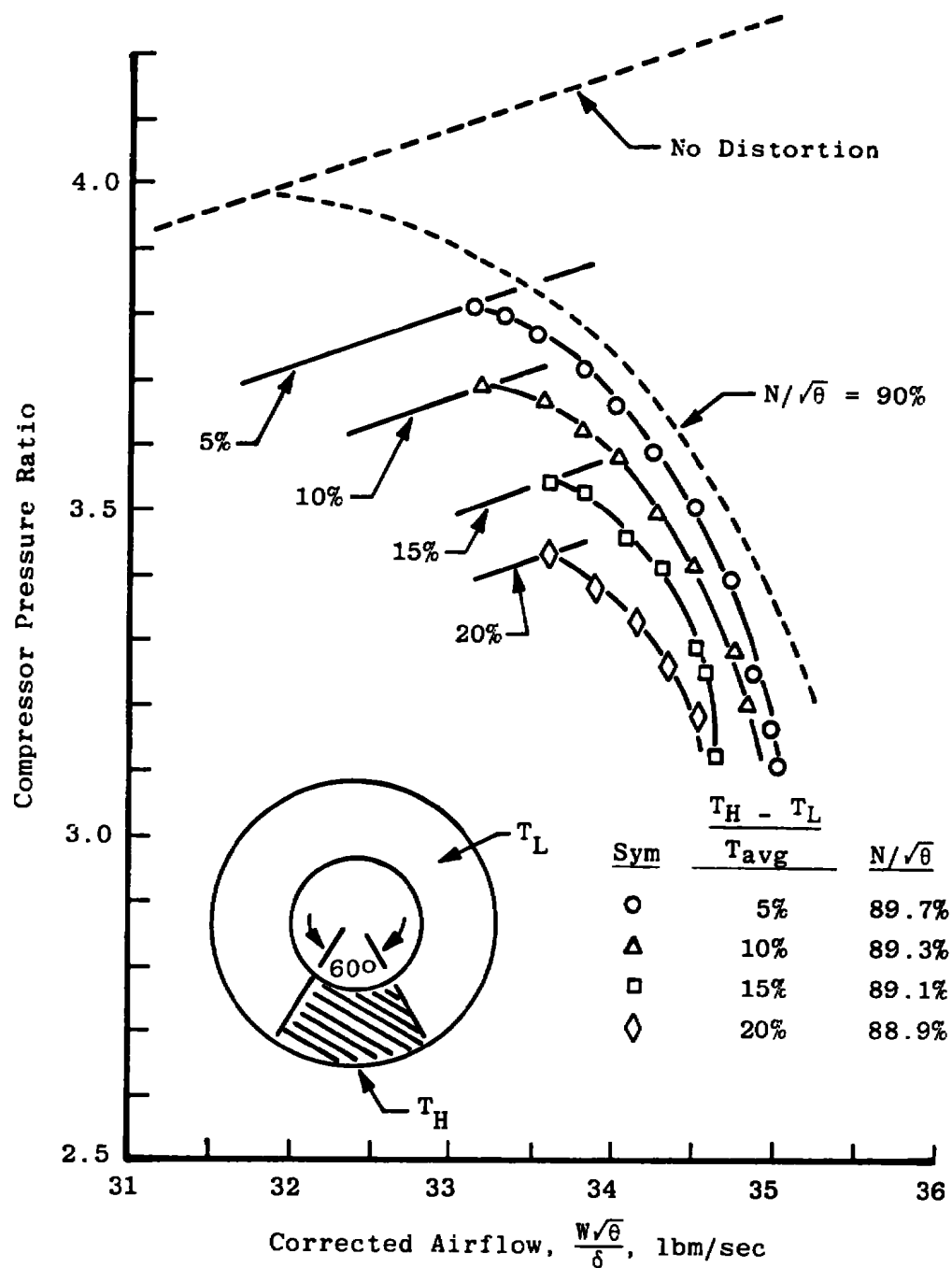
Figure 58. Model computed influence of circumferential temperature distortion on stability, XC-1 compressor.
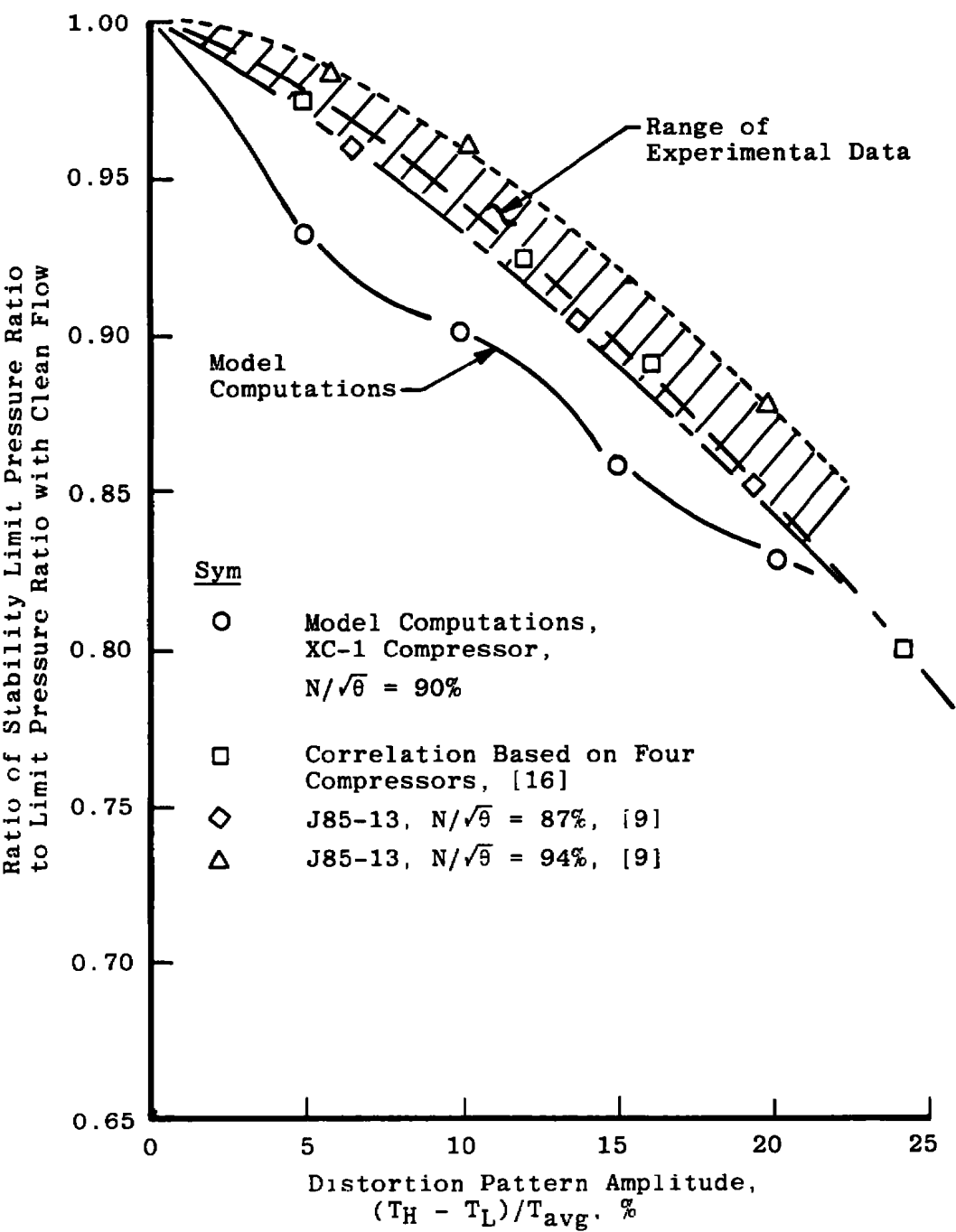
Figure 59.   Comparison of circumferential temperature
             distortion model computations with experimental
             results.

APPENDIX B

COMPRESSOR DETAILS AND STAGE CHARACTERISTICS

Allison XC-1 Compressor

Figure B-1 (Appendix C)[1] shows the overall com-
pressor map for the Allison XC-1 lift engine, four-stage
compressor. Key dimensions and design performance are given
in Table B-1 (Appendix C).[1] Stage characteristics used in
the model are given in Figs. B-2a through B-2d. The mean of
the outer and inner radii was used in the stage flow and
pressure coefficient calculations. All the information was
taken from [43]. Dimensions and data not tabulated in the
report were obtained from scaling drawings and figures.

NACA-8 Compressor

Figure B-3 gives the overall performance of the
NACA eight-stage research compressor. Principal dimensions
and design performance are given in Table B-2. Stage
characteristics are given in Figs. B-4a through B-4h. Mean
radii were used in the flow coefficient, equivalent pressure,
and equivalent temperature ratio computations. All infor-
mation on the NACA-8 compressor was taken from [44, 45, 46].

---

[1]All figures and tables for Appendix B appear in
Appendix C.

General Electric J85-13 Compressor

Overall performance of the J85-13 compressor modeled during this study is shown in Fig. B-5. The variable guide vane and compressor bleed schedules used in the model (and for which the compressor map of Fig. B-5 applies) are given in Fig. B-6. Key dimensions and design point performance is given in Table B-3. Rotor inlet air angles for which the stage characteristics were calculated are also given in Table B-3. Stage characteristics are shown in Figs. B-7a through B-7h. The first-stage flow and pressure coefficients were re-defined for this work in terms of a semi-empirical modified flow and pressure coefficient to account for variable guide vane effects. The modified coefficients are,

$$\phi_m = \frac{\cos \beta}{\frac{1}{\phi} - \sin \beta} \tag{B-1}$$

and

$$\psi_m^P = \frac{\psi^P}{\left[1 - \psi_m \sin \beta_1 \right]^2} , \tag{B-2}$$

where ϕ and ψ^P follow the conventional definitions given in the text. The value of β used is the guide vane angle from Fig. B-6.

Information on the J85-13 was taken from [47].
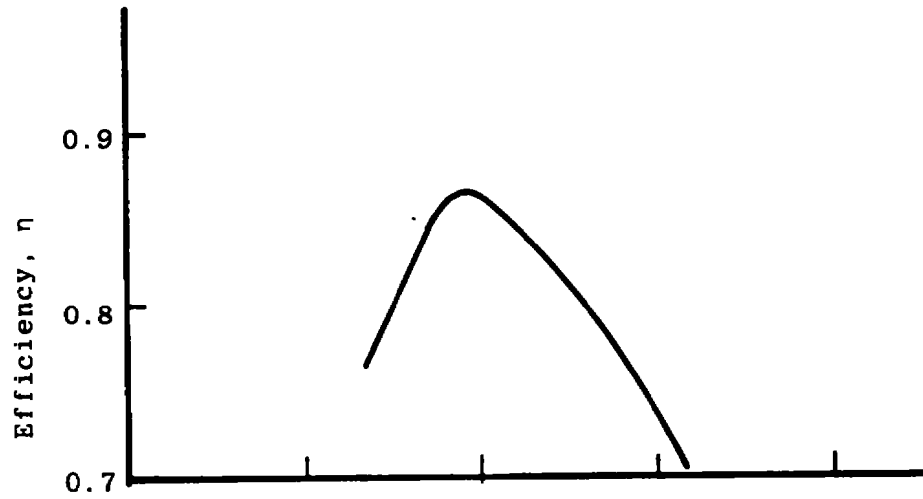
APPENDIX C

FIGURES AND TABLES FOR APPENDIX B
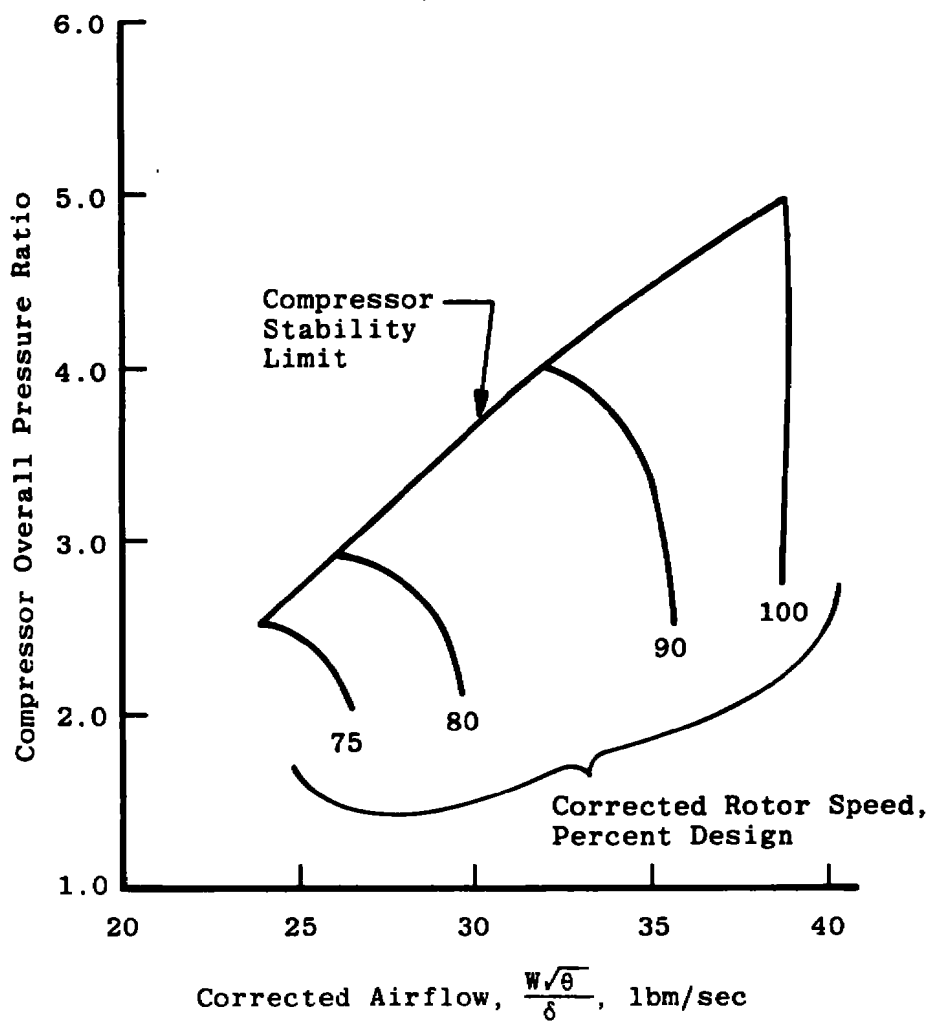
Figure B-1. XC-1 overall compressor performance
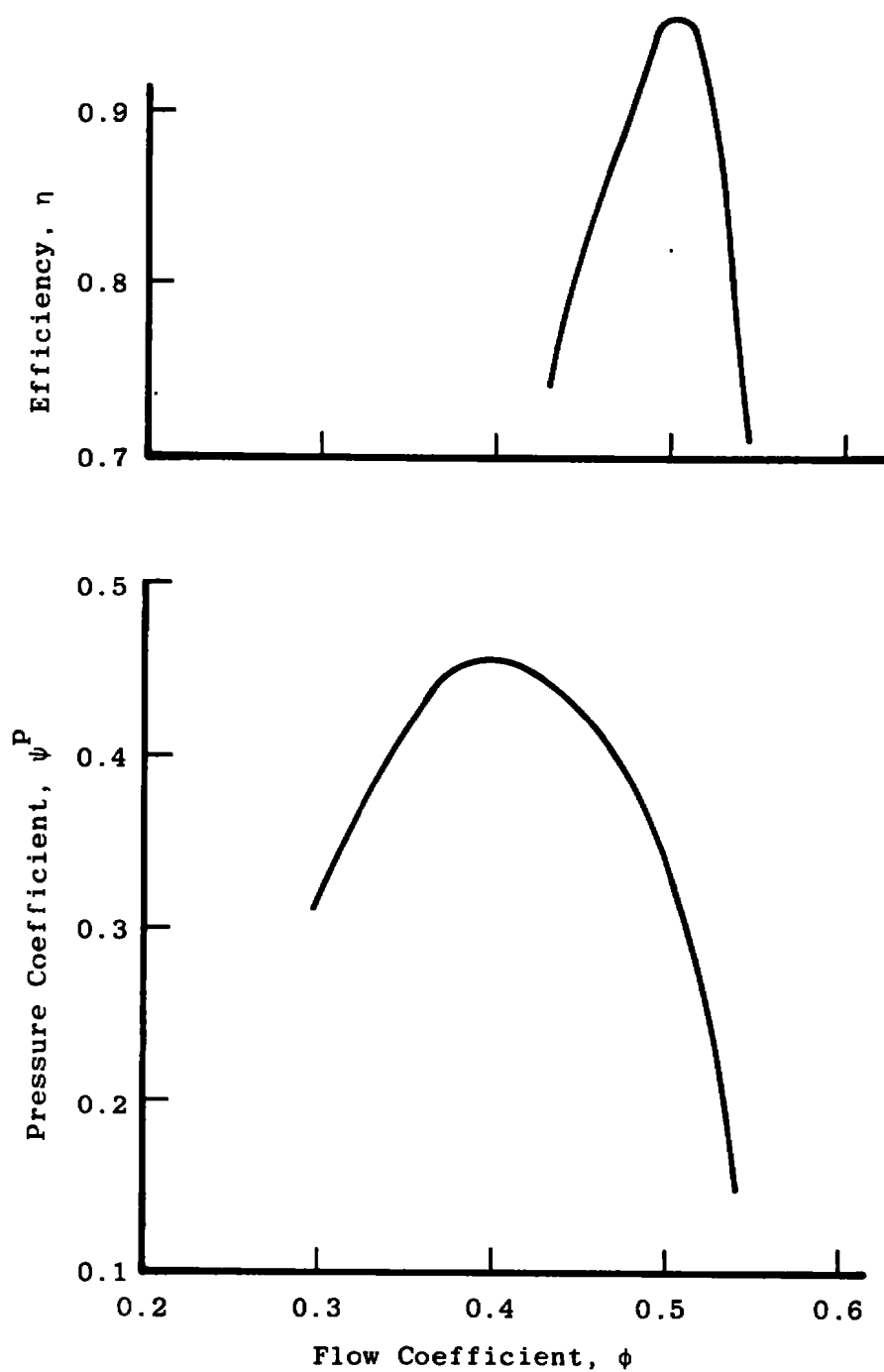characteristics.
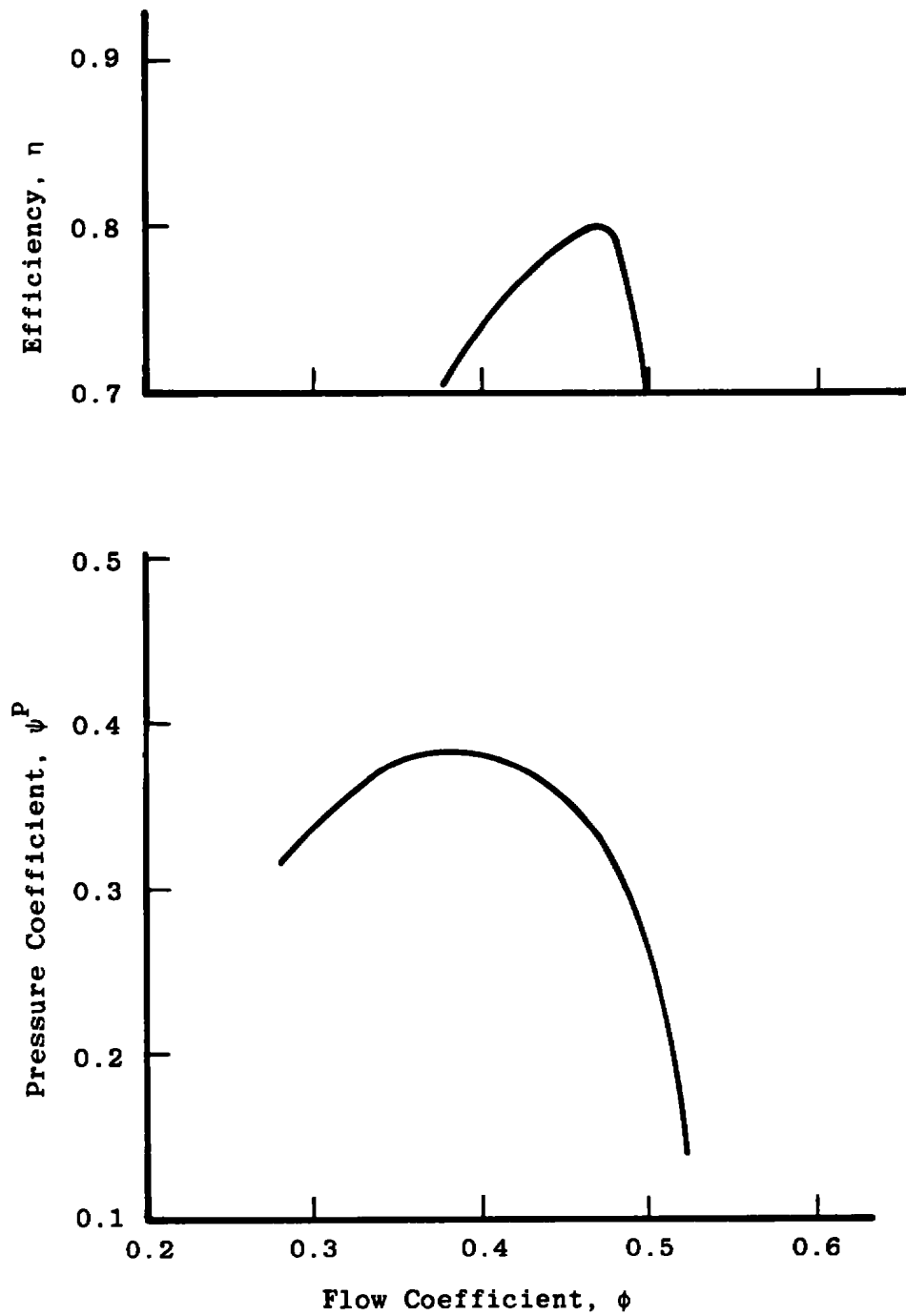
a. Stage 1

Figure B-2. XC-1 compressor stage characteristics.

239
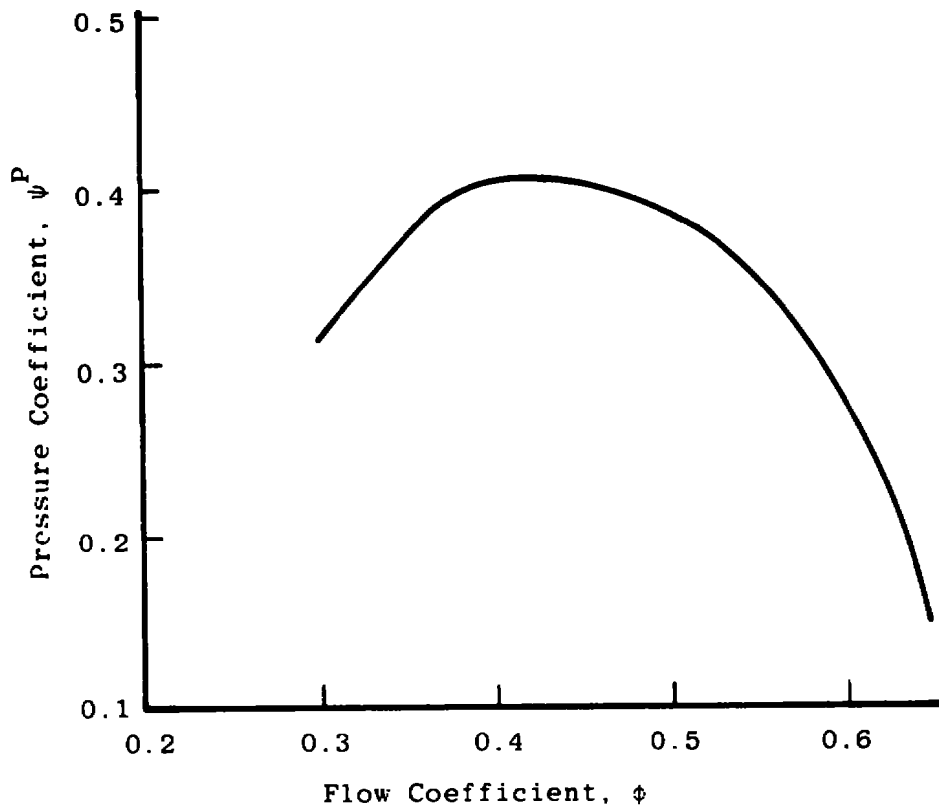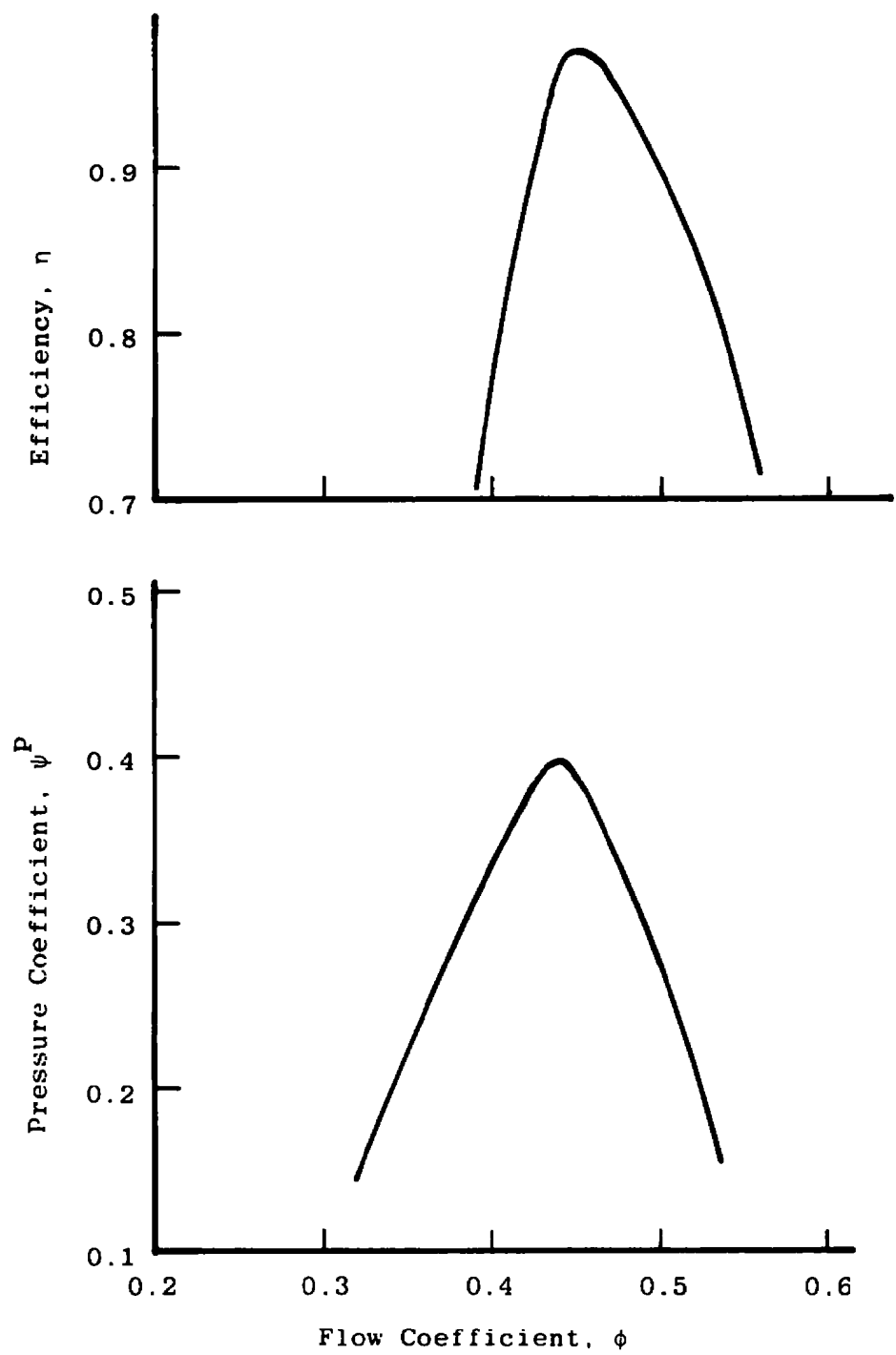
b. Stage 2

Figure B-2. (Continued).

c.   Stage 3

Figure B-2.   (Continued).

d.   Stage 4

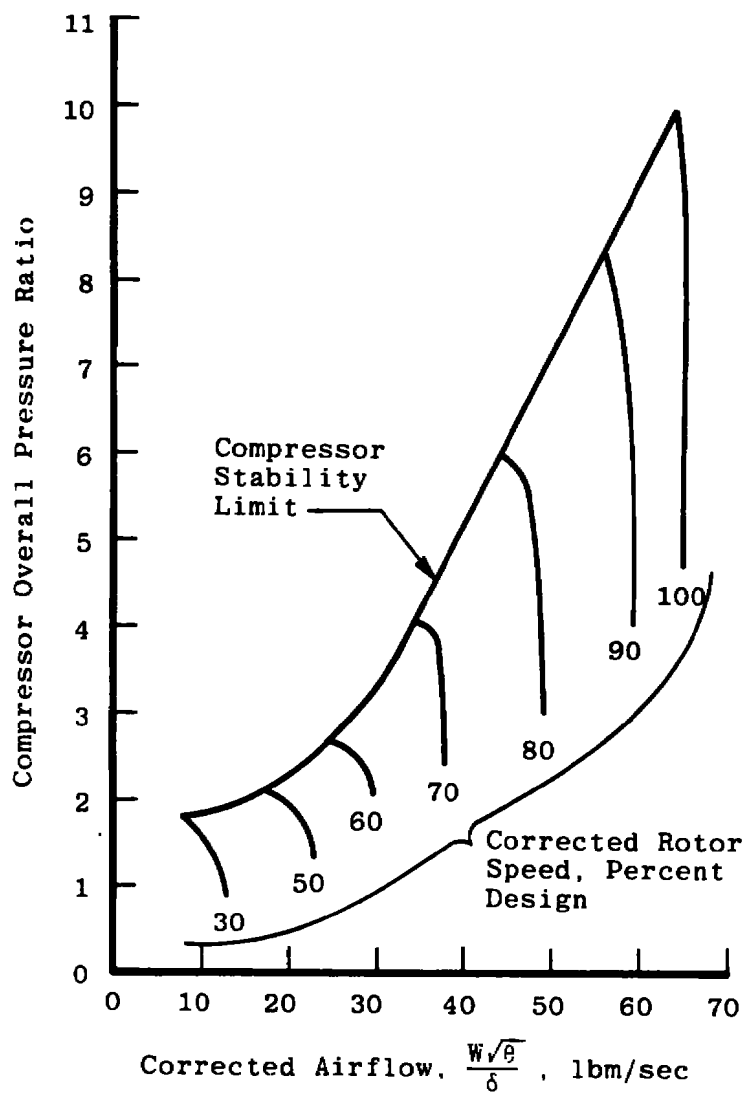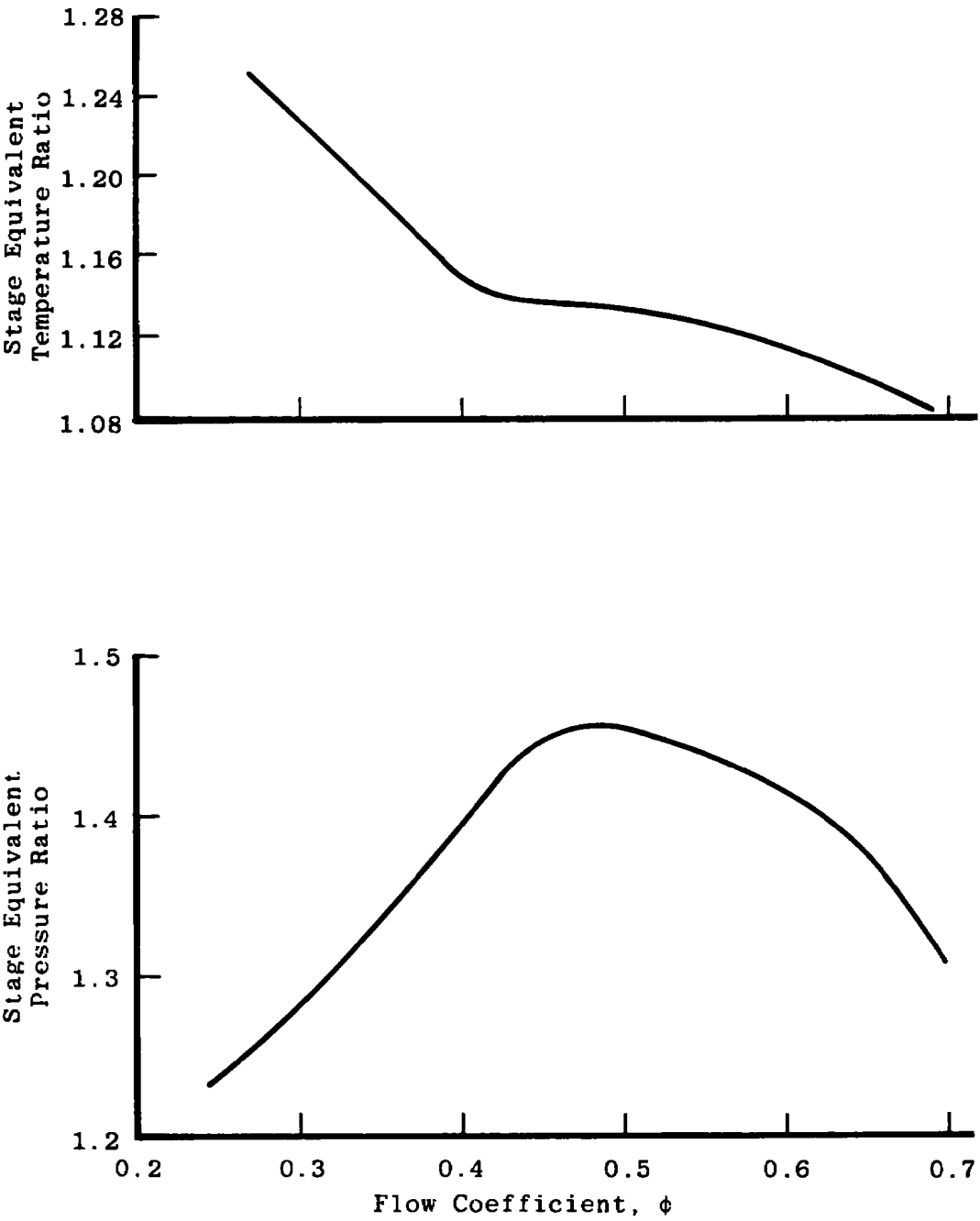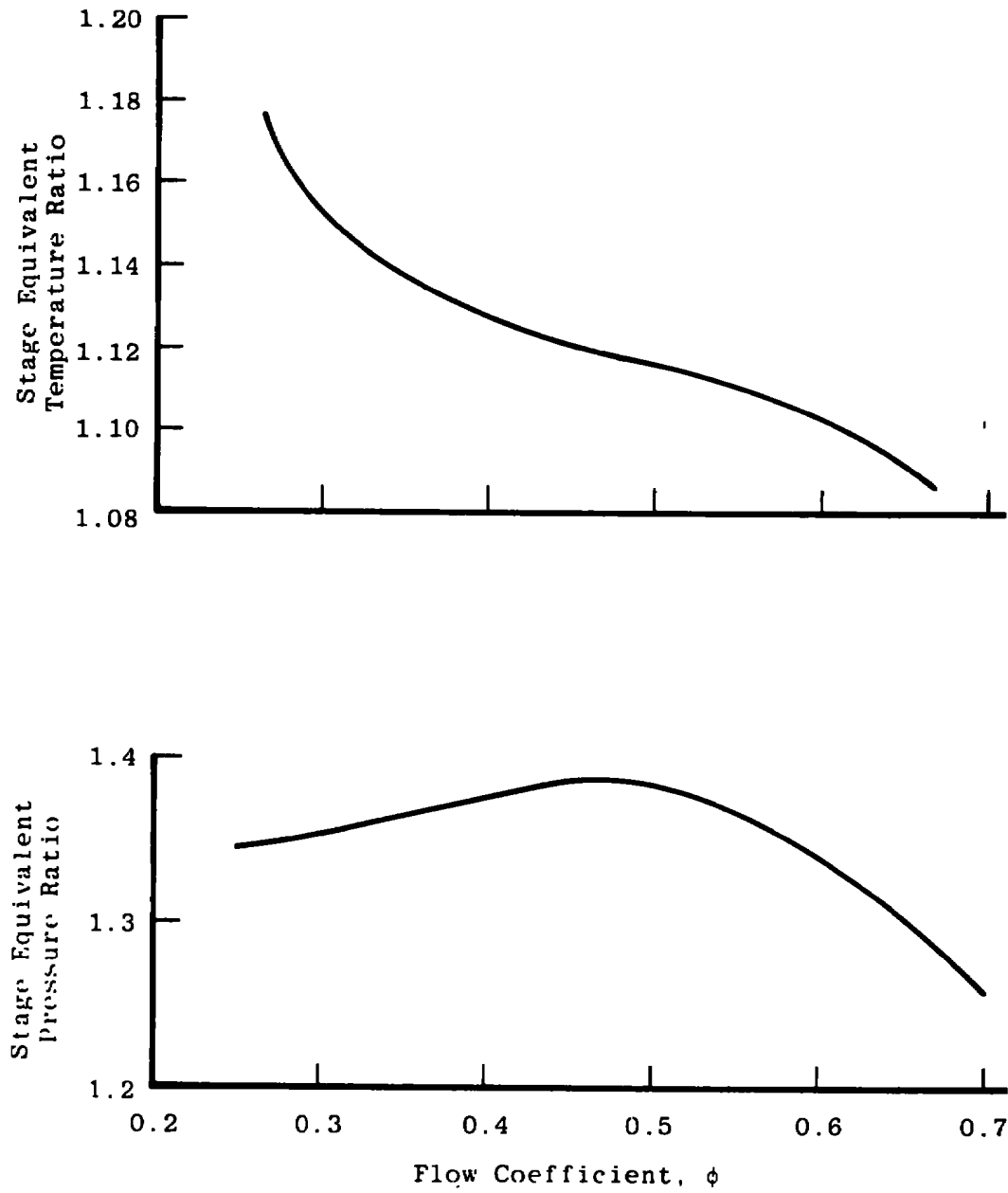Figure B-2.   (Continued).

Figure B-3. NACA-8 overall compressor performance characteristics.
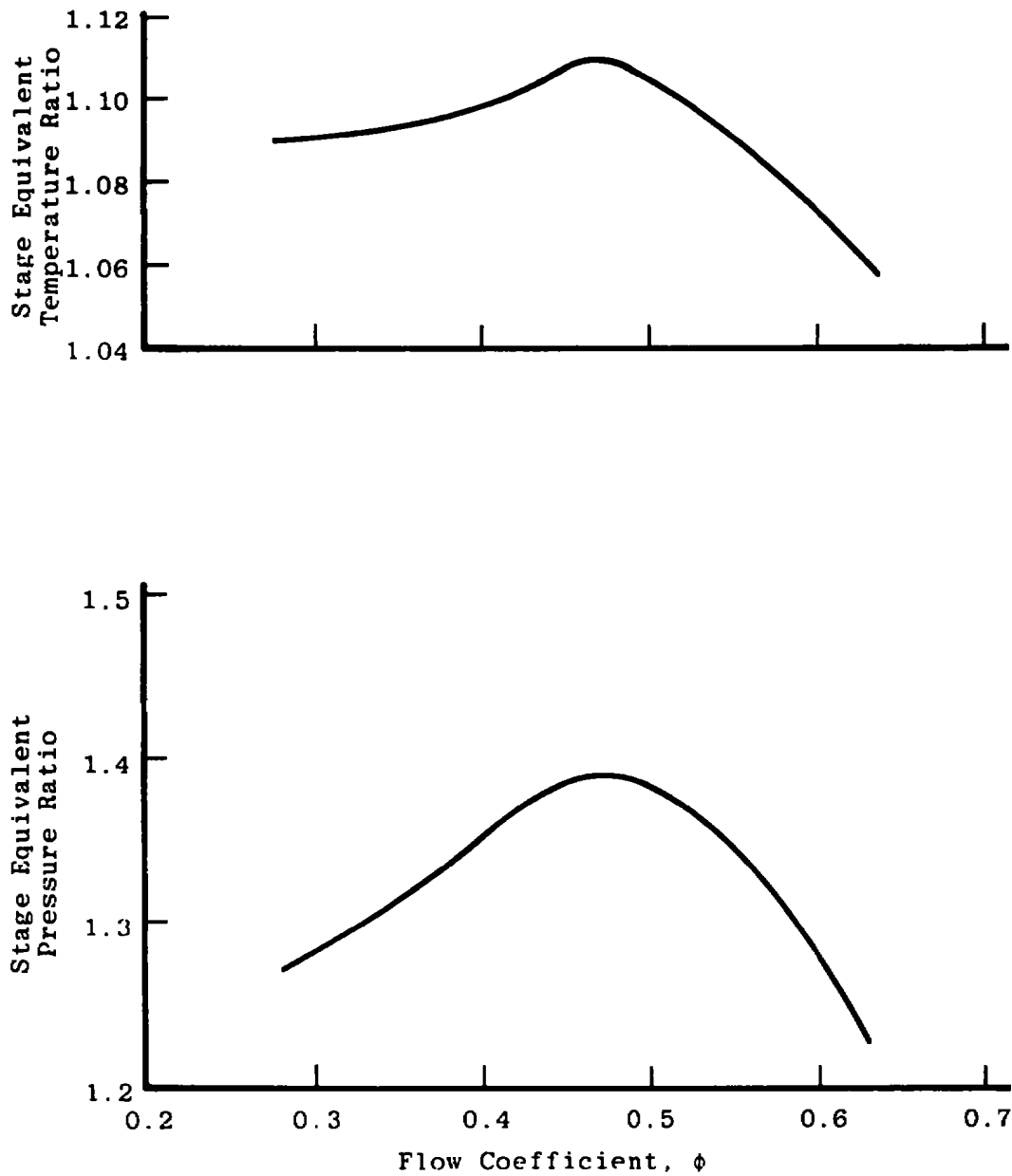
a. Stage 1

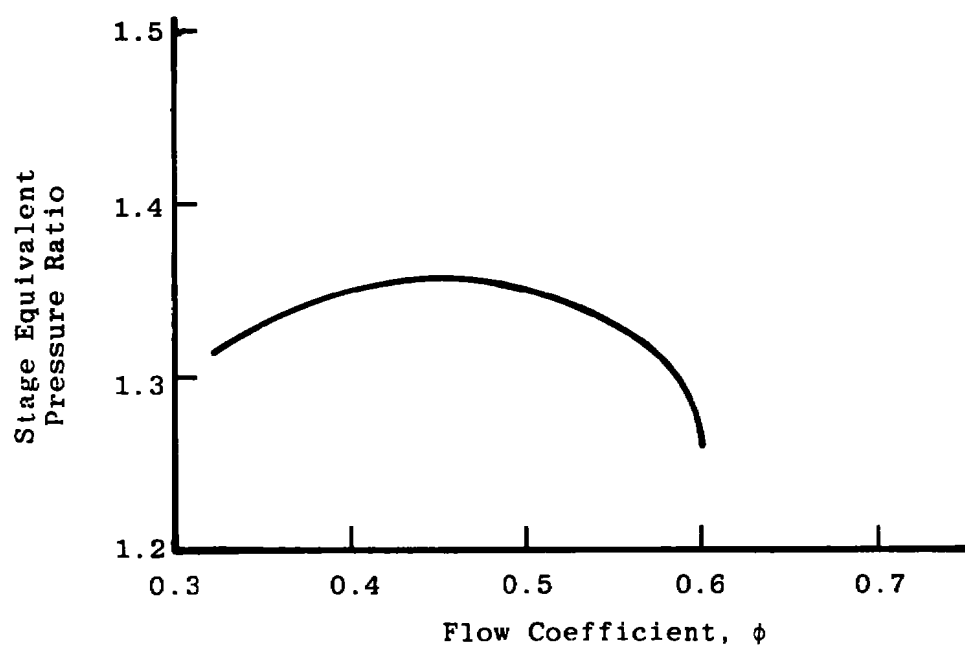Figure B-4. NACA-8 compressor stage characteristics.
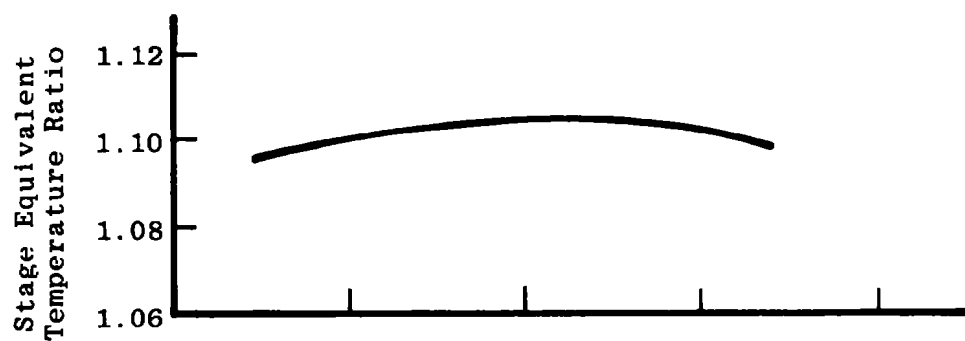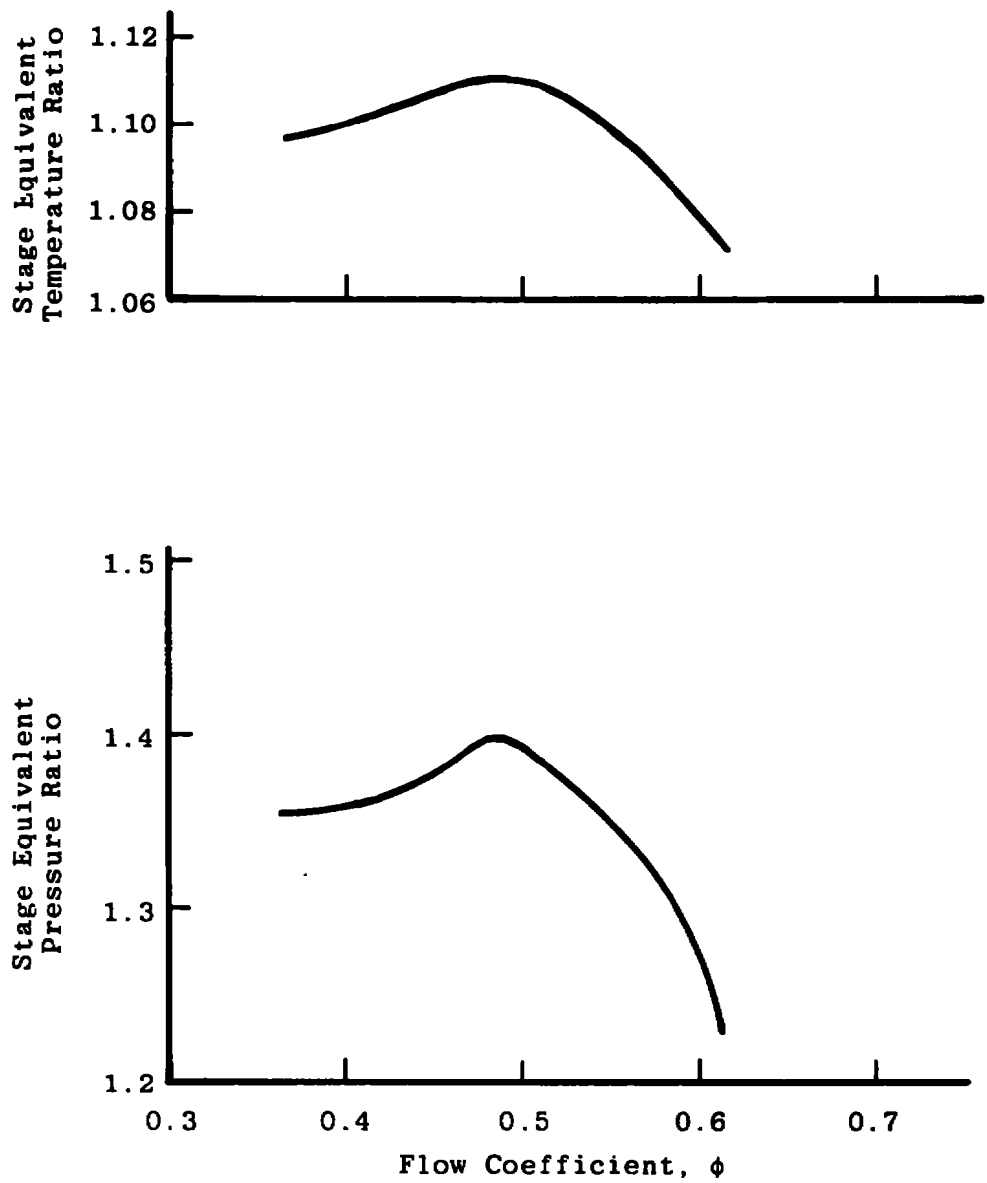
b. Stage 2

Figure B-4. (Continued).

c.   Stage 3

Figure B-4. (Continued).

d.   Stage 4

Figure B-4. (Continued).

247

e. Stage 5

Figure B-4. (Continued).

f. Stage 6

Figure B-4. (Continued).

g.   Stage 7

Figure B-4.   (Continued).

h. Stage 8

Figure B-4. (Continued).
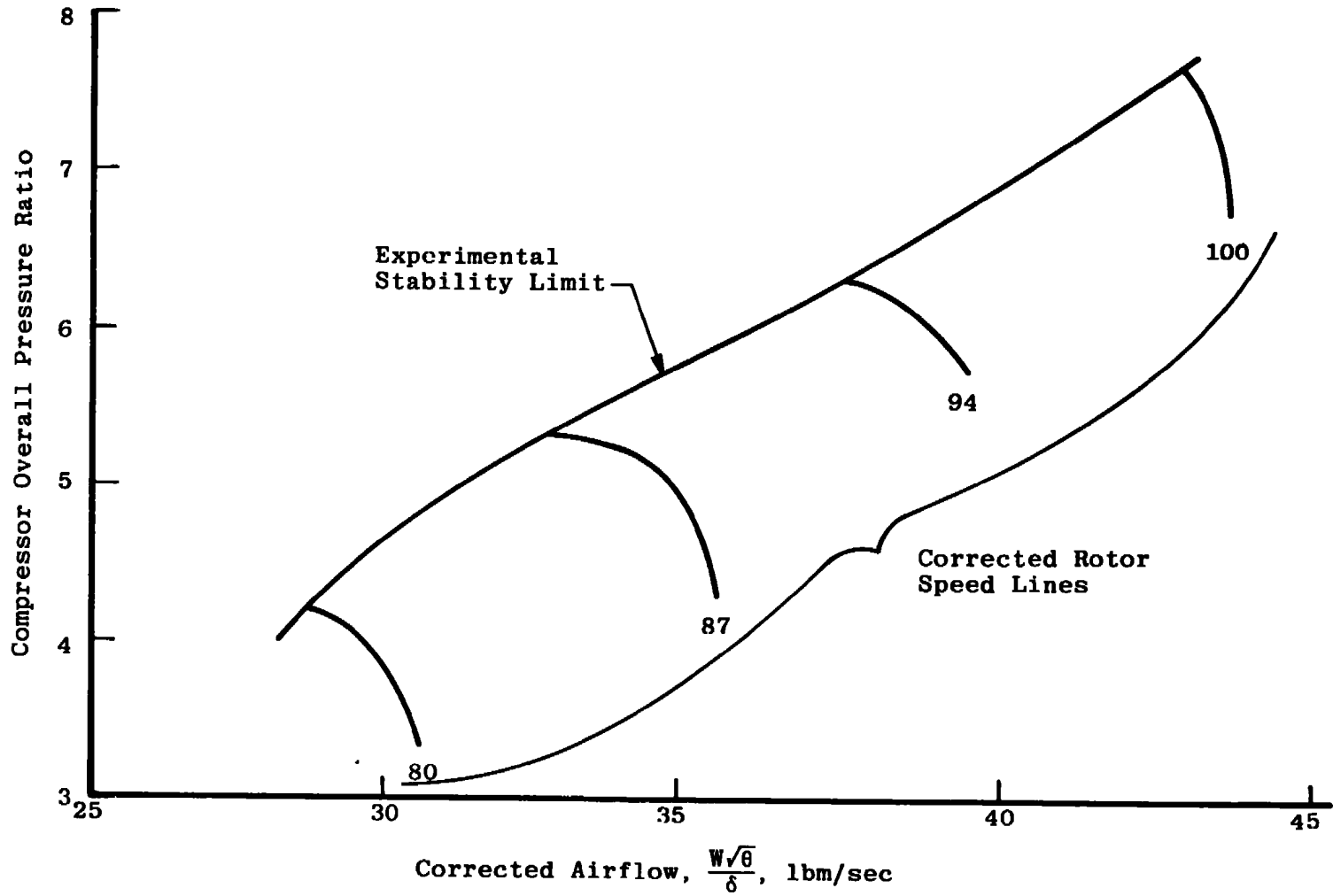
Figure B-5.   J85-13 overall compressor performance characteristics.
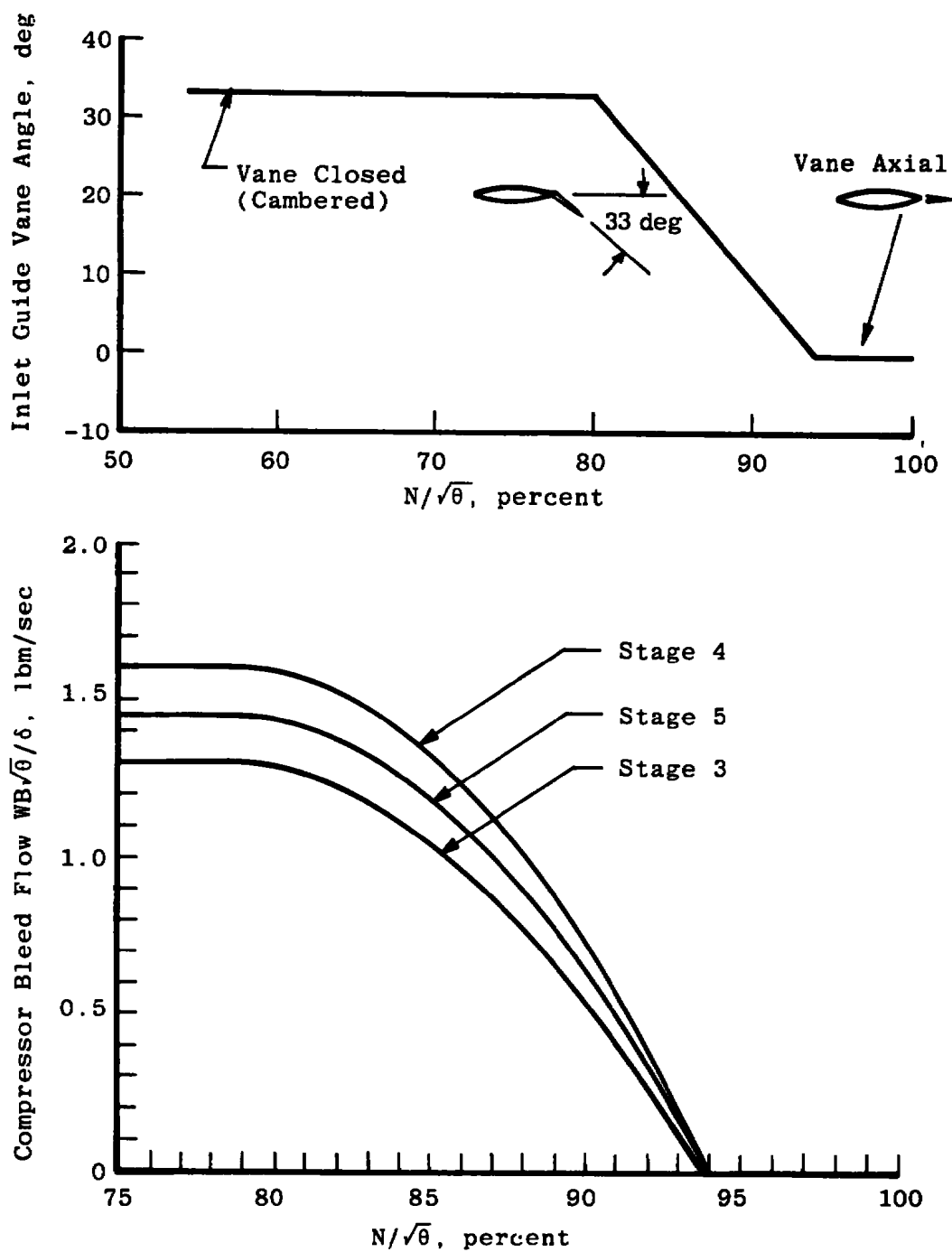
Figure B-6. Inlet guide vane and compressor bleed
schedules for J85-13 model.
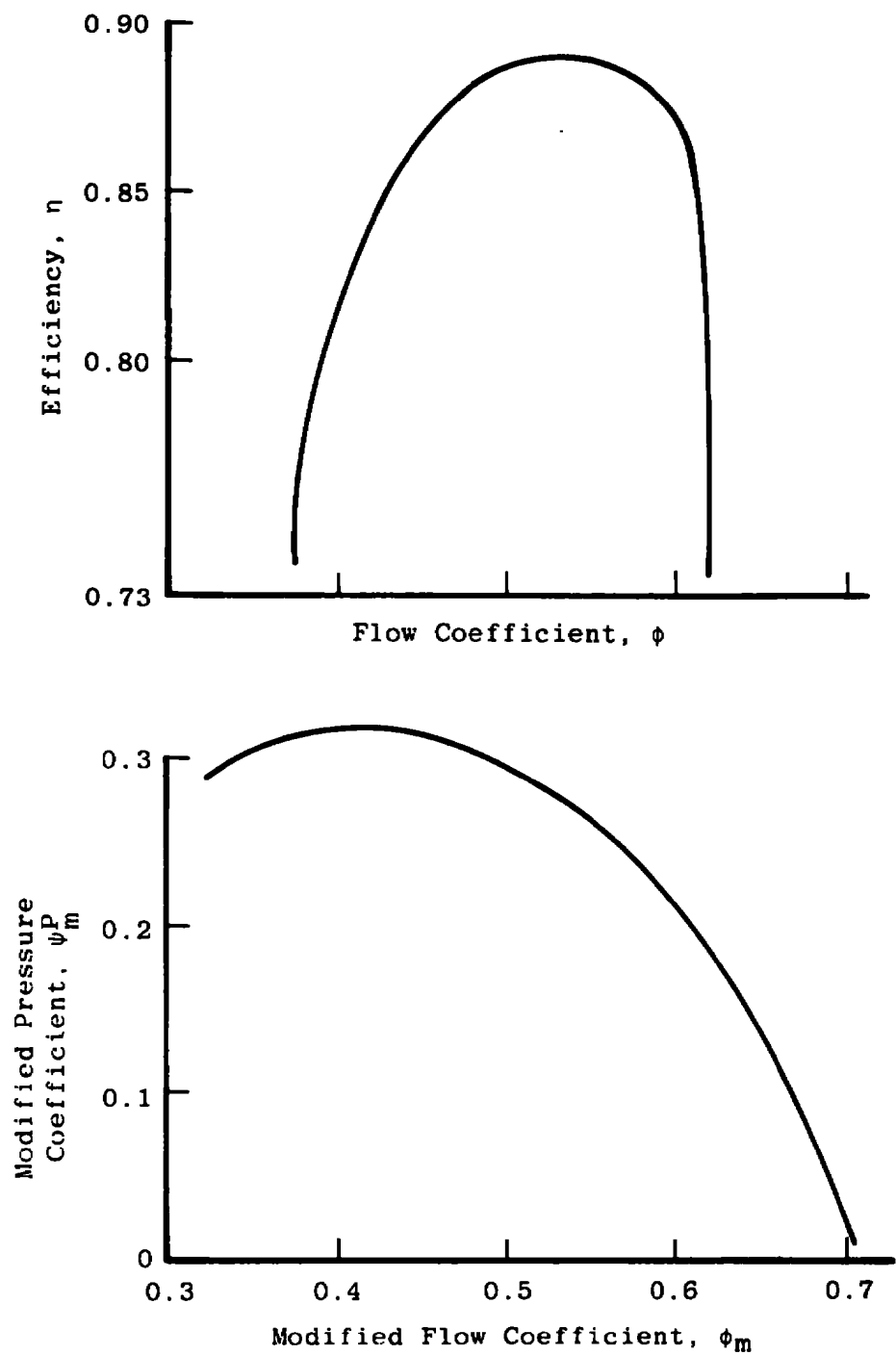
a. Stage 1

Figure B-7. J85-13 compressor stage characteristics.
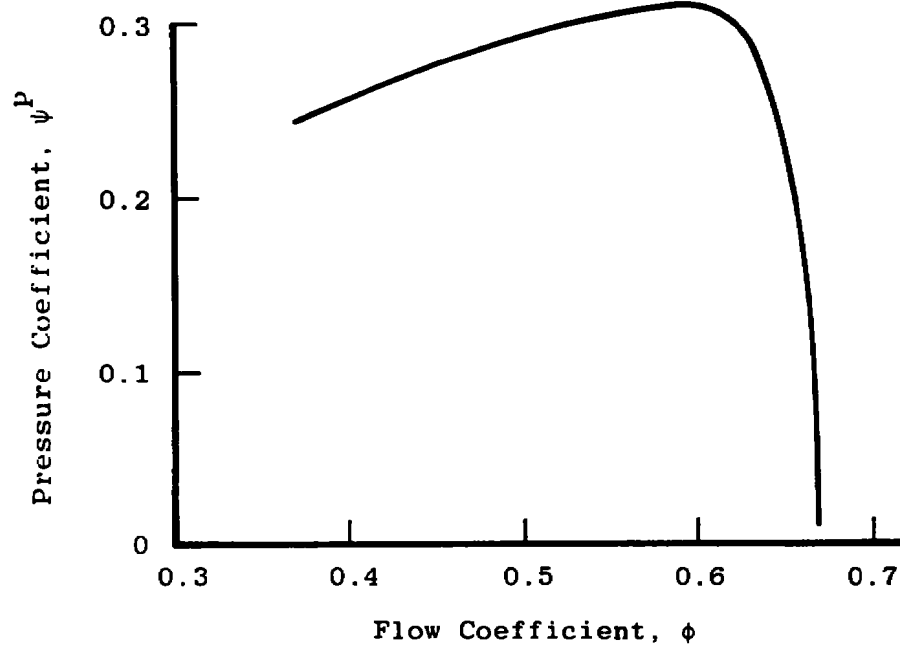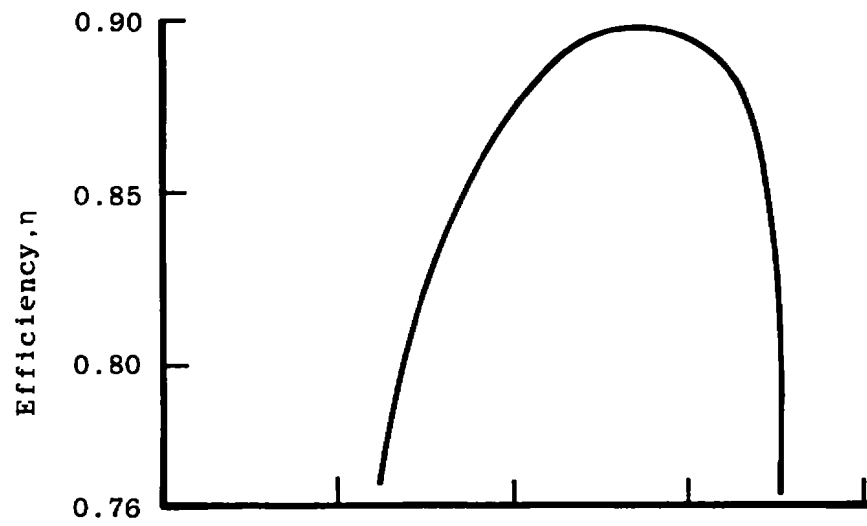
b. Stage 2

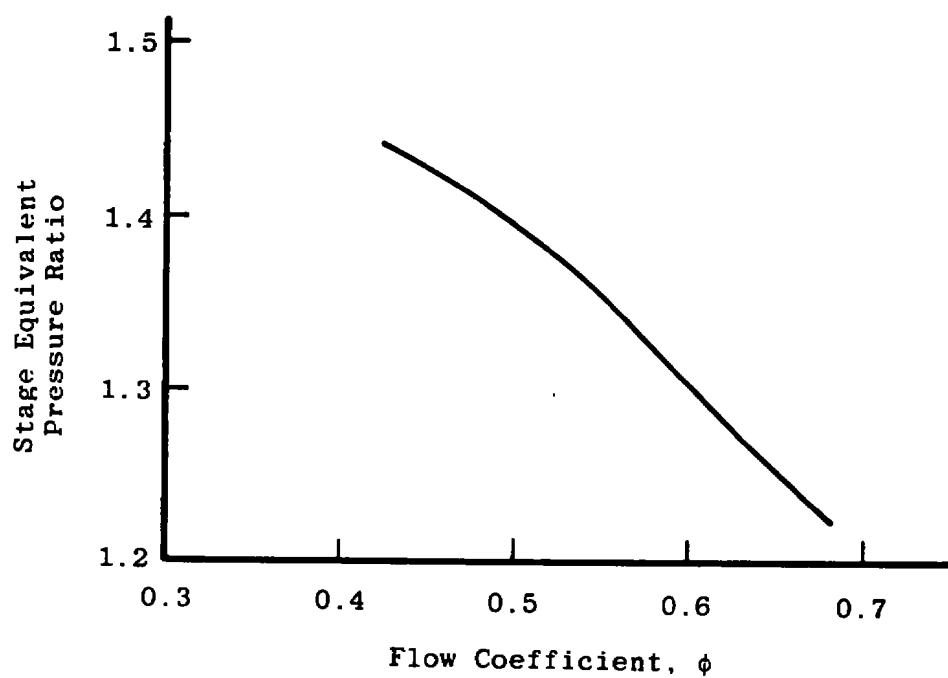Figure B-7. (Continued).
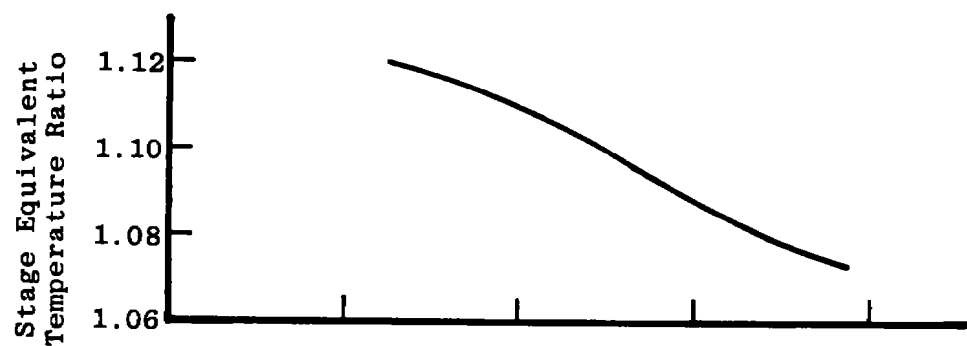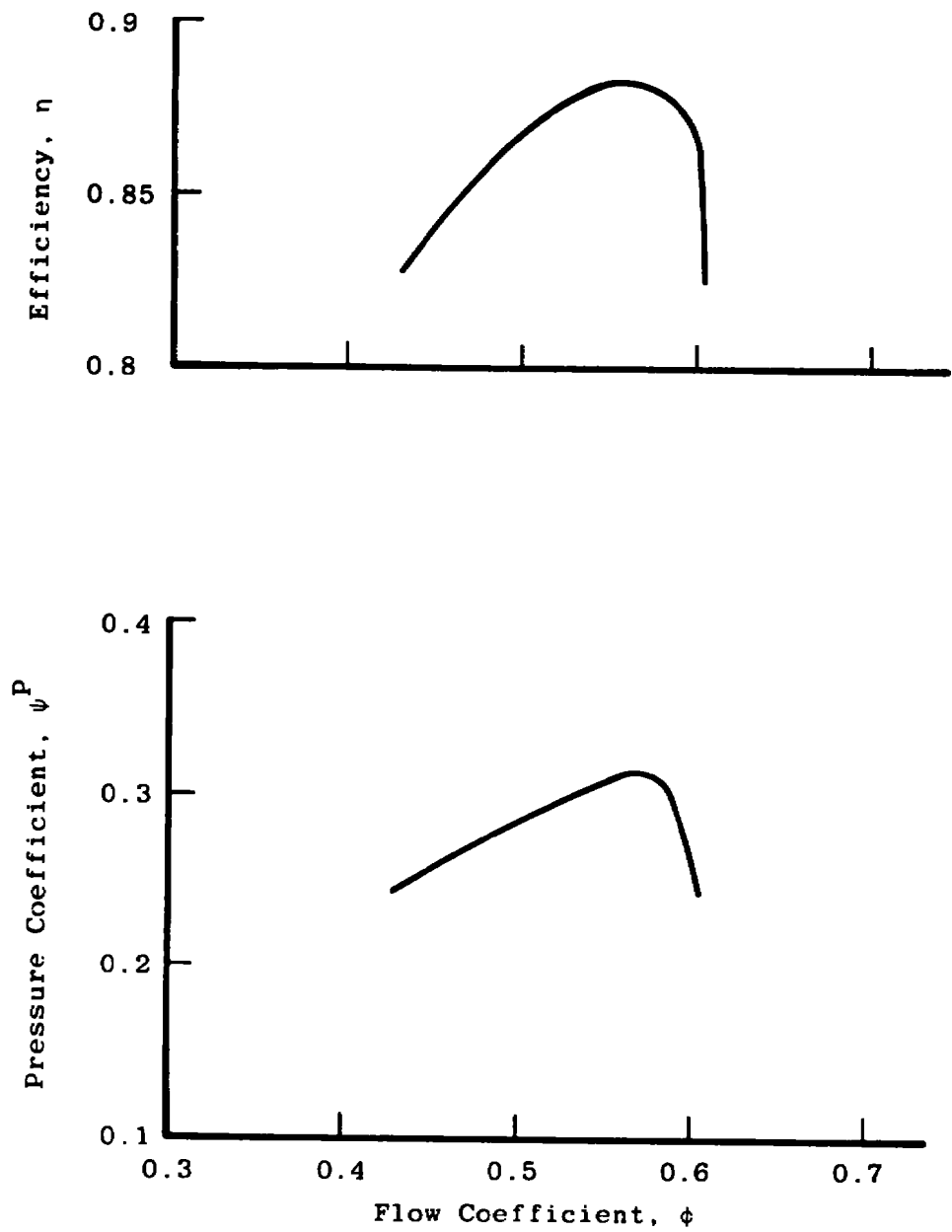
c. Stage 3

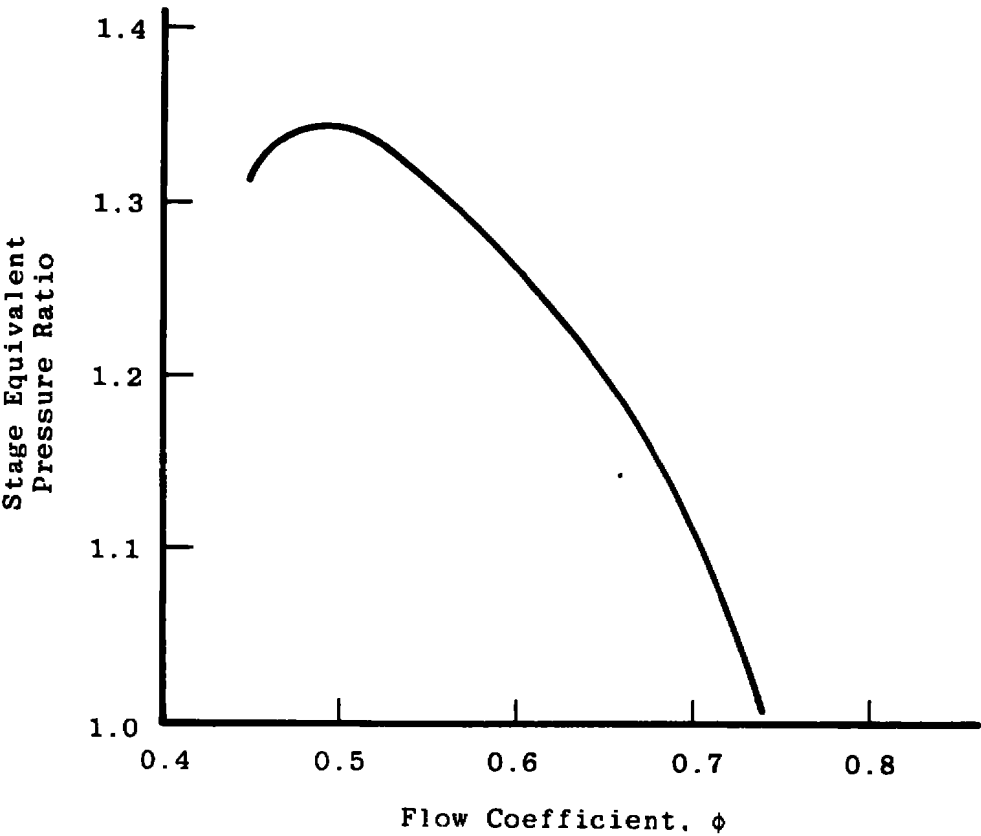Figure B-7. (Continued).
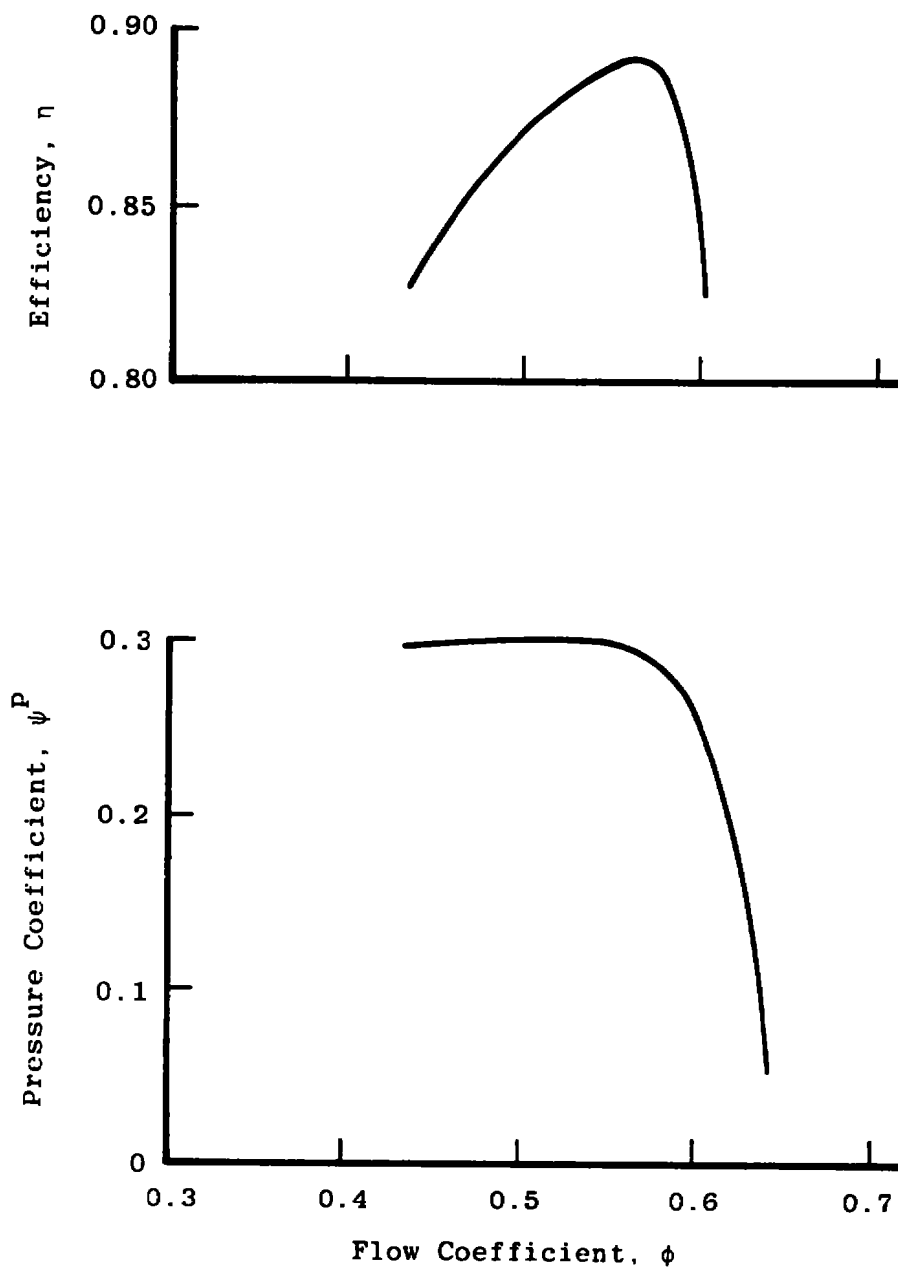
d. Stage 4

Figure B-7. (Continued).
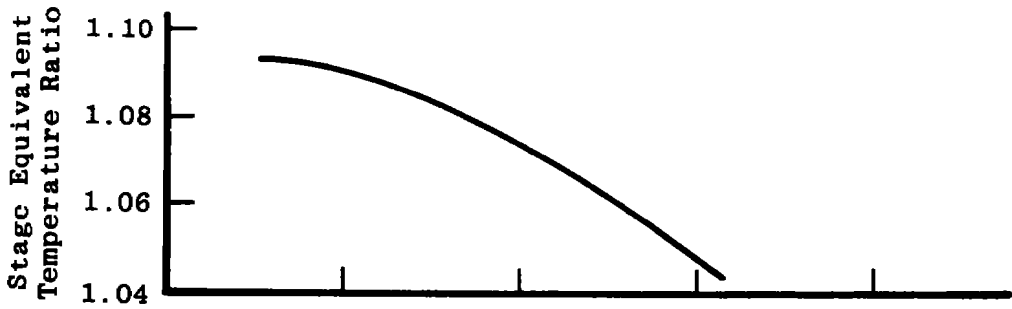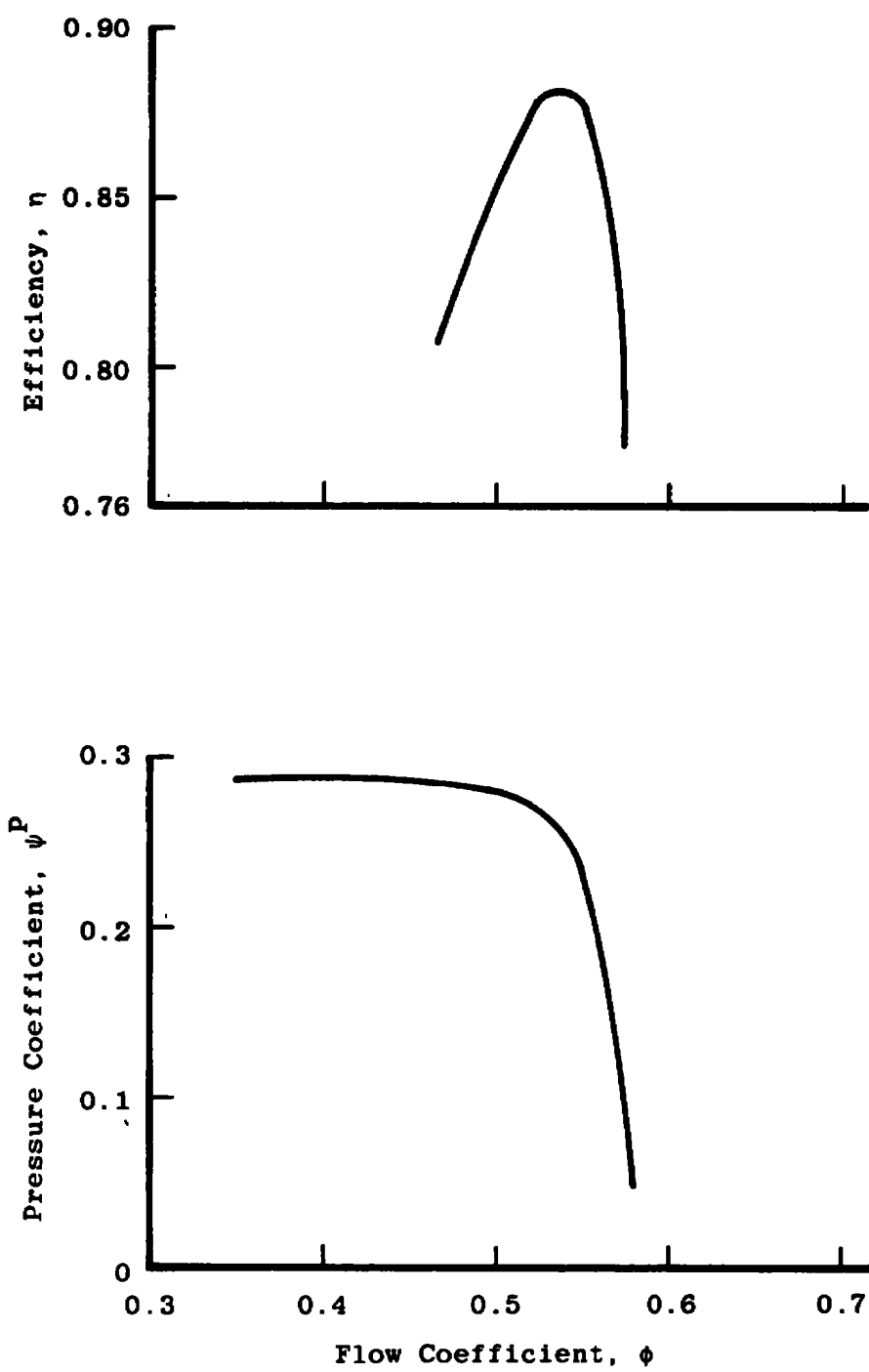
e. Stage 5

Figure B-7. (Continued).

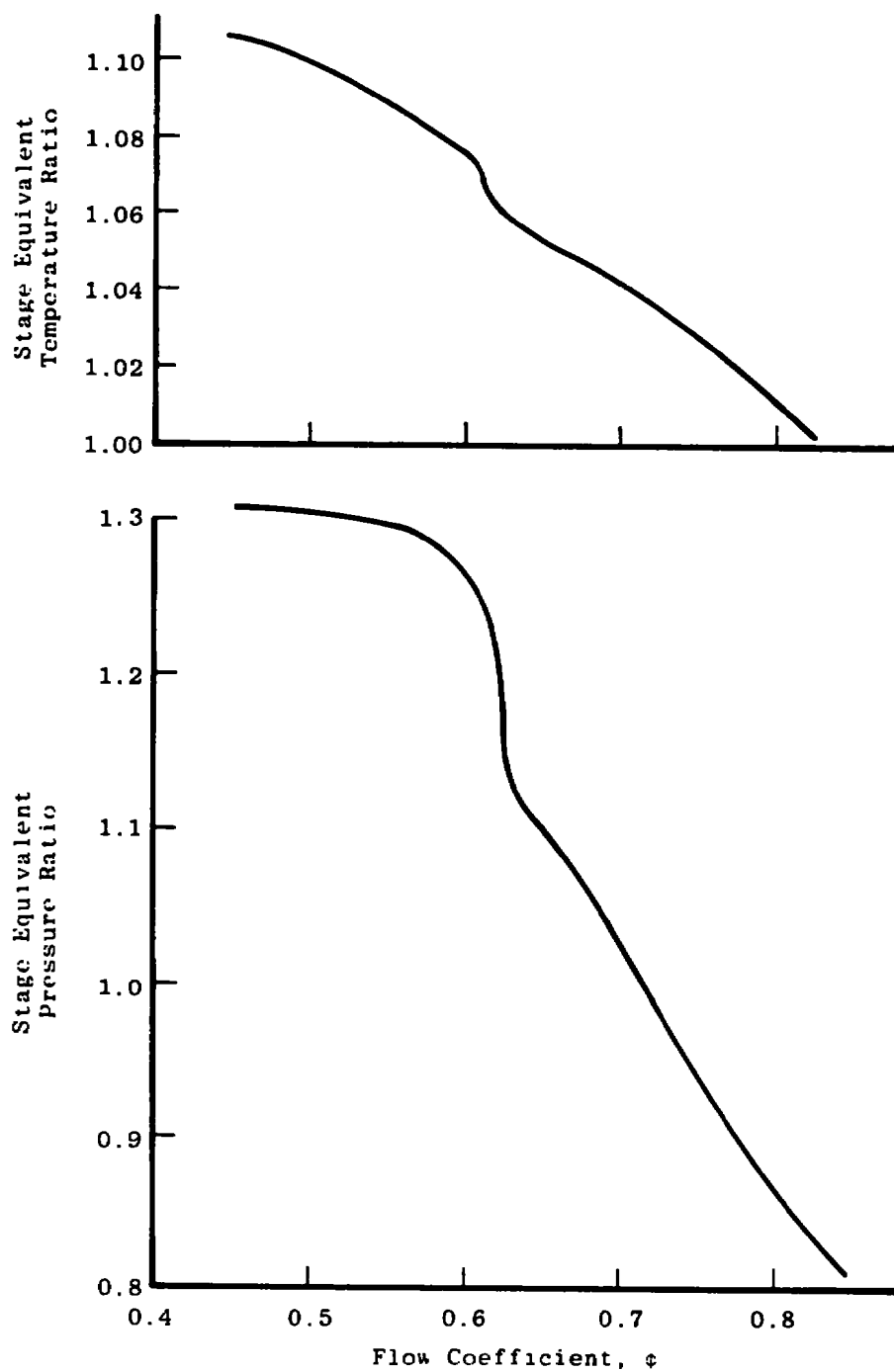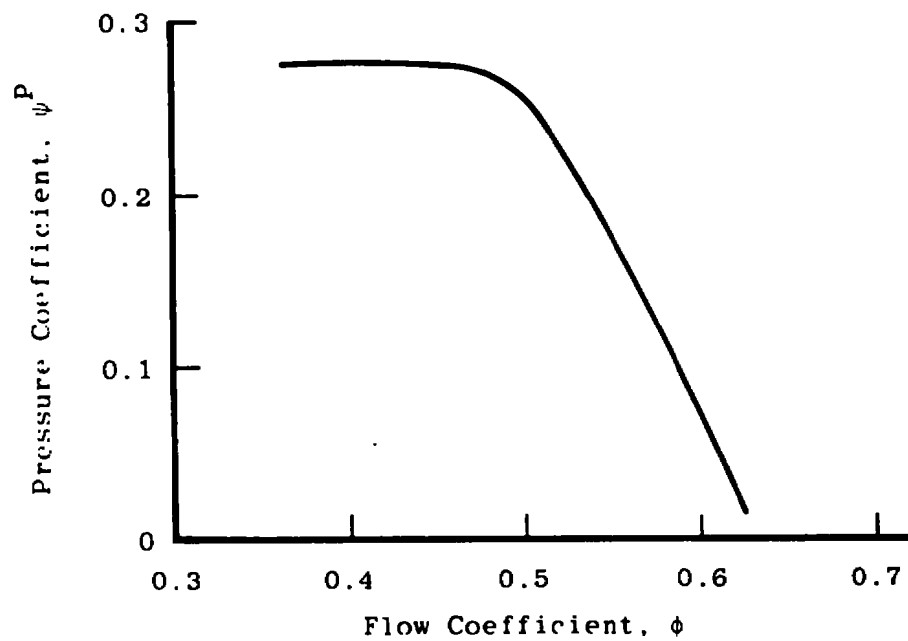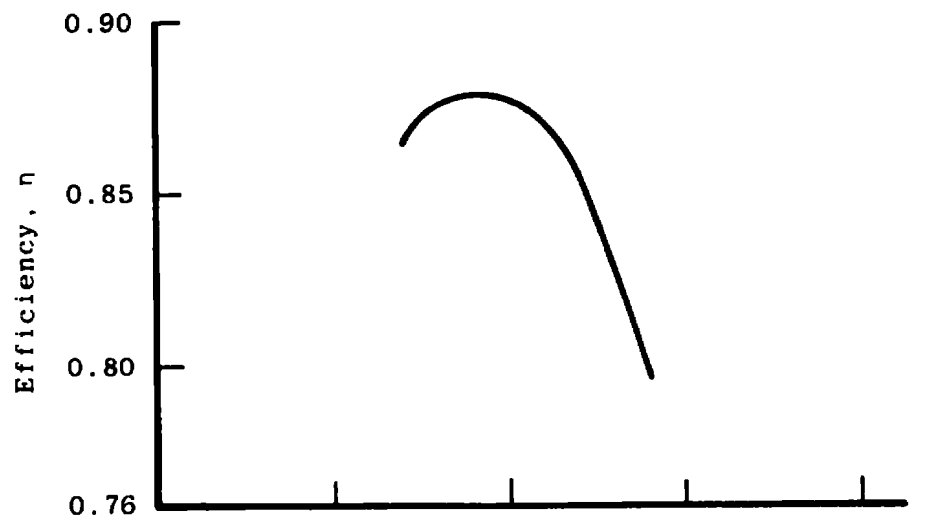f. Stage 6

Figure B-7. (Continued).
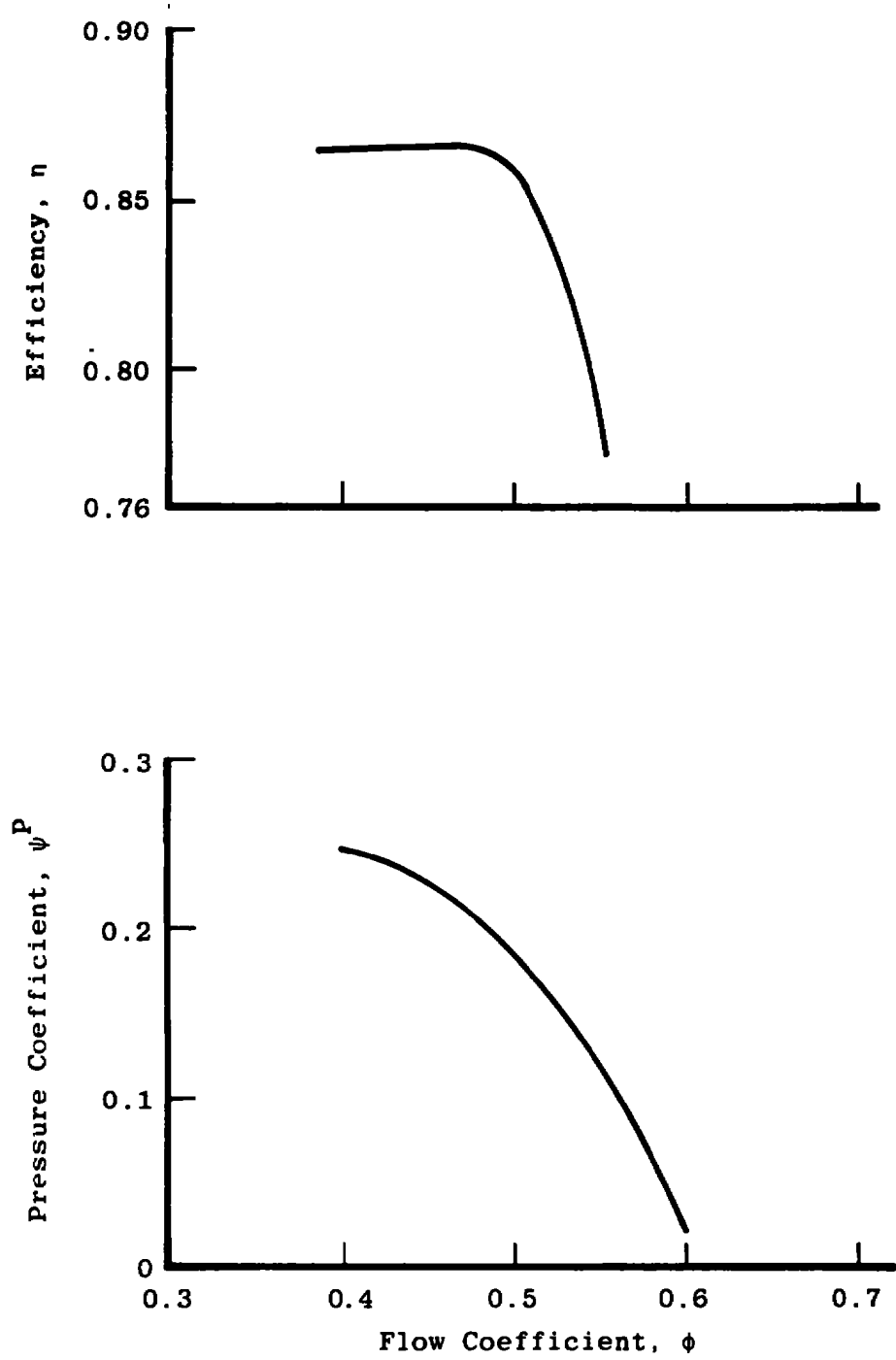
g. Stage 7

Figure B-7. (Continued).
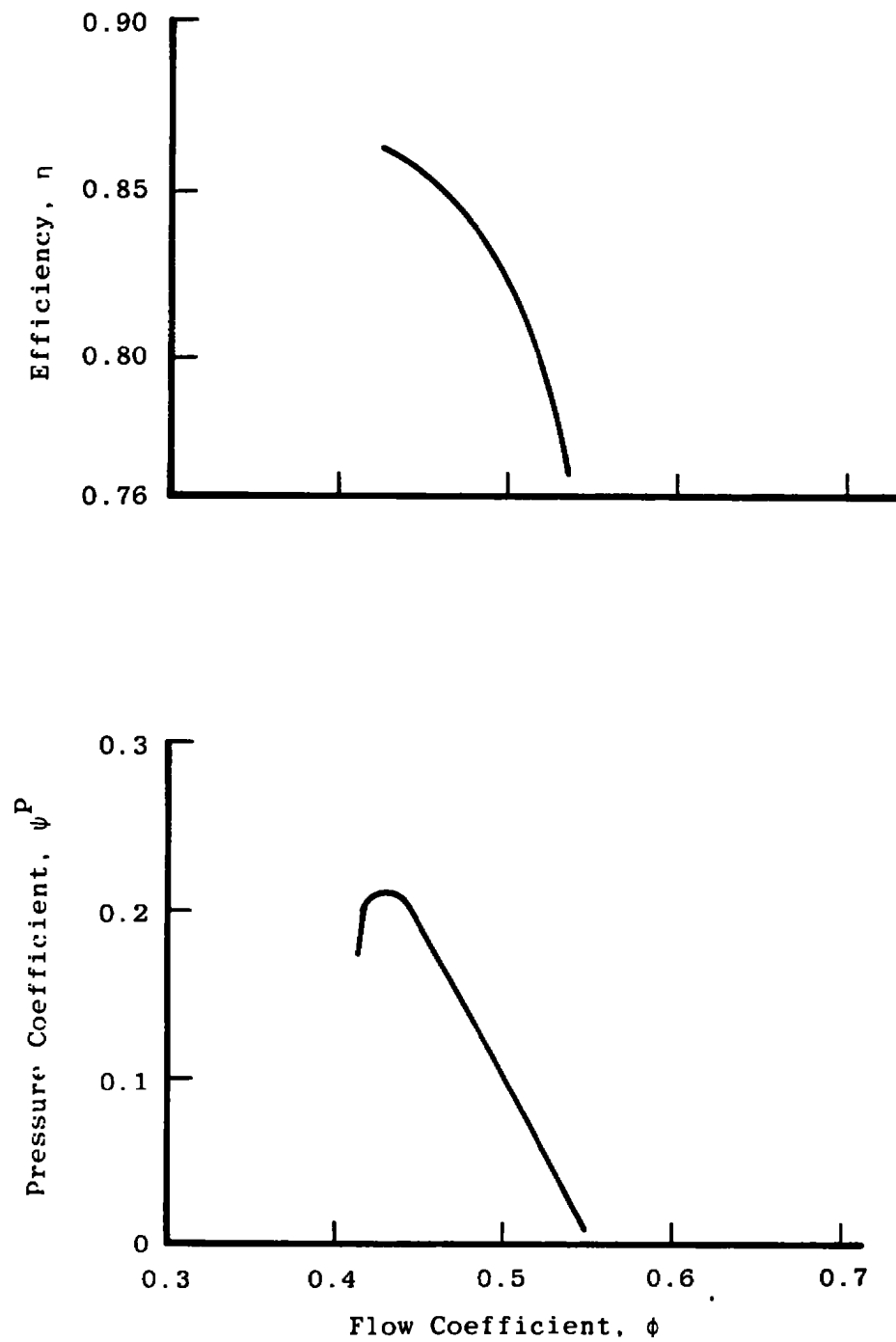
h. Stage 8

Figure B-7. (Continued).

Table B-1. Detroit Diesel Allison XC-1 Four-Stage
Lift Engine Compressor Model Details

	Geometry			
			Radius	
Stage (Station)	Area (ft^2)	Length (ft)	Outer (ft)	Inner (ft)
1	1.136	0.2165	0.6991	0.3565
2	0.8173	0.1558	0.6903	0.4651
3	0.6610	0.1558	0.6903	0.5159
4	0.5045	0.1386	0.6838	0.5540
5	0.4026	–	0.6816	0.5800

Design Point Performance

$N = 18,030$ rpm

$$\frac{W\sqrt{\theta}}{\delta} = 38.7 \text{ lbm/sec}$$

$PR = 4.92$ (maximum)

262

Table B-2. NACA Eight-Stage Research Compressor Details

| | | Geometry | | Radius | |
| Location | | Area | Length | Outer | Inner |
Station	Stage	(ft^2)	(ft)	(ft)	(ft)
1	*	2.182	0.475	0.8333	0
2	*	2.182	0.475		0
3	*	2.182	0.475		0
4	*	1.679	0.475		0.4000
5	1	1.679	0.475		0.4000
6	2	1.311	0.450		0.5265
7	3	1.173	0.283		0.5667
8	4	0.9960	0.292		0.6100
9	5	0.8352	0.258		0.6546
10	6	0.6860	0.242		0.6900
11	7	0.5681	0.250		0.7167
12	8	0.4737	0.242		0.7373
13	**	0.4737	0.242		0.7373
14	**	0.3129	0.500		0.7712
15	**	0.3129	0.500		0.7712
16	**	Variable	-	0.8333	-

*Inlet duct.

**Burner.

Design Point Performance

N = 13,380 rpm

$$\frac{W\sqrt{\theta}}{\delta} = 65 \text{ lbm/sec}$$

PR = 10.0 (maximum)

Table B-3.   General Electric J85-13 Eight-Stage
Compressor Details

	Geometry				
Location		Area	Length	Radius		Rotor Inlet
				Outer	Inner	Air Angle
Station	Stage	(ft^2)	(ft)	(ft)	(ft)	(deg)
1	*	1.300	0.1856	0.6708	0.1900	0
2	*	1.300	0.1856	0.6708	0.1900	0
3	*	1.300	0.1856	0.6708	0.1900	0
4	*	1.150	0.1856	0.6708	0.2812	0
5	1	1.066	0.1856	0.6458	0.3156	Scheduled
6	2	0.8395	0.1364		0.3935	5.4
7	3	0.6821	0.1116		0.4472	12.1
8	4	0.5630	0.09767		0.4878	14.8
9	5	0.4690	0.08725		0.5175	19.4
10	6	0.4055	0.07892		0.5367	23.2
11	7	0.3698	0.07750		0.5472	22.2
12	8	0.3580	0.09883		0.5506	21.6
13	**	0.3542	0.1000		0.5506	0
14	**	1.312	0.1000		0.2683	0
15	**	0.3542	0.1000		0.5506	0
16	**	Variable	–	0.6458	–	0

*Inlet duct.

**Burner.

Design Point Performance

$$N = 16,500 \text{ rpm}$$

$$\frac{W\sqrt{\theta}}{\delta} = 43 \text{ lbm/sec}$$

$$PR = 7.7 \text{ (maximum)}$$

NOMENCLATURE

A	Area
ACC	Projected area of control volume circumferential surface in the circumferential direction
ACR	Projected area of control volume circumferential surface in the radial direction
ARR	Projected area of control volume radially-facing surface in the radial direction
ARZ	Projected area of control volume radially-facing surface in the axial direction
AZ	Control volume area normal to axial direction
a	Acoustic velocity; blade spacing; a constant
C	Blade chord length
C_d	Blade drag coefficient
C_ℓ	Blade lift coefficient
CF(r)	Stage characteristic correction factor for radial variation
c_p	Specific heat at constant pressure
c_v	Specific heat at constant volume
CXFC	Circumferential crossflow coefficient
CXFR	Radial crossflow coefficient
D	Blade drag force
DLR	Dynamic lift amplitude ratioed to quasi-steady-state lift
EPR	Stage equivalent pressure ratio, Eq. (47)

ETR	Stage equivalent temperature ratio, Eq. (46)
e	Internal energy
F	Force of compressor blading and cases acting on fluid, including wall pressure area force
FC	Circumferential force acting on fluid in control volume
FR	Radial force acting on fluid in control volume
FZ	Force of compressor blading and cases acting on fluid in the axial direction
f	Frequency
f(...)	A function of ...
g(...)	A function of ...
H	Total enthalpy flux
HC	Total enthalpy flux transported across control volume circumferentially-facing boundary
HR	Total enthalpy flux transported across control volume radially-facing boundary
HZ	Total enthalpy flux transported across control volume axial-facing boundary
IMP	Impulse function, Eqs. (5) and (160)
IMPR	Ratio of stage exit to stage entry impulse functions
i	Axial location index
im	Adjacent axial location, i-1
ip	Adjacent axial location, i+1
j	Radial location index
jm	Adjacent radial location, j-1

jp	Adjacent radial location, j+1
k	Reduced frequency based on full blade chord length, Fig. 11
L	Total control volume length; blade lift force
M	Mach number
ME	Equivalent Mach number
MFF	Mass flow function, Eq. (74)
MFFE	Equivalent stage downstream mass flow function, Eq. (73)
N	Compressor rotor speed
$O(...)$	Order of magnitude of ...
P	Stagnation (total) pressure
PR	Stage total pressure ratio
PS	Static pressure
Q	Rate of heat addition to control volume
R	Gas constant
Re	Reynolds number
REI	Reynolds number index
r	Radius; coordinate in the radial direction
rms	Root-mean-square amplitude
s	Coordinate in the circumferential direction
T	Stagnation (total) temperature
TR	Stage total temperature ratio
TS	Static temperature
t	Time
t	Torque on a fluid element
U	Axial velocity

V	Velocity components other than axial (designated by subscript)
v	Radial velocity component in three-dimensional model development
vol	Volume
W	Mass flow rate; airflow rate
WB	Compressor bleed flow rate
WC	Mass flux across circumferentially-facing control volume boundary
WR	Mass flux across radially-facing control volume boundary
WS	Stage shaft work added to fluid in control volume
WZ	Mass flux across axially-facing control volume boundary
w	Circumferential velocity component in three-dimensional model development
X	Energy function, Eq. (8)
Y	Time derivative of a volume integral, Eq. (150)
y	A general dependent variable
z	Axial coordinate

Greek Symbols

α	Angle of attack
β	Flow direction angle relative to axial direction
λ	Ratio of specific heats
Δ	A difference

ΔP	Pressure fluctuation amplitude
δ	Ratio of compressor entry total pressure to standard day, sea-level-static pressure
ε	A constant; an error magnitude
η_{ad}	Stage adiabatic efficiency
θ	Angular location; ratio of compressor inlet total temperature to standard day, sea-level-static temperature
$\bar{\theta}$	Angular extent of low pressure region in circumferential distortion pattern
λ	Blade chord-to-axial direction angle or stagger angle
ρ	Density
ψ^P	Stage pressure coefficient
ψ^T	Stage temperature coefficient (stage loading parameter)
ω	Angular rotor speed; circular frequency

Superscripts

$-$	Average or effective value
P	Pertaining to pressure
T	Pertaining to temperature

Subscripts

$0,1,2,...$	Location or station designators
ad	Adiabatic
avg	Average value
crit	Critical value

dyn	Dynamic value
exit	Pertaining to control volume exit plane
H	High
i	Axial location index
im	Adjacent axial location, i-1
ip	Adjacent axial location, i+1
ijk	Three-dimensional location index, refers to value at location i, j, k
j	Radial location index
jm	Adjacent radial location, j-1
jp	Adjacent radial location, j+1
k	Circumferential location index
km	Adjacent circumferential location, k-1
kp	Adjacent circumferential location, k+1
L	Low
loc	Local value
m	Modified form; minus one
max	Maximum value
min	Minimum value
n	Last location, e.g., in, last axial location in control volume
p	Plus one
radial avg	Average value along a radius, average at constant θ
ref	Reference value
rel	Relative value, usually relative to rotor blade motion

ring avg	Average value along a circle, average at constant r
stall	Value at stall
ss	Steady-state value
sw	Swirl
wh	Wheel
z	Axial component